

# Operational Retrieval of Surface Soil Moisture using Synthetic Aperture Ra- dar Imagery in a Semi-arid Environment

---

Dissertation an der Fakultät für Geowissenschaften  
der Ludwig Maximilians Universität München



Vorgelegt von:

*Lu Dong*

Eingereicht: 10.10.2011



---

Gedruckt mit Unterstützung des Deutschen Akademischen Austauschdienstes

1. Gutachter: Prof. Dr. Ralf Ludwig
2. Gutachter: Prof. Dr. Karsten Schulz

Tag der mündlichen Prüfung: 19<sup>th</sup> December 2011

---

## Abstract

Within the context of the FP7 project CLIMB, according to various climate change scenarios the Mediterranean region will suffer further from higher temperature and less precipitation during the summer, on top of already dry and hot periods for the region. This climatic trend means a higher water usage projection for both urban and agricultural purposes in this already water scarce region. Suitable strategy and management for water usage is important for sustainable agricultural development. In this respect, good irrigation management is helpful for crops growing during summer. For this purpose, surface soil moisture information can be utilised for parameterising hydrological models.

In this dissertation on the *Operational Retrieval of Surface Soil Moisture using Synthetic Aperture Radar Imagery in a Semi-arid Environment*, the possibility and capability of an operational approach for surface soil moisture inversion using Synthetic Aperture Radar (SAR) imagery is investigated. For this topic, a well-equipped research based farm is selected as the study area on the island of Sardinia with its unique Mediterranean climate. The following aspects are focused on:

- 1) Exploration of the capability of current C-band SAR sensors – ASAR and Radarsat-2 – on surface soil moisture retrieval in terms of the accuracy and spatial scale, *e.g.* at field scale;
- 2) Development of a fully operational approach for surface soil moisture monitoring and mapping in the semi-arid environment;
- 3) Assessment of the capability of the Advanced Integral Equation Model (AIEM) in surface soil moisture inversion.

Extensive field work is conducted in the study area from late April to end of June in 2008 and 2009. *In situ* measurements, including surface soil moisture, surface roughness, soil texture, vegetation water content and height, crop distance and structure, and Leaf Area Index (LAI), are taken on corresponding and prepared bare soil fields and crop fields. Field campaigns are arranged in accordance with satellite passes. In total 26 ENVISAT/ASAR APS and 11 Radarsat-2 FQ mode images are acquired during the campaigns on a better than weekly basis.

---

None of the current approaches is applicable as a fully operational approach for surface soil moisture inversion, while roughness parameterisation is crucial but problematic, especially for small-scale studies, where fewer good results are reported from soil moisture inversion at field scale than at larger scales. To explore an operational approach, various existing semi-empirical and theoretical models are adopted. First, backscattering coefficients and *in situ* soil moisture measurements are carefully evaluated against empirical linear relationships according to different polarisations and ranges of incidence angle. Model assessment is taken for the Oh model, Dubois model, and three AIEM based approaches. The AIEM approaches are based on different roughness parameterisations – *in situ* rms height and correlation length, *in situ* rms height and empirical correlation length, and the third is adopting recently-developed Rahman approach, which is based on AIEM regression from multi-angular SAR images in extremely dry conditions. A systematic overestimation of 2–4dB is observed from the Oh model and the AIEM model which is coupled with *in situ* roughness measurements. Good agreement is found from the “AIEM + empirical correlation length” model. The *in situ* correlation length is clearly insufficient for roughness parameterisation at field scale. Afterwards, these approaches are evaluated against *in situ* soil moisture measurements. Semi-empirical models are able to provide reasonable soil moisture production after careful backscattering coefficient “correction” with the help of *in situ* roughness measurements or comparable remote sensing based inversion products. Without backscattering coefficient “correction”, the AIEM model, coupled with empirical correlation length, is able to provide accuracy in the order of 6 vol. %, which is slightly better than the performance in the Rahman approach.

As an operational approach, the Rahman method is further developed by introducing previously proved empirical length after careful consideration of the limitations of the original version, namely the Baghdadi-Rahman model. With one or more SAR images under the extremely dry conditions, surface soil moisture can be inverted with confidence of between 5–6 vol. % at field scale, regardless of SAR geometry. Good results are also achieved on different crop fields.

Outlooks are given on both technical and application perspectives based on further development of the proposed Baghdadi-Rahman model.

---

Overall, it is operationally viable to adopt the AIEM based model to retrieve surface soil moisture (at 5–8 cm depth level) with a confidence of 5–6 vol. % over agricultural fields at field scale on a weekly basis from co-polarisation C-band SAR in the semi-arid environment. The timely and accurate surface soil moisture monitor at field scale and over large areas from various SAR sensors from the proposed Baghdadi-Rahman model, along with a well integrated hydrological model and economic and policy based assessment for irrigation management, will contribute to the future of sustainable water resource management for agricultural usage in the water scarce semi-arid environment within the CLIMB framework.

Keywords: Operational Approach, Surface Soil Moisture, Synthetic Aperture Radar (SAR), Surface Roughness, Advanced Integral Equation Model (AIEM), CLIMB

---

## Preface

The thesis “*Operational Retrieval of Surface Soil Moisture using Synthetic Aperture Radar Imagery in a Semi-arid Environment*” is funded by the Deutscher Akademischer Austausch Dienst (DAAD) through the special programme Studies and Research in Sustainability. The work is carried out in the working group of Prof. Dr Ralf Ludwig in the Department of Geography at the Ludwig-Maximilians-Universität (LMU) Munich.

Radar remote sensing has become an increasingly demanding area of remote sensing in recent decades. Throughout the whole exploration period of the past three and a half years, radar remote sensing has been a challenging yet exciting area to me. I can still remember, when I telephoned my master supervisor, Prof. Daniel Donoghue at Durham University, for his assistance by way of a reference letter for my DAAD scholarship application in the autumn of 2007, he kindly indicated that my subject would be “radar” whereas the work I had mainly been doing was in optical remote sensing. Nevertheless it was my firm decision to do my PhD in Munich.

I am grateful for all the help and support that has been given to me during this time so that the work and thesis can be formulated.

First, I sincerely thank my supervisor at LMU Munich, Prof. Dr Ralf Ludwig, for his permanent support since the very beginning. Without his efficient help, I would not have been able to make a full DAAD scholarship application only two weeks before the deadline. I am also grateful for his support for domestic and international meetings and conferences, where I gained experience and confidence and managed to make some good friends as well as see beautiful places. I was even able to go home twice. Of course it is even greater that we share an interest in the greatest football club in the world – FC Bayern München – “Mia san mia!”

The service from DAAD should be marked with five stars (!) for all aspects. I send my great thanks to our programme coordinator Mrs Cordula Behrsing at DAAD for her excellent work and great patience through these years. Administration issues became far easier with her help. I certainly recommend the “did” deutsch-institut in Munich, which DAAD organised for the scholarship holders, to those who looked forward to enjoying

---

learning German from the very beginning. To me it was one of the best periods in Munich.

Although some of them have found a better way of life of their own after years in research, it was also a great experience to see our group growing. Mr Josef Schmid (preferably addressed as Seppo) and I have known each other since the first two months of the PhD during the hot and sparkling Sardinian summer. I should thank him not least for his most recent help in Matlab coding from the long story of our friendship. Mr Philip Marzahn has always provided his professional and patient advice as well as helping in many organisational roles. Ms Vera Erfurth is always kind and helpful in all the administration work. Thanks to all of the following for helping me integrate in the large group – in alphabetical order, they are: Sascha Berger, Patiwet Chalermpong, Vera Erfurth, Frank Ferber, Gudrun Lampart, Andi Jobst, Jochen Maier, Philip Marzahn, Inga May, Bano Mehdi, Swen Meyer, Dr Markus Muerth and Josef Schmid.

I also thank all other colleagues in the Department of Geography especially for those pleasant summer and Christmas parties and of course for the Oktoberfests. Among them, I appreciate all the help from my previous office mates – Dr Carola Weiß, Ms Johanna Dall’Amico, Mr Florian Schlenz, Mr Matthias Locherer and Mr Toni Frank. Also I truly enjoyed the dinners at Dr Daniel Waldman’s house and with Mr Stefan Härer in both Bavarian and Chinese restaurants. There were also a few cosy winter nights after the DD-seminars with Prof. Karsten Schulz and Dr Matthias Bernhardt. I also thank Ms Vera Falck for her efficient help with poster printing.

For the hard work in Sardinia, I offer grateful thanks to Ms Teresa Brandhuber (then a diploma student) from LMU Munich, Prof. Claudio Paniconi, Dr Imen Gherboudj (who is now at University of Sherbrooke) and Ms Rebecca Fillion from INRS Quebec, Mr Andrea Bez and Mr Filippo Cau from Cagliari and all staff at the *Azienda San Michele* and *AGRIS*. Sometimes, things can still work out with only limited yet communicable words and gestures.

In addition, special thanks are given to Dr Nicolas Baghdadi at CEMAGREF in Montpellier, for his always quick and professional response and suggestions on my research issues, which enlightened me during some of the toughest periods.

---

Hereby I sincerely thank all my friends in Munich – some of whom have now returned home or lived elsewhere in the world – for making my life away from home a lot more colourful. To name a few, they are in alphabetical order Dr Ying Cheng, Kang Deng, Lu Gao, Chen Hu, Dr. Na Li, Yujing Liu, Liang Ma, Xiaoguang Ma, Qi Qi, Dr Jimena Ruiz, Hongji Wang, Lei Wang, Baiquan Xu, Dr Shigeyuki Yamada, Dr Zheng Yin, Wei Zhang, Dr Yi (David) Zhang. I wish you all a happy future!

Last but not least, although they cannot be by my side most of the time, I am still more than happy to have the full support and understanding from my whole family in Wuhan, as well as from my girlfriend Xiaodong (Angelika) Wang.

Please forgive me if any names are forgotten here.

Again, my thanks to you all!

Munich, October 2011

*Lu Dong*



---

# Table of Contents

<b>List of Tables .....</b>	<b>XVII</b>
<b>List of Abbreviations.....</b>	<b>XIX</b>
<b>List of Symbols .....</b>	<b>XXI</b>
<b>Chapter 1 Introduction .....</b>	<b>- 1 -</b>
1.1. Climate Change and Water Security in the Mediterranean Region.....	- 1 -
1.2. The CLIMB Project .....	- 4 -
<b>Chapter 2 Surface Soil Moisture Retrieval Using SAR Remote Sensing – State of the Art .....</b>	<b>- 6 -</b>
2.1. State of the Art.....	- 7 -
<b>Chapter 3 Study Site and Field Characterisation .....</b>	<b>- 11 -</b>
3.1. Study Area .....	- 11 -
3.1.1. Sardinia and <i>Campidano</i> Plain.....	- 11 -
3.1.2. <i>Rio Mannu di San Sperate</i> .....	- 13 -
3.1.3. Climate .....	- 13 -
3.1.4. <i>Azienda San Michele</i> .....	- 16 -
3.2. Field Measurements.....	- 18 -
3.2.1. <i>In situ</i> measurement overview.....	- 18 -
3.2.2. Soil moisture.....	- 20 -
3.2.3. Roughness .....	- 27 -
3.2.4. Geophysical characteristics of bare fields.....	- 34 -
3.2.5. Crop fields .....	- 41 -
3.2.6. Crop field database .....	- 43 -
3.2.7. Other measurements .....	- 46 -
3.3. Summary .....	- 47 -

---

**Chapter 4 Synthetic Aperture Radar..... - 49 -**

4.1. Radar Fundamentals ..... - 49 -

4.2. Synthetic Aperture Radar ..... - 50 -

    4.2.1. SAR geometry ..... - 51 -

    4.2.2. Geometric distortion of SAR images ..... - 54 -

    4.2.3. SAR imagery processing ..... - 55 -

    4.2.4. Space-borne SAR sensors ..... - 64 -

4.3. C-band Microwave Interaction with Surface Geophysical Parameters ..... - 67 -

    4.3.1. Microwave interaction with surface geometric properties ..... - 68 -

    4.3.2. Microwave interaction with soils ..... - 69 -

4.4. SAR Imagery ..... - 69 -

4.5. Summary ..... - 71 -

**Chapter 5 Soil Moisture Retrieval Model – Evaluation and Assessment ..... - 73 -**

5.1. Model Description ..... - 73 -

    5.1.1. Semi-empirical models ..... - 74 -

    5.1.2. The theoretical model(s) ..... - 83 -

5.2. Data Verification ..... - 92 -

5.3. Model Evaluation ..... - 96 -

    5.3.1. Oh model ..... - 97 -

    5.3.2. Dubois model ..... - 101 -

    5.3.3. The semi-empirical model for ERS imagery evaluation ..... - 102 -

    5.3.4. AIEM evaluation ..... - 103 -

5.4. Model Assessment ..... - 107 -

    5.4.1. Oh model ..... - 107 -

    5.4.2. Dubois model ..... - 109 -

    5.4.3. The semi-empirical model for ERS imagery ..... - 109 -

    5.4.4. AIEM ..... - 110 -

5.5. Summary ..... - 118 -

**Chapter 6 Model Development, Evaluation and Sensitivity Analysis ..... - 122 -**

6.1. Rationale and Description of the Updated Rahman Approach ..... - 123 -

---

6.1.1. The model rationale— Limitations of Rahman approach .....	- 123 -
6.1.2. Description of the Baghdadi-Rahman model .....	- 124 -
6.1.3. Pre-assumption of the Baghdadi-Rahman model .....	- 124 -
6.2. Baghdadi-Rahman Model Assessment.....	- 124 -
6.2.1. The first assessment.....	- 124 -
6.2.2. In-field variability correction in extremely dry conditions .....	- 127 -
6.2.3. Application in crop fields.....	- 130 -
6.3. Evaluation of Baghdadi-Rahman Model.....	- 131 -
6.3.1. Oh model.....	- 131 -
6.3.2. AIEM .....	- 139 -
6.4. Sensitivity Analysis .....	- 141 -
6.4.1. Parameterisation of the AIEM simulation.....	- 141 -
6.4.2. Description of the AIEM simulation .....	- 142 -
6.4.3. Impact factor .....	- 144 -
6.5. Summary .....	- 146 -
<b>Chapter 7 Conclusion and Outlook.....</b>	<b>- 148 -</b>
7.1. Conclusions .....	- 148 -
7.2. Outlook.....	- 150 -
<b>References .....</b>	<b>- 152 -</b>
<b>Appendix A Regression Results for Adapted Rahman Approach .....</b>	<b>- 161 -</b>
<b>Appendix B Surface Soil Moisture Maps from the Baghdadi-Rahman Model... -</b>	<b>165 -</b>
<b>Curriculum Vitae .....</b>	<b>- 171 -</b>

---

## Table of Figures

<i>Figure 1.1 Schematic framework representing impacts of and responses to climate change and their linkages in the earth and human systems, reproduced from (IPCC 2007). .....</i>	<i>2 -</i>
<i>Figure 1.2 Relative percentage change in precipitation patterns – 2090–2099 vs. 1980–1999 based on the SRES A1B scenario for December to February (left) and June to August (right) (IPCC – WG1 – AR4). .....</i>	<i>2 -</i>
<i>Figure 1.3 Relative percentage change in runoff patterns for the period 2041–2060 based on the SRES A1B scenario, divided by 1900–1970 runoff. Reproduced from (Milly et al. 2005). Reproduction permitted by the publisher for this thesis. ....</i>	<i>3 -</i>
<i>Figure 1.4 Conceptual framework of CLIMB.....</i>	<i>4 -</i>
<i>Figure 3.1 Overview of the island of Sardinia masked by 10m spacing DTM grids obtained from Sardinia Territory – Planning and Landscape of Sardinia (Sardegna Territorio – Pianificazione e Paesaggio della Sardegna, <a href="http://www.sardegнатerritorio.it">http://www.sardegнатerritorio.it</a>). Major locations, the Rio Mannu di San Sperate Basin and the Campidano Plain, are marked. The study site, Azienda San Michele is located between the villages Ussana and Donori on the eastern edge of the Campidano Plain.....</i>	<i>12 -</i>
<i>Figure 3.2 Maximum temperature and precipitation during campaign periods – top: 2008 and bottom: 2009 (Data retrieved from the European Climate Assessment and Dataset project (<a href="http://eca.knmi.nl/">http://eca.knmi.nl/</a>) based on information from the Cagliari meteorological station).....</i>	<i>15 -</i>
<i>Figure 3.3 Modified figure from (Duce et al. 2004) showing the increasing trend of August and yearly average temperatures for north-west Sardinia for the period 2005 to 2099 from scenario B2. ....</i>	<i>15 -</i>
<i>Figure 3.4 Photo of corner reflector set up with Seppo Schmid and Dr Imen Gherboudj on 2<sup>nd</sup> May 2008. ....</i>	<i>18 -</i>
<i>Figure 3.5 Study fields are marked with field ID, coloured by land use in the Azienda San Michele in the UTM system with a geo-referenced aerial photo as background..</i>	<i>18 -</i>
<i>Figure 3.6 Exemplifying SP selection scheme by Field 32 and 10m spacing DTM grids obtained from Sardinia Territory – Planning and Landscape of Sardinia (Sardegna Territorio – Pianificazione e Paesaggio della Sardegna (<a href="http://www.sardegнатerritorio.it/">http://www.sardegнатerritorio.it/</a>)).</i>	<i>20 -</i>
<i>Figure 3.7 Two photos of SPs on one bare field taken on 2<sup>nd</sup> May 2008 and on one broad bean field taken on 7<sup>th</sup> May 2008. ....</i>	<i>20 -</i>

---

Figure 3.8 Taking soil samples for gravimetric soil moisture. In the photo: Seppo Schmid and the shadow of the author. Date: 3 <sup>rd</sup> May 2008.....	- 23 -
Figure 3.9 Putting wet soil samples into aluminium containers. In the photo: Andrea Bez. Date: 2 <sup>nd</sup> May 2009. ....	- 24 -
Figure 3.10 UMS INFIELD7 (left) and a broken ThetaProbe ML2x probe (right). ....	- 25 -
Figure 3.11 Comparison of surface soil moisture between gravimetric approach and using ThetaProbe ML2x at both 1–4 cm and 5–8 cm depths over the years 2008 and 2009, showing RMSE are 4.3 vol. % and 3.4 vol. % for comparisons on a sample point basis and on field averaged value basis, respectively.....	- 26 -
Figure 3.12 Photogrammetry system with aluminium frames, GCPs and Rollei d7 metric camera. ....	- 30 -
Figure 3.13 A pair of stereo photos taken on a sample point and the original colour photos are adjusted to 0-255 grey scale.....	- 31 -
Figure 3.14 Illustration of the terms and symbols in the semivariogram. ....	- 33 -
Figure 3.15 Soil moisture change and precipitation in mm through the campaigns of 2008 at both 1–4 cm and 5–8 cm depths for each study field. ....	- 36 -
Figure 3.16 Soil moisture change and precipitation in mm through the campaigns of 2009 at both 1–4 cm and 5–8 cm depths for each study field. ....	- 38 -
Figure 3.17 The variability of the rms height $s$ for four study fields during the two campaigns with the first two measurements of F11, F21 and F31 taken in 2008 while others were taken in 2009. ....	- 38 -
Figure 3.18 The variability of the correlation length $l$ with exponential autocorrelation function (top) and Gaussian autocorrelation function (bottom) for three study fields during the two campaigns with the first measurement of F21 and the first two measurements of F11 taken in 2008 and the others taken in 2009. ....	- 39 -
Figure 3.19 The field averaged standard deviation of the correlation length (with $R^2$ of 0.82 for exponential and of 0.64 for Gaussian ACFs) increases with the field averaged standard deviation of the rms height. ....	- 41 -
Figure 3.20 Field photos as (a) an overview of the wheat field W1 taken on 7 <sup>th</sup> May 2008, (b) a crop coverage photo taken on the bean field B1 on 8 <sup>th</sup> May 2008, (c) a plant profile photo on the canola field C1 taken on 6 <sup>th</sup> June 2008 and (d) a plant profile photo on the bean field B1 taken on 8 <sup>th</sup> May 2008.....	- 42 -

---

Figure 3.21 Temporal variability of surface soil moisture on crop fields in 2008 (top) and 2009 (bottom).....	44 -
Figure 3.22 Temporal variability of the vegetation water content on crop fields in 2008 (top) and 2009 (bottom).....	45 -
Figure 3.23 Temporal variability of the LAI on crop fields in 2008 (top) and 2009 (bottom)..	46 -
Figure 3.24 Soil texture triangle according to the USDA classification scheme (USDA 2011).	47 -
Figure 4.1 Illustration of geometry of a basic monostatic SAR system. ....	51 -
Figure 4.2 The synthetic aperture geometry. ....	52 -
Figure 4.3 An illustration of the geometric distortion in the SAR imagery assuming three identical surface structures.....	55 -
Figure 4.4 Illustration of EM wave vertical polarisation (top) and horizontal polarisation (bottom) after (Woodhouse 2006). ....	57 -
Figure 4.5 Different surface roughness status of the scattered field. Left: perfectly smooth surface; Middle: slightly rough surface; Right: very rough surface. ....	69 -
Figure 5.1 Geometry of the scattering problem. ....	83 -
Figure 5.2 Backscattering coefficients against surface soil moisture at 1–4 cm and 5–8 cm depths compared with empirical linear relationship derived from Baghdadi et al. (2006b) with (a) and (b) for HH polarisation and (c) for VV polarisation. ....	95 -
Figure 5.3 In-field backscattering coefficient variability from HH and VV polarisations for each study field on a pixel basis – each dot represents the standard deviation of backscattering coefficients from all pixels on each study field for one satellite pass. .	96 -
Figure 5.4 In-field variability of backscattering coefficients for both HH and VV polarisations on a pixel basis and local incidence angles. ....	96 -
Figure 5.5 Backscattering coefficients $\sigma_{HH}^0$ , $\sigma_{VV}^0$ and $\sigma_{HV}^0$ from SAR and estimations from Oh model 2002 and 2004 versions by using in situ field measurements. ....	99 -
Figure 5.6 Derived co-polarised ratio $p$ and co-polarised ratio $q$ from SAR imagery compared with estimated values from Oh 2002 (b) and 2004 (c) models by using in situ measurements. ....	101 -
Figure 5.7 Measured and estimated $\sigma_{hh}^0$ and $\sigma_{vv}^0$ from the Dubois model. ....	102 -
Figure 5.8 Comparison of SAR co-polarised backscattering coefficients from both ASAR and Radarsat-2 imagery and simulated backscattering coefficients by using the semi-	

---

empirical model for ESA imagery and in situ surface soil moisture measurements at 1–4 cm depth (a) and at 5–8 cm depth (b). .....	- 103 -
Figure 5.9 Estimated $\sigma_{HH}^0$ and $\sigma_{VV}^0$ derived from SAR and from the AIEM parameterised by in situ soil moisture $m_v$ , $s$ and $l$ ((a) and (b): exponential correlation function; (c) and (d): Gaussian correlation function) and by in situ soil moisture $m_v$ , $s$ and $l_{opt}$ ((e) and (f)) in terms of the local incidence angle. ....	- 107 -
Figure 5.10 Comparison between in situ surface soil moisture measurements (at 1–4 cm and 5–8 cm depths) and estimated values from $\sigma_{VV}^0$ , local incidence angle $\vartheta$ and effective rms height $ks$ . ....	- 108 -
Figure 5.11 Comparison between in situ surface soil moisture measurements (at 1–4 cm and 5–8 cm depths) and estimated values from $\sigma_{HV}^0$ , local incidence angle $\vartheta$ and effective rms height $ks$ . ....	- 108 -
Figure 5.12 Comparisons between in situ soil moisture measurements (at 1–4 cm (a) and 5–8 cm (b) depths) and estimated values using the semi-empirical model for ERS imagery. ....	- 110 -
Figure 5.13 Comparison between in situ soil moisture at 10 cm depth and estimated values by averaging estimations from the semi-empirical model for ERS imagery. ....	- 110 -
Figure 5.14 Comparisons between in situ soil moisture measurements (at 1–4 cm (a) and 5–8 cm (b) depths) and estimated values by using the AIEM with in situ measurements of $s$ and $l$ . ....	- 111 -
Figure 5.15 Comparison between in situ soil moisture at 5–8 cm depth and the average estimation by using the AIEM with in situ $s$ and $l$ . ....	- 112 -
Figure 5.16 Empirical correlation length and rms height for different incidence angle ranges and polarisations . ....	- 113 -
Figure 5.17 Comparisons between in situ soil moisture measurements (at 1–4 cm (a) and 5–8 cm (b) depths) and estimated values by using the AIEM with empirical correlation $l_{opt}$ . ....	- 114 -
Figure 5.18 Comparison between in situ soil moisture at 5–8 cm depth and the average estimation using the AIEM with empirical correlation length $l_{opt}$ . ....	- 114 -
Figure 5.19 In situ soil moisture measurement at 5–8 cm depth and Rahman estimations from $\sigma_{HH}$ . ....	- 118 -
Figure 6.1 Estimated soil moisture from both co-polarisations using Baghdadi-Rahman model and in situ soil moisture at 5–8 cm depth. ....	- 126 -

---

Figure 6.2 Averaged estimation from Baghdadi-Rahman model and in situ soil moisture at 5–8 cm depth. ....	- 127 -
Figure 6.3 Estimated soil moisture from both co-polarisations using the improved Baghdadi-Rahman model and in situ soil moisture at 5–8 cm depth. ....	- 129 -
Figure 6.4 Averaged estimation from the improved Baghdadi-Rahman model and in situ soil moisture at 5–8 cm depth.....	- 129 -
Figure 6.5 Estimated soil moisture errors and local incidence angle. ....	- 130 -
Figure 6.6 Soil moisture estimation from the Baghdadi-Rahman model and in situ soil moisture at 5–8 cm depth in crop fields, with separated RMSE for soil moisture lower than 20 vol. % and higher than 20 vol. %.....	- 130 -
Figure 6.7 Oh model performance using estimated ks and kl from $\sigma_{HH}^0$ using the Baghdadi-Rahman approach. ....	- 135 -
Figure 6.8 Oh model performance using estimated ks and kl from $\sigma_{VV}^0$ using the Baghdadi-Rahman approach. ....	- 138 -
Figure 6.9 Baghdadi-Rahman model evaluation through backscattering coefficient comparison between values derived from SAR imagery and simulated by the AIEM using in situ soil moisture values at 5–8 cm depth and estimated roughness ((a) from HH polarisation and (b) from VV polarisation) using the Baghdadi-Rahman model.-	- 140 -
Figure 6.10 Relationships between (a) incidence angle $\vartheta$ and $\sigma_{HH}^0$ ; (b) incidence angle $\vartheta$ and $\sigma_{VV}^0$ ; (c) correlation length $l$ and $\sigma_{HH}^0$ ; (d) correlation length $l$ and $\sigma_{VV}^0$ ; (e) surface soil moisture $m_v$ and $\sigma_{HH}^0$ ; (f) surface soil moisture $m_v$ and $\sigma_{VV}^0$ ; (g) rms height $s$ and $\sigma_{HH}^0$ and (h) rms height $s$ and $\sigma_{VV}^0$ plotted from the AIEM simulation. ....	- 144 -



# List of Tables

<i>Table 3.1 Climate statistics from Cagliari Elmas meteorological station for the years 1971–2000</i>	- 14 -
<i>Table 3.2 Modified table from (Duce et al. 2004) for LCA class change in terms of the area as a percentage of the total area of Sardinia with reference to period 1961–2000 and future climate change scenarios A2 and B2.</i>	- 16 -
<i>Table 3.3 Size and soil texture of the bare fields in the Azienda San Michele.</i>	- 17 -
<i>Table 3.4 Size of crop fields in the Azienda San Michele.</i>	- 17 -
<i>Table 3.5 Dataset through the year 2008–2009 for the Azienda San Michele.</i>	- 19 -
<i>Table 3.6 Rollei d7 interior orientation in the photogrammetric system in mm.</i>	- 31 -
<i>Table 3.7 GCP coordinates in cm of the photogrammetric system.</i>	- 31 -
<i>Table 3.8 In situ geophysical characteristics.</i>	- 34 -
<i>Table 3.9 Mean in-field variability of surface geophysical parameters for all dates.</i>	- 40 -
<i>Table 3.10 Soil texture and size of each test field.</i>	- 47 -
<i>Table 4.1 Mostly used microwave bands and their frequency and wavelength range.</i>	- 49 -
<i>Table 4.2 Technical configurations for different ASAR measurement modes.</i>	- 65 -
<i>Table 4.3 Technical configurations of different image swathes derived and adapted from (ESA 2007).</i>	- 66 -
<i>Table 4.4 Technical configurations of SLC data for different Radarsat-2 imaging modes adapted from (MDA 2011).</i>	- 67 -
<i>Table 4.5 SAR imagery collection.</i>	- 70 -
<i>Table 4.6 Range of backscattering coefficients <math>\sigma_{HH}^0</math>, <math>\sigma_{VV}^0</math> and <math>\sigma_{HV}^0</math> in dB, in situ surface soil moisture at 1–4 cm and 5–8 cm depths-<math>m_v</math> 1–4 cm and <math>m_v</math> 5–8 cm in vol. %, rms height <math>s</math> in cm and correlation length for Gaussian and exponential function <math>l_{Gau}</math> and <math>l_{exp}</math> in cm for each satellite acquisition.</i>	- 71 -
<i>Table 5.1 RMSE of the co-polarised ratio <math>p</math>, the cross-polarised ratio <math>q</math> and the backscattering coefficients from HH, VV and HV polarisations by using both 2002 and 2004 versions of the Oh model.</i>	- 97 -
<i>Table 5.2 Bias of the co-polarised ratio <math>p</math>, the cross-polarised ratio <math>q</math> and the backscattering coefficients from HH, VV and HV polarisations by using both 2002 and 2004 versions of the Oh model.</i>	- 97 -

---

Table 5.3 Selected SAR images with large local incidence angle differences but similar surface geophysical conditions for model regression step 1. .... - 116 -

Table 5.4 Coefficients for Rahman approach step 1. .... - 116 -

Table 5.5 Z-index for each field and polarisation. .... - 116 -

Table 5.6 Selected SAR images in extremely dry surface soil conditions for model regression. .... - 117 -

Table 5.7 Estimated  $k_s$  and  $k_l$  using the AIEM for each field and polarisation. .... - 117 -

Table 5.8 Soil moisture conversion statistics. .... **Error! Bookmark not defined.**

Table 6.1 Estimated  $k_s$  and  $k_l$  using the Baghdadi-Rahman model for each field and polarisation. .... - 126 -

Table 6.2 Selected SAR images for extremely dry surface soil conditions for model regression. .... - 127 -

Table 6.3 Estimated  $k_s$  and  $k_l$  using the improved Baghdadi-Rahman model for each field and polarisation. .... - 128 -

Table 6.4 Comparison between Oh model performance using in situ roughness measurements and roughness estimations from Baghdadi-Rahman model in terms of RMSE and bias for the model products. .... - 139 -

Table 6.5 Comparison between all backscattering coefficient simulations using the AIEM. - 141 -

Table 6.6 Statistics of the impact factor  $\xi$  of incidence angle  $\vartheta$ , rms height  $s$ , correlation length  $l$  and soil moisture  $m_v$  on backscattering coefficients of HH and VV polarisations. - 145 -

---

## List of Abbreviations

ACF	Autocorrelation Function
AIEM	Advanced Integral Equation Model
APS	Alternating Polarisation Mode
ASAR	Advanced Synthetic Aperture Radar
CLIMB	Climate Induced Changes on the Hydrology of Mediterranean Basins
CSA	Canadian Space Agency
DEM	Digital Elevation Model
DLR	German Aerospace Centre
DN	Digital Number
DTM	Digital Terrain Model
EM	Electromagnetic
ERS	European Remote Sensing Satellite
ESA	European Space Agency
GCP	Ground Control Point
GMM	Global Monitoring Mode
GO	Geometric-Optical Model
GPS	Global Positioning System
IPCC	Intergovernmental Panel on Climate Change
IEM	Integral Equation Model
JAXA	Japan Aerospace Exploration Agency
LAI	Leaf Area Index
LCA	Land Capability for Agriculture
LOOCV	Leave-One-Out-Cross-Validation
LPS	Leica Photogrammetry Suite
LUT	Look-Up-Table
m.a.s.l.	meter above sea level
MDA	MacDonald Dettwiler and Associate Ltd.

---

MLD	Multi-Look Detected
NMM3D	Numerical Maxwell Model in 3-D Simulations
NRCS	Normalised Radar Cross-Section
KA	Kirchhoff Approximation
PRI	Precision Images
RAR	Real Aperture Radar
RMSE	Root Mean Square Error
rms height	root mean square height
SAR	Synthetic Aperture Radar
SLAR	Side-Looking Airborne Radar
PDF	Probability Density Function
SLC	Single Looking Complex
SSM	Surface Soil Moisture
SP	sample point
SPM	Small Perturbation Method
SRES	Special Report on Emissions Scenarios
TDR	Time Domain Reflectometer
TanDEM-X	TerraSAR-X add-on for Digital Elevation Measurement
UHF	Ultra High Frequency
WS	Wide Swath
WP	Work Package

---

## List of Symbols

rms height	$s$
Correlation length	$l$
Wave number	$k$
Volumetric soil moisture	$m_v$
Gravimetric soil moisture	$m_g$
Mass of water	$M_w$
Mass of dry soil	$M_s$
Volume of water in the soil sample	$V_w$
Total volume of the soil sample	$V_t$
Volume of the dry soil in the soil sample	$V_s$
Volume of pores in the soil sample	$V_f$
Volume of air in the soil sample	$V_a$
Porosity	$f$
Water density	$\rho_w$
Dry bulk density	$\rho_h$
Dielectric constant	$\epsilon_r$
Height of the sample point $i$ during DEM generation	$Z_i$
Mean height of all points in during DEM generation	$\bar{Z}$
Spatial resolution of profile during DEM generation	$\Delta x$
Height of the point with horizontal displacement $j$ from the point $i$	$Z_{i+j}$
Semivariogram with lag as $x'$	$\gamma(x')$
variance	$c$
Gaussian correlation length	$l_{Gau}$
Exponential correlation length	$l_{Exp}$

---

Zenith angle	$\theta_z$
Gap fraction at the view zenith angle	$P(\theta_z)$
Look angle	$\theta_l$
Depression angle	$\theta_d$
Incidence angle	$\theta_i$
Local incidence angle	$\theta$
Velocity	$v$
Wavelength	$\lambda$
Slant range resolution	$\rho_s$
Speed of light	$c_0$
Bandwidth of the chirped pulse	$B_p$
Ground range resolution	$\rho_g$
Absolute speed of sensor along azimuth direction	$V_s$
Relative speed of the sensor along range direction	$V_r$
Time the SAR can differentiate signal	$T_d$
Doppler bandwidth	$B_D$
Angle between velocity vector and target	$\theta_a$
Length of SAR antenna	$D$
Amplitude of wave	$A$
Phase	$\Phi$
Electric field vector	$E$
Stokes parameter	$I_0, Q, U \text{ and } V$
Real part	$Re$
Imaginary part	$Im$
Orientation angle	$\psi$
Ellipticity angle	$\chi$

---

Incidence Stokes vector	$g_i$
Scattered Stokes vector	$g_s$
Mueller matrix	$M$
Range	$R$
Scattering matrix	$S$
Target vector	$K$
Coherency matrix	$T$
Pauli basis	$K_P$
Covariance matrix	$C$
Scattering cross-section	$\sigma$
Backscattering cross-section	$\sigma_b$
Energy intensity	$I_r$
Incidence energy intensity	$I_i$
Backscattering coefficient	$\sigma^0$
Brightness	$\beta^0$
Intensity of the pixel (i,j)	$I_{i,j}$
Antenna pattern gain	$G$
Cross-polarised ratio	$q$
Co-polarised ratio	$p$
Fresnel reflectivity	$\Gamma_0$
Roughness spectrum	$W_k$
Probability density function	$\emptyset$
Relative permittivity	$\mu_r$
Optimal correlation length	$l_{opt}$

Learn without thinking begets ignorance.  
Think without learning is dangerous.

---Confucius

## Chapter 1 Introduction

Natural Earth systems and human societal systems are closely linked with enormous complexity and interaction (Figure 1.1). As a crucial component in the Earth system, climate change has been raised and has become central as an issue overwhelmingly among scientists but also politicians as well as ordinary society members all over the globe during the past decades. Over 250 000 publications in science and social science alone refer to the topic of climate change dating back to the 19<sup>th</sup> century (through simply searching on the Web of Knowledge). The impacts of climate change will lead to the vulnerability of ecosystems, water resources and human health etc directly or indirectly, which will hence force socio-economic development to better adapt to the changes in the Earth systems. In this context, water resource vulnerability in the climate change conditions is focused on in this work.

### 1.1. Climate Change and Water Security in the Mediterranean Region

The latest synthesis report from the *Intergovernmental Panel on Climate Change (IPCC 2007)* emphasises the vulnerability of the Mediterranean and neighbouring regions to the impacts of climate change in numerous climate projections, which are based on various global and regional climate models (**Blenkinsop and Fowler 2007; Flocas et al. 2011**). In particular, water availability will deteriorate in the already water-stressed Mediterranean region (**Arnell 2004**). Even worse, the already hot and semi-arid climate is expected to become warmer and drier under various climate change scenarios (**IPCC 2007**), which hence will in turn put higher pressure on the vulnerability of freshwater resources in this region (**Vorosmarty et al. 2000**).

Both historical observations and modelling-based climate projections show that the mean temperature in the central-west Mediterranean region is on an upward trajectory. About 0.8°C/100 year increase is found for the 20<sup>th</sup> century and this figure can reach 5–



7°C for summers and 3–4°C for winters *e.g.* for the Iberian peninsula by the end of the 21<sup>st</sup> century (Diffenbaugh et al. 2007). This potential trend of surging temperature will result in an intensified hydrological cycle for the Mediterranean region with increasing extreme precipitation events and a significant decrease in annual precipitation (Norrant and Douguedroit 2006; Ludwig et al. 2011).

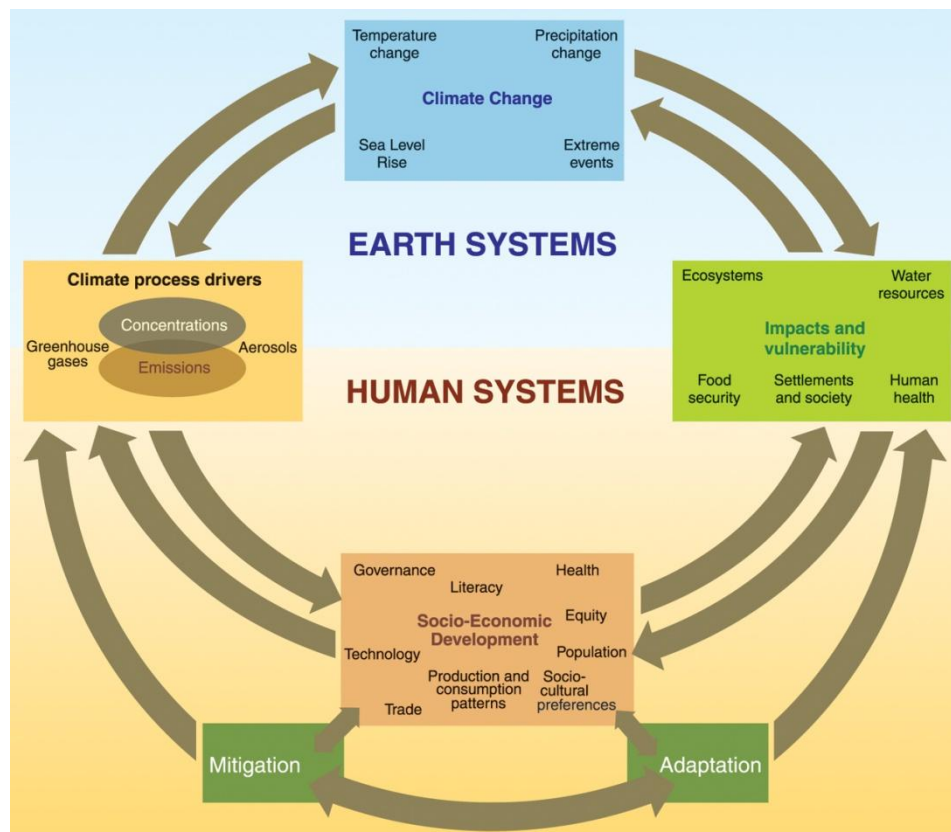


Figure 1.1 Schematic framework representing impacts of and responses to climate change and their linkages in the earth and human systems, reproduced from (IPCC 2007).

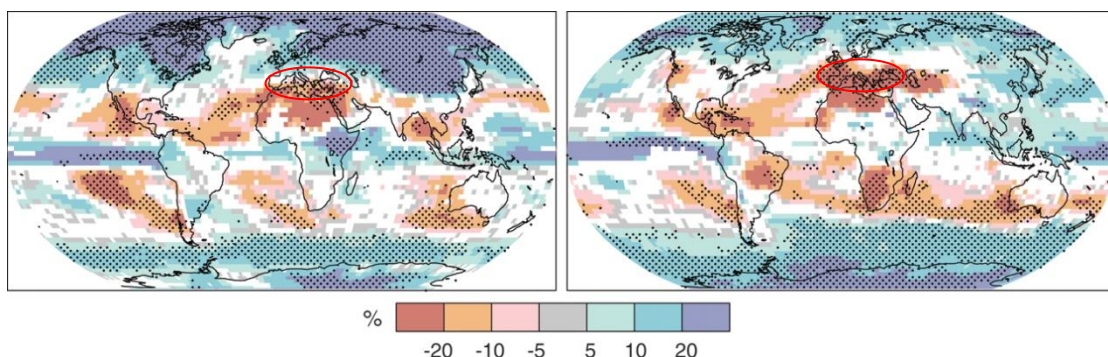
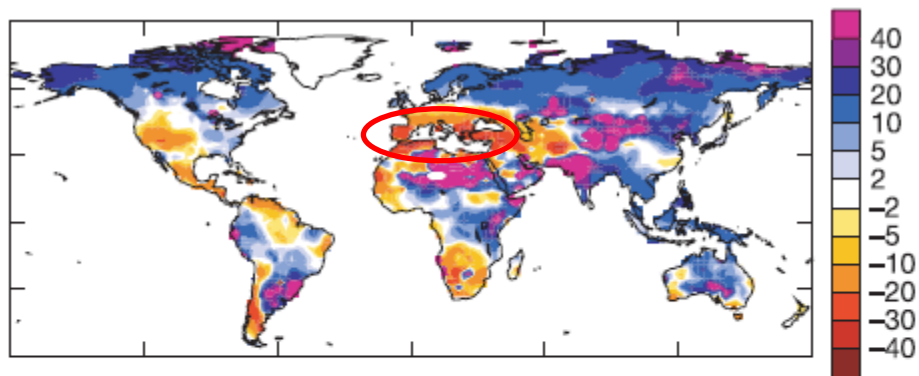


Figure 1.2 Relative percentage change in precipitation patterns – 2090–2099 vs. 1980–1999 based on the SRES A1B scenario for December to February (left) and June to August (right) (IPCC – WG1 – AR4).

Figure 1.2 shows significant negative change in annual precipitation for the Mediterranean region (circled in red) with a multi-model averaged projection to the last ten years of the 21<sup>st</sup> century compared to the 1980–1990 period based on the Special Report on Emissions Scenarios (SRES) A1B (IPCC 2007). In addition, modelled groundwater recharge dropped severely, by more than 70%, along the south rim of the Mediterranean Sea compared to the period 1961–1990 (IPCC 2007), which is confirmed by recent studies in the ENSEMBLES project (van der Linden and Mitchell 2009). Consequently, Figure 1.3 illustrates negative runoff change based on the SRES A1B scenario for the Mediterranean catchments for the period 2041–2060 compared to the period 1900–1970 (Milly et al. 2005). Strong increases in drought frequencies due to both climate change and water consumption impacts are expected over Southern Europe under the A2 scenario (Weiß et al. 2007).



**Figure 1.3** Relative percentage change in runoff patterns for the period 2041–2060 based on the SRES A1B scenario, divided by 1900–1970 runoff. Reproduced from (Milly et al. 2005). Reproduction permitted by the publisher for this thesis.

Based on the above projections, uncertainties in freshwater security, including water limitation, scarcity and quality concerns for the Mediterranean region are raised, whereas the changes in the hydrologic cycle will give rise to increasing potential for tensions and conflict among the political and economic factors in the Mediterranean region (Ludwig et al. 2011). The IPCC raised plans for adoption by different sectors (IPCC 2007). For the agriculture sector, therefore, good water use and irrigation management has to be implemented at both strategy and policy framework levels in a new conceptual framework to significantly reduce existing uncertainties in climate change impact analysis. This purpose is closely implemented within the European Union 7<sup>th</sup>

Framework Programme – Climate Induced Changes on the Hydrology of Mediterranean Basins (CLIMB).

## 1.2. The CLIMB Project

The CLIMB consortium ([www.climb-fp7.eu](http://www.climb-fp7.eu)), coordinated by Prof. Dr Ralf Ludwig at the Ludwig-Maximilians-Universität Munich, is constituted by a total of nineteen partners, comprising four European Member States (Italy, Austria, Germany, and France), four SICA countries (Turkey, Tunisia, Egypt, Palestinian-administered areas) and one non-EU member country (Canada). CLIMB is embedded in a cluster of independent EU-projects with Water Availability and Security in Southern Europe and the Mediterranean (WASSERMed) and Climate Change, Hydro-Conflicts and Human Security (CLICO).

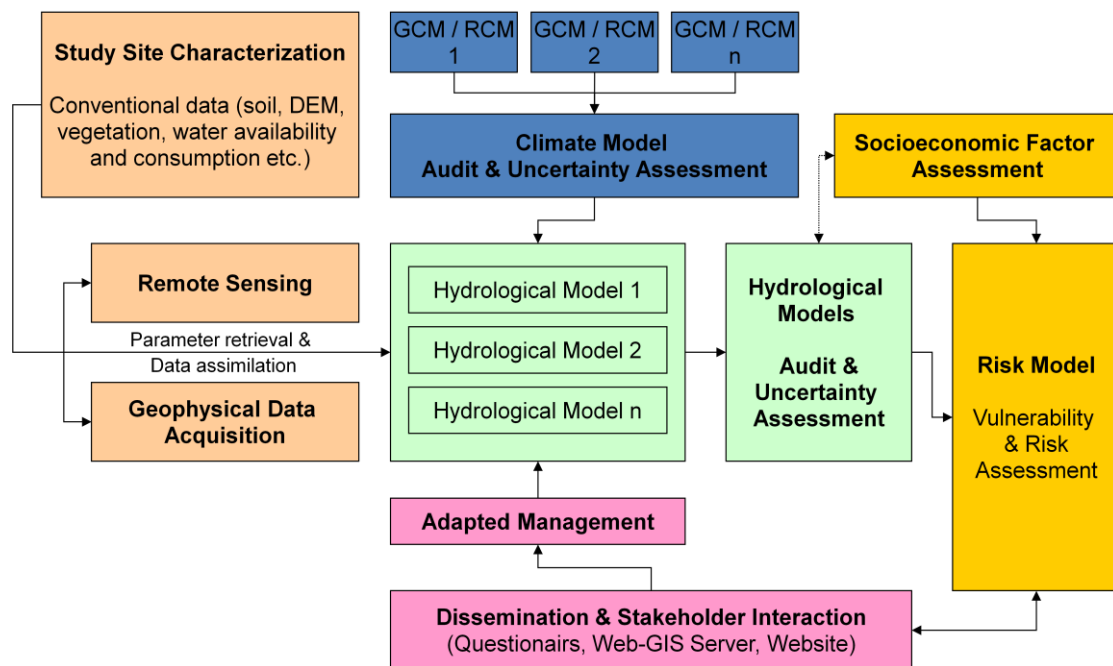


**Figure 1.4 Conceptual framework of CLIMB**

The project is targeted towards the quantification of and, ultimately, a reduction in uncertainties in the understanding of climate change impacts on the water sector in the Mediterranean and assessing and communicating the associated risks for water security in the region. One of the main targets will be to create an integrated risk assessment tool for adaptive water resource management and best agricultural practice under climate

change conditions. A total of seven study sites are chosen including the *Rio Mannu di San Sperate* in Southern Sardinia, Italy.

The conceptual framework of CLIMB comprises eight Work Packages (WPs) as demonstrated in Figure 1.4. This work focuses on study site characterisation and parameter retrieval using remote sensing techniques.

Study the past, if you would divine the future.

---Confucius

## **Chapter 2 Surface Soil Moisture Retrieval Using SAR Remote Sensing – State of the Art**

Although representing only 0.0012% of all water available on Earth, surface soil moisture plays a crucial role in different hydrological processes (**Chow et al. 1988**). It controls the infiltration rate of the precipitation, and hence the amount of runoff the precipitation event produces, which then influences erosion processes and potential flooding impacts (**Wei et al. 2007; Abu-Zreig et al. 2011; Li et al. 2011**). Furthermore, surface soil moisture has impacts on the evapotranspiration rate and thus the micro-meteorology (**Liang et al. 2010; Vivoni et al. 2010; Schelde et al. 2011**) and hence interferes with energy flux and carbon cycles (**Walker and Houser 2004**). This study highlights the importance of surface soil moisture on its temporal and spatial variation concerning important water resource management decisions (**Verhoest et al. 2008**), such as irrigation management (**Bailey et al. 1996; Vedula and Kumar 1996; Bastiaanssen et al. 2000; Zribi et al. 2011**). Within the context introduced in Chapter 1, well monitored surface soil moisture at both fine time and spatial resolutions is required to assist good water-use and irrigation management at both strategy and policy framework levels through hydrological modelling under the climate change uncertainties in the Mediterranean region.

Wagner (**2007**) reviewed the progress in soil moisture retrieval from three types of microwave sensors and concluded that upcoming radiometer and scatterometer systems will be able to assist an operational approach for coarse-scale (25–50 km) soil moisture measurements within a few years, while much more effort is necessary for a scale finer than 1 km from Synthetic Aperture Radar (SAR). This is due to a strong difficulty in characterising surface roughness for site-independent modelling. Similar conclusions are agreed by Thoma et al. (**2008**).

Since several satellite-borne sensors were launched in the 1990s, SAR is the most common imaging active microwave configuration to provide small-scale soil moisture patterns thanks to its high resolution of a few square metres and its operational capability under all weather conditions as well as day and night (**Moran et al. 2004; Wagner et al. 2007; Verhoest et al. 2008**). Studies show that to positively impact soil moisture forecasts, several conditions are to be met: a better than 5 vol. % accuracy of near-surface soil moisture; observations at half the land surface model spatial resolution; and 1–5 day repeat time. The latter is less important than accuracy requirements and the spatial resolution (**Walker and Houser 2004**). With the combination of the currently operated SAR sensors – *e.g.* ASAR and Radarsat-2 – the repeat time requirement can also be satisfied (**Baghdadi et al. 2008**). In terms of the measurement depth, microwave penetration depth is found to increase with the wavelength and decrease with soil moisture value, *e.g.* a wave at 4GHz frequency (C-band, equivalent to a wavelength of 7.5 cm) penetrates to a depth of over 20 cm in absolutely dry soil and to marginally deeper than 1 cm when soil moisture reaches 40 vol. % in loamy soil (**Ulaby et al. 1996**). SAR backscatter from the Earth's surface is sensitive to surface soil moisture (a combination of dielectric constant and soil properties) and surface roughness – normally parameterised by the rms height  $s$ , correlation length  $l$  and autocorrelation function (ACF) (**Baghdadi et al. 2007; Zribi et al. 2007**). In addition, SAR imaging geometry, *e.g.* incidence angle  $\theta$  and polarisation, will also largely influence the received backscattered signal for a given wavelength. Note that the above terminology will be explained in Chapter 3 and Chapter 4.

## **2.1. State of the Art**

Most studies, if not all, have aimed at an operational solution for surface soil moisture retrieval at a better accuracy for hydrological models at different spatial scales. For both flood forecasting and drought monitoring, a good knowledge of root zone soil moisture at the catchment or smaller scales helps considerably for the accuracy of estimations (**Wagner et al. 2007**). Various studies show good agreement with SAR based soil moisture retrieval and *in situ* measurements on big or small catchment scales, but a great dispersion in between is more likely to happen at field scale (*e.g.* (**Cognard et al. 1995; Moran et al. 2004; Alvarez-Mozos et al. 2006; Mattia et al. 2006; Thoma et al. 2006;**

**Rahman et al. 2008**). No evidence is found that C-band data can contribute to fine spatial pattern (~15m) of soil moisture while only L-band data can help retrieve soil moisture at 1 ha scale (**Western et al. 2001; Jonard et al. 2011**). Based on a review of current and upcoming SAR sensors, it is anticipated that ASAR is able to provide soil moisture measurements for field size of two hectares or more and the Radarsat-2 would be able to manage field sizes above 0.3 hectares (**Baghdadi et al. 2008**). However, it becomes more difficult for small-scale measurements due to significant spatial soil moisture variability (**Western et al. 2002**) as well as the large effects from surface roughness for bare soil.

Verhoest et al. (2008) and Lievens et al. (2009) extensively reviewed the roughness parameterisation problems encountered for soil moisture retrieval on bare surfaces from SAR and pointed out that for an operational scale of soil moisture mapping new techniques for retrieving surface soil moisture while circumventing surface roughness or those with remote sensing driven surface roughness characterisation are the areas to explore. Since surface soil moisture and surface roughness are two unknowns in an operation, single frequency, single polarisation, single incidence angle or single temporal treatment of the SAR scene is insufficient and several combinations are explored to overcome the limitation, such as multi-frequency (**Ferrazzoli et al. 1997; Bindlish and Barros 2000; Pierdicca et al. 2008**), multi-polarisation (**Hajnsek et al. 2003; Shi et al. 2005; Baghdadi et al. 2006b; Rao et al. 2008; Saradjian and Hosseini 2011**), multi-incidence angle (**Zribi et al. 2005; Zribi et al. 2006b; Baghdadi et al. 2006b; Baghdadi et al. 2007**) and multi-temporal (**Moran et al. 2000; Susan Moran et al. 2000; Svoray and Shoshany 2004; Baghdadi et al. 2009; Mattia et al. 2009; Baghdadi et al. 2010**). It is claimed that the former three approaches are not yet applicable to satellite systems although good results are found in laboratory or airborne SAR systems (**Wagner et al. 2007**). A more recent study improved the situation and demonstrated an applicable approach combining multi-incidence angle and multi-temporal treatments in a semi-arid environment from limited SAR images and along with significant restrictions on SAR configurations and surface conditions (**Rahman et al. 2008**).

Since almost a decade ago studies have adopted a multi-incidence angle approach to eliminating the roughness effect (**Srivastava et al. 2003; Zribi et al. 2005; Zribi et al.**

2006a; Zribi et al. 2006b; Baghdadi et al. 2006b; Baghdadi et al. 2007; Le Morvan et al. 2008; Lievens et al. 2009). Empirically calibrated coefficients are used for soil moisture retrieval based on two pairs of images with significantly different incidence angles (10° and 23° for lower incidence angles and 41° and 46° for higher incidence angles) from Radarsat-1 data and results were verified with only a total of five samples per scene (Srivastava et al. 2003). A minimum RMSE of soil moisture of 3.5 vol. % is found during the calibration phase for a relatively small dataset of 17–21 samples under the condition of at least two images with different (20° and 40°) incidence angles being available from both ASAR and Radarsat-1 data, where the empirical relationships cover the range of incidence angle from 21°–25° for VV polarisation, from 20°–28°, 34°–37° and 38°–45° for HH polarisation, and from 20°–24°, 24°–37° and from 40°–44° for HV polarisation for clay loam sites (Baghdadi et al. 2006b). Clearly certain restrictions are noted for different ranges of incidence angle and different polarisations, especially for VV polarisation. An even better result is achieved by Baghdadi et al. (2007), though a wide range of surface soil moisture, *e.g.*  $m_v < 20$  vol. % is yet to be verified (Baghdadi et al. 2002; Baghdadi et al. 2007).

Efforts have been elaborated to semi-arid environments through the past decade or so (Sano 1997; Moran et al. 2000; Susan Moran et al. 2000; Svoray and Shoshany 2004; Mattia et al. 2006; Thoma et al. 2006; Baup et al. 2007; Santanello et al. 2007; Zribi et al. 2011). Good results have been reported recently from using ASAR imagery, *e.g.* RMSE of the order of 4 vol. % and 5 vol. % are achieved on olive fields and wheat fields, however aided by *in situ* roughness measurements and with limited database (Zribi et al. 2011).

After a review of current operational SAR sensors through a large database and investigation in the upcoming SAR sensors, it is concluded that the recently launched Radarsat-2 (Morena et al. 2004) has the possibility to provide surface soil moisture retrieval at higher resolution by acquiring metre scale data and it is agreed that a RMSE of around 6 vol. % from C-band, single incidence angle data is generally achieved (Baghdadi et al. 2008). While extensive studies have been conducted for ASAR imagery, to the best knowledge of the author no encouraging result among limited publica-



tions on surface soil moisture retrieval from Radarsat-2 data has been reported (*e.g.* (Merzouki et al. 2010; Gherboudj et al. 2011)).

Radar remote sensing has been used for retrieving and mapping surface soil moisture for decades. For this purpose, various models have been developed, ranging from empirical models based on extensive databases (Hallikainen et al. 1985; Oh et al. 1992; Deroin et al. 1997; Zribi and Dechambre 2003), to relatively site-independent semi-empirical models (Dubois et al. 1995; Oh et al. 2002; Thoma et al. 2006; Loew et al. 2006a; Loew and Mauser 2006b) and to site-independent theoretical backscatter models (Fung and Pan 1987; Wu and Chen 2004; Wu et al. 2008; Song et al. 2009; Huang et al. 2010). Good performance of empirical models is limited to those target sites with similar soil parameters and radar configurations as experimental measurements during the model development process. For bare soil study, those models developed by Oh and Dubois are widely used. In addition, many efforts have been devoted to understanding physical interaction between radar backscattering and surface geophysical parameters through theoretical backscattering modelling. The Integral Equation Model (IEM) is one the most widely used numerical backscatter models for bare soil surfaces thanks to its large roughness validity domain, with several further developments such as the AIEM, although fewer applications have been reported (Wu et al. 2008; Brogioni et al. 2010; Nearing et al. 2010). Others include the Small Perturbation Method (SPM), the Kirchhoff Approximation (KA) and the Numerical Maxwell Model in 3-D Simulations (NMM3D) (Fung et al. 1992; Chen et al. 2003; Huang et al. 2010).

Based on the above overview, this work will elaborate the study of surface soil moisture retrieval from SAR data in depth and with the following aims:

- 1) Explore the capability of current C-band SAR sensors ASAR and Radarsat-2 on surface soil moisture retrieval in terms of the accuracy and spatial scale, *e.g.* at field scale;
- 2) Develop a fully operational approach for surface soil moisture monitoring and mapping in the semi-arid environment;
- 3) Assess the capability of the AIEM in surface soil moisture inversion.

Achievements are reached by hard work  
rather than recreation.  
Actions are done after thorough considera-  
tion rather than casual decision.  
---Han Yu, Poet in Tang Dynasty

## Chapter 3 Study Site and Field Characterisation

This chapter consists of three parts. The first part starts with an overview of the geographic and climatic characteristics and impacts in climate change scenarios on, in particular, agriculture water usage on the island of Sardinia, specifically the *Campidano* Plain. The study site, *Azienda San Michele*, is also described. The second part describes campaign schemes and field measurements for surface soil moisture and surface roughness parameters accompanied by the geophysical characteristics of the bare fields based on the *in situ* measurements. Vegetation parameters are also described and illustrated.

### 3.1. Study Area

#### 3.1.1. Sardinia and *Campidano* Plain

Autonomous Sardinia is the second largest island in the Mediterranean Sea narrowly after the island of Sicily. Located approximately between 8° E–10° E and 39° N–41° N, with equivalent distance to the continents of Europe and Africa, Sardinia covers a land surface area of 23,833 km<sup>2</sup> (Vogiatzakis et al. 2008). The elevation of Sardinia ranges from sea level up to about 1,829m on the *Punta La Marmora* of the *Gennargentu* range in the eastern part of the island, with the majority mountainous area (Figure 3.1). The complexity of landscapes in Sardinia can be traced to the geological history of the Precambrian era (Vogiatzakis et al. 2008).

The *Campidano* Plain, as the largest plain of Sardinia of an area of about 2,500 km<sup>2</sup> – around one tenth of the whole island – is located in the south-western portion of the island (Figure 3.1). The alluvial plain is between 12 and 25 km wide, extending about 110 km from the Gulf of *Oristano* on the western coast to the Gulf of *Cagliari* on the southern coast (Schmid 2008). It separates Sardinia into two sections of highlands – the relatively small *Iglesiente* on the south-west and the *Sulcis* covering the whole other

northern and eastern part of Sardinia. With one of the few major and the largest river on the island – the *Tirso* – flowing through it, the *Campidano* Plain is the agricultural heartland of Sardinia with cereal grains, olives, almonds, vegetables, fruit, and grapes for wine as the primary agricultural products.

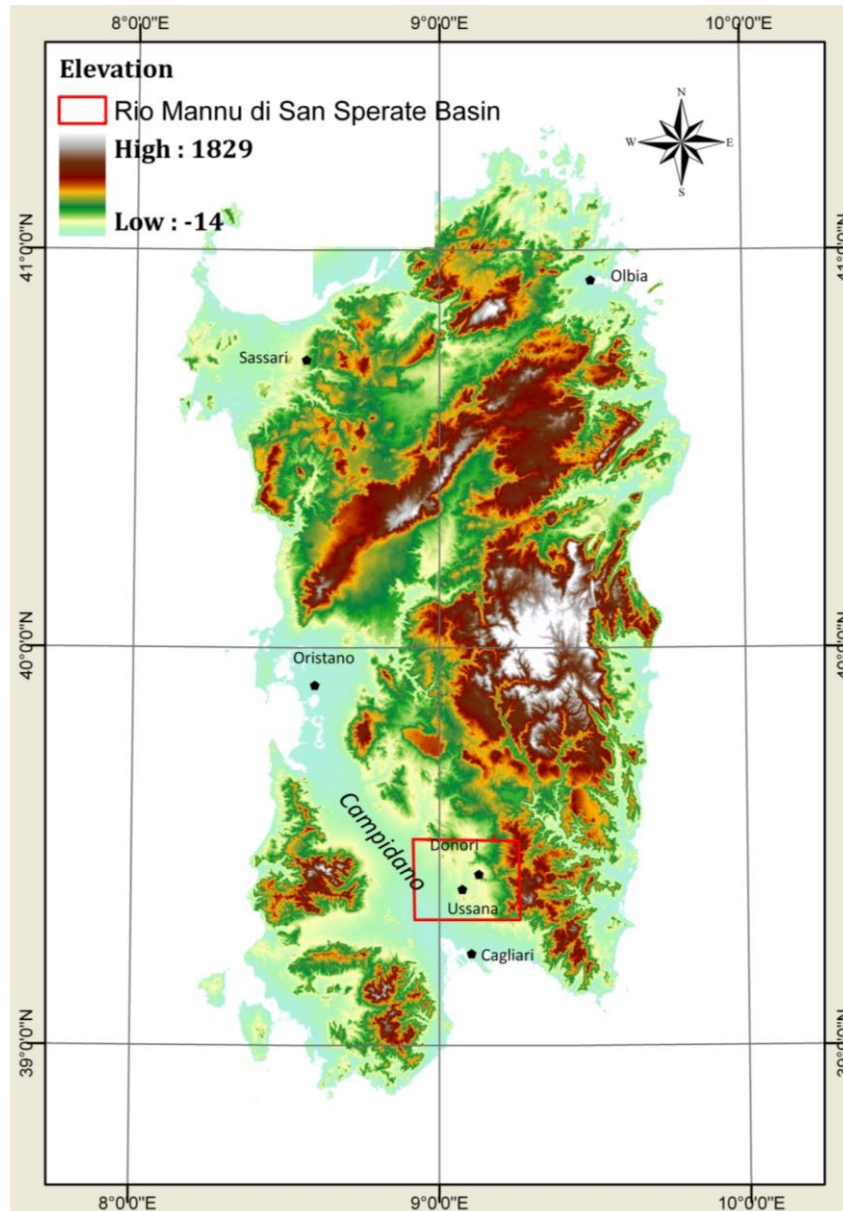


**Figure 3.1** Overview of the island of Sardinia masked by 10m spacing DTM grids obtained from *Sardinia Territory – Planning and Landscape of Sardinia (Sardegna Territorio – Pianificazione e Paesaggio della Sardegna, <http://www.sardegнатerritorio.it>)*. Major locations, the Rio Mannu di San Sperate Basin and the Campidano Plain, are marked. The study site, Azienda San Michele is located between the villages Ussana and Donori on the eastern edge of the Campidano Plain.

### 3.1.2. Rio Mannu di San Sperate

The southern part of the *Campidano* Plain belongs to the *Rio Mannu di San Sperate* Basin, which drains an area of 472 km<sup>2</sup> in the southern part of Sardinia. A stream flow gauge was installed at the basin outlet, *Monastir* (a small town about 2 km west of *Us-sana*), and collected measurements from 1925 to 1963. A small reservoir is present at the basin outlet and is used by ENAS, an agency of the *Regione Autonoma della Sardegna* government managing water, to collect water for multiple uses. The basin is mainly covered by agricultural fields and grassland, while only a small percentage of its area is occupied by forest, in the south-east of the basin. Small urban areas are also present inside the watershed. The soil in the mountainous part of the basin is classified as brown soils and lithosols on crystalline schists and quartzites. The lower areas on the other hand are brown soils, regosols and vertisols or marls, sandstones and conglomerates. The floodplain is characterised by alluvial soils, predominantly gravel or sandy gravel. The basin ranges in elevation from 62m to 842m above the sea level (m.a.s.l.) with an average of 295.5 m.a.s.l. The headwater of the main river channel is located in the mountains of *Sette Fratelli* (south-east of the basin), an area with higher elevation (up to 800 m.a.s.l.) and rugged terrain.

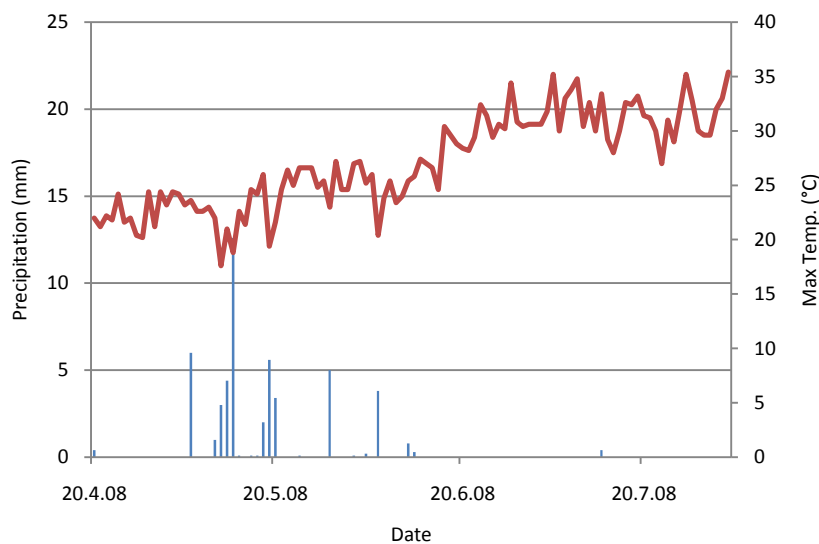
### 3.1.3. Climate

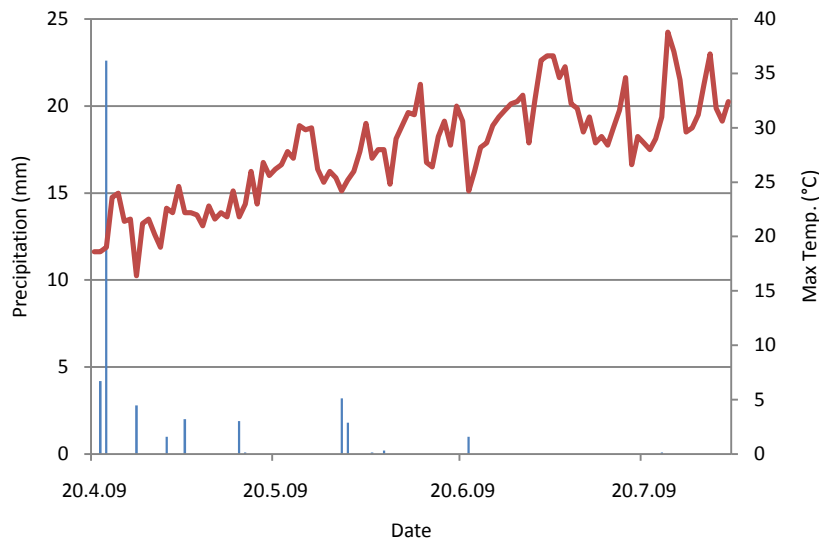
The climate of Sardinia is mainly influenced by Mediterranean Sea breezes, as typical in the region, consisting of warm and dry summers and cold and humid winters with a feature of strong wind with unforeseen rain (**Vogiatzakis et al. 2008**). The *Mistral*, which blows from the north-west through the *Campidano* Plain, is the dominant wind on the island, among two other strong influential winds, namely the *Libeccio* from the south-west and the *Ponente* from west (**Vogiatzakis et al. 2008**). The yearly precipitation for the *Campidano* Plain ranges from 400mm/a~500mm/a in the southern part to 600mm/a~700mm/a in the northern part (**Chessa and Delitala 1997**). Table 3.1 lists monthly and yearly climate statistics in terms of temperature, precipitation and humidity for the period 1971–2000 from the meteorological station of Cagliari *Elmas*, about 15 km from the study site. The table highlights the warm and dry summers, while half of July and August sees maximum temperatures of over 30°C and with less than 8 mm of monthly precipitation.

**Table 3.1 Climate statistics from Cagliari Elmas meteorological station for the years 1971–2000**

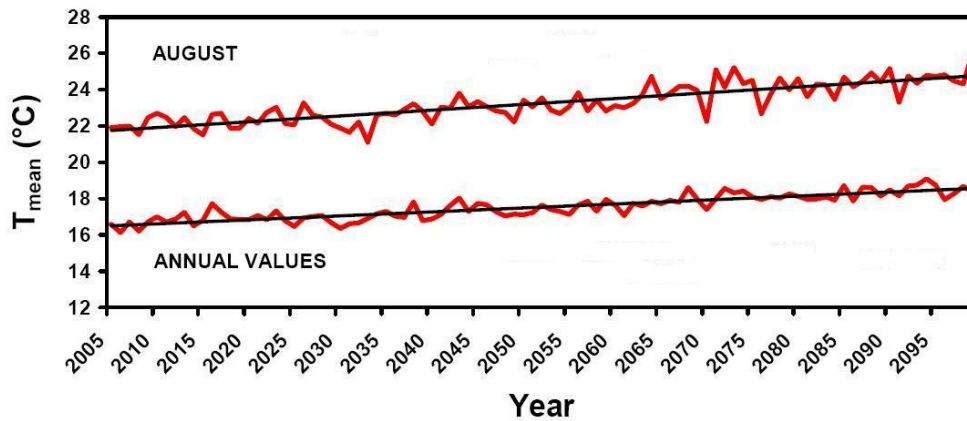
CAGLIARI ELMAS (1971–2000)	Monthly												Yearly
	Jan.	Feb.	Mar.	Apr.	May	Jun.	Jul.	Aug.	Sep.	Oct.	Nov.	Dec.	
T. max. medium (°C)	14.3	14.8	16.5	18.6	22.9	27.3	30.4	30.8	27.4	23.1	18.3	15.4	21.7
T. min. medium (°C)	5.5	5.8	7.1	8.9	12.4	16.2	18.9	19.6	17.1	13.7	9.3	6.6	11.8
Hot days (Tmax ≥ 30 °C)	0	0	0	0	0	5	17	19	5	0	0	0	46
Cold days (Tmin ≤ 0 °C)	2	1	0	0	0	0	0	0	0	0	0	1	4
Precipitation (mm)	49.7	53.3	40.4	39.7	26.1	11.9	4.1	7.5	34.9	52.6	58.4	48.9	427.5
Rainy days (≥ 1 mm)	7	7	7	7	4	2	1	1	4	7	7	7	61
Relative Humidity (%)	79	76	74	72	71	67	65	66	70	76	79	80	72.9

Figure 3.2 illustrates the climate conditions during campaign periods in 2008 and 2009. There is hardly any precipitation from June through the summer in each year while the maximum temperature varies from around 30°C up to 38°C. However, the amount of precipitation varies in late spring, while 2009 saw an extremely dry May according to the historical average and led to a hotter summer than 2008.





**Figure 3.2** Maximum temperature and precipitation during campaign periods – top: 2008 and bottom: 2009 (Data retrieved from the European Climate Assessment and Dataset project (<http://eca.knmi.nl/>) based on information from the Cagliari meteorological station).



**Figure 3.3** Modified figure from (Duce et al. 2004) showing the increasing trend of August and yearly average temperatures for north-west Sardinia for the period 2005 to 2099 from scenario B2.

The warm and dry situation in the summer and on a yearly basis is amplified by future climate variability analysis. Climate scenarios A2 and B2 showed an increase in annual mean temperature of about 1–5°C along with a decrease in annual mean rainfall of about 100 mm up to the year 2100 (Duce et al. 2004), while Figure 3.3 exemplifies a clear upward temperature trend in both August and yearly average throughout the 21<sup>st</sup> century for north-west Sardinia based on scenario B2. Based on their analysis, half of the *Campidano* Plain will be downgraded from most suitable land in terms of pedo-climate Land Capability for Agriculture (LCA) from the period 1971–2000 to least suit-

able land for the period 2070–2099 under climate change scenario A2. The term LCA classifies land into four categories – most suitable, moderately suitable, least suitable and not suitable – in terms of its range of quality and potential productivity for agricultural purposes (Duce et al. 2004). Table 3.2 shows a significant and alarming shrinkage of the most suitable land and expansion of the least suitable land in the LCA class for Sardinia under both climate change scenarios A2 and B2.

**Table 3.2 Modified table from (Duce et al. 2004) for LCA class change in terms of the area as a percentage of the total area of Sardinia with reference to period 1961–2000 and future climate change scenarios A2 and B2.**

LCA class	Area as percentage of total area of Sardinia (%)		
	1961–2000	Scenario A2	Scenario B2
most suitable	23.7	10.5	14.0
moderately suitable	27.7	19.3	19.7
least suitable	17.4	38.4	35.4
not suitable	31.2	31.8	30.9

Characterised as a semi-arid region, the *Campidano* Plain is extremely vulnerable to climate change (Duce et al. 2004) and human use (Vogiatzakis et al. 2008). The environmental degradation leads to several concerns including water resource management for agricultural purposes in this water scarcity situation.

#### 3.1.4. Azienda San Michele

The study site, *Azienda San Michele*, with a total area of 4.35 km<sup>2</sup>, is located on the eastern edge of the *Campidano* Plain, between the villages *Ussana* and *Donori*, with central coordinates of 39°25'N, 9°06'E (Figure 3.1). The *Azienda* is one of the well-equipped research based farms operated by the *Agencia per la Ricerca in Agricoltura*, AGRIS (the Agricultural Research Agency of Sardinia). Part of the *Azienda* (approximately 2 km<sup>2</sup>) is located in a hilly area with Maquis shrubland vegetation that is also a centre of wildlife animal restocking. In the north-eastern part, the *Azienda* is delimited by the San Michele hill. At the bottom of this hill, the river *Rio Flumineddu* joins the *Rio Mannu*. The *Azienda* has been used for decades to investigate agricultural genetics for the more efficient farming of durum wheat in climatic conditions with frequent drought periods.

Several bare fields, marked in beige in figure 3.5, ranging from 1.7 ha to 4.4 ha, are prepared during each campaign and crop fields are also included such as broad bean and wheat (two major agricultural products in Sardinia marked in green and orange respectively) as well as canola (marked in yellow). Red lines define field boundaries for the *Azienda*. Grey parts denote buildings. A trihedral corner reflector, built by the *Institut national de la recherche scientifique. Centre Eau, Terre & Environnement, Quebec* (INRS, Quebec), with edge length of 1m, is set up at the north-west corner of Field 11 (abbreviated as F11) and its orientation is adjusted to each satellite pass (Figure 3.4). The size and soil texture of the bare fields are given in Table 3.3, ranging from 1.7 ha for F11 to 4.4 ha for F21. The sizes of the crop sample fields are given in Table 3.4, ranging from 1.7 ha of a canola field to 7.5 ha of a broad bean field in 2008. Note that F32 is treated separately, namely F32\_high and F32\_low. Explanation will be given after the description of the sample point (SP) selection scheme.

**Table 3.3 Size and soil texture of the bare fields in the Azienda San Michele.**

ID	Sand (%)	Clay (%)	Silt (%)	Size (Hectare)
F11	51	17	32	1.7
F21	47	32	21	4.4
F31	58	24	18	2.6
F32_high	44	35	21	2.9
F32_low	44	35	21	2.1

**Table 3.4 Size of crop fields in the Azienda San Michele.**

ID	Crop type	Size (Hectare)
W1	wheat	3.9
B1	broad bean	7.5
B2	broad bean	3.0
B3	broad bean	2.4
C1	canola	1.7





Figure 3.4 Photo of corner reflector set up with Seppo Schmid and Dr Imen Gherboudj on 2<sup>nd</sup> May 2008.

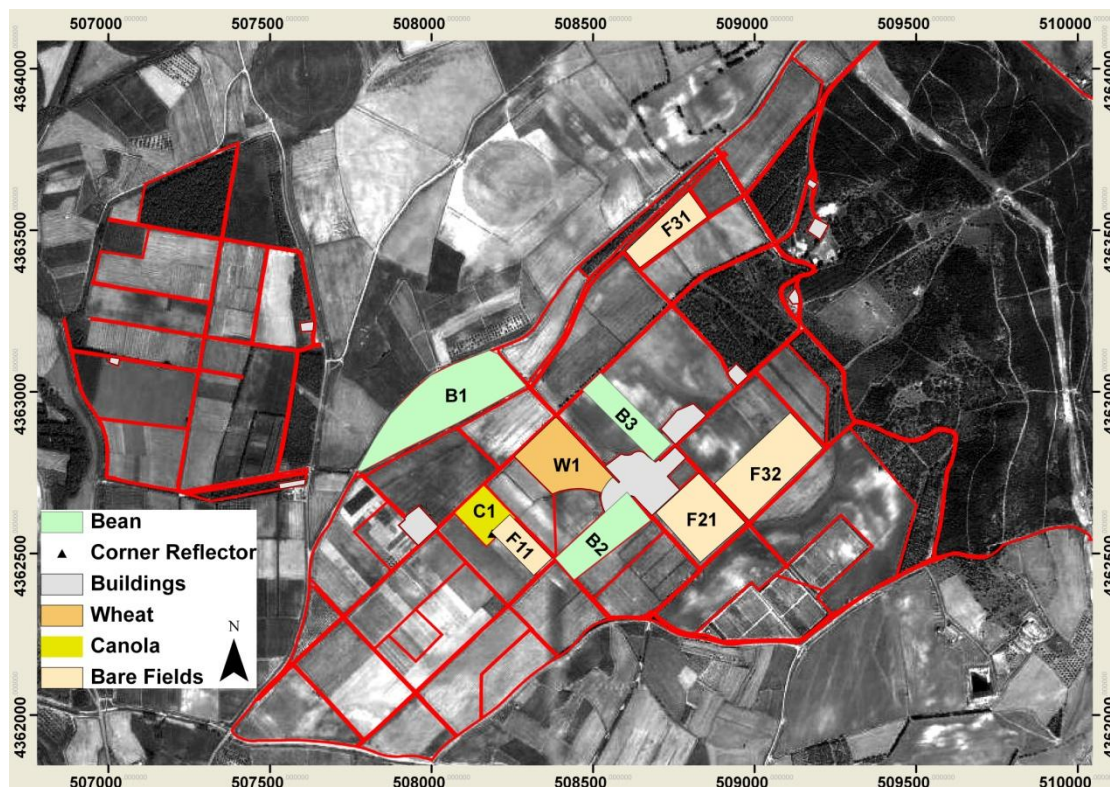


Figure 3.5 Study fields are marked with field ID, coloured by land use in the Azienda San Michele in the UTM system with a geo-referenced aerial photo as background.

## 3.2. Field Measurements

### 3.2.1. *In situ* measurement overview

Extensive field measurements are conducted during the campaigns in 2008–2009. Table 3.5 lists the parameters measured, with a corresponding short description, such as the methods and equipment used. Detailed description of field measurements will be given in Section 3.2.2.

Five sample points (SPs) are selected and marked with sticks on each field. The SP selection scheme is exemplified by F32. Overall, SPs are equally distributed according to the field shape and local terrain characteristics for a better representation of the test fields as illustrated in Figure 3.6. SPs with labels and brightly-coloured bands are fixed at different heights to the ground according to the surrounding obstacles, i.e. labels and bands are higher in the canola field than those on bare fields (Figure 3.7). For F32, the south-west facing slope in the middle part of the rectangular field separates the field into two parts with significant elevation difference between both parts. Therefore, one SP, i.e. SP2, is selected at the edge of the slope in the centre part of the field while those two “separated” parts are represented by two separate SPs. Because significant slope may lead to a significant difference in surface soil moisture distribution within F32, F32 is treated as F32\_high and F32\_low separately for further study.

**Table 3.5 Dataset through the year 2008–2009 for the Azienda San Michele.**

Parameter	Note
Soil moisture ( $m_v$ )	<ul style="list-style-type: none"> <li>• Five repetitions at five sample points at 1–4 cm and 5–8 cm depths on each field (including bare and crop) for almost every satellite pass.</li> <li>• Both gravimetric method and ThetaProbe ML2x are used.</li> </ul>
rms height $s$	Close-range photogrammetric measurements using the Rollei D7 camera for each bare field on a weekly basis.
Soil type	Granulometric method is used for five samples per bare field.
LAI	LAI-2000 Plant Canopy Analyzer is used. Five samples are taken for each sample point.
Biomass	Two samples of 1m <sup>2</sup> crops are taken for each sample point.
Vegetation height	10 samples are taken for each sample point.
Row distance	5 samples are taken for each sample point.
Plant density	Plant number per m <sup>2</sup> is counted and two samples are taken for each sample point.
GPS coordinates	Magellan GPS NAV 5000.
Field photos	Digital cameras.

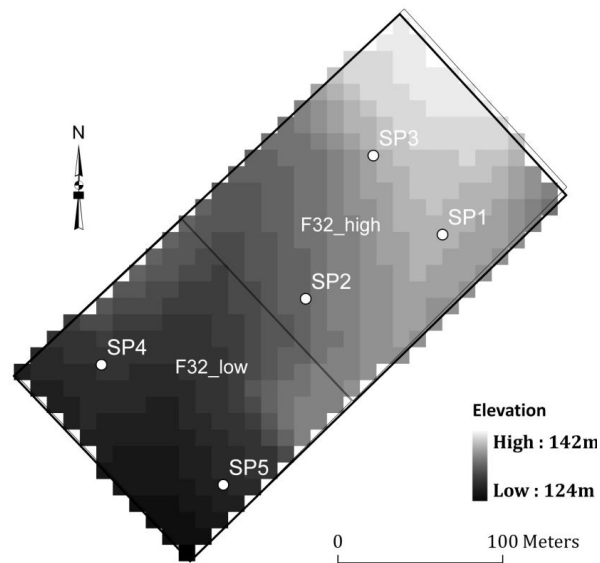


Figure 3.6 Exemplifying SP selection scheme by Field 32 and 10m spacing DTM grids obtained from Sardinia Territory – Planning and Landscape of Sardinia (Sardegna Territorio – Pianificazione e Paesaggio della Sardegna (<http://www.sardegnaterritorio.it/>)).



Figure 3.7 Two photos of SPs on one bare field taken on 2<sup>nd</sup> May 2008 and on one broad bean field taken on 7<sup>th</sup> May 2008.

### 3.2.2. Soil moisture

#### 3.2.2.1. Volumetric and gravimetric soil moisture

Many indexes or parameters are related to the proportion of soil, water and air in a sample. The following subsection will only list those related to soil moisture. Soil moisture, also termed soil water content or soil wetness, can be expressed in both gravimetric and volumetric perspectives. The gravimetric soil moisture  $m_g$ , also termed mass wetness, is defined as the ratio of the mass of water to the mass of dry soil particles (Hillel 1998):

$$m_g = M_w/M_s$$

3.1

where  $M_w$  and  $M_s$  denote the mass of water and the mass of dry soil in the sample respectively. Dry soil normally refers to a mass of a certain amount of soil dried in an oven at over 105°C for over 24 hours. Therefore this reference is implemented as the guideline of gravimetric measurements in this study.

The volumetric soil moisture  $m_v$ , similarly also termed volume wetness, is defined as a percentage of the total volume of water to the total volume of the sample (Hillel 1998):

$$m_v = \frac{V_w}{V_t} = V_w/(V_s + V_f)$$

3.2

where  $V_w$ ,  $V_t$ ,  $V_s$  and  $V_f$  denote the volume of water in the sample, the total volume of the sample, the volume of the dry soil and the volume of pores. The volume of pores  $V_f$  is defined as (Hillel 1998):

$$V_f = V_a + V_w$$

3.3

where  $V_a$  denotes the volume of air in the sample. When the sample is saturated, the volumetric soil moisture is equal to porosity  $f$ , which is an index of the relative pore space in a soil generally ranging from 30% to 60%, frequently used by ecologists and agronomists (Hillel 1998):

$$f = \frac{V_f}{V_t} = (V_a + V_w)/(V_s + V_a + V_w)$$

3.4

Gravimetric soil moisture can be converted to volumetric soil moisture through:

$$m_v = (M_w/M_s) * (M_s * \rho_w/V_t) = m_g * \rho_w * \rho_b$$

3.5

where  $\rho_w$  and  $\rho_b$  denote the water density and the dry bulk density.

For clarity, all soil moisture values are expressed in volumetric terms in this study. Surface soil moisture measurements are taken each day in accordance with satellite pass time, i.e. sampled in the morning of a descending pass and in the late afternoon in case of an ascending pass. The following subsections will explain the *in situ* soil moisture measurement scheme in more detail.

### **3.2.2.2. Gravimetric measurement**

The gravimetric measurement is the direct and conventional method for measuring soil moisture. However, the method is destructive to soil, time-consuming and an impractical measurement on the field, because samples have to be taken from field to laboratory, each sample has to be weighed before and after drying in an oven, and a minimum of 24 hours is needed for drying in the oven. In addition, collecting, labelling, weighing and noting for a large number of samples requires significant patience and concentration. In this study, five repetitions are taken for each SP on each field. These repetition locations are randomly selected around the SPs. For each repetition, two aluminium rings are overlaid and hammered vertically from the surface soil to a deeper soil layer. After clearing the soil surrounding these rings with a shovel, two samples of soil of 100 cm<sup>2</sup> each are carefully collected and sealed in two plastic bags immediately to eliminate evaporation. The corresponding field ID, SP ID, repetition ID, soil layer depth (*i.e.* 1–4 cm or 5–8 cm) and the collection time are marked on each plastic bag, *e.g.* F21SP3R15cm for the soil sample at 1–4 cm depth for the 3<sup>rd</sup> repetition for sample point 3 and Field 21.



**Figure 3.8 Taking soil samples for gravimetric soil moisture. In the photo: Seppo Schmid and the shadow of the author. Date: 3<sup>rd</sup> May 2008.**

Each wet soil sample is weighed in the plastic bag in a light aluminium container in the laboratory. Note that different containers have to be treated separately due to different weights. After drying at 105°C in the oven for a minimum 24h, samples are taken out for re-weighing. All weights are noted carefully on a table for each depth, repetition, sample point, field ID and collection date and time. Volumetric soil moisture is then calculated using Equation 3.5.



**Figure 3.9** Putting wet soil samples into aluminium containers. In the photo: **Andrea Bez**. Date: **2<sup>nd</sup> May 2009**.

Due to the high requirement of the gravimetric method, only limited dates are chosen for a reference database in each campaign. Subsection 3.2.2.3 will describe a more novel and mobile sensor using the ThetaProbe ML2x, which is one of a number of sensors that can be based on electric resistance, neutron scattering, Gamma ray absorption and the Time Domain Reflectometer (TDR) (**Topp et al. 1980; Hillel 1998**).

### **3.2.2.3. Theta Probe ML2x**

There has been recent progress in developing various soil moisture sensors based on electromagnetic theory which has been widely accepted for dielectric constant measurement, *e.g.* TDR (**Kelleners et al. 2009**) and many others (**Blonquist et al. 2005**). The Theta Probe (ThetaProbe ML2x, Delta-T Devices, Cambridge, UK) measurement is a relatively new method: it is an impedance probe which functions on the equivalent degree of accuracy and reduces the complexity and expense, compared with the TDR measurement (**Miller 1967**). The probe measures volumetric soil moisture by the determination of dielectric constant, also termed relative permittivity, of water:

$$M_v = (\sqrt{\varepsilon_r} - a_0)/a_1$$

## 3.6

where the dielectric constant  $\varepsilon_r$  in the soil describes the ratio, as dielectric, of the capacitance of a capacitor (four parallel metal rods for the ThetaProbe ML2x as shown in [Figure 3.10](#)) with the soil sample to the capacitance of the same capacitor with air.  $a_0$  and  $a_1$  are two constants dependent on soil type, which are generalised as 1.6 and 8.4 for mineral soils and 1.3 and 7.7 for organic soils. *In situ* calibration can also be taken when necessary (**Miller and Gaskin**). The derivation of the linear relationship between the square root of dielectric constant  $\sqrt{\varepsilon_r}$  and volumetric soil moisture  $m_v$  is found in many publications (**Topp et al. 1980; Whalley 1993**).



**Figure 3.10** UMS INFIELD7 (left) and a broken ThetaProbe ML2x probe (right).

Figure 3.10 shows two photos of the ThetaProbe ML2x. The one on the left shows it in a working condition for measuring soil moisture at 5–8 cm depth, where the probe is connected to the mobile UMS INFIELD7 data logger, where volumetric soil moisture can be read directly or stored. The photo on the right shows a broken probe with one bending rod due to strong resistance of stones in deep soil. It signals that care must be taken on similar measurement in the fields.

As with the gravimetric scheme, surface soil moisture is measured by the probe at both 1–4 cm and 5–8 cm depths for five repetitions around each of the five sample points on each field. The only difference is that two measurements are taken for top 1–4 cm soil moisture, including one vertically from the soil surface and one horizontally to a soil



profile. The vertical and horizontal values are averaged as the mean of the soil moisture at top 1–4 cm depth for the repetition of the sample point.

To evaluate the probe approach, Figure 3.11 compares its measurements with volumetric soil moistures derived from the gravimetric approach at both 1–4 cm and 5–8 cm depths. The grey points indicate soil moisture measurements at each sample point, while the black points are field average values. It shows that field averaged values yield a lower root mean square error (RMSE) of 3.4 vol. % compared to 4.3 vol. % from comparison on the sample point basis for both campaigns in 2008 and 2009. In addition, the mobile probe approach tends to slightly overestimate the soil moisture to field average scale.

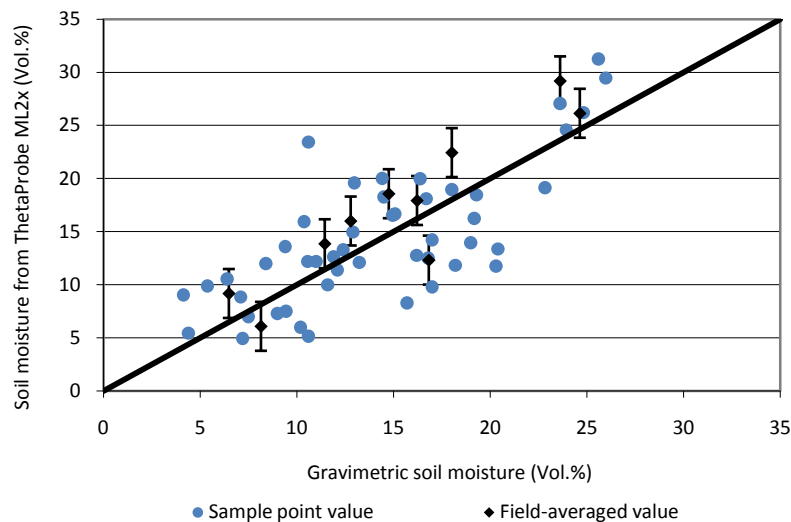


**Figure 3.11 Comparison of surface soil moisture between gravimetric approach and using ThetaProbe ML2x at both 1–4 cm and 5–8 cm depths over the years 2008 and 2009, showing RMSE are 4.3 vol. % and 3.4 vol. % for comparisons on a sample point basis and on field averaged value basis, respectively.**

In addition to field measurement, a meteorological station was set up on the field F11 during the year 2008 with additional continuous (every 10 mins) soil moisture measurements available at 10 cm and 20 cm depths. Unfortunately, the data logger became defective as a result of a flashing incident and was therefore unavailable for the year 2009. The station data is not presented here since it is not used in this work. For more detail, the diploma thesis (in German) of Josef (Seppo) Schmid can be referred to (Schmid 2008).

### 3.2.3. Roughness

Apart from the dielectric constant in the soil, soil surface geometry, i.e. surface roughness, also contributes significantly to backscattering coefficients in the SAR system. The following subsections will introduce the statistical description of surface roughness and various *in situ* measurements.

#### 3.2.3.1. Statistical description of surface roughness

Surface roughness is described as the surface variance compared to a smooth ‘reference surface’, and is normally defined in two aspects: the vertical variance, namely the root mean square of the surface height, rms height  $s$  and the horizontal variance, namely the correlation length  $l$ , associated with different autocorrelation function (ACF). The rms height  $s$  is defined mathematically as:

$$s = \sqrt{\frac{\sum_{i=1}^n (Z_i - \bar{Z})^2}{n - 1}}$$

3.7

where  $Z_i$  and  $\bar{Z}$  denote the height of the point  $x_i$  on the profile surface and the mean height of all points on the profile and  $n$  denotes the total number of points. In practice all 1D or 2D profiles are sampled with a displacement. The rms height is found to increase in accordance with the increase of profile length for a 1D profile (**Oh and Kay 1998; Baghdadi et al. 2000; Callens et al. 2006**), while the relationship is not found in studies of 2D profiles.

The normalised ACF  $\rho(x')$  for a horizontal displacement  $x' = j\Delta x$ , where  $\Delta x$  is the spatial resolution of the profile, is defined as:

$$\rho(x') = \frac{\sum_{i=1}^{N-j} Z_i Z_{i+j}}{\sum_{i=1}^N Z_i^2}$$

3.8

where  $Z_{i+j}$  denotes the height of the point with the horizontal displacement  $j$  from the point  $x_i$ . In this case, the correlation length  $l$  is defined as the horizontal displacement  $x'$  at which the ACF  $\rho(x')$  between each two points on the profile yields a value smaller than  $1/e \approx 1/2.7183 \approx 0.3679$ , which is defined mathematically as:

$$\rho(l) = 1/e$$

3.9

Therefore  $l$  becomes positively infinite on a perfectly smooth surface. Two basic autocorrelation functions are widely used as Gaussian and exponential functions for backscattering models (**Fung 1994**). They are described as:

$$\rho(x') = e^{-|x'|/l}$$

3.10

for the exponential correlation function and as:

$$\rho(x') = e^{-x'^2/l^2}$$

3.11

for the Gaussian function, while significantly different results are found in the correlation length  $l$  from different autocorrelation functions (**Verhoest et al. 2008**).

### 3.2.3.2. *In situ measurement approaches*

Several approaches have been developed to measure and estimate surface roughness parameters including those mechanical instruments with physical contact with the soil surface, such as pin profilometer and meshboard, and those instruments with no physical contact, such as laser profiler and digital photogrammetry. The main techniques for soil moisture measurements have been reviewed recently by Bittelli (**2011**).

A pin profilometer consists of a board marked with reference grids along a number of vertically movable pins which can fall closely onto the soil surface and their horizontal and vertical positions are either registered electronically or photographed and then digitised later to create a profile with both horizontal and vertical information of each position that the pins are located. A meshboard is a gridded board, which needs to be inserted in the soil before the photographing and digitisation. Both pin profilometer and meshboard have the advantage of being rather low cost compared to the “close-range” remote sensing approaches. While the pin profilometer has the disadvantage of the possibly destructive effect of the pins and limited vertical and horizontal resolutions (**Jester and Klik 2005**), the meshboard approach is limited by the difficulty of insertion of the meshboard into rough soil sufficiently deep (**Verhoest et al. 2008**).

A laser profiler consists of a horizontally positioned rail and movable laser scanner along a rail connected and powered by an electric motor. The beamer detects the vertical distance from beamer to soil surface and records the horizontal position simultaneously to a data logger (**Mattia et al. 2003; Alvarez-Mozos et al. 2009**). The technique benefits from high resolutions in both horizontal and vertical directions (**Jester and Klik 2005**), but is restricted to conditions where wind is limited, optical reflectivity is stable and no vegetation is present along the rail, otherwise errors may be introduced (**Darboux and Huang 2003; Mattia et al. 2003; Jester and Klik 2005**).

This study adopts a 2D close-range photogrammetric approach as described in the following subsection.

### ***3.2.3.3. The close-range photogrammetric approach***

The photogrammetric approach has been used in soil surface measurement for over 30 years, (e.g. (**Gabriels and Boodt 1980; Merel and Farres 1998; Rieke-Zapp and Nearing 2005**)). (**Zribi et al. 2000; Blaes and Defourny 2008; Heng et al. 2010**) demonstrated the capability of close-range photogrammetry in measuring surface roughness. This study deploys a digital photogrammetric system by Mr Philip Marzahn and updated based on Marzahn and Ludwig (**2009**).

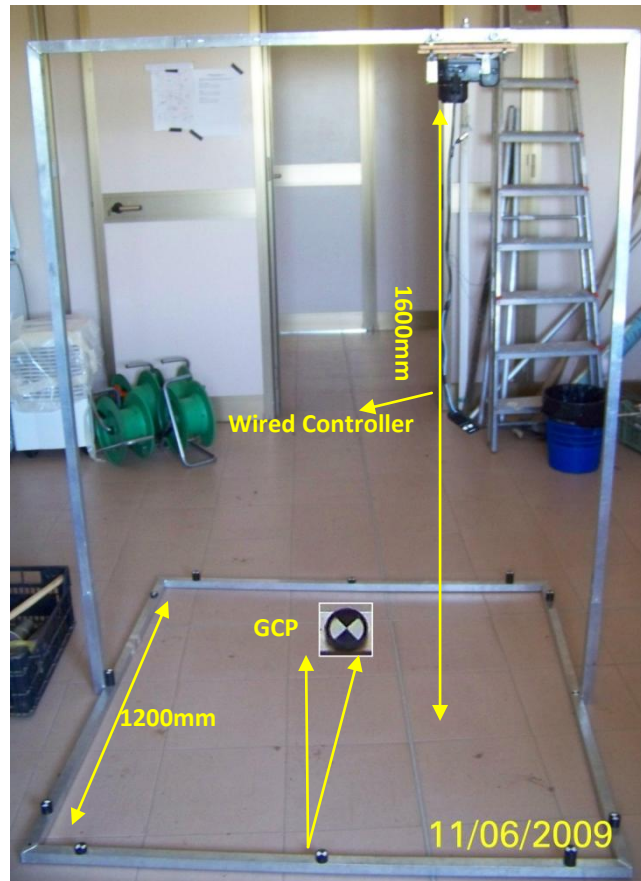


**Figure 3.12** Photogrammetry system with aluminium frames, GCPs and Rolleiflex d7 metric camera.

The acquisition system consists of a set of aluminium frames along with 12 ground control points (GCPs) and a Rolleiflex d7 metric camera as shown in Figure 3.12. A 1200 mm  $\times$  1200 mm square aluminium frame is set as the base of the system with three GCPs on each side, whose coordinates ( $x$ ,  $y$  and  $z$ , listed in Table 3.7) are arbitrarily determined with a calliper to ensure an accuracy of 0.1 mm (Marzahn and Ludwig 2009) during the system development, which is described in Lascelles et al. (2002). The Rolleiflex d7 is mounted on the rail parallel to the ground with a vertical distance of 1600 mm. The camera is movable along the rail with a baseline of 640 mm. Therefore, an approximately 65% overlap of two images at each sample point can be ensured for stereo imaging. Similar to soil moisture measurement, five pairs of stereo images are taken for each of the five sample points on each bare field. In addition, a wired controller is connected with the camera to avoid human shadow on the photos.

**Table 3.6 Rollei d7 interior orientation in the photogrammetric system in mm.**

focal	focal length	x0	y0
	7.43	0.17	0.01
radial lens distortion	k0	k1	k2
	0.019	-2.461e-3	3.978e-5

**Table 3.7 GCP coordinates in cm of the photogrammetric system.**

ID	1	2	3	4	5	6	7	8	9	10	11	12
x	1.25	1.25	1.25	12.5	62.5	112.5	123.73	123.73	123.73	112.5	62.5	12.5
y	12.5	62.5	112.5	123.73	123.73	123.73	112.5	62.5	12.5	1.25	1.25	1.25
z	4.5	6.5	3	5	3.5	6	5	2.5	4.5	6	4	3.5

The Leica Photogrammetry Suite (LPS 9.3) is used to generate a digital terrain model (DTM) from stereo image pairs. The interior information of the camera is known and set out in Table 3.6. Stereo photos are adjusted to grey scale (exemplified in Figure 3.13) and the exterior orientation is set up for the stereo photo pair using the 12 GCPs and additional tie-points are derived. A matching process is taken between both images with the minimum correlation coefficient set as 0.65 from a 11 × 11 kernel (Linder 2003). In the final step, the generated DTMs are interpolated to grids with a resolution of 4 mm.

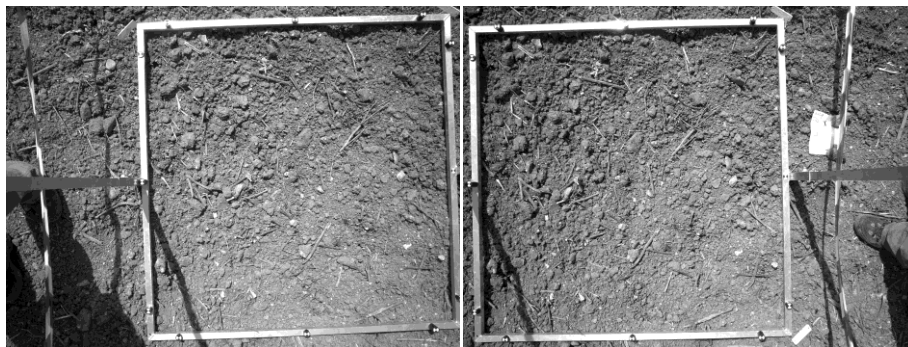


**Figure 3.13 A pair of stereo photos taken on a sample point and the original colour photos are adjusted to 0-255 grey scale.**

After generating a DTM for each sample point, rms height  $s$  is easily achieved by statistical calculation in ArcGIS 9.x, though more efforts are needed to estimate the correlation length. Oliver and Webster (1986) and Robert and Richards (1988) started to use the semivariogram for modelling random variables of geomorphic properties and Curran (1988) first introduced the tool into remote sensing phenomena, which can be random, continuous and unlimitedly variable. The method has recently been adopted for

a Canadian study site (**Merzouki et al. 2008**). The semivariogram is deployed in this study to measure the correlation length. A semivariogram is a widely used geostatistical measure of, in this case, the variance of height of the sample point in a 1D or 2D profile with respect to other sample points, which are a fixed distance apart on the profile surface, which is defined mathematically as:

$$\gamma(x') = \frac{1}{2N(x')} \sum_{i=1}^N [Z(x_i) - Z(x_i + x')]^2$$

### 3.12

where  $Z(x_i)$  is the value of the random variable  $Z$ , i.e. the height of the point compared to the 'reference surface' at the point  $x = x_i$ ,  $Z(x_i + x')$  is the value of  $Z$ , at a distance  $x'$  from the point  $x_i$ , also termed lag, and  $N(x')$  is the number of pairs of sampling points with a lag of  $x'$  (**Jury and Horton 2004**). Figure 3.14 illustrates the terms and symbols in the semivariogram for correlation length estimation. The black dots represent the samples on the measured profile with the lag  $x'$  as the horizontal axis and the semivariogram  $\gamma(x')$  as the vertical axis. In addition to the lag  $x'$ , the sill  $s$  denotes the maximum the semivariogram can achieve, the nugget  $c_0$  denotes the point on the semivariogram axis where the extrapolated relationship  $\gamma(x')/x'$  intercepts with the semivariogram axis and the variance  $c$  is calculated by the sill minus the nugget (**Curran 1988**). The correlation length  $l$  is marked as the range beyond which samples are randomly correlated.

As stated before, the Gaussian and exponential models are the two most widely used fitting models to sample semivariograms for correlation length. The semivariogram function in the geostatistical module in ArcGIS 9.x is used in this study.

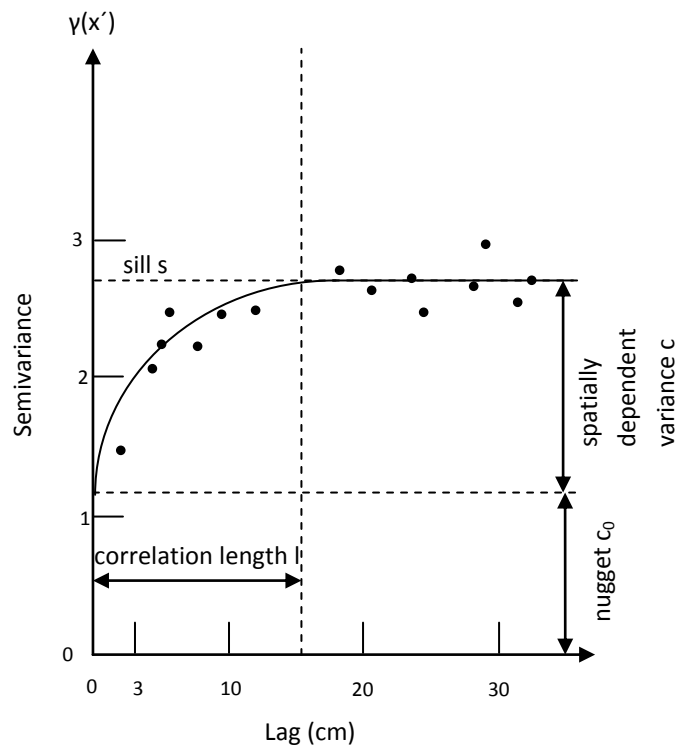


Figure 3.14 Illustration of the terms and symbols in the semivariogram.

#### 3.2.3.4. In-field and temporal variability of surface roughness

Alvarez-Mozos et al. (2009) raised the issue of spatial variability of surface roughness and hence the in-field variability and found that large in-field variability can easily introduce an error of 2dB to the IEM backscattering coefficient estimation, therefore producing an over 10 vol. % error into surface soil moisture estimation. An accurate surface roughness measurement is necessary for roughness parameterisation.

A few studies have shown that surface roughness parameter values remain stable during a long period, (e.g. (Verhoest et al. 1998; Alvarez-Mozos et al. 2006; Thoma et al. 2006), while many others have found the rms height  $s$  decays over time and the correlation length varies in an uncertain trend, which may be due to increasing numbers of rainfall incidents (Zobeck and Onstad 1987; Jester and Klik 2005; Callens et al. 2006; Alvarez-Mozos et al. 2009). Therefore, both spatial and temporal variability of surface roughness are investigated for the study site in the following subsections through *in situ* measurement analysis.



### 3.2.4. Geophysical characteristics of bare fields

Basically, *in situ* measurements assume the mean of sampling values can be treated as equivalent to the field average values, and thus to match the scale of SAR observation. Therefore, it is also crucial to confirm the assumption before applying the values to modelling. The same reason is applied to the investigation of in-field soil moisture variability. In addition, a close investigation of temporal and spatial variability of roughness parameters in each test field is needed.

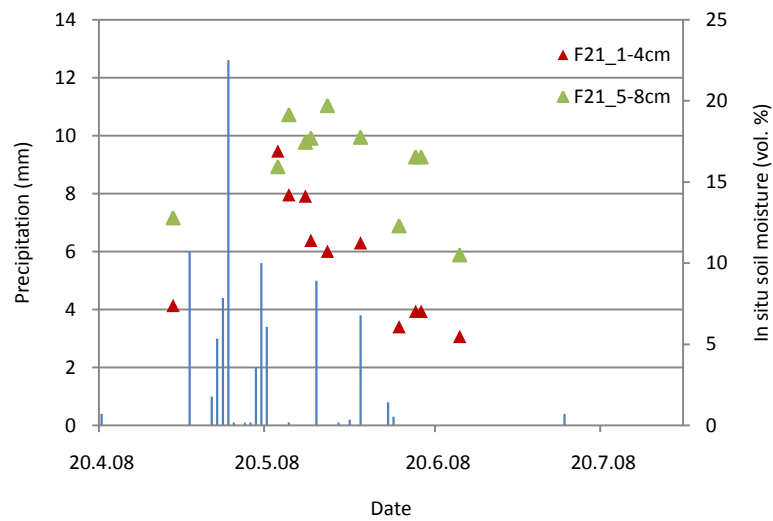
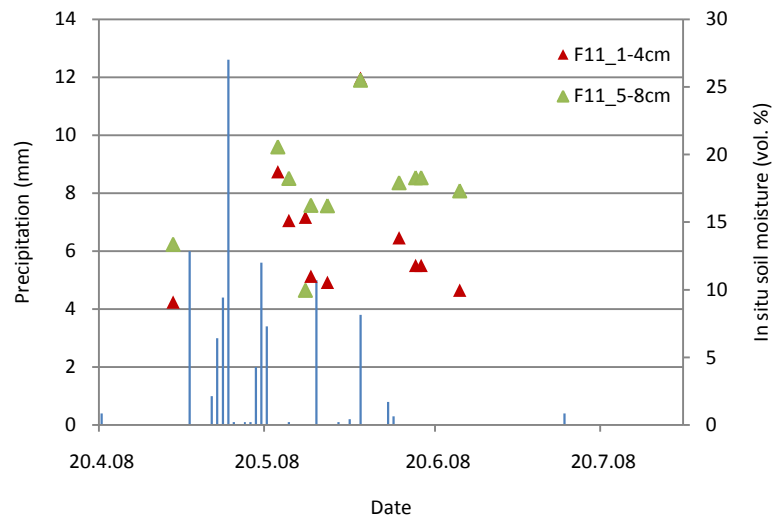
To start with, Table 3.8 demonstrates the minimum and maximum values for all test fields of the field averaged soil moisture at 1–4 and 5–8 cm depths, the rms height  $s$  and the correlation length  $l_{Gau}$  and  $l_{exp}$  – the correlation length based on Gaussian and exponential functions respectively. Campaigns mainly cover the months of May and June. During these periods, the soil moisture at both depths ranges from a wet condition with nearly 30 vol. % to an extremely dry condition (~3 vol. %). Between all the test fields, the difference of rms height  $s$  can reach about 1.5 cm, while correlation length has larger variations for different fields. The following parts will explore the trend of change of surface soil moisture and roughness parameters over study fields during the campaigns.

**Table 3.8 In situ geophysical characteristics.**

	$m_v$ 1–4 cm (vol. %)	$m_v$ 5–8 cm	$s$ (cm)	$l_{Gau}$ (cm)	$l_{exp}$ (cm)
Min.	1.33	3.06	1.71	15.35	20.04
Max.	25.64	29.18	3.22	28.24	45.21

Figure 3.15 and Figure 3.16 illustrate a downward trend of the soil moisture at both 1–4 cm and 5–8 cm depths for all study fields during the campaigns. Average values of all samples on each field are used to represent the field average value. In both years, soil moisture conditions are similar on a year-to-year basis in a way that the soil moisture at 1–4 cm depth retreats from around 15 vol. % at the end of April to about 5 vol. % at the end of June each year, while soil moisture at 5–8 cm depths behaves in a more stable fashion between 10–20 vol. %. Due to an unusual week of constant rain in the late April in 2009, the soil moisture at both depths reached the highest level of both campaign periods on 28<sup>th</sup> April 2009. Note that the two large peaks on 7<sup>th</sup> June 2008 and 17<sup>th</sup> June

2008 are due to a pre-planned irrigation operation on F11 while a smaller-scale irrigation operation was undertaken on F21 on 17<sup>th</sup> June 2008, which introduced only a moderate peak on the figure. One more irrigation operation was undertaken on F11 on 13<sup>th</sup> June 2009. In addition, rainfall effects are also well observed. Field measurements clearly represent both impacts from meteorological and human intervention aspects.



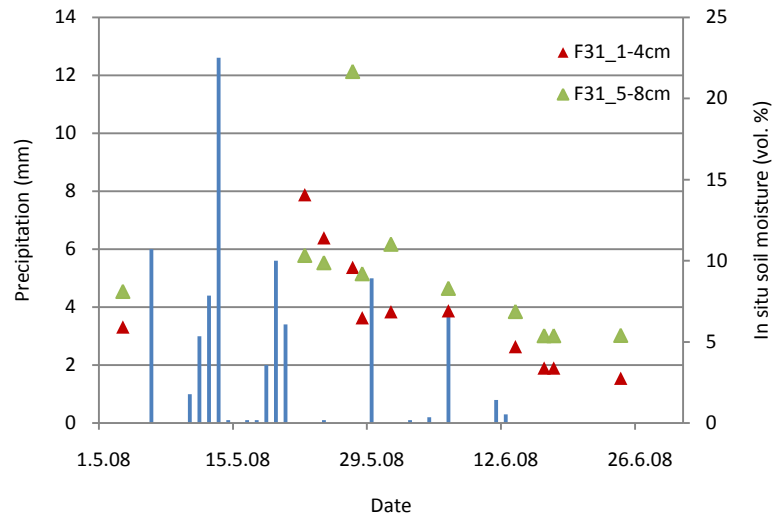
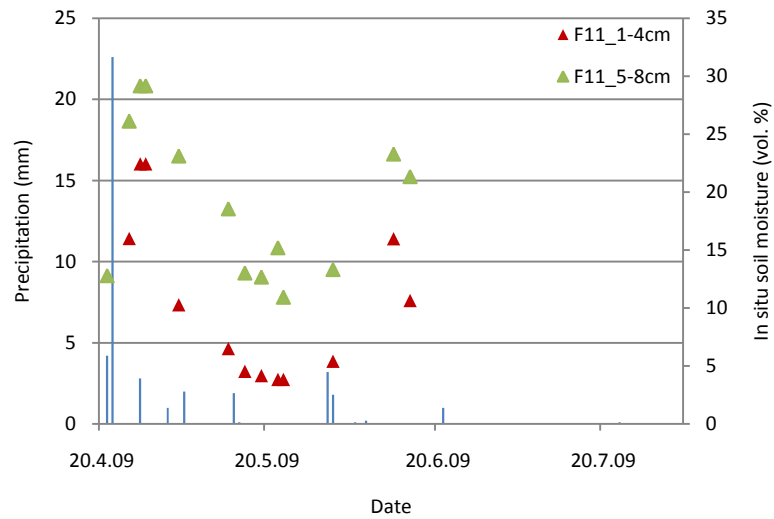
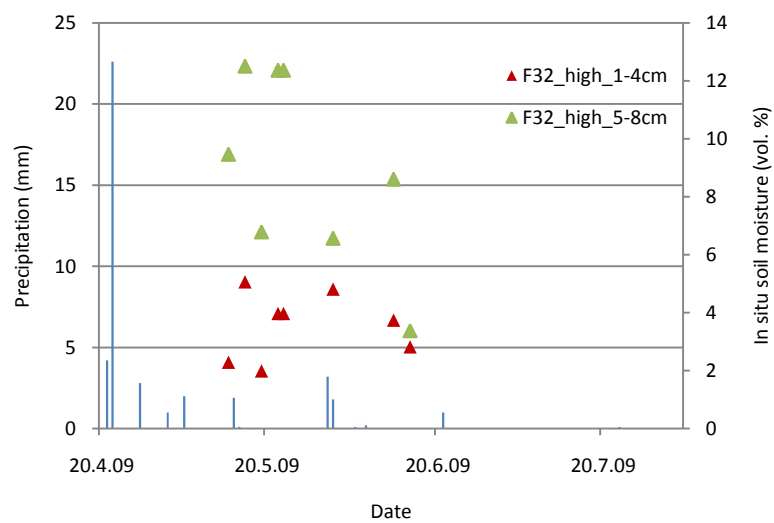
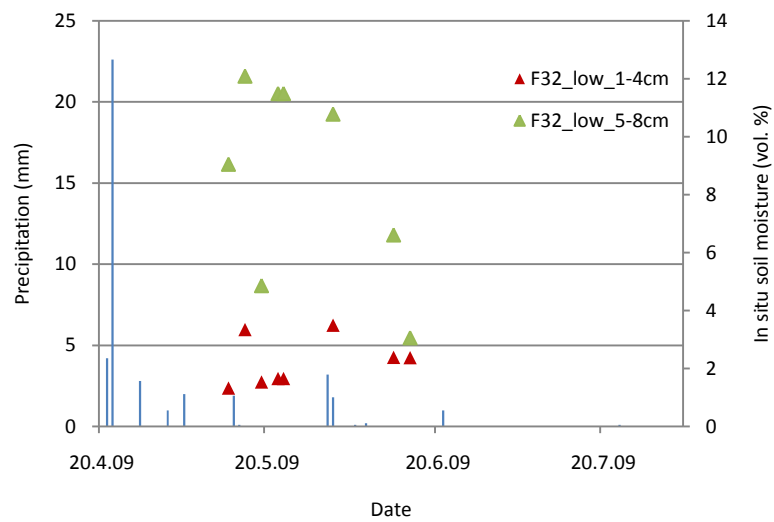
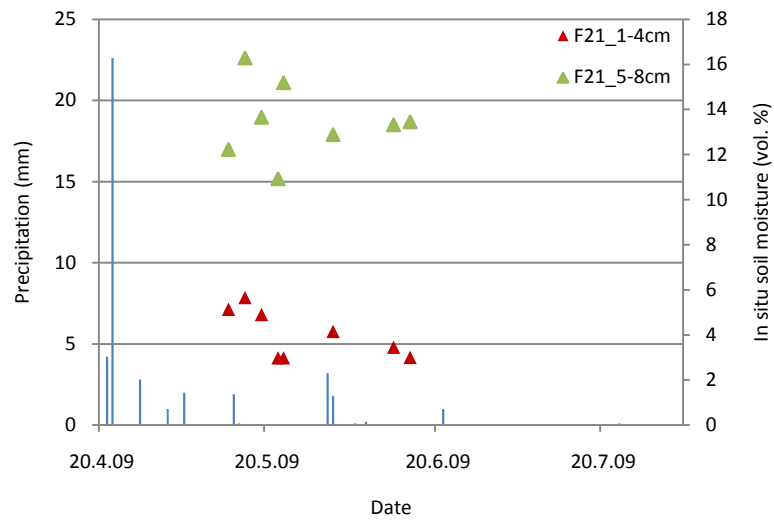


Figure 3.15 Soil moisture change and precipitation in mm through the campaigns of 2008 at both 1–4 cm and 5–8 cm depths for each study field.





**Figure 3.16 Soil moisture change and precipitation in mm through the campaigns of 2009 at both 1–4 cm and 5–8 cm depths for each study field.**

Figure 3.17 illustrates the change of the rms height  $s$  for all four bare fields during the two campaigns. The measured rms height is found to be very stable within 0.5 cm within a campaign period, especially for the year 2009. An overall trend of decay of the rms height is observed. Note the first two measurements were taken in 2008 and the rms height of F11 increases considerably from the year 2008 to the year 2009. In addition, one sample of F21 was missing in 2008 on the figure due to a quality problem in the original photos. Figure 3.18 illustrates the correlation length samples for F11, F21 and F32 (F32\_low and F32\_high) during the campaign periods with exponential shape autocorrelation function on the top and Gaussian shape autocorrelation length on the bottom. Unfortunately, in one sample from each of F21 and F31 it was not possible to find the exponential shape of correlation length within the available profile, which indicates a lack of size in certain conditions for this camera system to measure the correlation length with exponential shape of autocorrelation function. Apart from this, large variations (between 5 and 10 cm) are found (except for F32 with the Gaussian autocorrelation function) in both exponential and Gaussian correlation length.

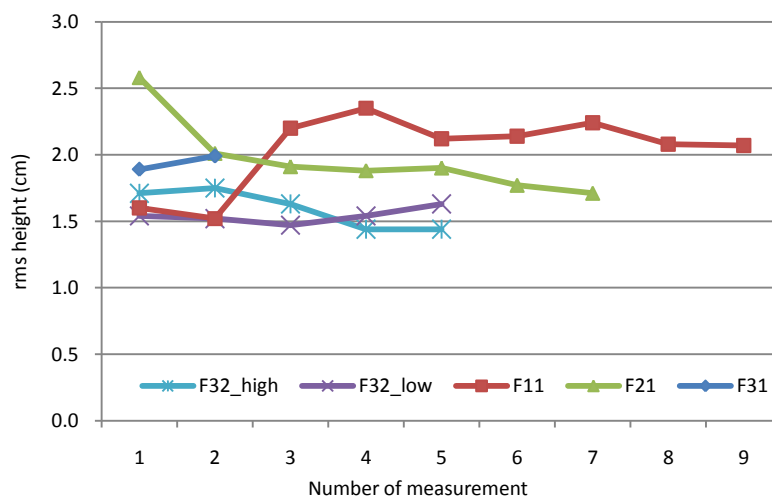


**Figure 3.17 The variability of the rms height  $s$  for four study fields during the two campaigns with the first two measurements of F11, F21 and F31 taken in 2008 while others were taken in 2009.**

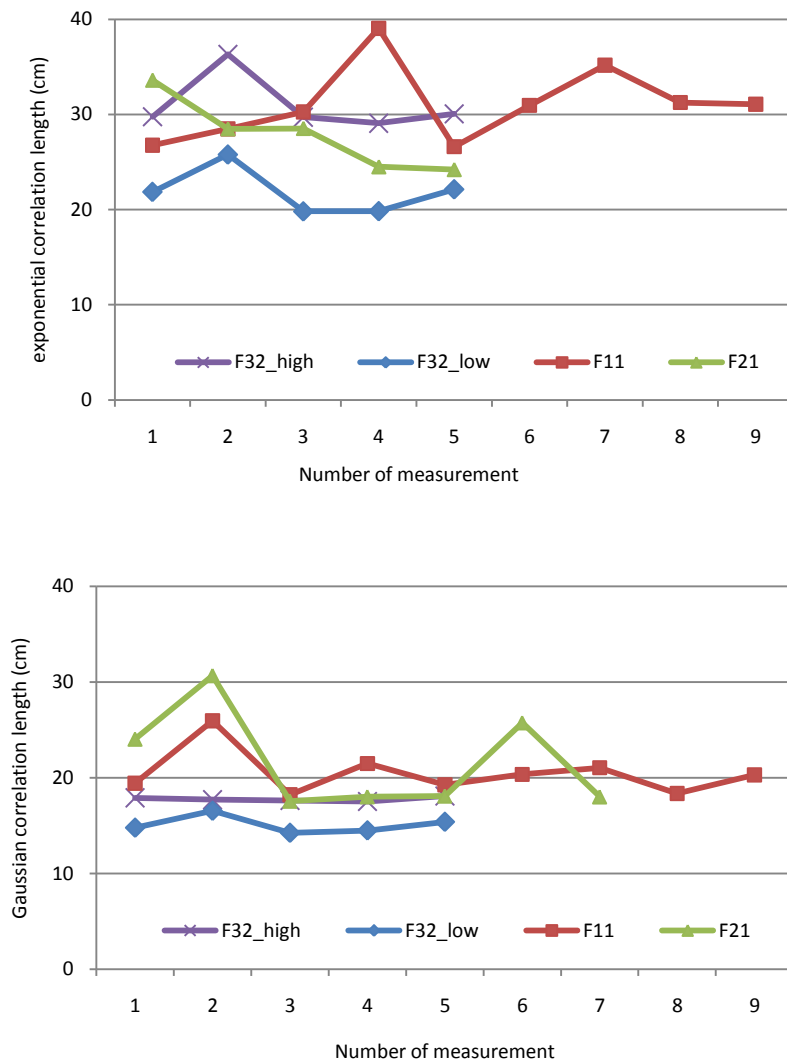


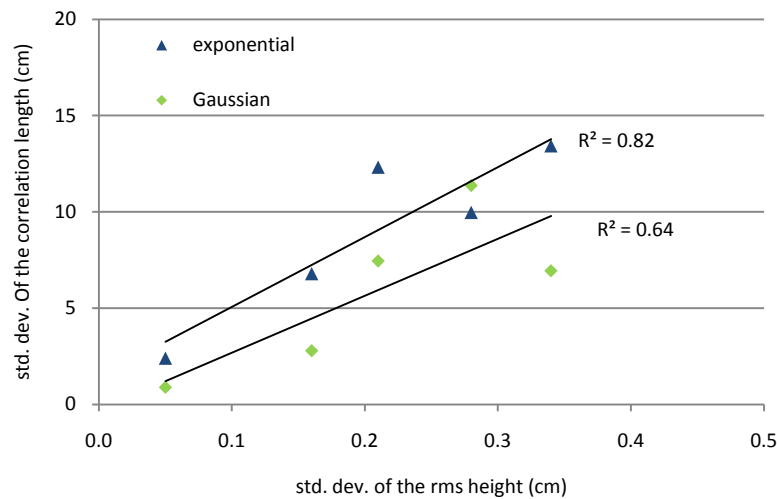
**Figure 3.18** The variability of the correlation length  $l$  with exponential autocorrelation function (top) and Gaussian autocorrelation function (bottom) for three study fields during the two campaigns with the first measurement of F21 and the first two measurements of F11 taken in 2008 and the others taken in 2009.

To further investigate the spatial variability of both soil moisture and roughness parameters, Table 3.9 shows the in-field variability, in terms of the mean of the absolute values and the mean variation among SPs, of soil moisture at both depths and roughness parameters. F32 is separated into two parts, as mentioned in the previous section, F32\_low and F32\_high. The mean standard deviations of surface soil moisture among SPs for every study field are well under 4 vol. %. Note that even within the *Azienda*, field average soil moisture can yield a difference of more than 10 vol. %. However, the in-field rms height and correlation length among SPs have large standard deviations. The mean variation is taken by averaging the results of mean of measurement values

divided by the mean of standard deviation among SPs. It is clear that *in situ* measurements have reasonably small variance – about 20% – in soil moisture measurements at both depths except in extremely dry conditions, which is the case for F32, where the mean variation for 1–4 cm depth and 5–8 cm depth reaches 51% and 38% respectively. The sampling scheme is also approved through the variation assessment of the rms height. The field average standard deviation ranges from 0.05 cm for the field F32\_low to 0.34 cm for the field F21. The mean variation of rms height ranges from 3% to a maximum of 17%. Compared to soil moisture and rms height, the field averaged standard deviations of the correlation length are larger on wet soils than on dry soils, ranging from 11% to 46% for exponential shape autocorrelation function and from 7% to 42% for the Gaussian shape autocorrelation function. In addition, Figure 3.19 shows a clear positive correlation between the field averaged standard deviation of rms height and of correlation length with both exponential and Gaussian shape of ACF.  $R^2$  are 0.82 and 0.64 respectively.

**Table 3.9 Mean in-field variability of surface geophysical parameters for all dates.**

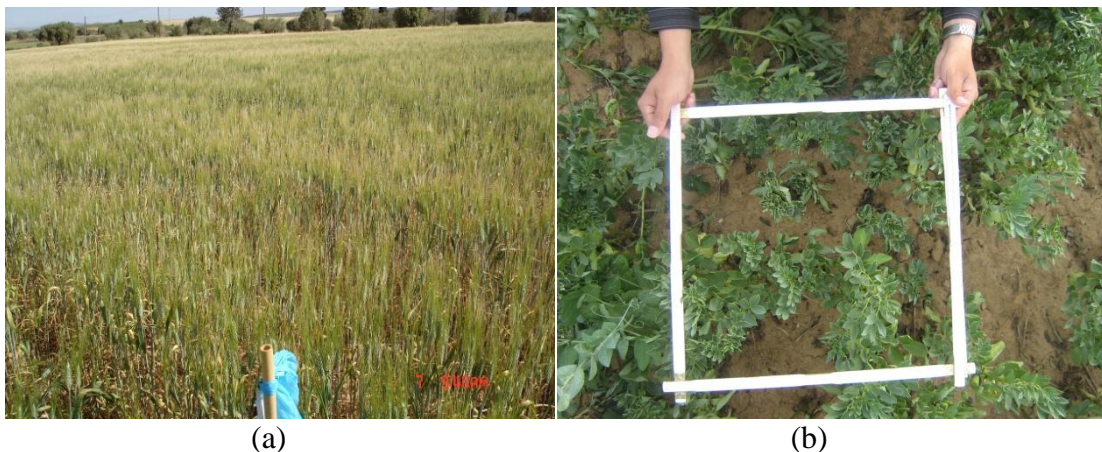
field	mean 1- 4cm $m_v$ (vol. %)	std. dev. (vol. %)	mean 5- 8cm $m_v$ (vol. %)	std. dev. (vol. %)	mean $s$ (cm)	std. dev. (cm)	mean $l_{exp}$ (cm)	std. dev. (cm)	mean $l_{Gau}$ (cm)	std. dev. (cm)
F11	14.03	3.08	20.14	3.59	2.04	0.21	31.07	12.32	20.84	7.45
F21	10.40	2.64	16.69	3.72	1.97	0.34	29.03	13.43	21.72	6.94
F31	6.85	1.27	8.46	1.61	1.94	0.28	24.06	9.97	26.80	11.37
F32_low	2.23	0.78	8.68	1.84	1.65	0.05	21.89	2.40	15.08	0.89
F32_high	3.58	1.82	9.01	3.44	1.48	0.16	30.99	6.79	17.76	2.79
variation	18%~51%		18%~38%		3%~17%		11%~46%		7%~42%	



**Figure 3.19** The field averaged standard deviation of the correlation length (with  $R^2$  of 0.82 for exponential and of 0.64 for Gaussian ACFs) increases with the field averaged standard deviation of the rms height.

### 3.2.5. Crop fields

In addition to measurements on bare fields, fields planted with different crops are also prepared (Figure 3.5). Their sizes are given in Table 3.4. The same selection scheme of SPs is adopted for these fields. Several parameters are measured on these fields including soil moisture at 1–4 cm and 5–8 cm depth, the vegetation water content, the Leaf Area Index (LAI), the row distance if applied, the plant density, the plant profile, the crop coverage and the vegetation height. Figure 3.20 demonstrates measurements on planted fields by a group of field photos of different types of crop.





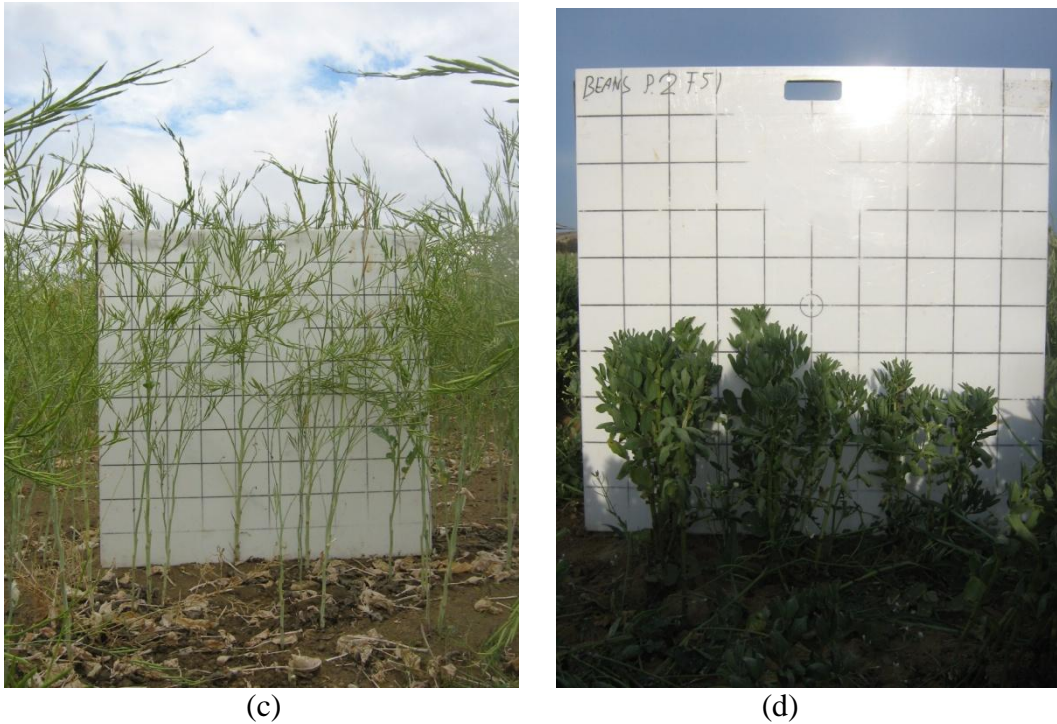


**Figure 3.20** Field photos as (a) an overview of the wheat field W1 taken on 7<sup>th</sup> May 2008, (b) a crop coverage photo taken on the bean field B1 on 8<sup>th</sup> May 2008, (c) a plant profile photo on the canola field C1 taken on 6<sup>th</sup> June 2008 and (d) a plant profile photo on the bean field B1 taken on 8<sup>th</sup> May 2008.

### 3.2.5.1. Soil water content and vegetation water content

The soil moisture measurements are the same as the sampling scheme on the bare fields. Similarly, two plots of 1m<sup>2</sup> vegetation are carefully cut from the soil surface for each sample point. These samples are sealed and labelled before weighing in the laboratory. After drying in the oven at 85°C for 24h, the vegetation water content is calculated by the difference in the weight of the wet and the dried sample. The values of the two samples for each sample point are averaged as the value for the sample point and the values of all sample points are averaged to represent the study field.

### 3.2.5.2. LAI

The Leaf Area Index (LAI) is defined as the dimensionless ratio of total upper leaf surface of vegetation divided by the surface area of the land where the vegetation grows. It is mathematically expressed as in Miller (1967):

$$LAI = 2 \int_0^{\frac{\pi}{2}} \ln \left[ \frac{1}{P(\theta_z)} \right] \cos\theta \sin\theta d\theta$$

### 3.13

where  $\theta_z$  and  $P(\theta_z)$  denote the view zenith angle and the gap fraction at the view zenith angle.

While several approaches have been reported in literature (**Chen et al. 1997**), the LAI-2000 Plant Canopy Analyzer (LI-COR, Lincoln, Nebraska) is used in this work. This equipment is regarded as a convenient version of a technique of hemispherical photography which is used for characterising plant canopies using optical measurement taken looking upward through an extreme wide-angle lens (fish-eye) (**Madgwick and Brumfiel. GI 1969; Whitmore et al. 1993; Chen et al. 1997**). Five sample measurements are taken for each sample point and all samples are averaged to represent the field average value.

#### 3.2.5.3. Other vegetation parameters

Row distance can only be measured in the wheat field in this work, since both broad beans and canola are randomly distributed. Since stems of wheat are regularly located, only one measurement per sample point is taken. Field averaged value is taken as the mean of the five samples. The plant density is calculated by counting crop stems per  $m^2$ . Similar to the measurement of vegetation water content, two samples are taken for each sample point and all samples are averaged to represent the whole field. One crop profile photo is taken for each sample point with a  $1m \times 1m$  gridded plastic board as reference (Figure 3.20 (c) and (d)), while these photos can be used to rebuild vegetation structure. Similarly, one crop coverage photo is taken for each sample point from the top for the area within a 25 cm by 25 cm frame (Figure 3.20 (b)). Ten plants around each sample point are chosen randomly for crop height measurement, and all samples are averaged to represent the field average crop height.

#### 3.2.6. Crop field database

On crop fields, surface soil moisture shows a slightly different trend as the values are higher at the peak but drop quickly to below 10 vol. % in most cases for both 1–4 cm

depth and 5–8 cm depth as shown in Figure 3.21. The dynamic surface soil moisture for all crop fields is well recorded. In addition, surface soil moisture in different crop fields is of less variance than on bare fields.

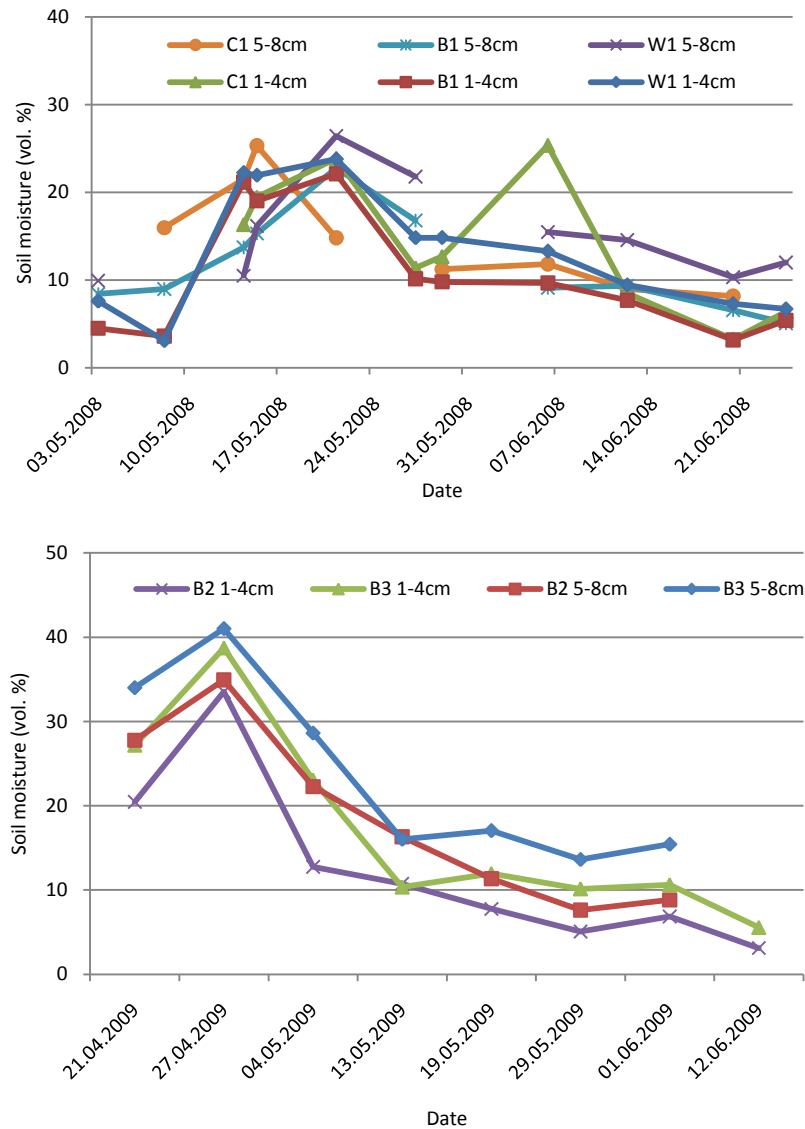


**Figure 3.21 Temporal variability of surface soil moisture on crop fields in 2008 (top) and 2009 (bottom).**

Although with limited measurements, Figure 3.22 shows trends of the phenology stages of different crops in terms of the vegetation water content per m<sup>2</sup>. Beans grow until mid-May while both wheat and canola show a constant decrease in terms of biomass. Much more precipitation in late spring in 2009 than in 2008 may have accelerated the growing period of beans for a few days, in terms of the maximum vegetation water con-

tent per unit area on 11<sup>th</sup> May 2009 compared to 15<sup>th</sup> May 2008 and the beans dried up much more quickly in 2009 than in 2008.

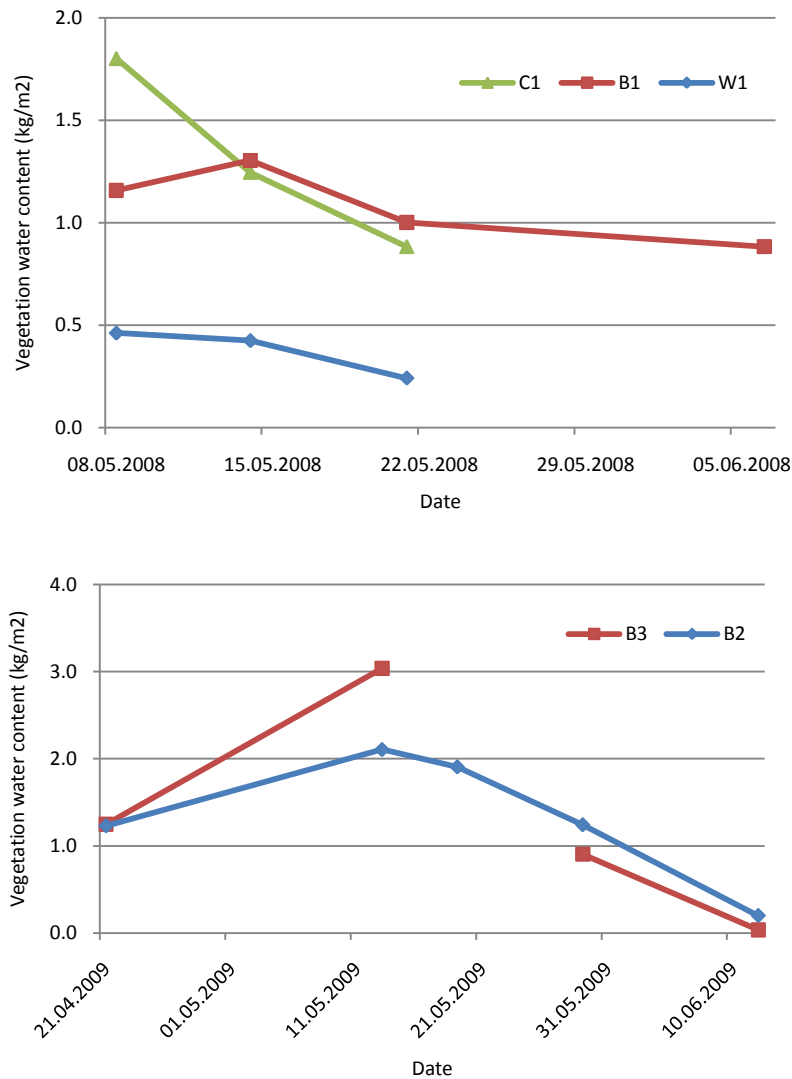


**Figure 3.22 Temporal variability of the vegetation water content on crop fields in 2008 (top) and 2009 (bottom).**

Figure 3.23 plots the temporal LAI change for all crop fields through the campaigns. A few unexpected extreme values may indicate that the five samples for each of the five SPs are not sufficient to represent an accurate trend of the LAI, although the downward trend of the LAI through May and June is clear for all types of crop.

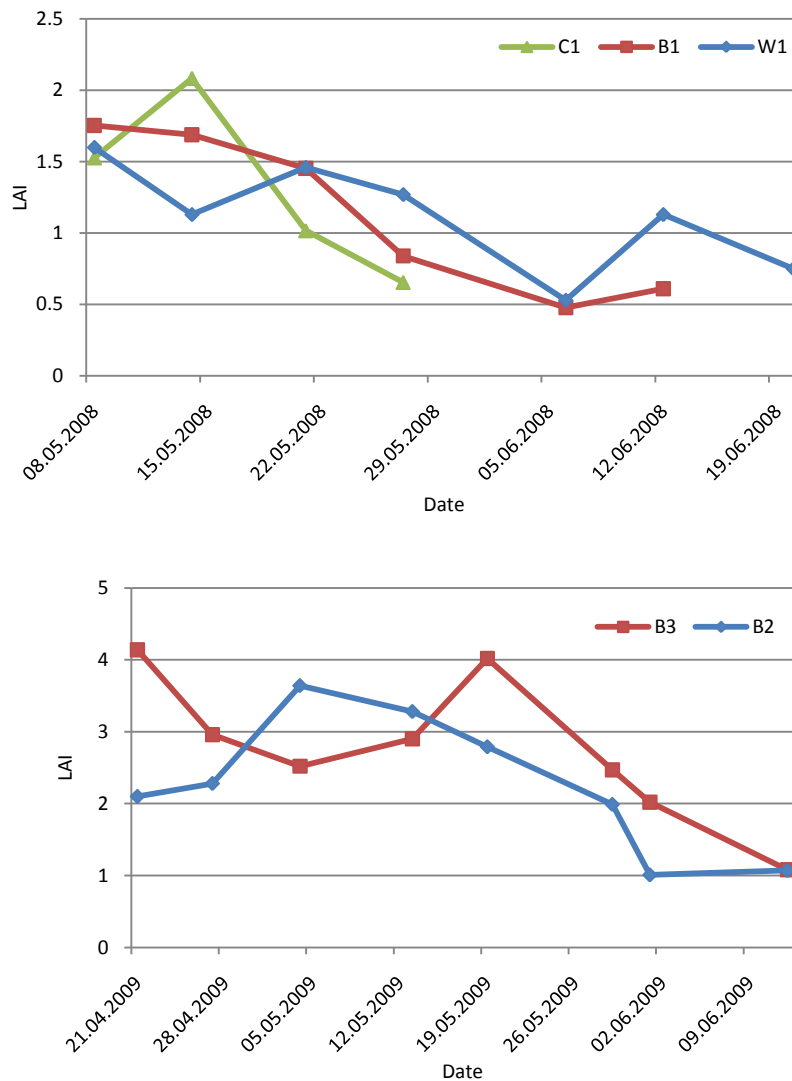


Figure 3.23 Temporal variability of the LAI on crop fields in 2008 (top) and 2009 (bottom).

### 3.2.7. Other measurements

In addition, soil texture is measured using the granulometric method by taking five soil samples per bare field, while each sample is sealed and labelled in a plastic bottle with a volume of 1000 cm<sup>3</sup>. After laboratory measurements, field average soil texture is listed in Table 3.10. Soil texture is traditionally classified by particle sizes in soil, namely sand, silt and clay, in descending order. In accordance with USDA (United States Department of Agriculture) soil taxonomy, the soil type of each study field is also added to the table according to their fractions in a sample.

**Table 3.10 Soil texture and size of each test field.**

Field	Soil type	Sand (%)	Clay (%)	Silt (%)	Size (Hectare)
F11	loam	51	17	32	1.7
F21	sandy clay loam	47	32	21	4.4
F31	sandy clay loam	58	24	18	2.6
F32	clay loam	44	35	21	4.9

Additional data are acquired as GPS coordinates for all field corners, SPs on fields and corner reflector and irrigation pipes for mapping purposes.

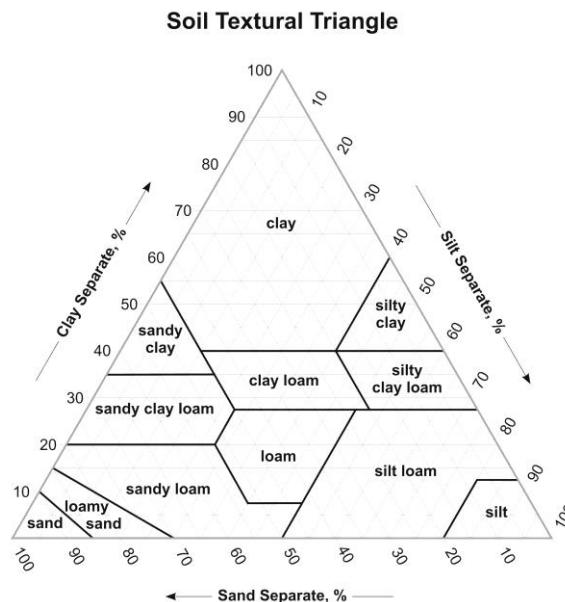


**Figure 3.24 Soil texture triangle according to the USDA classification scheme (USDA 2011).**

### 3.3. Summary

Chapter 3 starts with an introduction focusing on the geographical and climatic characteristics of the study site of this work – the *Azienda San Michele* on the largest plain of the island of Sardinia, *the Campidano* Plain. By emphasising the intrinsic and increasing water usage pressure in various climate change scenarios in the Mediterranean semi-arid region, the importance of timely and spatially cost effective surface soil moisture mapping and monitoring is raised.

Two field campaigns are conducted for this work in 2008 and 2009, covering the late spring and early summer of each year, when a trend from wet to extremely dry conditions can be observed (Figure 3.15 and Figure 3.16). The principles of soil moisture and roughness parameter measurement are explained along with widely used *in situ* measurement techniques. For soil moisture measurements, both the conventional gravimetric method and a more modern and mobile approach – the ThetaProbe ML2x – are adopted. A photogrammetry based surface soil roughness system is deployed in this work, which has the advantage of timely and cost effective field measurements of 3D representation of the geometry of the sampled soil surface. Based on this, detailed *in situ* measurement schemes in this work are given. The *in situ* database is carefully analysed for an overview of the geophysical characteristics of the study sites through the campaigns in terms of absolute values and temporal variability. Further investigations are taken on the spatial variability of both soil moisture and roughness parameters within sample points on each of the study fields.

The in-field variability of surface soil moisture at both depths is found within 4 vol. %. While limited rain events are available during the summer for the study site, the measured rms height remains constant (Figure 3.17). However, the correlation length with both exponential and Gaussian ACFs varies considerably through the campaigns (Figure 3.18). It is also found that the variation of the correlation length among SPs has a strong positive linear correlation with the variation of the rms height among sample points (Figure 3.19). The coverage of the designed camera system is found to be insufficient in certain cases to estimate correlation length with exponential ACF, but reliable for rms height measurements over the study fields.

Although the main purpose of the work is on the SAR technique of geophysical parameter retrieval on bare soil surface, measurements of surface soil moisture and several vegetation parameters are also conducted on different crop fields. The data are utilised in Chapter 6 for exploring the extension of the performance of the surface geophysical parameter retrieval model on crop fields.

Enjoy a grander sight by climbing to a  
greater height.

---Wang Zhihuan, Poet in Tang Dynasty

## Chapter 4 Synthetic Aperture Radar

This chapter starts by describing the technical fundamentals of radar, and then gives an introduction to Synthetic Aperture Radar (SAR), where various sensors are in operation (Ryerson and American Society for Photogrammetry and Remote Sensing. 1998; Woodhouse 2006; Richards 2009). The SAR geometry and its image processing are focused on, along with the fundamental relationship between the SAR image and surface geophysical parameters.

### 4.1. Radar Fundamentals

The term ‘radar’ stands for *Radio detection and ranging*, which operates in the microwave range in the electromagnetic (EM) spectrum, with longer wavelengths beyond the visible and the thermal infrared range. Most applications are within 1 GHz and 40 GHz in frequency (Table 4.1). Note the P band and the Ultra High Frequency (UHF) band are partly overlapped. Benefiting from the long waves, radar systems are free from cloud cover compared to optical sensors. Radar is also an active sensor, which transmits and receives electromagnetic signal backscattered from the target or surface. Therefore, radar is characterised by its capability of working day and night independent of weather conditions.

**Table 4.1 Mostly used microwave bands and their frequency and wavelength range.**

Band	Frequency (GHz)	Wavelength (cm)
P	0.22-0.39	77-136
UHF	0.3-1	30-100
L	1-2	15-30
S	2-4	7.5-15
C	4-8	3.75-7.5
X	8-12	2.4-3.75
Ku	12-18	1.67-2.4
K	18-26.5	1.17-1.67
Ka	26.5-40	0.75-1.18



A radar system transmits microwave signals to a target or surface, depending on its frequency, polarisation and transmitting geometry of the sensor including the incidence angle, the swathe and the resolution element. After receiving backscattered signals from the target or the surface with post-processing, an observed scene consists of parameters as signal amplitude, polarisation, phase information and target position. Various types of radar systems have been designed for different purposes on the scene parameters, such as altimeter, scatterometer, and imaging radar, which includes real aperture radar (RAR) or side-looking airborne radar (SLAR) and synthetic aperture radar (SAR) (Ryerson and American Society for Photogrammetry and Remote Sensing. 1998).

An imaging system is considered to be able to measure “properties related to the spatial variability” directly and generate a two-dimensional radar image of the scene from the echoes received from the target or surface (Woodhouse 2006). Section 4.2 will focus on SAR and further explain the system.

## 4.2. Synthetic Aperture Radar

SAR is a relatively new technique. For a concise summary of the technical perspectives, six basic principles are given for SAR as the coherent scene illumination, image power mapping, well behaved transformation, conservation of energy, conservation of confusion and conservation of coordinates (Ryerson and American Society for Photogrammetry and Remote Sensing. 1998).

The geometry of a basic monostatic SAR system is illustrated in Figure 4.1, where  $\theta_l$  denotes the look angle – the angle from the nadir direction to the sensor’s line of sight,  $\theta_d$  denotes depression angle – the angle from the sensor’s line of sight to the sensor local horizontal line and  $\theta_i$  denotes the incidence angle – the angle from the normal to a pre-defined local reference surface to the sensor’s line of sight, while the local incidence angle  $\theta$  is the angle from the normal to the actual surface to the sensor’s line of sight. The synthetic aperture refers to a method of processing echoes received from a target or surface to increase the spatial resolution on the azimuth direction by using the Doppler beam sharpening approach and coherently combining a series of low-resolution antennae. Some terms can be clarified to better explain SAR geometry.

4.2.1. SAR geometry

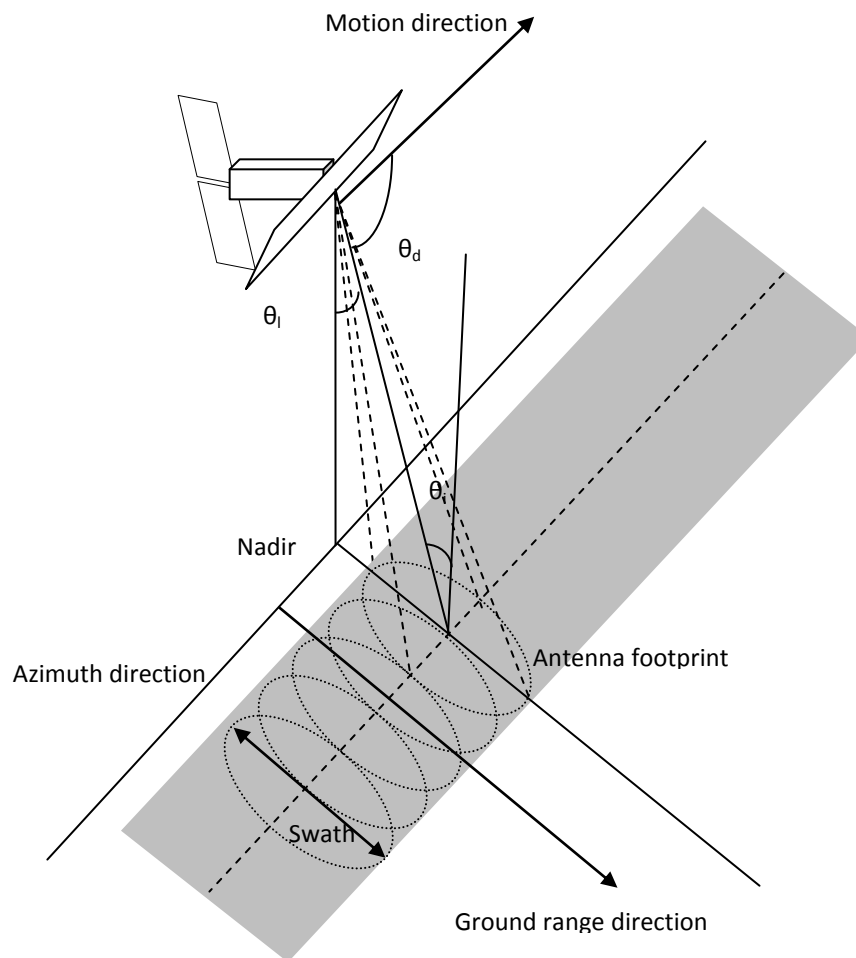


Figure 4.1 Illustration of geometry of a basic monostatic SAR system.

The Doppler frequency shift  $f_D$  is defined as:

$$f_D = \frac{v}{\gamma}$$

4.1

where  $v$  and  $\gamma$  denote the relative velocity and the wavelength of the signal.

The monostatic system, compared to a bistatic system, co-locates the transmitter and receiver on the same platform. In the monostatic system, a beam is transmitted from the sensor to illuminate an antenna footprint on the surface following the sensor's motion

direction (Figure 4.1). The footprint is structured by two perpendicular axes – the azimuth and the ground range. The azimuth direction is the direction parallel to the sensor’s motion direction on the surface. The range, also termed the slant range, means the actual range measured by the sensor based on the time delay of transmitting and receiving. When the reference surface is transformed to the actual surface, the slant range is renamed the ground range. The slant range resolution  $\rho_s$ , with unit of frequency, is defined as:

$$\rho_s = \frac{c_0}{2B_p}$$

### 4.2

where  $c_0$  and  $B_p$  denote the speed of light and the bandwidth of the chirped pulse used in the SAR system to maintain a long pulse (Woodhouse 2006), while the ground range resolution  $\rho_g$ , with unit of metres, can be transformed by considering the local incidence angle  $\theta$  as:

$$\rho_g = \frac{\rho_s}{\sin\theta}$$

### 4.3

Therefore, a generally coarser resolution can be found when approaching the nadir direction due to the shrinking incidence angle.

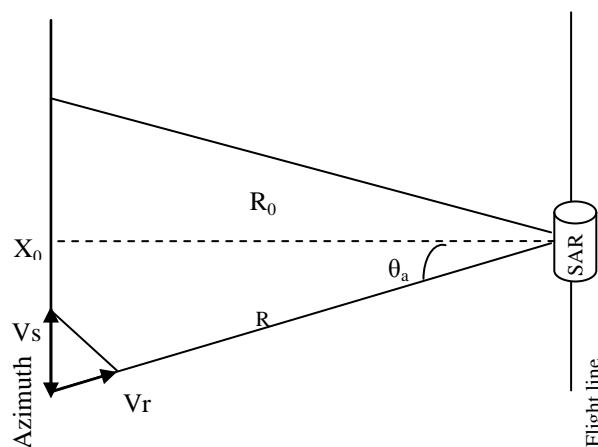


Figure 4.2 The synthetic aperture geometry.

Before calculating the azimuth resolution, the geometry of the synthetic aperture is illustrated by introducing the factor of the Doppler frequency shift as in Figure 4.2, which is drawn from the perspective of the SAR sensor.  $V_s$  and  $V_r$  denote the absolute speed of the sensor along the azimuth direction and the relative speed of the sensor along the range direction to the target respectively. In this case, the time the SAR takes to differentiate signals  $T_d$  can be described in units of seconds as:

$$T_d = \frac{V_s}{B_D}$$

**4.4**

where  $B_D$  stands for the Doppler bandwidth – the frequency separation on the  $R$  direction and on the  $R_0$  direction. To determine the temporal resolution  $T_d$  and hence the azimuth spatial resolution  $\rho_a$ , the Doppler bandwidth  $B_D$  has to be solved, which depends on the maximum and the minimum relative velocity between the target and the SAR sensor. When the target enters or leaves the beam of the SAR sensor, the maximum relative velocity is achieved as:

$$V_r = V_s * \sin\theta_a$$

**4.5**

where  $\theta_a$  denotes the angle between the velocity vector and the direction of the target. When the target is at the zero-Doppler position  $X_0$ , the minimum relative velocity is achieved as  $-V_r$ . In this case, the Doppler frequency range is between  $f_0-f_D$  and  $f_0+f_D$ , where  $f_0$  and  $f_D$  denote the original transmitted beam frequency and the Doppler frequency respectively. The latter is calculated by:

$$f_D = \frac{2V_r}{\lambda}$$

**4.6**

Therefore, the Doppler bandwidth  $B_D$  can be calculated by:

$$B_D = (f_0 + f_D) - (f_0 - f_D) = 2f_D = \frac{4V_r}{\lambda} = \frac{4V_s \sin\theta_a}{\lambda}$$

**4.7**

In the synthetic aperture system,  $\theta_a$  is small, while the target is overwhelmingly smaller than the sensor's shift. Therefore

$$\sin\theta_a \approx \theta_a = \frac{\lambda}{2D}$$

**4.8**

where  $D$  denotes the real length of the SAR antenna. In this case, the spatial azimuth resolution  $\rho_a$  can be achieved by substituting Equations 4.5–4.8 to Equation 4.4:

$$\rho_a = \frac{D}{2}$$

**4.9**

A smaller length of SAR antenna can lead to a finer spatial azimuth resolution.

#### **4.2.2. Geometric distortion of SAR images**

Due to the side-looking geometry, geometric distortions are intrinsic characteristics of SAR images.

##### **4.2.2.1. Layover and foreshortening**

As stated before, the relationship between the ground range and the slant range depends on the difference between the actual surface and the reference surface. Therefore, a frequently found feature on SAR imagery is the layover when the actual surface varies significantly from the reference surface. As illustrated in the middle rectangle in Figure 4.3, the up slope becomes narrower than the same degree of down slope on the slant range image, as well as in the ground range image. In extreme cases, when the echo from the peak of the target is received earlier than the near end bottom of the target as the left rectangle shows, the peak of the target will appear 'falsely' closer to the nadir position than the bottom of the target. Note the slope degree and the distance of the target to the nadir position are two important factors to the layover effect, while the larger

the slope is and the closer the target is to the nadir position, a stronger layover effect is more likely to appear in the SAR image.

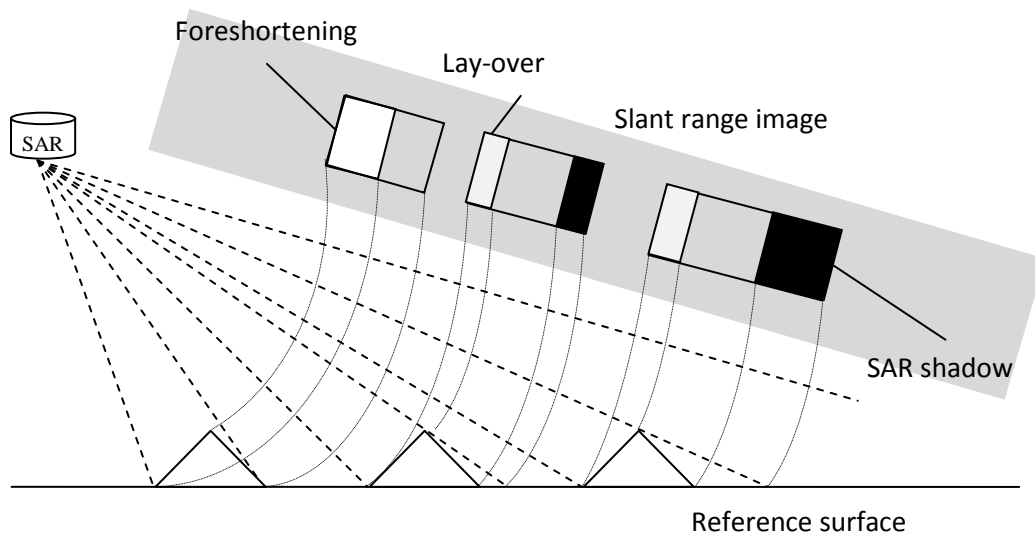


**Figure 4.3** An illustration of the geometric distortion in the SAR imagery assuming three identical surface structures.

#### 4.2.2.2. SAR shadow

Also illustrated in Figure 4.3, the SAR shadow happens in the target area behind a large slope, where no echoes are received due to the blockage effect from the large down slope. In this case, the local incidence angle is larger than  $90^\circ$  in the direction facing the SAR sensor. The larger the slope is, the larger the area of SAR shadow appears. Apart from these geometric distortions in SAR imagery, to process the original SAR images requires further efforts.

#### 4.2.3. SAR imagery processing

Each pixel of a SAR image represents the signal response in terms of amplitude and phase at different polarisations for a certain length in range and azimuth direction. The amplitude and phase information is described by a complex number. The description of SAR imagery processing starts with several core terms in qualifying and quantifying the echoed information, *e.g.* polarisation, phase and the backscattering coefficient. Two important procedures in SAR imagery processing are followed — the speckle filter and geometric correction.

#### 4.2.3.1. Polarisation

One of the most important properties for EM waves is polarisation, which describes the way the wave oscillates. In the SAR system, the Earth's surface is used as the reference surface and the horizontal and vertical directions are defined according to the relationship between the plane on which the wave propagates and the reference surface. Figure 4.4 illustrates the vertical and horizontal polarisations for EM waves. In both cases, the wave propagates to the  $z$  direction, with phase  $\Phi = [0, 2\pi]$ .  $A$  and  $\lambda$  are the amplitude and the wavelength of the wave respectively. The main difference between these two polarised waves is that for the oscillation component in  $x$  direction,  $E_h$  equals zero in the vertical polarisation while for the oscillation component in  $y$  direction,  $E_v$  equals zero in the horizontal polarisation. When  $|E_h| = |E_v| = A$ , the polarisation is defined as circular polarisation; exceptions are when in phase difference  $\Delta\Phi = n\pi$ , where  $n = 0, 1, 2, \dots, \infty$ , the polarisation becomes linear polarisation and this term applies to the case when  $|E_h| \neq |E_v|$ . When  $E_h \neq E_v \neq 0$ , the polarisation is defined as elliptical polarisation. The following parts in this subsection will briefly introduce the mathematical description of polarisation.

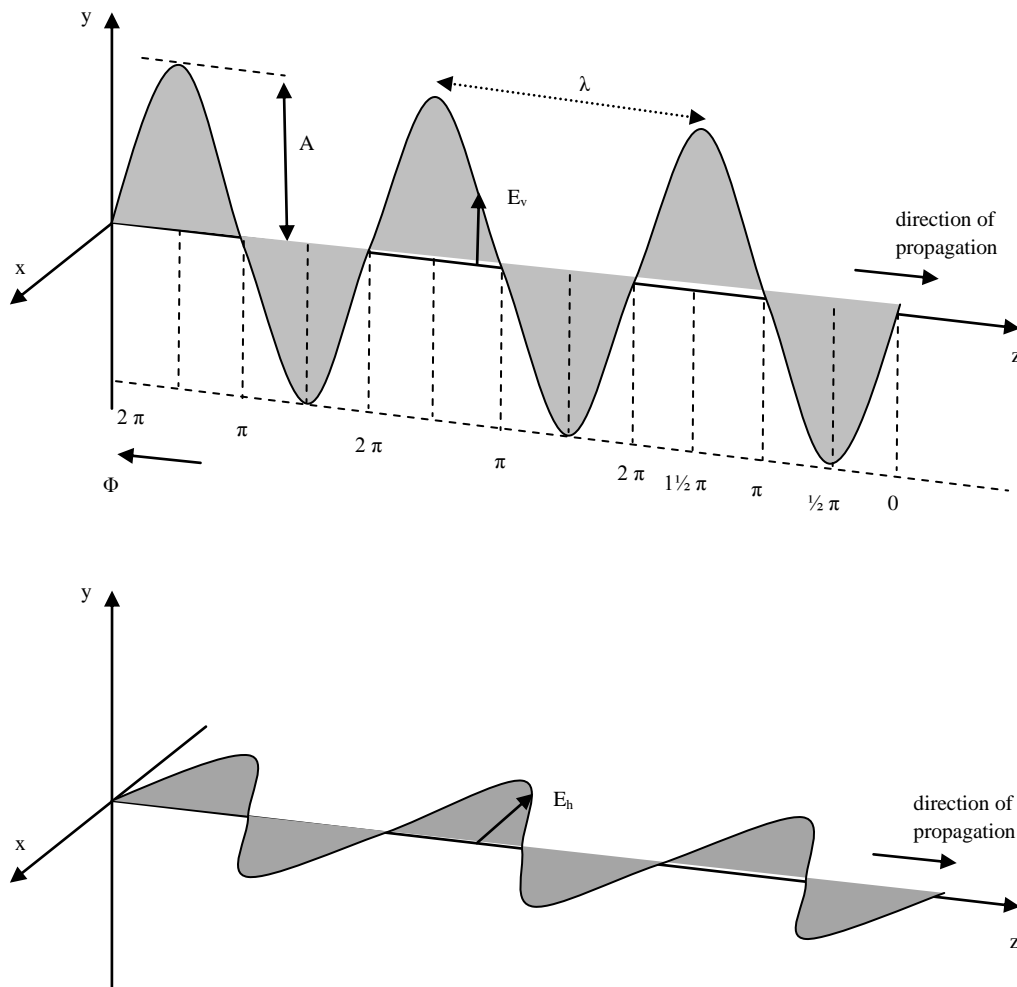


Figure 4.4 Illustration of EM wave vertical polarisation (top) and horizontal polarisation (bottom) after (Woodhouse 2006).

The modified Stokes vector, consisting of four parameters, is introduced to fully describe a polarised wave (Woodhouse 2006):

$$g_m = \begin{bmatrix} I_v \\ I_h \\ U \\ V \end{bmatrix} = I_0 \begin{bmatrix} \frac{1}{2}(1 + \sin 2\psi \cos 2\chi) \\ \frac{1}{2}(1 - \sin 2\psi \cos 2\chi) \\ \sin 2\psi \cos 2\chi \\ \sin 2\chi \end{bmatrix}$$

#### 4.10

where  $I_0$  is the first of the four Stokes parameters, which is a measure of the total amount of energy in the polarised wave and defined as:



$$I_0 = \langle E_x^2 + E_y^2 \rangle = \langle E_x^2 \rangle + \langle E_y^2 \rangle$$

**4.11**

where  $E_x$  and  $E_y$  are the two electric field vectors, as a whole to represent the wave vector.  $I_x$  and  $I_y$  are described as:

$$I_x = |E_x|^2 = (I_0 - Q)/2$$

**4.12**

$$I_y = |E_y|^2 = (I_0 + Q)/2$$

**4.13**

where  $Q$  reflects the tendency of the polarisation to be more vertical or horizontal as mathematically defined as:

$$Q = \langle E_y^2 \rangle - \langle E_x^2 \rangle$$

**4.14**

and the other two Stokes parameters  $U$  and  $V$  are joined to represent the phase difference  $\Delta\Phi$  between the horizontal and vertical tendency of the wave:

$$U = 2E_y E_x \cos\Delta\Phi = 2\text{Re}E_y E_x^*$$

**4.15**

$$V = 2E_y E_x \sin\Delta\Phi = 2\text{Im}E_y E_x^*$$

**4.16**

where  $Re$  and  $Im$  refer to the real part and the imaginary part of the field components and the superscript  $*$  refers to the complex conjugate of the number. The orientation angle  $\psi$  and the ellipticity angle  $\chi$  are defined as:

$$\psi = \tan^{-1}\left(\frac{|E_y|}{|E_x|}\right)$$

**4.17**

$$\chi = \tan^{-1}\left(\frac{b}{a}\right)$$

4.18

where  $a$  and  $b$  are the major and minor axes respectively of the projected polarisation ellipse.

The original Stokes vector is given as:

$$g = \begin{bmatrix} I_0 \\ Q \\ U \\ V \end{bmatrix} = I_0 \begin{bmatrix} 1 \\ \cos 2\psi \cos 2\chi \\ \sin 2\psi \cos 2\chi \\ \sin 2\chi \end{bmatrix}$$

4.19

and they are related by  $g = U g_m$ , where

$$U = \begin{bmatrix} 1 & 1 & 0 & 0 \\ 1 & -1 & 0 & 0 \\ 0 & 0 & 1 & 0 \\ 0 & 0 & 0 & 1 \end{bmatrix}$$

For a SAR system, the signal is transmitted from the sensor and scattered from the target on the surface and received as backscatter. Therefore, a relationship between the incidence Stokes vector  $g_i$  and scattered Stokes vector  $g_s$ :

$$g_s = M g_i$$

4.20

where  $M$  is a matrix related to the polarisation properties. When considering the relationship between incidence Stokes vector  $g_i$  and the received Stokes vector  $g_r$ , the distance from the target to the sensor, the range  $R$  needs to be taken into account, and therefore:

$$g_r = \frac{1}{4\pi R^2} M g_i$$

4.21

In this case, the  $M$  is normally referred to as the *Mueller matrix*. A thorough description of the form of the Mueller matrix can be found in Cloude and Pottier (1996).

To better facilitate two Stokes vectors in the linear polarisation system, an alternative scattering matrix  $S$  is introduced as:

$$S = \begin{pmatrix} S_{VV} & S_{VH} \\ S_{HV} & S_{HH} \end{pmatrix}$$

**4.22**

The alternative scattering matrix  $S$  is a matrix consisting of four scattering complex numbers to describe the amplitude and phase of each linear polarisation direction. VV and HH are defined as cross-polarisations and HV and VH are considered as co-polarisations. In most natural conditions, the two co-polarised scattering measurements are equalled as  $S_{HV} = S_{VH}$ . In this case, a target vector  $K$  is introduced as:

$$K = [S_{VV} \quad S_{HV} \quad S_{HH}]^T$$

**4.23**

where  $T$  is the transpose of the vector. A more commonly used term, the Pauli basis  $K_P$ , is used as:

$$K_P = \frac{1}{\sqrt{2}} [S_{HH} + S_{VV} \quad S_{HH} - S_{VV} \quad 2S_{HV}]^T$$

**4.24**

The factor  $1/\sqrt{2}$  is used to normalise the result. Two other commonly found matrices are the *covariance matrix*  $C$  and the *coherency matrix*  $T$ , which are described as:

$$C = KK^{*T} = \begin{bmatrix} S_{VV} \\ S_{HH} \\ S_{HV} \end{bmatrix} [S_{VV}^* \quad S_{HH}^* \quad S_{HV}^*] = \left\langle \begin{bmatrix} |S_{VV}|^2 & S_{VV}S_{HH}^* & S_{VV}S_{HV}^* \\ S_{HH}S_{VV}^* & |S_{HH}|^2 & S_{HH}S_{HV}^* \\ S_{HV}S_{VV}^* & S_{HV}S_{HH}^* & |S_{HV}|^2 \end{bmatrix} \right\rangle$$

**4.25**

$$\begin{aligned}
 T &= K_p K_p^{*T} = \frac{1}{2} \begin{bmatrix} S_{HH} + S_{VV} \\ S_{HH} - S_{VV} \\ 2S_{HV} \end{bmatrix} [(S_{HH} + S_{VV})^* \quad (S_{HH} - S_{VV})^* \quad 2S_{HV}^*] \\
 &= \frac{1}{2} \begin{bmatrix} |S_{HH} + S_{VV}|^2 & (S_{HH} + S_{VV})(S_{HH} - S_{VV})^* & 2(S_{HH} + S_{VV})S_{HV}^* \\ (S_{HH} - S_{VV})(S_{HH} + S_{VV})^* & |S_{HH} - S_{VV}|^2 & 2(S_{HH} - S_{VV})S_{HV}^* \\ 2S_{HV}(S_{HH} + S_{VV})^* & 2S_{HV}(S_{HH} - S_{VV})^* & 4|S_{HV}|^2 \end{bmatrix}
 \end{aligned}
 \tag{4.26}$$

#### 4.2.3.2. Backscattering coefficient

The scattered field of the electromagnetic energy is defined as the difference between the field with the existence of the target and the field without the existence of the target (Skolnik 2001). In a natural environment, the incidence signal can be scattered in any direction with different ratio to the total energy. Within the observation angle  $\theta_l$  (Figure 4.1), the effectiveness of scattered energy is described by a term named the scattering cross-section  $\sigma$ , which is mathematically described in  $\text{m}^2$  as:

$$\sigma(\theta_l) = \frac{\text{Scattered power per unit solid angle into direction } \theta_l}{\text{Intensity of the original incidence plane wave}/4\pi}
 \tag{4.27}$$

where  $4\pi$  is used to normalise the plane wave to the solid angle, while the solid angle equals  $4\pi$  for a full sphere. Only the energy scattered back to the SAR sensor can be recorded by the sensor and this amount of energy is termed the backscattering cross-section  $\sigma_b$ , which also in units of  $\text{m}^2$  is defined as:

$$\sigma_b = \frac{I_r}{I_i} 4\pi R^2
 \tag{4.28}$$

where  $I_r$  and  $I_i$  denote the received energy intensity and incidence energy intensity.

The above defined backscattering cross-section  $\sigma_b$  refers to discrete targets rather than an extended surface area in the natural environment. To relate the backscattered signal to the actual geometrical area  $A$ , the quantity of the backscattered signal is normalised to the area  $A$  by a term backscattering coefficient  $\sigma^0$ , also termed *sigma nought*, or the

normalised radar cross-section (NRCS). The backscattering coefficient  $\sigma^0$  is unitless as expressed as:

$$\sigma^0 = \frac{\sigma_b}{A}$$

4.29

When the surface topography is unknown, another measure, the brightness, also termed *beta nought*  $\beta^0$ , is related to the sigma nought by:

$$\beta^0 = \sigma^0 \sin \theta_i$$

4.30

Pixel values of SAR images can be calibrated to either backscattering coefficient or brightness, while in this study only the backscattering coefficient  $\sigma^0$  is used. Different algorithms are used for different sensors and products. For ASAR APS mode the backscattering coefficient  $\sigma^0$  is calculated by Equation 4.31 (**Rosich and Meadows 2004**):

$$\sigma_{i,j}^0 = \frac{I_{i,j}^2}{k} \frac{1}{G(\theta_{i,j})^2} \left(\frac{R_{i,j}}{R_r}\right)^3 \sin^2(\theta_{i,j})$$

4.31

where  $I_{i,j}$ ,  $k$ ,  $G$ ,  $\theta_{i,j}$ ,  $R_{i,j}$ ,  $R_r$  and  $\theta_{i,j}$  denote the intensity, also termed the digital number (DN) of the pixel (i,j), the absolute calibration constant, the antenna pattern gain, the look angle for the pixel (i,j), the slant range for the pixel (i,j), the reference slant range and the incidence angle for the pixel (i,j).

The backscattering coefficient  $\sigma^0$  is calibrated for Radarsat-2 SLC products first to the brightness  $\beta_{i,j}^0$  of the pixel (i,j) by RSI (**2000**):

$$\beta_{i,j}^0 = 10 * \log_{10} \left[ (DNI_{i,j}^2 / A2_{i,j})^2 + (DNQ_{i,j}^2 / A2_{i,j})^2 \right]$$

4.32

where  $DNI_{i,j}$  and  $DNQ_{i,j}$  denote the intensity of the  $I$  and  $Q$  components of the pixel (i,j) and  $A2_{i,j}$  corresponds to the range dependent gain. Afterwards, the backscattering coef-

ficient  $\sigma^0$  is converted from the brightness by using Equation 4.30. The pixel with larger backscattering coefficient or intensity appears brighter than the pixel with smaller backscattering coefficient or intensity.

#### **4.2.3.3. Speckle**

Resulting from interference of the coherent backscattering of individual scatters within a pixel, appearing as “salt and pepper” granular noise-like features on the image, speckle is one the main features of SAR images compared to optical images. It happens when the variation of backscattering amplitude and phase appears to fluctuate randomly across a homogeneous target, while however the same pattern of speckle will occur when a second SAR image is taken in the same geometry and the surface does not change between the two images’ acquisition (**Woodhouse 2006**). Obviously, these speckle features create complexities in SAR image processing and have to be maximally eliminated.

Several approaches can be applied to reduce the speckle effect. They are categorised into the following three parts (**Lee et al. 1994**):

- 1) In the first category, backscattering signals from several sub-apertures of the whole synthetic aperture are incoherently averaged to reduce the speckle variance. This approach is also named the multi-look process (**Porcello et al. 1976**). An N-look approach can reduce the standard deviation of speckle by a factor of  $\sqrt{N}$  while the spatial resolution is coarsened by a factor of N (**Lee et al. 1994**).
- 2) In addition, various statistics filters can be applied to the speckles in the spatial domain of the SAR image. Among all, Lee (including the refined Lee filter) and Frost are two of the widely used filters (**Lee 1980; Frost et al. 1981; Lee 1981**). Other filters include the box filter, the median filter, the geometrical filter and the morphological filter (**Crimmins 1985; Crimmins 1986; Safa and Flouzat 1989; Lee et al. 1994**).
- 3) The third category uses backscattering signals from different polarisations and/or different frequencies (**Novak and Burl 1990; Lee et al. 1991**).

A full description of the details of these approaches is beyond the scope of this work. This work uses a combination of a  $7 \times 7$  sigma filter (Lee 1983) and a  $3 \times 3$  median filter following a similar approach suggested in Lee et al. (1994).

#### 4.2.3.4. Geometric correction

As described before, geometric distortion happens when the actual terrain differs from the reference surface and therefore detailed topographic information is needed for geometric correction. Based on sufficient topographic information being retrieved from a digital elevation model (DEM), SAR images can be geo-coded through:

$$\Delta R \simeq h / \tan \theta_i$$

4.33

where  $\Delta R$  denotes the target position difference between on the actual terrain and on the reference surface, while  $h$  and  $\theta_i$  are the height of the target above the reference surface and the incidence angle respectively. Further geo-correction can be done by pre-set metallic corner reflectors as unknown ground control points. Note that no geometric correction can compensate for the layover and SAR shadow effects from a single SAR geometry.

#### 4.2.4. Space-borne SAR sensors

A large number of airborne systems have been used in the past, while space-borne SAR platforms have been developed largely in more recent decades. Especially since the European Space Agency (ESA) launched the European Remote Sensing Satellite (ERS) series – the ERS 1/2 in 1991 and 1995, respectively – space-borne SAR platforms have been able to provide a significant amount of valuable Earth observation. The ERSs were followed by the Radarsat-1/2 which were launched by the Canadian Space Agency (CSA) in 1995 and 2007, respectively and the Advanced Synthetic Aperture Radar (ASAR) launched by the ESA on the platform of Envisat in 2002. Apart from these C-band sensors, the Japan Aerospace Exploration Agency (JAXA) launched L-band SAR sensor ALOS/Daichi in 2006 while most recently the German Aerospace Centre (DLR) successfully launched the X-band SAR sensors TerraSAR-X and TanDEM-X (Ter-

raSAR-X add-on for Digital Elevation Measurement) in 2007 and 2010, respectively. In this work, only the C-band ASAR and Radarsat-2 imagery are used.

**4.2.4.1. ASAR**

ASAR, the successor of the previously launched ERS-1/2, is mounted along with nine other optical or radar instruments, on the Envisat platform, which was designed and launched in 2002 by the ESA. ASAR is an imaging microwave radar sensor operated at C-band with a full active array antenna equipped with distributed transmit and receive modules. The sensor is able to cover the region near the poles on a daily basis and the equator on a weekly basis (ESA 2007). By providing images with different incidence angles, dual-polarisation and wide swath coverage, ASAR can be used for both global and regional objectives. Seven swathe positions are provided as from IS1 to IS7 when using the Image Mode, which gives incidence angles ranging from 15° to 45° with a nominal spatial resolution of 30m. Two other measurement modes cover larger areas, the Wide Swath (WS) and Global Monitoring Mode (GMM). Both of them provide swathe coverage of 405 km, while the spatial resolutions are 150m and 1000m respectively. Detailed technique parameters of different modes are summarised in Table 4.2. Note the Alternating Polarisation Mode (APS) provides three dual-polarisation options. The Single Look Complex (SLC) APS mode images with HH and VV polarisations are acquired for this work. The SLC means that one real and one imaginary component are used for each pixel to represent the amplitude and phase of the backscattered signal with the full azimuth bandwidth. Other SAR formats include multi-look detected (MLD) and precision images (PRI) (Woodhouse 2006).

**Table 4.2 Technical configurations for different ASAR measurement modes.**

Imaging Mode	Polarisation	Resolution (m)	Swathe Width (km)
Image Mode	HH or VV	30	< 100
Wave Mode	HH or VV	30	5×5 vignettes
Wide Swath Mode	HH or VV	150	> 400
Global Monitoring Mode	HH or VV	1000	> 400
Alternating Polarisation Mode	HH and VV or HH and HV or VV and VH		< 100

As in the Image Mode, seven options of image swathe are selectable from IS1 to IS7. Due to different look angles, the swathe width, ground position from nadir and the inci-



dence angle range vary for different image swathes. Generally, smaller incidence angles accompany larger swathe widths and closer ground positions from nadir (Table 4.3).

**Table 4.3 Technical configurations of different image swathes derived and adapted from (ESA 2007).**

Image Swathe	Swathe Width (km)	Ground position from nadir (km)	Incidence Angle Range (°)
IS1	105	187– 292	15.0– 22.9
IS2	105	242– 347	19.2– 26.7
IS3	82	337– 419	26.0–31.4
IS4	88	412– 500	31.0–36.3
IS5	64	490– 555	35.8–39.4
IS6	70	550– 620	39.1–42.8
IS7	56	615– 671	42.5–45.2

#### **4.2.4.2. Radarsat-2**

The Radarsat-2 was launched in 2007 for continuity with the Radarsat-1 mission, which was launched in 1995. The Radarsat-2 mission was designed and constructed with co-operation between government and private industry – the CSA and MacDonald Dettwiler and Associates Ltd. (MDA). Radarsat-2 is operated at full-polarised C-band microwave at about 5.5 GHz. Five different products, which are Single Look Complex (SLC), Path Image Plus (SGX), Path Image (SGF), Map Image (SSG) and Precision Map Image (SPG) are available for 17 different beam modes. As only SLC data are acquired for this work, the configurations of SLC data are selected as an example of the various beam modes for Radarsat-2 (Table 4.4).

**Table 4.4 Technical configurations of SLC data for different Radarsat-2 imaging modes adapted from (MDA 2011).**

Imaging Mode	Polarisation Options	Resolution (m)	Nominal		Incidence angle (°)
			Swathe	Width	
			(km)		
Fine	Single or Dual	5.2×7.7	50		30–50
Wide Fine	Single or Dual	5.2×7.7	150		20–40
Standard	Single or Dual	9.0	or 100		20–52
Extended Low	HH	9.0×7.7	170		10–23
Extended High	HH	13.5×7.7	75		49–60
Wide	Single or Dual	13.5×7.7	150		20–45
ScanSAR narrow	Single or Dual	79.9-37.7×60	300		20–46
ScanSAR wide	Single or Dual	160-72.1×100	500		20–49
Fine Quad-pol (FQ)	Quad	5.2×7.6	25		18–49
Wide FQ	Quad	5.2×7.6	25		18–42
Standard Quad-pol	Quad	9.0	or 25		18–49
Wide Standard Quad-pol	Quad	13.5×7.6 9.0	or 25		18–42
Ultra-Fine	HH or VV or HV or VH	1.6×2.8	20		20–49
Wide Ultra-Fine	HH or VV or HV or VH	1.6×2.8	50		29–50
Spotlight	HH or VV or HV or VH	1.6×0.8	18		20–49
Multi-Look Fine	HH or VV or HV or VH	3.1×4.6	50		29–50

### 4.3. C-band Microwave Interaction with Surface Geophysical Parameters

Since the C-band signal is minimally affected by the atmospheric properties, the main interaction between incidence signal and backscattered signal rooted from the surface geometric properties, *e.g.* surface roughness (in proportion to the wavelength) and reflectivity (dielectric properties). Therefore, Section 4.3 describes the effects of soil roughness and soil moisture on SAR images separately.

### 4.3.1. Microwave interaction with surface geometric properties

Before using the term roughness, a rough surface needs to be defined for the SAR waves. Two criteria are concerned in defining smooth surface, namely the Rayleigh criterion and the Fraunhofer criterion, which are described in Equations 4.34 and 4.35 respectively:

$$s_{smooth} < \frac{\lambda}{8\cos\theta_i} \tag{4.34}$$

$$s_{smooth} < \frac{\lambda}{32\cos\theta_i} \tag{4.35}$$

where  $s$ ,  $\lambda$  and  $\theta_i$  denote the standard deviation of the surface height from the mean height of the surface – the rms height – the incident signal wavelength and the incidence angle respectively. Only when the rms height  $s$  of the surface meets with the Fraunhofer criterion in SAR backscattering modelling can the surface can be considered a smooth surface. Therefore, the rms height  $s$  of a rough surface is at least 0.175 cm for a C-band system (when  $\lambda = 5.6$  cm).

For a perfectly smooth surface, no backscatter can be received from the SAR sensor, while the reflection angle equals the incidence angle which is a non-zero value. When the surface is rough, a portion of the incident wave is able to backscatter to the SAR sensor. Figure 4.5 illustrates the scattered field defined by incidence angle and surface roughness. The same incidence angle is applied to three different conditions of surface roughness – perfectly smooth on the left, slightly rough in the middle and very rough surface on the right. On the slightly rough surface, the scattered intensity differs from the scatter angle with dominant scatter direction. This phenomenon decays on a very rough surface, where scatters become diffused. Therefore, the backscattering signal is closely related with the surface roughness conditions. Note that for the slightly rough surface, a smaller incidence angle leads to a stronger backscatter.

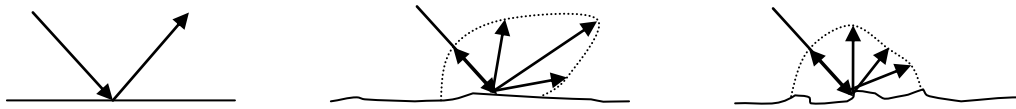


**Figure 4.5** Different surface roughness status of the scattered field. Left: perfectly smooth surface; Middle: slightly rough surface; Right: very rough surface.

#### 4.3.2. Microwave interaction with soils

Apart from the surface roughness effects, the SAR signal is also affected by dielectric properties of soils. Soils are composed of soil particles (*e.g.* sand, clay and silt), air and water. The soil particles are generally much smaller than the C-band wavelength and therefore the bulk dielectric property plays a dominant role in the SAR signal interaction with soils. The sensitivity of SAR signal to soil moisture is due to the fact that the dielectric constant varies significantly in liquid water and totally dry soil. However, the status of water determines its contribution to the dielectric constant, while only the free water molecules can be stimulated to the rotational energy states from EM waves, and bound water molecules are absorbed by soil particles.

It is found that the real part of the dielectric constant  $\epsilon'$  increases from approximately 3 in totally dry soil to approaching 80 in saturated soil while the imaginary part increases similarly at a slower rate, for a certain frequency of wave between 1.4GHz and 18GHz (Ulaby et al. 1986). In addition, the penetration increases with signal wavelength but decreases with soil moisture. It is also reckoned that volume scatters increase when the wave penetrates deeper into dry soil.

#### 4.4. SAR Imagery

A total of 13 ASAR APS images with HH and VV polarisations and 11 Radarsat-2 FQ images are acquired over the campaign periods in 2008 and 2009 covering late spring to early summer each year (Table 4.5). Incidence angle ranges from 19° to 41° with most cases around 23°. Both ascending and descending modes are included. An average weekly coverage is guaranteed during the campaigns. For a concise illustration, figures in Table 4.6 are limited to one decimal point. If no roughness measurement was taken on the same date as the SAR acquisition, the measurement on the closest date is substituted.

**Table 4.5 SAR imagery collection.**

ID	Date (yyyymmdd)	Sensor	Normalised Incidence angle (°)	Orbit	Polarisations
1	20080503	ASAR	23	Desc.	HH, VV
2	20080522	ASAR	23	Desc.	HH, VV
3	20080524	Radarsat-2	22	Desc.	HH, VV, HV, VH
4	20080527	Radarsat-2	21	Asc.	HH, VV, HV, VH
5	20080528	ASAR	19	Asc.	HH, VV
6	20080531	ASAR	29	Asc.	HH, VV
7	20080606	ASAR	41	Asc.	HH, VV
8	20080613	Radarsat-2	27	Asc.	HH, VV, HV, VH
9	20080616	ASAR	23	Asc.	HH, VV
10	20080617	Radarsat-2	22	Desc.	HH, VV, HV, VH
11	20080624	Radarsat-2	28	Desc.	HH, VV, HV, VH
12	20090421	ASAR	19	Asc.	HH, VV
13	20090425	Radarsat-2	22	Desc.	HH, VV, HV, VH
14	20090427	ASAR	23	Asc.	HH, VV
15	20090428	Radarsat-2	21	Asc.	HH, VV, HV, VH
16	20090504	ASAR	29	Desc.	HH, VV
17	20090513	ASAR	19	Asc.	HH, VV
18	20090516	ASAR	29	Asc.	HH, VV
19	20090519	Radarsat-2	22	Desc.	HH, VV, HV, VH
20	20090522	Radarsat-2	21	Asc.	HH, VV, HV, VH
21	20090523	ASAR	23	Desc.	HH, VV
22	20090601	ASAR	23	Asc.	HH, VV
23	20090612	Radarsat-2	22	Desc.	HH, VV, HV, VH
24	20090615	Radarsat-2	21	Asc.	HH, VV, HV, VH

**Table 4.6 Range of backscattering coefficients  $\sigma_{HH}^0$ ,  $\sigma_{VV}^0$  and  $\sigma_{HV}^0$  in dB, in situ surface soil moisture at 1–4 cm and 5–8 cm depths- $m_v$  1–4 cm and  $m_v$  5–8 cm in vol. %, rms height  $s$  in cm and correlation length for Gaussian and exponential function  $l_{Gau}$  and  $l_{exp}$  in cm for each satellite acquisition.**

ID	$\sigma_{HH}^0$ (dB)	$\sigma_{VV}^0$ (dB)	$\sigma_{HV}^0$ (dB)	$m_v$ 1–4 cm (vol. %)	$m_v$ 5–8 cm (vol. %)	$s$ (cm)	$l_{Gau}$ (cm)	$l_{exp}$ (cm)
1	-11.3~-10.2	-9.7~-8.0	n/a	5.9~9.1	8.1~13.4	1.6~2.6	19.4~27.0	26.8~33.6
2	-9.8~-8.7	-8.4~-6.8	n/a	14.1~18.7	10.3~20.6	1.5~2.0	24.0~27.0	28.5~33.6
3	-9.9~-8.5	-9.9~-8.2	-22.6~-19.0	11.4~15.1	9.9~19.2	1.5~2.0	24.0~27.0	28.5~33.6
4	-9.1~-7.7	-10.0~-8.1	-21.8~-17.2	9.6~15.4	10.0~21.7	1.5~2.0	24.0~27.0	28.5~33.6
5	-7.5~-6.3	-8.2~-5.8	n/a	6.5~11.4	9.2~17.7	1.5~2.0	24.0~27.0	28.5~33.6
6	-10.5~-7.9	-9.1~-7.3	n/a	6.9~10.7	11.0~19.7	1.5~2.0	24.0~27.0	28.5~33.6
7	-9.0~-8.6	-10.0~-7.8	n/a	6.9~25.6	8.3~25.5	1.5~2.0	26.0~30.6	28.5~33.6
8	-9.9~-9.0	-10.4~-9.2	-21.2~-16.1	4.7~13.8	6.9~17.9	1.5~2.0	26.0~30.6	28.5~33.6
9	-8.8~-8.3	-9.0~-7.3	n/a	3.4~11.8	5.4~18.3	1.5~2.0	26.0~30.6	28.5~33.6
10	-10.1~-9.0	-10.1~-9.8	-21.0~-17.8	3.4~11.8	5.8~18.3	1.5~2.0	26.0~30.6	28.5~33.6
11	-10.9~-9.7	-11.4~-9.1	-21.5~-17.0	2.8~10.0	5.4~17.3	1.5~2.0	26.0~30.6	28.5~33.6
12	-9.6	-8.3	n/a	12.8	12.8	2.2	18.2	30.3
13	-7.7	-8.2	-16.1	16.0	26.1	2.2	18.2	30.3
14	-5.4	-5.8	n/a	22.4	29.2	2.4	21.5	39.0
15	-5.1	-5.5	-14.5	22.4	29.2	2.4	21.5	39.0
16	-9.0	-8.2	n/a	10.3	23.1	2.1	19.3	26.6
17	-9.1~-7.7	-8.7~-8.4	n/a	1.3~6.5	9.0~18.6	1.5~2.1	14.8~20.3	21.9~31.0
18	-8.7~-8.0	-9.2~-7.0	n/a	3.4~5.7	12.1~16.3	1.5~2.2	16.5~21.0	25.8~36.3
19	-9.2~-8.4	-9.4~-8.6	-18.0~-16.0	1.5~4.9	4.9~13.7	1.5~2.2	16.5~21.0	25.8~36.3
20	-8.6~-6.8	-8.8~-7.1	-17.3~-14.1	1.7~4.0	10.9~15.2	1.5~2.1	14.2~18.4	19.8~31.2
21	-10.3~-9.7	-9.0~-7.2	n/a	1.7~4.0	10.9~15.2	1.5~2.1	14.2~18.4	19.8~31.2
22	-9.2~-8.2	-8.5~-7.7	n/a	3.5~5.4	6.6~13.3	1.5~2.1	14.5~25.7	19.8~38.9
23	-9.3~-7.4	-8.7~-7.3	-19.0~-16.2	2.4~16.0	6.6~23.3	1.4~2.1	15.4~20.3	22.1~31.1
24	-8.3~-6.7	-9.0~-7.4	-18.3~-14.4	2.4~10.6	3.1~21.3	1.4~2.1	15.4~20.3	22.1~31.1

#### 4.5. Summary

Chapter 4 provides a fundamental theoretical and practical background to SAR remote sensing systems and the data characteristics specifically regarding the relationship between surface geophysical parameters. The chapter starts with a brief introduction of the fundamentals of radar with a focus on the SAR system. The principles of imaging geometry including polarimetry in the SAR system is further clearly defined and explained accompanied by SAR-related phenomena *e.g.* geometric distortion. Furthermore, a full SAR image processing scheme is provided including calibration, speckle filtering and geometric correction. The two SAR sensors/platforms are introduced and characterised. The last part of the chapter briefly describes the fundamental interaction between surface geophysical parameters and SAR signal. A full list of SAR images is provided ac-

accompanied with technical configurations (Table 4.5). In addition, the range of backscattering coefficients, soil moisture at both depths and surface roughness parameters are associated with each image acquisition to parameterise the geophysical conditions for each satellite pass. The next chapter will start using these interactions from a modelling perspective.

The top class of virtue is like water, which benefits ten thousand objects without any demands for return.

---Lao Zi

## Chapter 5 Soil Moisture Retrieval Model – Evaluation and Assessment

This chapter starts with a detailed description of the selected widely used semi-empirical models – the Oh model, Dubois model and one semi-empirical model for ERS imagery, followed by an introduction to a theoretical backscattering model, the Integral Equation Model (IEM). A further development of the IEM – the Advanced IEM (AIEM) – is also described. It is necessary to verify the remotely sensed data as well as *in situ* measurements before implementing them into models and therefore field measured surface soil moisture and SAR retrieved backscattering coefficients are verified against empirical relationships (**Baghdadi et al. 2006b**) in Section 5.2. Evaluations of these models are conducted in Section 5.3 by using SAR imagery and *in situ* measurements as described in the Chapter 4. Their performances in surface soil moisture retrieval are assessed against *in situ* measurement in Section 5.4. A short summary is given in Section 5.5.

### 5.1. Model Description

In this section, three semi-empirical surface soil moisture retrieving models are described, followed by an introduction to theoretical backscattering models – the IEM and the AIEM. In addition, two approaches to simplified roughness parameterisation – the empirical correlation length (**Baghdadi et al. 2006b**) and the Rahman approach (**Rahman et al. 2007; Rahman et al. 2008**) – are highlighted before implementing them into the AIEM.



### 5.1.1. Semi-empirical models

#### 5.1.1.1. Oh model

Based on theoretical backscattering models, scatterometer measurements and airborne SAR data, Oh elaborated over the years a semi-empirical backscattering model for full-polarisation microwave over bare soil fields (Oh et al. 1992; Oh et al. 1994; Oh et al. 2002; Oh 2004). (Oh et al. 1992) used a truck-based scatterometer (LCX POLAR-SCAT (Tassoudji et al. 1989)) and recorded full-polarimetric signals at L-, C- and X-band with incidence angles ranging between 10° and 70°. This version of the model covers the conditions of surface roughness and soil moisture as:  $0.1 < ks < 6.0$ ,  $2.6 < kl < 19.7$  and  $9 \text{ vol. \%} < m_v < 31 \text{ vol. \%}$ . Two polarised ratios are introduced: the co-polarised ratio  $p$  ( $= \sigma_{HH}^0 / \sigma_{VV}^0$ ) and the cross-polarised ratio  $q$  ( $= \sigma_{HV}^0 / \sigma_{VH}^0$ ). Through observations of radar backscatter data and scattering behaviour knowledge, the cross-polarised ratio  $q$  is empirically described as:

$$q = 0.23\sqrt{\Gamma_0}[1 - e^{-ks}]$$

**5.1**

where  $\Gamma_0$  denotes the Fresnel reflectivity of the soil surface at nadir,  $s$  is the rms height of roughness in cm,  $k$  ( $=2\pi/\lambda$ ) is the wave number of radar signal with wavelength of  $\lambda$  in cm,  $\epsilon_r$  denotes the dielectric constant of the soil surface as:

$$\Gamma_0 = \left[ \frac{1 - \sqrt{\epsilon_r}}{1 + \sqrt{\epsilon_r}} \right]^2$$

**5.2**

In addition, the co-polarised ratio  $p$  is found to be  $\leq 1$  for all angles and empirically determined as:

$$p = \left[ 1 - \left( \frac{2\theta}{\pi} \right)^{(1/3\Gamma_0)} e^{-ks} \right]^2$$

**5.3**

where  $\theta$  is the incidence angle in radian.

Both ratios  $p$  and  $q$  are sensitive to dielectric constant and rms height  $s$ , while the former effect is dominant. Furthermore,  $\sigma_{HH}^0$ ,  $\sigma_{VV}^0$  and  $\sigma_{HV}^0$  are empirically expressed by Equations 5.4–5.6:

$$\sigma_{HH}^0 = f\sqrt{p}\cos^3\theta[\Gamma_v(\theta) + \Gamma_h(\theta)] \tag{5.4}$$

$$\sigma_{VV}^0 = \frac{f\cos^3\theta}{\sqrt{p}}[\Gamma_v(\theta) + \Gamma_h(\theta)] \tag{5.5}$$

$$\sigma_{hv}^0 = q\sigma_{vv}^0 \tag{5.6}$$

where

$$f = 0.7[1 - e^{-0.65(ks)^{1.8}}] \tag{5.7}$$

By ignoring the imaginary part of dielectric constant  $\epsilon''_r$ ,  $\Gamma_\theta$ ,  $\epsilon'_r$  and hence  $m_v$  and  $ks$  can be easily inverted from above equations based on Hallikainen et al. (1985).

Oh et al. (1994) extended the previous model by introducing phase difference statistics into surface parameter expressions and surface ACF. The soil moisture estimation is found to be improved by using polarimetric radar data from the same scatterometer as in Oh et al. (1992). Measured correlation function can be expressed as:

$$p(\xi) = [1 - \xi^2/(al)^2]e^{-\xi/bl} \tag{5.8}$$

where  $a$  and  $b$  are constants depending on the ACF and  $l$  is the correlation length. Based on the behaviour of theoretical models – the SPM and the KA (Ulaby et al. 1986) –  $\sigma_{VV}^0$  can be expressed as:

$$\sigma_{VV}^0 = 13.5e^{-1.4(ks)^{0.2}} \frac{1}{\sqrt{p}} \Gamma_h(ks)^2 (\cos\theta)^{3.25-0.05kl} e^{-(2kscos\theta)^{0.6}} W_k$$

**5.9**

where  $W_k$  denotes the roughness spectrum corresponding to Equation 5.8 as:

$$W_k = \frac{(kl)^2}{1 + (2.6klsin\theta)^2} \left\{ 1 - 0.71 \frac{1 - 3(2.6klsin\theta)^2}{[1 + (2.6klsin\theta)^2]^2} \right\}$$

**5.10**

and  $\Gamma_h$  is expressed by:

$$\Gamma_h = \left| \frac{\cos\theta - \sqrt{\epsilon_r - \sin^2\theta}}{\cos\theta + \sqrt{\epsilon_r - \sin^2\theta}} \right|^2$$

**5.11**

The co-polarised ratio  $p$  and cross-polarised ratio  $q$  are adjusted as:

$$p = \left[ 1 - \left( \frac{2\theta}{\pi} \right)^{\frac{0.314}{\Gamma_0}} \right]^2$$

**5.12**

$$q = 0.25\sqrt{\Gamma_0}(0.1 + \sin^{0.9}\theta)[1 - e^{-(1.4-1.6\Gamma_0)ks}]$$

**5.13**

Oh et al. (1993) empirically determined the degree of correlation  $\alpha$  as:

$$\alpha = [1 - 0.2(\sin\theta)^{A(ks,\Gamma_0)}](\cos\theta)^{B(ks,\Gamma_0)}$$

**5.14**

where

$$A(ks, \Gamma_0) = (16.5\Gamma_0 + 5.6)e^{-41.6ks\Gamma_0^2}$$

**5.15**

and

$$B(ks, \Gamma_0) = 8.1\Gamma_0 k s e^{-1.8ks} \tag{5.16}$$

Therefore, surface soil moisture  $m_v$ , rms height  $s$  and correlation length  $l$  can all be easily inverted from the above equations with known polarimetric data.

Oh et al. (2002) incorporated airborne SAR data and improved the model for the degree of correlation  $\alpha$  and the co-polarised phase difference  $\zeta$  as well as backscattering coefficients. This version of the model is able to invert volumetric soil moisture instead of the complex dielectric constant. The ensemble-averaged differential Mueller matrix for microwave backscattering model over bare field is introduced. It is found that the probability density function (PDF) of the co-polarised phase angle ( $\phi_c = \phi_{hh} - \phi_{vv}$ ) other than the cross-polarised phase angle ( $\phi_x = \phi_{hv} - \phi_{vv} = \phi_{vh} - \phi_{vv}$  according to the reciprocity relation), is sensitive to incidence angle, the radar wavelength, the soil moisture and surface roughness, while the PDF of  $\phi_c$  is characterised by the degree of correlation  $\alpha$  and mean value of the co-polarised phase difference  $\zeta$  as (Sarabandi 1992):

$$f_{\phi}(\phi_c) = \frac{1 - \alpha^2}{2\pi(1 - X^2)} \left\{ 1 + \frac{X}{\sqrt{1 - X^2}} \left[ \frac{\pi}{2} + \tan^{-1} \left( \frac{X}{\sqrt{1 - X^2}} \right) \right] \right\} \tag{5.17}$$

where

$$X = \alpha \cos(\phi_c - \zeta) \tag{5.18}$$

Empirically,  $\sigma_{HV}^0$ ,  $p$  and  $q$  and are proposed as:

$$\sigma_{HV}^0 = 0.11 m_v^{0.7} \cos^{2.2} \theta [1 - e^{-0.32(ks)^{1.8}}] \tag{5.19}$$

$$p = 1 - \left(\frac{\theta}{90^\circ}\right)^{0.35} m_v^{-0.65} e^{-0.4(ks)^{1.4}} \quad 5.20$$

$$q = 0.1\left(\frac{S}{l} + \sin 1.3\theta\right)^{1.2} [1 - e^{-0.9(ks)^{0.8}}] \quad 5.21$$

Therefore,  $\sigma_{VV}^0$  and  $\sigma_{HH}^0$  are expressed as:

$$\sigma_{VV}^0 = \frac{\sigma_{HV}^0}{q} = \frac{0.11m_v^{0.7} \cos^{2.2}\theta [1 - e^{-0.32(ks)^{1.8}}]}{0.1\left(\frac{S}{l} + \sin 1.3\theta\right)^{1.2} [1 - e^{-0.9(ks)^{0.8}}]} \quad 5.22$$

$$\begin{aligned} \sigma_{HH}^0 &= p\sigma_{HH}^0 = \frac{p}{q}\sigma_{HV}^0 \\ &= \frac{1 - \left(\frac{\theta}{90^\circ}\right)^{0.35} m_v^{-0.65} e^{-0.4(ks)^{1.4}}}{0.1\left(\frac{S}{l} + \sin 1.3\theta\right)^{1.2} [1 - e^{-0.9(ks)^{0.8}}]} 0.11m_v^{0.7} \cos^{2.2}\theta [1 - e^{-0.32(ks)^{1.8}}] \end{aligned} \quad 5.23$$

The degree of correlation  $\alpha$  and the co-polarised phase difference  $\zeta$  are described as:

$$\alpha = 1 - (0.17 + 0.01kl + 0.5m_v)(\sin\theta)^{1.1(ks)^{-0.4}} \quad 5.24$$

$$\zeta = (0.44 + 0.95m_v - 1.0\frac{S}{l})\theta \quad 5.25$$

while the differential Mueller matrix is approximated as:

$$M^0 = \begin{bmatrix} \langle |S_{vv}^0|^2 \rangle & \langle |S_{hv}^0|^2 \rangle & 0 & 0 \\ \langle |S_{hv}^0|^2 \rangle & \langle |S_{hh}^0|^2 \rangle & 0 & 0 \\ 0 & 0 & \langle \text{Re}(S_{vv}^0 S_{hh}^{0*}) \rangle + \langle |S_{hv}^0|^2 \rangle & -\langle \text{Im}(S_{vv}^0 S_{hh}^{0*}) \rangle \\ 0 & 0 & \langle \text{Im}(S_{vv}^0 S_{hh}^{0*}) \rangle & \langle \text{Re}(S_{vv}^0 S_{hh}^{0*}) \rangle - \langle |S_{hv}^0|^2 \rangle \end{bmatrix}$$

**5.26**

and its elements can be described using  $\alpha$  and  $\zeta$  as (Sarabandi et al. 1992; Ulaby et al. 1992):

$$\langle \text{Re}(S_{vv}^0 S_{hh}^{0*}) \rangle = \alpha \cos \zeta \sqrt{M_{11}^0 M_{22}^0}$$

**5.27**

$$\langle \text{Im}(S_{vv}^0 S_{hh}^{0*}) \rangle = -\alpha \cos \zeta \sqrt{M_{11}^0 M_{22}^0}$$

**5.28**

Therefore, all elements can be described from backscattering coefficients and the two phase difference parameters  $\alpha$  and  $\zeta$  as:

$$M_{11}^0 = \frac{1}{4\pi} \sigma_{vv}^0$$

**5.29**

$$M_{22}^0 = \frac{1}{4\pi} \sigma_{hh}^0$$

**5.30**

$$M_{12}^0 = M_{21}^0 = \frac{1}{4\pi} \sigma_{hv}^0$$

**5.31**

$$M_{33}^0 = \frac{1}{4\pi} (\alpha \cos \zeta \sqrt{\sigma_{vv}^0 \sigma_{hh}^0} + \sigma_{hv}^0)$$

**5.32**

$$M_{44}^0 = \frac{1}{4\pi} (\alpha \cos \zeta \sqrt{\sigma_{vv}^0 \sigma_{hh}^0} - \sigma_{hv}^0) \tag{5.33}$$

$$M_{43}^0 = -M_{34}^0 = \frac{1}{4\pi} \alpha \cos \zeta \sqrt{\sigma_{vv}^0 \sigma_{hh}^0} \tag{5.34}$$

A comparison between the measured and estimated differential Mueller matrix found good agreement (Oh et al. 1992). Note that Equation 5.21 is in contrast with Equation 5.13, where the cross-polarised ratio  $q$  is sensitive to the soil moisture.

Due to the insensitivity to  $s/l$ , Oh (2004) ignored the correlation length  $l$  in a new expression of the cross-polarised ratio  $q$  that,

$$q = 0.095(0.13 + \sin 1.5\theta)^{1.4} (1 - e^{-1.3(ks)^{0.9}}) \tag{5.35}$$

It is also claimed that the co-polarised ratio  $p$  is not suitable for retrieving soil moisture readings on very rough or dry conditions due to its insensitivity in those conditions.

#### **5.1.1.2. Dubois model**

Dubois et al. (1995) introduced a semi-empirical model to reproduce backscattering coefficients  $\sigma_{hh}^0$  and  $\sigma_{vv}^0$  for bare soil surfaces. The model is developed based on a large dataset of scatterometer data (LCX POLARSCAT and RASAM systems (Tassoudji et al. 1989; Wegmuller et al. 1994)) and assessed on both airborne and space-borne SAR data (i.e. AIRSAR and SIR-C). The large selection of different instruments increased the probability of the model’s applicability to different soil surfaces and instruments. The expressions are described as

$$\sigma_{HH}^0 = 10^{-2.75} \left( \frac{\cos^{1.5}\theta}{\sin^5\theta} \right) 10^{0.028\epsilon \tan\theta} (k s \sin\theta)^{1.4} \lambda^{0.7} \tag{5.36}$$

$$\sigma_{VV}^0 = 10^{-2.35} \left( \frac{\cos^3 \theta}{\sin^3 \theta} \right) 10^{0.046 \varepsilon \tan \theta} (ks \sin \theta)^{1.1} \lambda^{0.7}$$

**5.37**

where  $\varepsilon$  is the real part of the dielectric constant. The model is recommended in conditions where  $1.5 \text{ GHz} \leq f \leq 11 \text{ GHz}$ ,  $ks \leq 2.5$ ,  $\theta \geq 30^\circ$  and  $m_v \leq 35 \text{ vol. \%}$ . This is due to several discrepancies being found between the Dubois model and theoretical models: the model predicts that the co-polarised ratio  $p$  increases with roughness which is in contrast to the SPM prediction, where roughness is not taken, accounted for by  $p$ . In addition, the model predicts that  $\sigma_{HH}^0$  will be larger than  $\sigma_{VV}^0$  when  $ks \sin \theta$  is large, which is also in contrast with the geometric-optical model (GO) and the IEM and SAR observations.

### **5.1.1.3 The semi-empirical model for ERS imagery**

Loew et al. (2006a) presented a semi-empirical surface soil moisture retrieval scheme for ENVISAT ASAR Wide Swath Mode imagery, which is adapted from an existing algorithm originally designed for the ERS imagery (Rombach and Mauser 1997). Due to the restriction of the original algorithm to the incidence angle of ERS data (approximately  $23^\circ$ ), incidence angles from different image swathes are normalised to compensate for variability in imaging geometry to reference geometry by a simple statistical approach, which calibrates existing images to reference geometry without roughness information, rather taking into account the impact of land use (biomass) and soil texture. For the statistical approach, backscattering coefficients based on a six-year database were derived according to different land uses and regressed with incidence angle variability (Loew et al. 2006a). A  $5^\circ$  step is chosen between incidence angle range  $15^\circ$  and  $45^\circ$ , while backscattering coefficients of pixels with homogeneous land use type, are averaged, *e.g.* for bare soil and wheat. A linear relationship between  $\sigma^0$  and incidence angle  $\theta$  is found as in the modified Equation 5.38. In addition, season effect, *i.e.* summer and winter, is treated separately.

$$\sigma_{23}^0 / \sigma_{\theta}^0 = (\alpha * 23 + \beta) / (\alpha * \theta + \beta)$$

**5.38**



where  $\sigma_{\theta}^0$  is the backscattering coefficient of specific land use type bare soil in this study at the incidence angle  $\theta$ .  $\alpha$  and  $\beta$  denote model regression coefficients, which are set to -62.3 and 3341.7 respectively for bare soil for the summer period. Note that the backscattering coefficient unit is linear in Equation 5.38.

Furthermore, the shape of the relationship between the backscattering coefficient to dielectric constant of the soil is very similar for various land cover types (**Loew et al. 2006a**). Therefore, the real part of the dielectric constant  $\epsilon_r$  is empirically related to land use specific backscattering coefficients at an incidence angle of 23 ° as:

$$\epsilon_r = a + b\sigma^0 (dB) + c(\sigma^0)^2 (dB^2)$$

### 5.39

where  $a$ ,  $b$  and  $c$  are empirical coefficients for specific land use based on extensive statistical analysis, which equals 34.20, 4.42 and 0.15 respectively for bare soil and  $\sigma^0$  as the normalised backscattering coefficient in dB. The coefficient of determination for this statistical model is high ( $R^2=0.90$ ) for bare soil fields in the published experiment. Since the empirical database is based on different surface roughness conditions, the relationship between dielectric constant and backscattering coefficient is considered to represent the mean surface roughness of the bare soil surface over the two test sites in western and southern Germany (**Loew et al. 2006a**).

With additional *in situ* soil texture information,  $m_v$  can be converted from the real part of the dielectric constant  $\epsilon$  commonly through a polynomial expression (**Hallikainen et al. 1985**).

### 5.1.2. The theoretical model(s)

#### 5.1.2.1. The Integral Equation Model (IEM) and the Advanced IEM (AIEM)

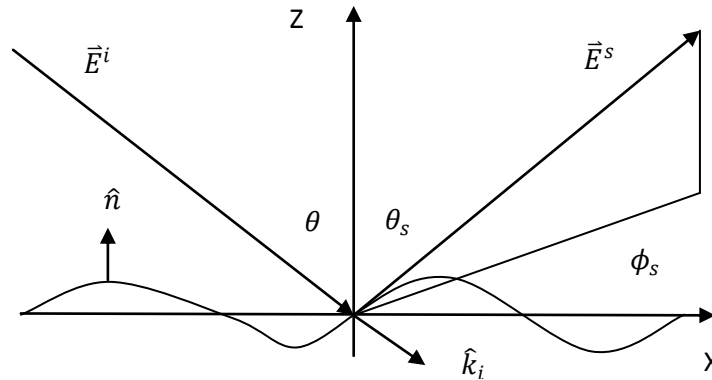


Figure 5.1 Geometry of the scattering problem.

The general geometry of the scattering is illustrated in Figure 5.1, where  $\vec{E}^i$  and  $\vec{E}^s$  are the incident and scattering field amplitudes respectively,  $\hat{k}_i$  is the unit vector in the incidence direction,  $\hat{n}$  is the unit normal vector at the surface point.

Fung and Pan (1987) and Fung et al. (1992) developed a new scattering model for a perfectly conducting, randomly rough surface with a simple conceptual basis of integral equations for the tangential surface fields. Explicit functions of scattering coefficients are given for both high and low frequency. The IEM describes scattering terms for co-polarisation with single scattering and multiple scattering (Equation 5.40), which are treated differently on different roughness conditions. When surface roughness is defined as slightly rough ( $ks < 3$ ), the single scattering terms are derived from the SPM; when surface roughness is defined as rough ( $ks > 3$ ) and surface slope is small, the single scattering terms are derived from the standard Kirchhoff model; while if the surface slope is large, multiple scattering terms are considered. The cross-polarised backscattering coefficient contains only multiple scattering terms.

$$\sigma_{qp}^0 = \sigma_{qp}^S + \sigma_{qp}^M$$

5.40

where  $q, p$  denote the received and transmitted polarisations respectively;  $S$  and  $M$  denote single and multiple backscattering respectively.

The final backscattering coefficient of both co-polarisations over bare soil surfaces is expressed as:

$$\begin{aligned} \sigma_{pp}^0 = & \frac{k^2}{2} |f_{pp}|^2 e^{-4s^2 k^2 \cos^2 \theta} \sum_{n=1}^{+\infty} \frac{(4s^2 k^2 \cos^2 \theta)^2}{n!} W^{(n)}(2k \sin \theta, 0) \\ & + \frac{k^2}{2} \operatorname{Re}(f_{pp}^* F_{pp}) e^{-3s^2 k^2 \cos^2 \theta} \sum_{n=1}^{+\infty} \frac{(4s^2 k^2 \cos^2 \theta)^2}{n!} W^{(n)}(2k \sin \theta, 0) \\ & + \frac{k^2}{8} |F_{pp}|^2 e^{-2s^2 k^2 \cos^2 \theta} \sum_{n=1}^{+\infty} \frac{(s^2 k^2 \cos^2 \theta)^2}{n!} W^{(n)}(2k \sin \theta, 0) \end{aligned}$$

**5.41**

where  $p = H$  or  $V$  and  $W^{(n)}$  is the two-dimensional Fourier transform of the roughness spectrum of the surface related to the  $n$ -th power of the surface correlation function  $\rho(x, y)$  as:

$$W^{(n)}(k, \varphi) = \int_0^{2\pi} \int_0^{\infty} \rho^n(x, y) e^{-jkr \cos s(\varphi - y)} x dx dy$$

**5.42**

$f_{pp}$  is a dimensionless function of the incidence angle and the Fresnel reflection coefficient as

$$f_{hh} = -2R_{\perp} / \cos \theta$$

**5.43**

$$f_{vv} = 2R_{\parallel} / \cos \theta$$

**5.44**

where  $R_{\perp}$  and  $R_{\parallel}$  are the Fresnel reflection coefficients.

$F_{pp}$  is a dimensionless function of the incidence angle, the Fresnel reflection coefficient, the relative permittivity  $\mu_r$  and the relative dielectric constant  $\epsilon_r$  as:

$$\begin{aligned}
 F_{hh}(u, v) = & - \left[ (1 + R_{\perp}) \frac{1}{q} - (1 - R_{\perp}) \frac{\mu_r}{q_t} \right] (1 - R_{\perp}) C_4 \\
 & - \left[ (1 + R_{\perp}) \frac{1}{q} - (1 - R_{\perp}) \frac{1}{q_t} \right] (1 + R_{\perp}) C_5 \\
 & - \left[ (1 + R_{\perp}) \frac{1}{q} - (1 - R_{\perp}) \frac{1}{\epsilon_r q_t} \right] (1 - R_{\perp}) C_6 \\
 & + \left[ (1 - R_{\perp}) \frac{1}{q} - (1 + R_{\perp}) \frac{\epsilon_r}{q_t} \right] (1 + R_{\perp}) C_1 \\
 & - \left[ (1 - R_{\perp}) \frac{1}{q} - (1 + R_{\perp}) \frac{1}{q_t} \right] (1 - R_{\perp}) C_2 \\
 & - \left[ (1 - R_{\perp}) \frac{1}{q} - (1 + R_{\perp}) \frac{1}{\mu_r q_t} \right] (1 + R_{\perp}) C_3
 \end{aligned}$$

**5.45**

$$\begin{aligned}
 F_{vv}(u, v) = & - \left[ (1 - R_{\parallel}) \frac{1}{q} - (1 + R_{\perp}) \frac{\mu_r}{q_t} \right] (1 + R_{\parallel}) C_1 \\
 & + \left[ (1 - R_{\parallel}) \frac{1}{q} - (1 + R_{\parallel}) \frac{1}{q_t} \right] (1 - R_{\parallel}) C_2 \\
 & + \left[ (1 - R_{\parallel}) \frac{1}{q} - (1 + R_{\parallel}) \frac{1}{\epsilon_r q_t} \right] (1 + R_{\parallel}) C_3 \\
 & + \left[ (1 + R_{\parallel}) \frac{1}{q} - (1 - R_{\parallel}) \frac{\epsilon_r}{q_t} \right] (1 - R_{\parallel}) C_4 \\
 & + \left[ (1 + R_{\parallel}) \frac{1}{q} - (1 - R_{\parallel}) \frac{1}{q_t} \right] (1 + R_{\parallel}) C_5 \\
 & + \left[ (1 + R_{\parallel}) \frac{1}{q} - (1 - R_{\parallel}) \frac{1}{\mu_r q_t} \right] (1 - R_{\parallel}) C_6
 \end{aligned}$$

**5.46**

where  $q = (k^2 - u^2 - v^2)^{1/2}$ ,  $q_t = (k_t^2 - u^2 - v^2)^{1/2}$  and the subscript t denotes the transmitted quantities in the lower medium (Figure 5.1). Coefficients  $C_1$ – $C_6$  are the results of the triple cross products and dot products. Their general forms and specific forms for  $u = k \sin \theta$  and  $v = 0$  are given as:

$$C_1(u, v) = \hat{h}_s \cdot \bar{n} \times \bar{n}' \times \bar{h} = -k \left[ 1 + \frac{k_x - u}{k_z^2} (k_x + u) \right] \quad 5.47$$

$$C_1(k_x, 0) = -k \quad 5.48$$

$$C_2(u, v) = \hat{h}_s \cdot \bar{n} \times (\bar{n}' \times \hat{v}) \times \bar{g} = \frac{1}{k} [(u - k_x)u - v^2] \quad 5.49$$

$$C_2(k_x, 0) = 0 \quad 5.50$$

$$C_3(u, v) = \hat{h}_s \cdot \bar{n} \times (\bar{n}' \cdot \hat{v}) \times \bar{g} = -\frac{u^2}{k} \quad 5.51$$

$$C_3(k_x, 0) = -k \sin^2 \theta \quad 5.52$$

$$C_4(u, v) = -k \left[ \left( \cos^2 \theta - \frac{v^2}{k^2} \right) + \cos \theta \sin \theta \frac{k_x + u}{k_z} \right] \quad 5.53$$

$$C_4(k_x, 0) = -k(1 + \sin^2 \theta) \quad 5.54$$

$$\begin{aligned} C_5(u, v) &= \hat{v}_s \cdot \bar{n} \times (\bar{n}' \times \hat{h}) \times \bar{g} \\ &= \frac{1}{k} [(k_x + u)u - v^2] - \frac{\sin \theta}{k_z^2} [(u - k_x)u + v^2](k_z + u) \end{aligned} \quad 5.55$$

$$C_5(k_x, 0) = 2k \sin^2 \theta \tag{5.56}$$

$$C_6(u, v) = \hat{v}_s \cdot \bar{n} \times (\bar{n} \cdot \hat{h}) \times \bar{g} = \frac{v^2}{k \cos^2 \theta} \tag{5.57}$$

$$C_6(k_x, 0) = 0 \tag{5.58}$$

The cross-polarised field coefficients are given as:

$$\begin{aligned} F_{hv}(u, v) = & \left[ (1 - R) \frac{1}{q} - (1 + R) \frac{\mu_r}{q_t} \right] (1 + R) B_1 \\ & - \left[ (1 - R) \frac{1}{q} - (1 + R) \frac{1}{q_t} \right] (1 - R) B_2 \\ & - \left[ (1 - R) \frac{1}{q} - (1 + R) \frac{1}{\epsilon_r q_t} \right] (1 + R) B_3 \\ & + \left[ (1 + R) \frac{1}{q} - (1 - R) \frac{\epsilon_r}{q_t} \right] (1 - R) B_4 \\ & + \left[ (1 + R) \frac{1}{q} - (1 - R) \frac{1}{q_t} \right] (1 + R) B_5 \\ & + \left[ (1 + R) \frac{1}{q} - (1 - R) \frac{1}{\mu_r q_t} \right] (1 - R) B_6 \end{aligned} \tag{5.59}$$

$$\begin{aligned}
 F_{vh}(u, v) = & \left[ (1 - R) \frac{1}{q} - (1 + R) \frac{\mu_r}{q_t} \right] (1 + R) B_4 \\
 & + \left[ (1 - R) \frac{1}{q} - (1 + R) \frac{1}{q_t} \right] (1 - R) B_5 \\
 & + \left[ (1 - R) \frac{1}{q} - (1 + R) \frac{1}{\varepsilon_r q_t} \right] (1 + R) B_6 \\
 & + \left[ (1 + R) \frac{1}{q} - (1 - R) \frac{\varepsilon_r}{q_t} \right] (1 - R) B_1 \\
 & - \left[ (1 + R) \frac{1}{q} - (1 - R) \frac{1}{q_t} \right] (1 + R) B_2 \\
 & - \left[ (1 + R) \frac{1}{q} - (1 - R) \frac{1}{\mu_r q_t} \right] (1 - R) B_3
 \end{aligned}$$

**5.60**

where coefficients  $B_1$ - $B_6$  are given as:

$$B_1(u, v) = \hat{v}_s \cdot \bar{n} \times (\bar{n} \times \hat{h}) = -(uv)/(k \cos \theta)$$

**5.61**

$$B_2(u, v) = \hat{v}_s \cdot \bar{n} \times (\bar{n} \times \hat{v}) \times \bar{g} = -(2uv)/(k \cos \theta)$$

**5.62**

$$B_3(u, v) = \hat{v}_s \cdot \bar{n} \times (\bar{n} \cdot \hat{v}) \bar{g} = (uv)/(k \cos \theta)$$

**5.63**

$$B_4(u, v) = \hat{h}_s \cdot \bar{n} \times (\bar{n} \times \hat{v}) = -(uv)/(k \cos \theta)$$

**5.64**

$$B_5(u, v) = \hat{h}_s \cdot \bar{n} \times (\bar{n} \times \hat{h}) \times \bar{g} = (2uv)/(k \cos \theta)$$

**5.65**

$$B_6(u, v) = \hat{h}_s \cdot \bar{n} \times (\bar{n} \times \hat{h}) \bar{g} = -(uv)/(k \cos \theta)$$

**5.66**

$pp$  denotes the co-polarisation (= HH or VV),  $Re$  is the real part of the complex number, and  $f_{pp}^*$  is the conjugate of the complex number  $f_{pp}$ .

Wu and Chen (2004) and Wu et al. (2008) extended the IEM by 1) retaining all the phase terms in the spectral representation of the Green's function and 2) replacing the Fresnel reflection coefficients by a transition function including surface roughness and permittivity. Since the surface roughness information is the most problematic, *i.e.* rms height  $s$  and correlation length  $l$ , they have to be treated carefully. Brogioni et al. (2010) assessed the AIEM validity for RMS height and correlation length and slightly extended it from the IEM validity from Marcelloni et al. (2000). They found that the valid RMS height increases from ~0.77–11.1 cm with the correlation length, which validates through ~0.11–110 cm for C-band signal for the AIEM.

#### **5.1.2.2 The Baghdadi empirical correlation length**

Baghdadi et al. (2006a) proposed to replace  $l$  by a fitting parameter “ $l_{opt}$ ” through the IEM, which depends on a given radar wavelength  $f$ , incidence angle  $\theta$ , rms height  $s$  and polarisation. The Gaussian function is adopted for correlation function. The function for the empirical correlation lengths with C-band signal are described as in Equations 5.67 and 5.68:

$$l_{opt}(s, \theta, hh) = 0.162 + 3.006 (\sin 1.23\theta)^{-1.494} s \tag{5.67}$$

$$l_{opt}(s, \theta, vv) = 1.281 + 0.134 (\sin 0.19\theta)^{-1.59} s \tag{5.68}$$

Good results are reported (Baghdadi et al. 2007; Baghdadi et al. 2011a; Baghdadi et al. 2011b).

#### **5.1.2.3. The Rahman approach**

Rahman et al. (2008) introduced a novel approach to solving the IEM for both surface soil moisture and surface roughness by using only multi-angle radar images and IEM



simulation, with no ancillary data. In other words, the model is calibrated by using the theoretical model only, without any *in situ* measurements or SAR imagery. The approach is adopted in this study using the AIEM instead.

The approach requires at least three radar images for coefficient derivation: two radar images with different incidence angles but identical surface geophysical conditions and a third radar image with the same satellite configuration as one of the previous two images and with extremely dry soil surface conditions (*e.g.*  $m_v \leq 3$  vol. %). Basically, this approach uses three functions for 1) rms height  $s$ , correlation length  $l$  and backscattering coefficient difference  $\Delta\sigma^0$ , on the same surface moisture condition and with the same satellite configuration; 2) rms height  $s$ , correlation length  $l$  and backscattering coefficient in an extremely dry condition  $\sigma_{dry}^0$  and 3) rms height  $s$ , correlation length  $l$ , backscattering coefficient  $\sigma^0$  and volumetric surface soil moisture  $m_v$ .

Backscatter is simulated by the AIEM for the whole valid range of surface roughness parameters, *i.e.*  $0.1 \text{ cm} \leq s \leq 3 \text{ cm}$  and  $1 \text{ cm} \leq l \leq 15 \text{ cm}$ . In accordance with the chosen radar image configuration, backscatter simulations are selected for polynomial fitting processes. Coefficients are retrieved after the regressions for each of the three functions and rms height  $s$ , correlation length  $l$  and surface soil moisture  $m_v$  are solved as described in the following steps, while coefficients are derived from Rahman et al. (2008):

Step 1:  $\Delta\sigma^0$  is defined as the backscattering coefficient difference from different incidence angles but over the surface with similar geophysical conditions. Zribi and Dechambre (2003) empirically co-related the backscattering difference  $\Delta\sigma^0$  with  $(ks)^2/kl$ , namely the Z-index. Two SAR images, which satisfy the condition, are selected. Based on the corresponding SAR configuration, backscatter is simulated using the IEM on combinations of all roughness and soil moisture conditions. Hence, the  $\Delta\sigma^0$  are calculated for different roughness (as stated in the previous paragraph) and surface soil moisture conditions ( $1 \text{ vol. \%} \leq m_v \leq 30 \text{ vol. \%}$ ). All combinations of backscattering coefficient difference  $\Delta\sigma^0$ , rms height  $s$  and correlation length  $l$  are used for a polynomial fitting regression as in Equation 5.69. The Z-index is found to be better represented by  $(ks)^{2.5}/kl$  (Rahman et al. 2008) and the expression is given as

$$Z = g(\Delta\sigma^0) = (0.618 + 0.09\Delta\sigma^0)/(1 - 0.138\Delta\sigma^0)$$

**5.69**

where  $g$  is the function name and  $R^2=0.998$  and  $RMSE=0.02$  (**Rahman et al. 2008**).

Step 2: Rahman et al. (2007) complemented by Zribi et al. (2007) with a possibility to derive rms height  $s$  and correlation length  $l$  from  $\sigma_{dry}^0$ , the backscattering coefficient in the extremely dry condition, *i.e.*  $m_v \leq 3$  vol. %. The relationship is described in Equation 5.70. One radar scene in extreme dry condition is used to provide the  $\sigma_{dry}^0$ . Backscatter is simulated by the IEM using the following parameterisations: surface soil moisture  $m_v$  is set as 3 vol. %; the incidence angle is set to the same incidence angle as one of the two scenes used in step 1; the whole valid range of surface roughness conditions is used. All combinations of rms height  $s$ , correlation length  $l$  and  $\sigma_{dry}^0$  are selected for a polynomial fitting regression. This relationship is described as

$$\begin{aligned} \sigma_{dry}^0 &= h(kskl) \\ &= -27.94 + 32.58ks - 1.4kl - 18.78(ks)^2 + 0.05(kl)^2 \\ &\quad + 0.86kskl + 2.65(ks)^3 + 0.12(ks)^2kl - 0.04ks(kl)^2 \end{aligned}$$

**5.70**

where  $h$  is the function name and  $R^2 = 0.987$  and  $RMSE = 0.65$  (**Rahman et al. 2008**).

Step 3: Based on the general term in the IEM as described in the model description section,

$$\sigma_{pq}^0 = f(ks, kl, SSM, \theta)$$

**5.71**

where  $p$  and  $q$  denote the transmitting and receiving polarisations respectively, *i.e.* HH, HV, VH or VV. After substituting Equations 5.69 and 5.70 for Equation 5.72, an expression is obtained between the retrieved backscattering coefficient  $\sigma_{pq}^0$  from the SAR image, backscattering coefficient difference  $\Delta\sigma^0$  as described in step 1, backscattering coefficient in the extreme dry condition  $\sigma_{dry}^0$ , the surface soil moisture  $m_v$  and local incidence angle  $\theta$ :

$$\sigma_{pq}^0 = \omega(\Delta\sigma^0, \sigma_{dry}^0, m_v, \theta) = \varphi(ks, kl, m_v, \theta)$$

**5.72**

Therefore, the  $m_v$  can be solved by

$$m_v = \varphi^{-1}(ks, kl, \sigma^0, \theta)$$

**5.73**

The function  $\varphi^{-1}$  is presumed to be polynomial. The simulated IEM backscattering coefficients are used for polynomial fitting regression, for all valid roughness conditions, possible surface soil moisture values, *i.e.*  $1 \leq m_v \leq 30$  vol. % and possible incidence angles, *i.e.*  $10 \leq \theta \leq 45^\circ$ . This expression is given by Equation (5.74):

$$\begin{aligned} \ln(m_v) &= 0.353 + 1.384 \ln(-\sigma^0) - 0.913\{\ln(-\sigma^0)\}^2 - 1.735 \ln(l) \\ &+ 0.947\{\ln(kl)\}^2 + 0.013\{\ln(kl)\}^3 - 0.017\{\ln(kl)\}^4 \\ &- 1.791 \ln(ks) + 5.475\{\ln(ks)\}^2 + 0.743\{\ln(ks)\}^3 \\ &+ 0.087\{\ln(ks)\}^4 - 1.95 \ln(ks) \ln(kl) - 1.0\{\ln(ks)\}^2 \ln(kl) \\ &- 0.187\{\ln(ks)\}^3 \ln(kl) + 0.006 \{\ln(kl)\}^2 \ln(ks) \\ &+ 0.048\{\ln(kl)\}^3 \ln(ks) + 0.055 \{\ln(kl)\}^2 \{\ln(ks)\}^2 \\ &+ 1.291 \ln(-\sigma^0) \ln(ks) + 0.07 \ln(-\sigma^0) \ln(kl) \\ &- 0.084 \ln(-\sigma^0) \{\ln(kl)\}^2 - 0.688 \ln(-\sigma^0) \{\ln(ks)\}^2 \end{aligned}$$

**5.74**

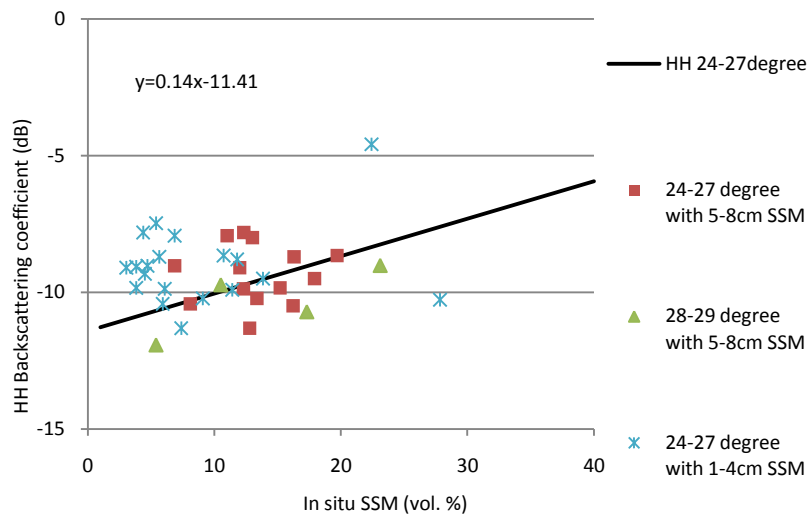
where  $R^2=0.996$  and  $RMSE=0.04$ .

## **5.2. Data Verification**

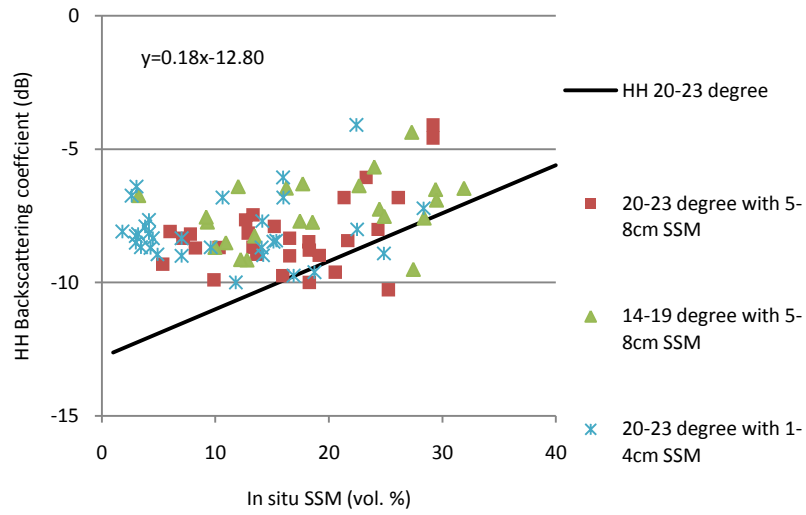
Baghdadi et al. (2006b) introduced a set of empirical linear relationships between backscattering coefficients and volumetric surface soil moisture for different polarisations and incidence angle ranges. The line represents a medium surface roughness condition from a large database and separates the space into two zones in terms of roughness condition – rougher and smoother zones. In theory, sample points below the line are in the smoother zone and those above the line are in the rougher zone. The distance between

each sample point and the corresponding line indicates the roughness scale, *i.e.* longer distance indicates a rougher or smoother condition depending on which zone the point is located in.

In this study, surface soil moisture values at both 1–4 cm and 5–8 cm depths are taken into account initially. Figure 5.2 shows the plotted backscattering coefficients, surface soil moisture values and the linear relationship corresponding to polarisations and incidence angle ranges. Each dot represents a sample corresponding to one field and one SAR acquisition. Field average values (of *e.g.* backscattering coefficients, soil moisture etc.) are taken as samples. The equations in Figure 5.2(a) and (c) are noted from Baghdadi (2011) and the equation in Figure 5.2(b) is published in Baghdadi et al. (2006b). Figure 5.2(a) takes a total of 15 samples with local incidence angle range of 24–27° from HH polarisation and shows that the backscattering coefficients fit better with soil moisture at 5–8 cm than at 1–4 cm especially for those extremely dry conditions. The plot was extended by adding 4 samples of backscattering coefficients with local incidence angles between 28–29° from HH polarisation, which also fit well with the linear relationship. Figure 5.2(b) plots a total of 32 samples of the backscattering coefficients with local incidence angles between 20–23° from HH polarisation with *in situ* soil moisture measurements. Almost all samples fall into the “rougher zone”. Again, samples from the driest conditions from 1–4 cm depth show significant bias against the line with “overestimation” of backscattering coefficients. The plot was extended with an additional 14 samples, of which backscattering coefficients from HH polarisation are with local incidence angles between 14–19°. Figure 5.2(c) plots a total of 31 samples of the backscattering coefficients with local incidence angles between 22–25° from VV polarisation and *in situ* soil moisture measurements. The plot was extended by implementing a further 36 samples of backscattering coefficients with local incidence angles between 18–21° and 26–29° from VV polarisation. Samples are distributed above and below the line in balance. Samples from the driest conditions show a slight “overestimation” of backscattering coefficients at both 1–4 cm and 5–8 cm depths.



(a)



(b)

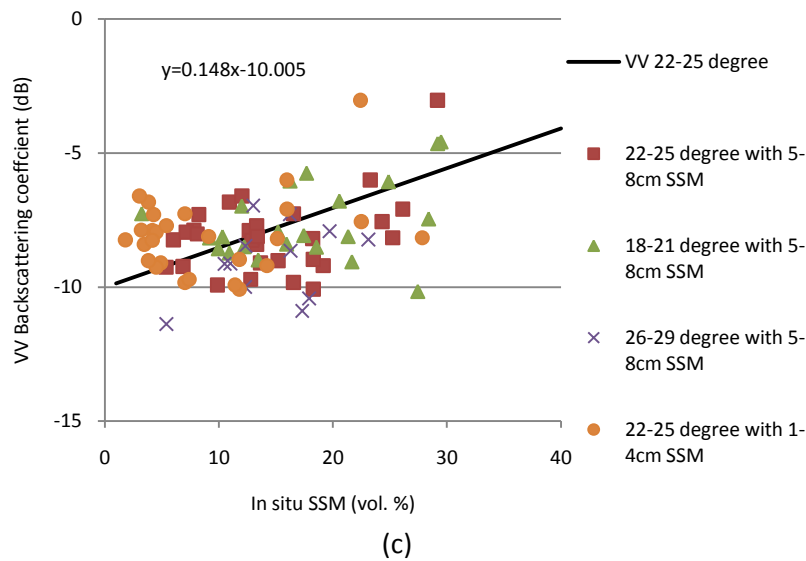


**Figure 5.2 Backscattering coefficients against surface soil moisture at 1–4 cm and 5–8 cm depths compared with empirical linear relationship derived from Baghdadi et al. (2006b) with (a) and (b) for HH polarisation and (c) for VV polarisation.**

Although not all samples can be verified due to the limited empirical relationships for different incidence angle ranges, the above analysis proves that backscattering coefficients from both co-polarisations and listed local incidence angles agree with empirical relationships well and better than the samples with soil moisture values at 1–4 cm depth, especially for the low soil moisture region, where backscattering coefficients tend to be higher than the theoretical estimations, especially from HH polarisation. These empirical linear relationships are also potentially valid for wider ranges of incidence angle. Overall, both co-polarised backscattering coefficients and soil moisture are verified and they will be used for further studies and the soil moisture values at 5–8 cm depth fit better than those at 1–4 cm depth.

It is found that the in-field variability can be a major error source for backscattering simulation by all models/approaches and hence soil moisture and roughness estimation retrieval. Figure 5.3 plots the mean of standard deviation of backscattering coefficients over each field on a pixel basis for each SAR acquisition. The average of those mean standard deviations is 1.03dB for combined HH and VV polarisations. According to the linear relationships in Figure 5.2, the amount of bias could potentially introduce an uncertainty between 5.7 and 7.5 vol. % to soil moisture estimation depending on the inci-

dence angles. Figure 5.4 illustrates that the in-field variability is independent of local incidence angle.

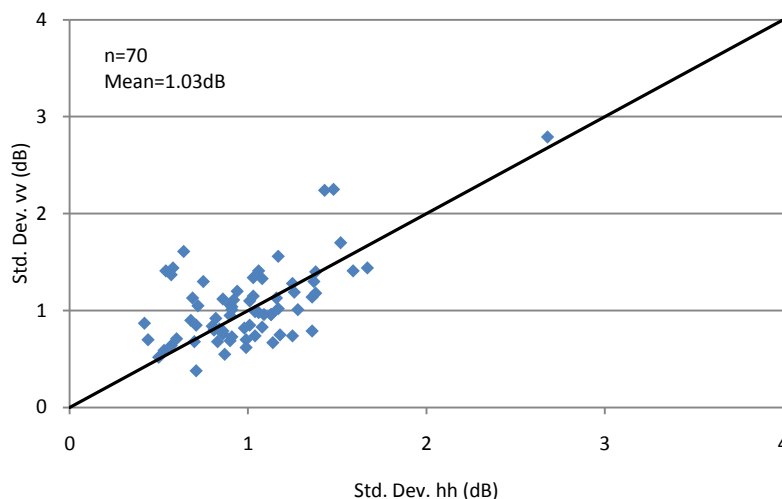


**Figure 5.3** In-field backscattering coefficient variability from HH and VV polarisations for each study field on a pixel basis – each dot represents the standard deviation of backscattering coefficients from all pixels on each study field for one satellite pass.

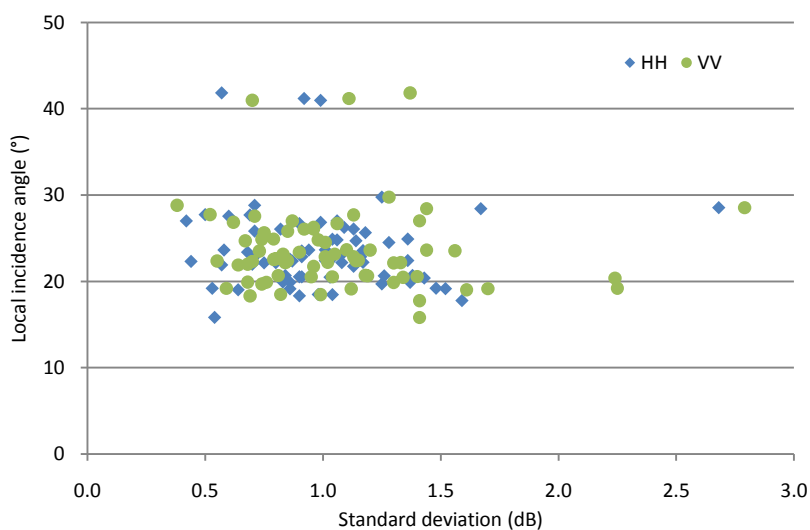


**Figure 5.4** In-field variability of backscattering coefficients for both HH and VV polarisations on a pixel basis and local incidence angles.

### 5.3. Model Evaluation

In this section, all the models are evaluated through comparisons between derived and simulated backscattering coefficients both from SAR and from modelling. *In situ* measurements of both soil moisture and surface roughness are used for parameterisation.

### 5.3.1. Oh model

Both the 2002 and the 2004 versions of the Oh model are selected for evaluation. While no cross-polarisation signals are available from ASAR images in this study, modelled  $\sigma_{HV}^0$  and  $q$  are only compared with corresponding values calculated from Radarsat-2 images. Obviously, the only difference from both versions is in the cross-polarisation ratio  $q$  and backscattering coefficient from VV polarisation  $\sigma_{VV}^0$ , where  $ks/kl$  is substituted with a coefficient in the 2004 version. Table 5.1 and Table 5.2 list the RMSE and the bias of modelled parameters, respectively. The 2004 version simulated slightly smaller RMSE for  $q$ ,  $\sigma_{HH}^0$  and  $\sigma_{VV}^0$  as of 4.15dB, 3.68dB and 3.57dB compared to 4.86dB, 4.44dB and 4.31dB correspondingly from the 2002 version of the model. Similarly, the 2004 version also yields smaller bias for the three parameters as of 3.58dB, 3.18dB and 3.06dB compared to 4.39dB, 4.05dB and 3.93dB according to the 2002 version of the model. 1.03dB and 3.08dB RMSE are found for the co-polarised ratio  $p$  and  $\sigma_{HV}^0$  respectively, while their bias is 0.12dB and 0.06dB respectively. Note that averages of 4.06dB and 3.94dB overestimation are found from both co-polarisations by using the 2002 and the 2004 version models respectively. Therefore, corresponding backscattering coefficient corrections are needed in surface soil moisture retrieval to compensate for the model's intrinsic effect.

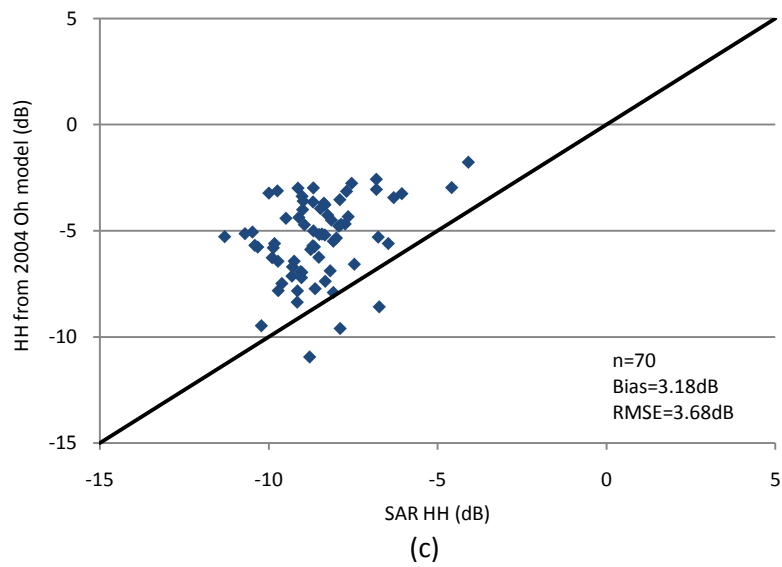
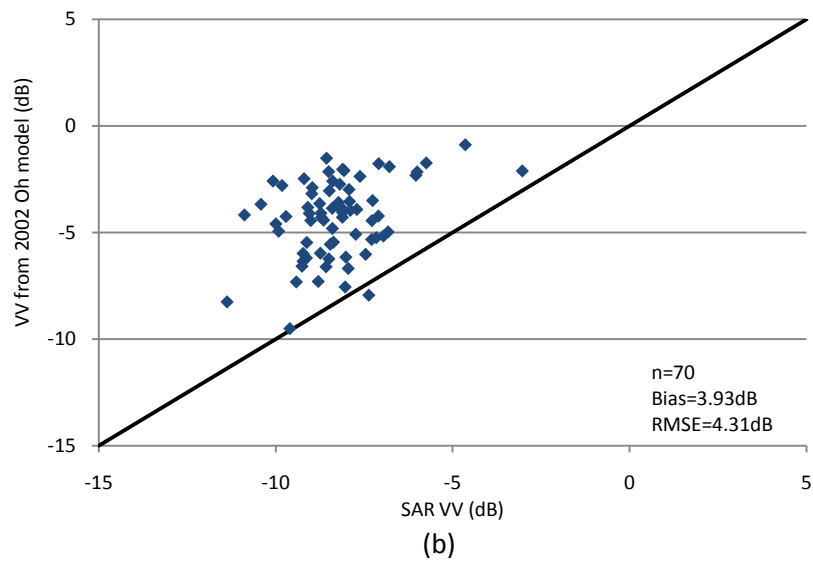
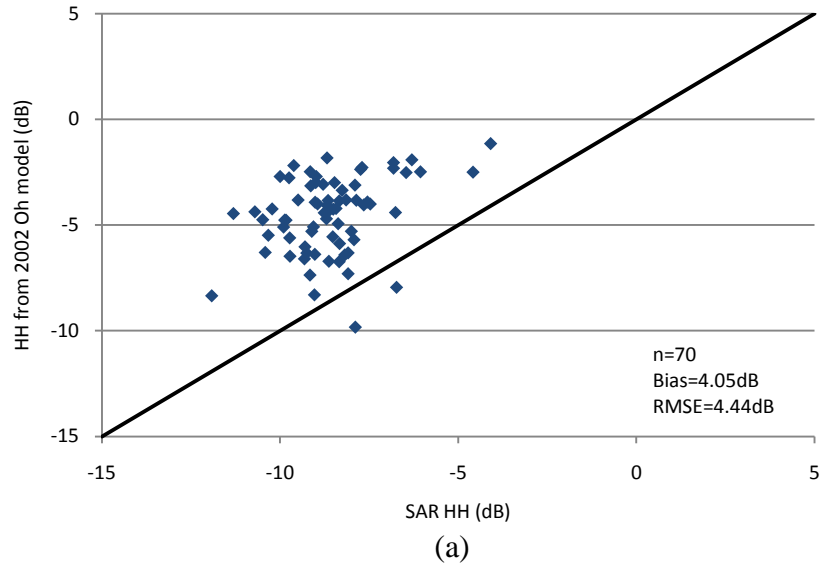
**Table 5.1 RMSE of the co-polarised ratio  $p$ , the cross-polarised ratio  $q$  and the backscattering coefficients from HH, VV and HV polarisations by using both 2002 and 2004 versions of the Oh model.**

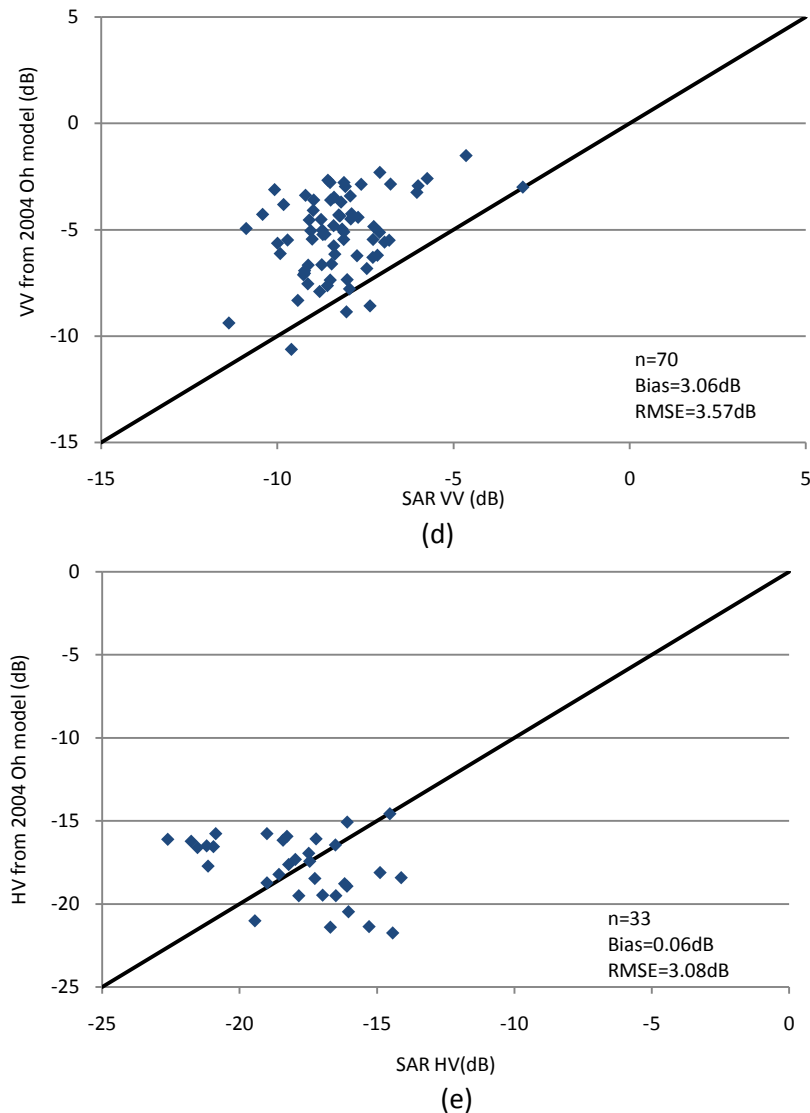
Model version	$p$ (dB)	$q$ (dB)	$\sigma_{HH}^0$ (dB)	$\sigma_{VV}^0$ (dB)	$\sigma_{HV}^0$ (dB)
2002	1.03	4.86	4.44	4.31	3.08
2004		4.15	3.68	3.57	

**Table 5.2 Bias of the co-polarised ratio  $p$ , the cross-polarised ratio  $q$  and the backscattering coefficients from HH, VV and HV polarisations by using both 2002 and 2004 versions of the Oh model.**

Model version	$p$ (dB)	$q$ (dB)	$\sigma_{HH}^0$ (dB)	$\sigma_{VV}^0$ (dB)	$\sigma_{HV}^0$ (dB)
2002	0.12	4.39	4.05	3.93	0.06
2004		3.58	3.18	3.06	



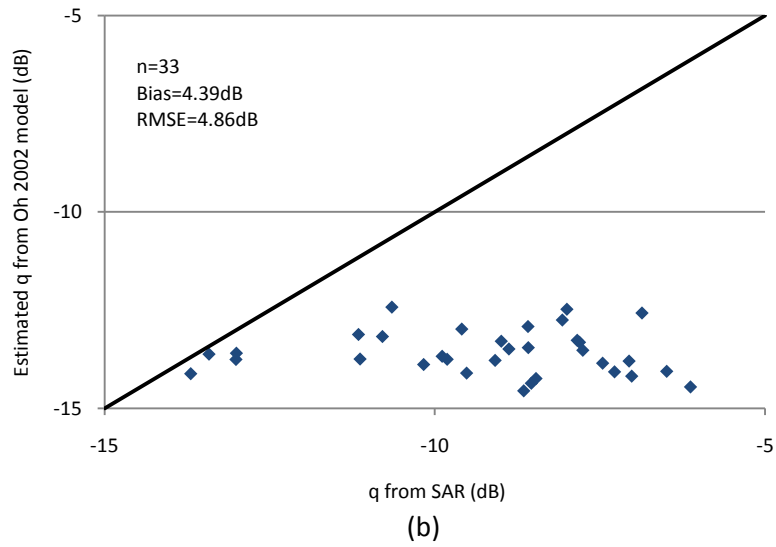
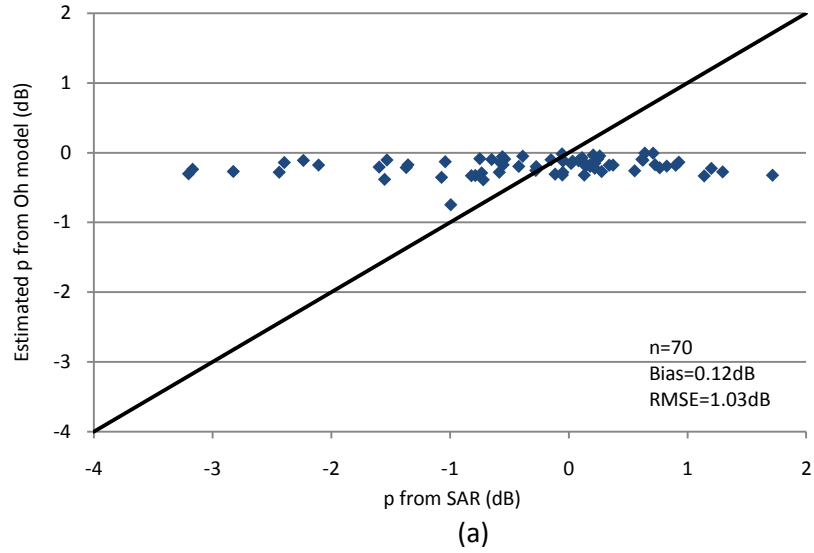




**Figure 5.5 Backscattering coefficients  $\sigma_{HH}^0$ ,  $\sigma_{VV}^0$  and  $\sigma_{HV}^0$  from SAR and estimations from Oh model 2002 and 2004 versions by using *in situ* field measurements.**

Figure 5.5 plots backscattering coefficients  $\sigma_{HH}^0$ ,  $\sigma_{VV}^0$  and  $\sigma_{HV}^0$  from SAR and estimations from Oh model 2002 and 2004 versions by using *in situ* field measurements. A total of 70 samples are plotted for co-polarisation derived from both ASAR and Radarsat-2 imagery and 33 samples are plotted for cross-polarisation from Radarsat-2 imagery only. Figure 5.6 plots comparisons between derived co- and cross-polarised ratios  $p$  and  $q$  and those values estimated from Oh model 2002 and 2004 versions by using *in situ* measurements. For a total of 70 samples, the RMSE of the ratio  $p$  reaches slightly over 1dB although the bias is as small as 0.12dB, the same for both versions. The RMSE and the bias of the ratio  $q$  decrease from 4.86dB and 4.39dB to 4.15dB and

3.58dB respectively from the 2002 version to the 2004 version Oh model for a total of 33 samples from Radarsat-2 imagery.



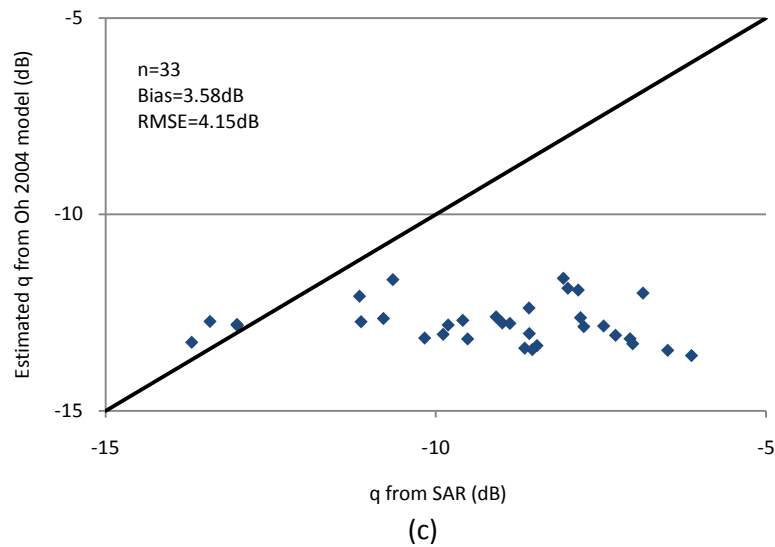


**Figure 5.6** Derived co-polarised ratio  $p$  and co-polarised ratio  $q$  from SAR imagery compared with estimated values from Oh 2002 (b) and 2004 (c) models by using in situ measurements.

### 5.3.2. Dubois model

As mentioned in the model description section, the best performance of the Dubois model requires the following conditions:  $1.5 \text{ GHz} \leq f \leq 11 \text{ GHz}$ ,  $ks \leq 2.5$ ,  $\theta \geq 30^\circ$  and  $m_v \leq 35 \text{ vol. \%}$ . For application purposes, the conditions can be met in most cases, especially for longer wavelength SAR, such as L-band data. However, only 2 out of 37 images are acquired with incidence angles larger than  $30^\circ$  in our image database. In addition, a few measurements show that the  $ks$  is larger than 2.5. Therefore, model conditions cannot be perfectly fulfilled in this study. Nevertheless, all Radarsat-2 and ASAR images are used for evaluation of co-polarisation backscattering based on the Dubois model. As found in data verification, surface soil moisture at 5–8 cm depth is used for the model evaluation. Table 5.8 at the end of this section shows systematic overestimations of about 6.98dB and 2.37dB from HH and VV polarisations respectively from a total of 70 samples. VV polarisation yields much smaller RMSE and bias of 2.95dB and 2.25dB compared with 7.12dB and 6.59dB respectively, from HH polarisation. Therefore, corresponding backscattering coefficient corrections are needed for surface soil moisture retrieval in later studies, similar to with the Oh model.

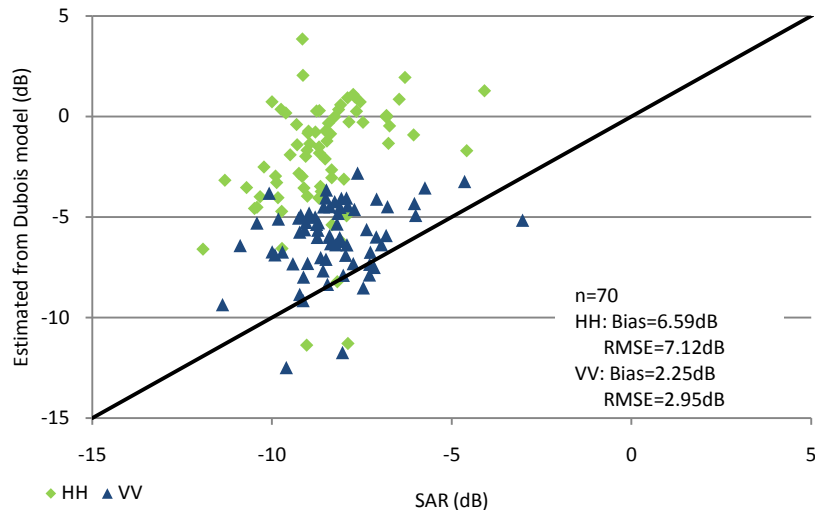
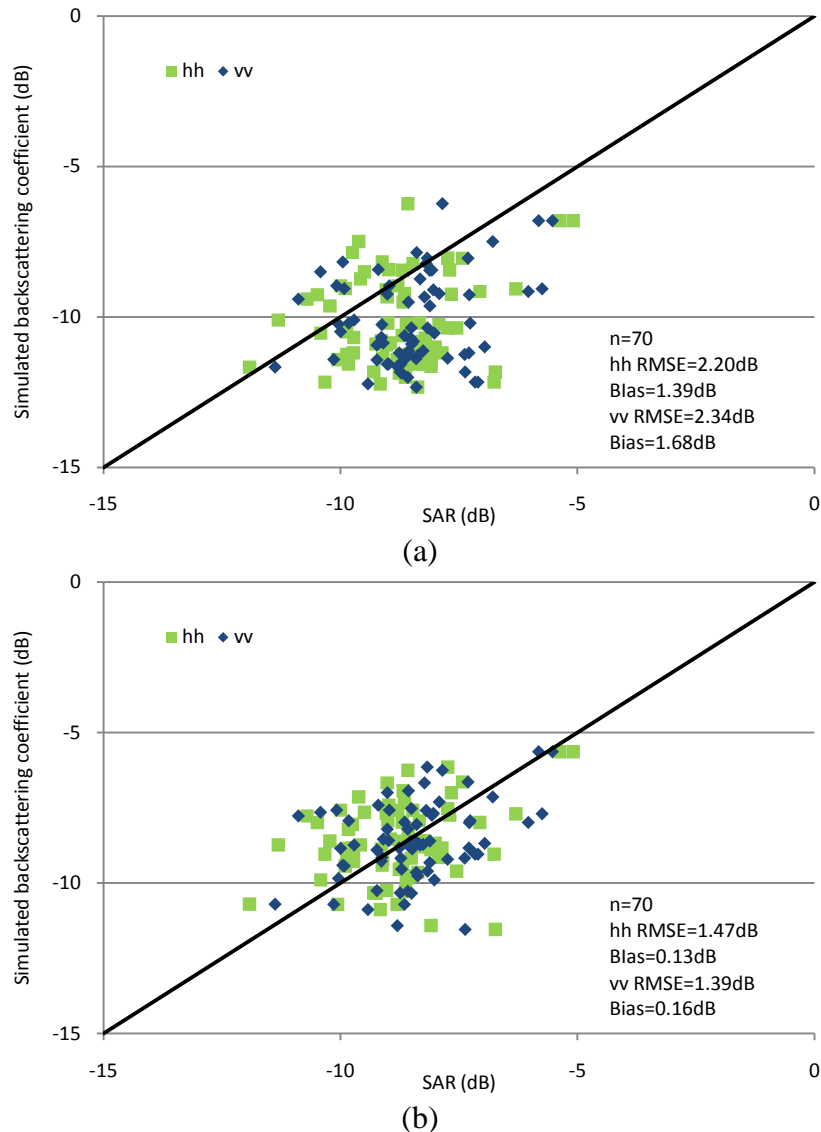


Figure 5.7 Measured and estimated  $\sigma_{hh}^0$  and  $\sigma_{vv}^0$  from the Dubois model.

### 5.3.3. The semi-empirical model for ERS imagery evaluation

Figure 5.8 illustrates the comparison between backscattering coefficients  $\sigma_{HH}^0$  and  $\sigma_{VV}^0$  derived from SAR imagery and estimated by using the original coefficients in the semi-empirical model for ERS imagery. *In situ* surface soil moisture at both 1–4 cm and 5–8 cm depths are used and are shown separately in Figure 5.8(a) and Figure 5.8(b) respectively. A total of 70 samples are plotted as for all other models. In agreement with the previous data verification, surface soil moisture measured at 5–8 cm depth yields smaller RMSE and especially smaller bias from backscattering coefficients from both HH and VV polarisations. In comparison, the RMSE and the bias for  $\sigma_{HH}^0$  decrease from 2.20dB and 1.39dB to 1.47dB and 0.13dB respectively and from 2.34dB and 1.68dB to 1.39dB and 0.16dB correspondingly for  $\sigma_{VV}^0$ .



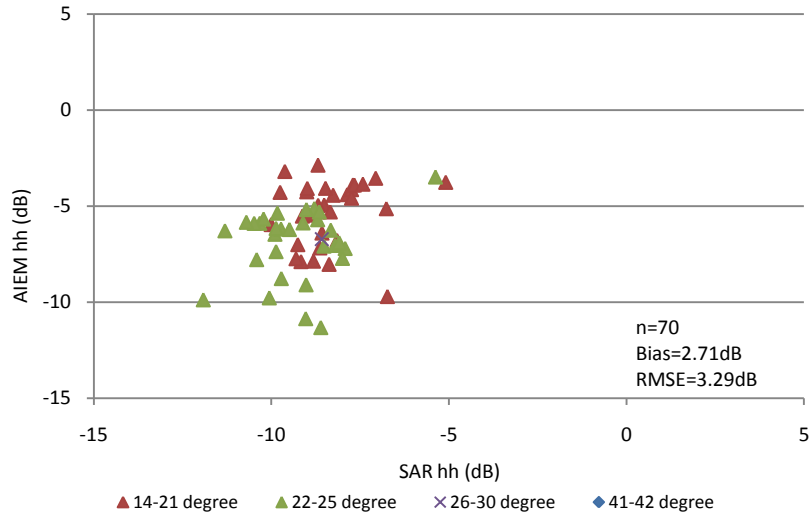
**Figure 5.8 Comparison of SAR co-polarised backscattering coefficients from both ASAR and Radarsat-2 imagery and simulated backscattering coefficients by using the semi-empirical model for ESA imagery and in situ surface soil moisture measurements at 1–4 cm depth (a) and at 5–8 cm depth (b).**

#### 5.3.4. AIEM evaluation

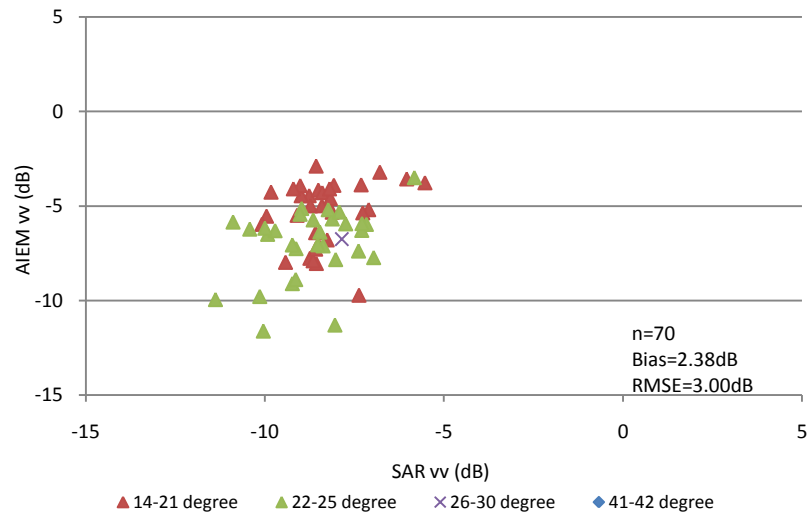
As described in the model description part, to simulate backscattering coefficients, the following inputs are needed: the correlation length  $l$ , the rms height  $s$ , the real part of the dielectric constant  $\epsilon_r$ , the imaginary part of the dielectric constant  $\epsilon_i$ , correlation function, polarisation  $pq$  and incidence angle  $\theta$ . Among these, the polarisation and incidence angle are directly derived by processed SAR imagery; real and imaginary parts of the dielectric constant are calculated from *in situ* soil moisture measurements by the

empirical model (Hallikainen et al. 1985) given the known soil texture status. Therefore, different treatments of surface roughness will lead to different backscattering coefficient simulations. In this study, two approaches are deployed for model evaluation, 1) to use *in situ* roughness measurements and 2) to couple the *in situ* rms heights and the empirical correlation length  $l_{opt}$  instead of the measured correlation length (Baghdadi et al. 2006a), as the correlation length is the most problematic surface roughness parameter.

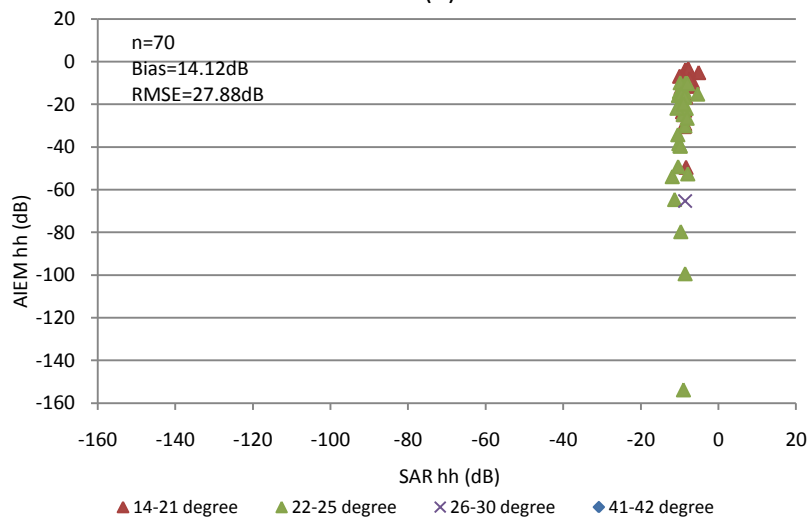
Figure 5.9 demonstrates backscattering coefficients derived from SAR imagery and estimations from the AIEM simulation for both co-polarisations. Both exponential and Gaussian ACFs are used for the AIEM coupled with measured  $s$  and  $l$ . Samples are marked according to different ranges of incidence angle, *i.e.* 14–19°, 20–23°, 24–27°, 28–30° and 41–42°. Figure 5.9(a) and (b) are derived from *in situ* soil moisture and roughness measurements with exponential ACF, Figure 5.9(c) and (d) are derived from *in situ* soil moisture and roughness measurements with Gaussian ACF, while Figure 5.9(e) and (f) are plotted from the empirical correlation length instead of the measured correlation length (Baghdadi et al. 2006a). The estimations with *in situ* measurements and exponential ACF show overestimation of about 2.71dB and 2.38dB from HH and VV polarisations respectively and RMSE of about 3.29dB and 3.00dB from HH and VV polarisations. The estimations with *in situ* measurements and Gaussian ACF show significant bias and RMSE of over 14dB and 27dB respectively from HH and VV polarisations. Therefore, a matter of about 2.5dB of backscattering correction is employed in surface soil moisture retrieval when using the AIEM and *in situ* roughness data, to compensate for the systematic overestimation. Gaussian ACF is omitted due to large bias and error. The estimations with *in situ*  $s$  and empirical  $l_{opt}$  yield better fitting results with bias less than 1dB and RMSE less than 2dB from both co-polarisations.



(a)

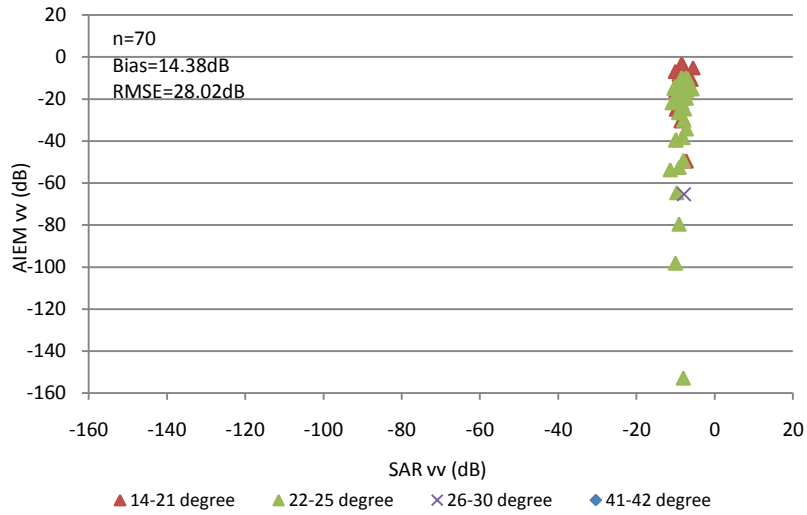


(b)

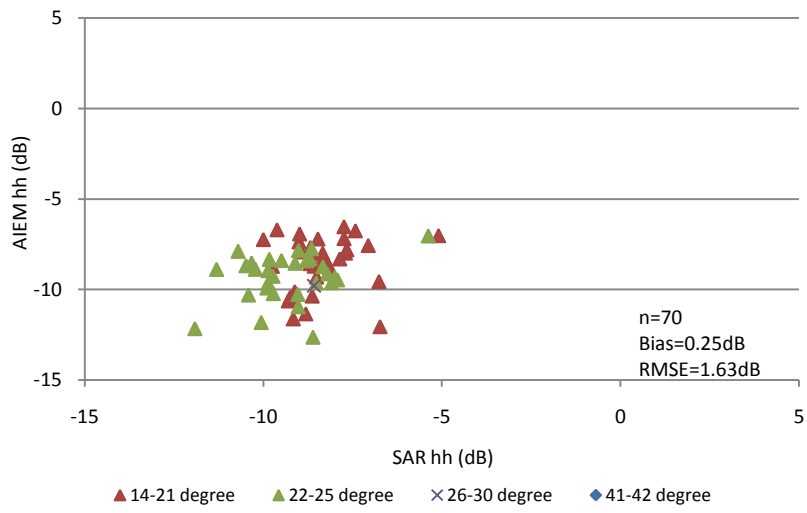


(c)

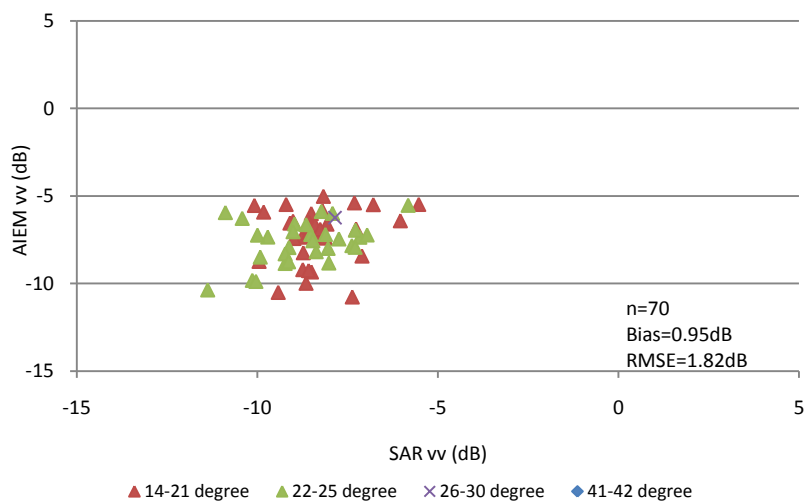




(d)



(e)



(f)

**Figure 5.9** Estimated  $\sigma_{HH}^0$  and  $\sigma_{VV}^0$  derived from SAR and from the AIEM parameterised by *in situ* soil moisture  $m_v$ ,  $s$  and  $l$  ((a) and (b): exponential correlation function; (c) and (d): Gaussian correlation function) and by *in situ* soil moisture  $m_v$ ,  $s$  and  $l_{opt}$  ((e) and (f)) in terms of the local incidence angle.

Based on the methodology of Rahman’s approach, no backscattering simulation can be made.

## 5.4. Model Assessment

### 5.4.1. Oh model

For experimental purposes, *in situ* rms height measurement is used, while several approaches can be adopted for surface soil moisture retrieval by the Oh model based on the model description, such as 1) derived from  $p$ ,  $ks$  and  $\theta$  through Equation 5.19; 2) derived from  $\sigma_{HV}^0$ ,  $ks$  and  $\theta$  through Equation 5.21; and 3) substituting Equation 5.21 for Equations 5.20 or 5.75 and Equation 5.16 and derived  $m_v$  from  $\sigma_{VV}^0$ ,  $ks$  and  $\theta$  through Equation 5.16. In the following, the expression of  $q$  from the 2004 version model is used.

$$\frac{0.11m_v^{0.7} \cos^{2.2}\theta(1 - e^{-0.32(ks)^{1.8}})}{\sigma_{VV}^0} = 0.095(0.13 + \sin 1.5\theta)^{1.4}(1 - e^{-1.3(ks)^{0.9}})$$

**5.75**

All these three approaches are adopted in this study, noting that a 3.1dB backscattering coefficient correction is taken based on the model evaluation findings for HH and VV polarisations (Figure 5.5). It is found that due to the large RMSE of estimation of the co-polarised ratio  $p$  (Figure 5.6), the first approach is unable to derive soil moisture for all samples. Results from the other two approaches are shown in Figure 5.10 and Figure 5.11.

Figure 5.10 compares the *in situ* surface soil moisture measurements (at 1–4 cm and 5–8 cm depth respectively) and estimated values from  $\sigma_{VV}^0$ , local incidence angle  $\theta$  and effective rms height  $ks$  with the second approach using the Oh model. The figure shows a total of 70 samples for each set of comparison. The comparison of *in situ* soil moisture 5–8 cm depth shows a slightly better agreement with model estimation of 8.64 vol. % and 2.03 vol. % for RMSE and bias compared to 9.16 vol. % and 3.78 vol. % for their

counterparts of 1–4 cm depth’ measurements. Figure 5.11 shows a poor result comparing the *in situ* surface soil moisture measurements (at 1–4 cm and 5–8 cm depth respectively) and estimated values from  $\sigma_{HV}^0$ , local incidence angle  $\theta$  and effective rms height  $k_s$  with the third approach using the Oh model. With a limited 33 samples, model estimations yield RMSE and bias of 12.63 vol. % and 7.46 vol. % compared to *in situ* soil moisture measurements at 1–4 cm depth and accordingly 8.46 vol. % and 2.03 vol. % compared to *in situ* soil moisture measurements at 5–8 cm depth. Significant overestimations are shown for samples, especially from drier field conditions.

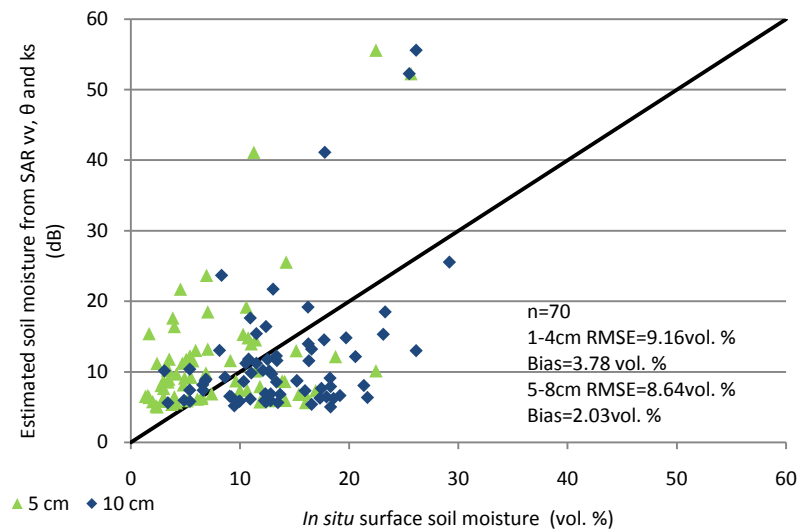


Figure 5.10 Comparison between *in situ* surface soil moisture measurements (at 1–4 cm and 5–8 cm depths) and estimated values from  $\sigma_{vv}^0$ , local incidence angle  $\theta$  and effective rms height  $k_s$ .

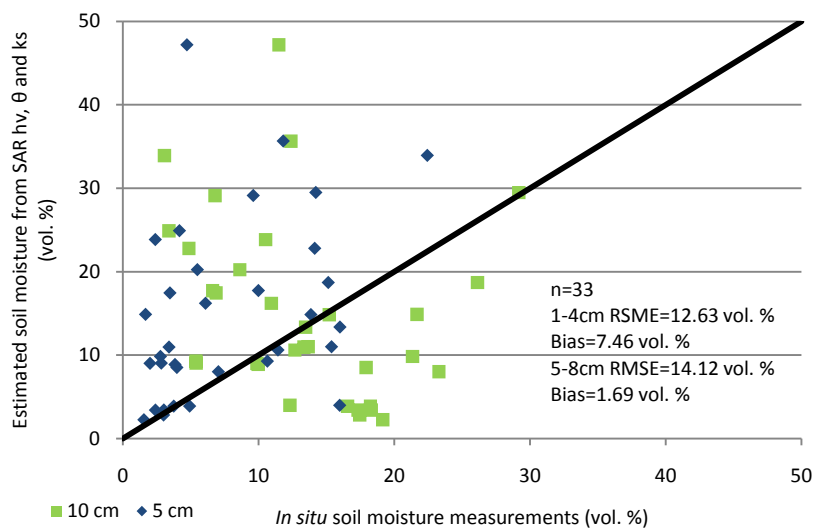


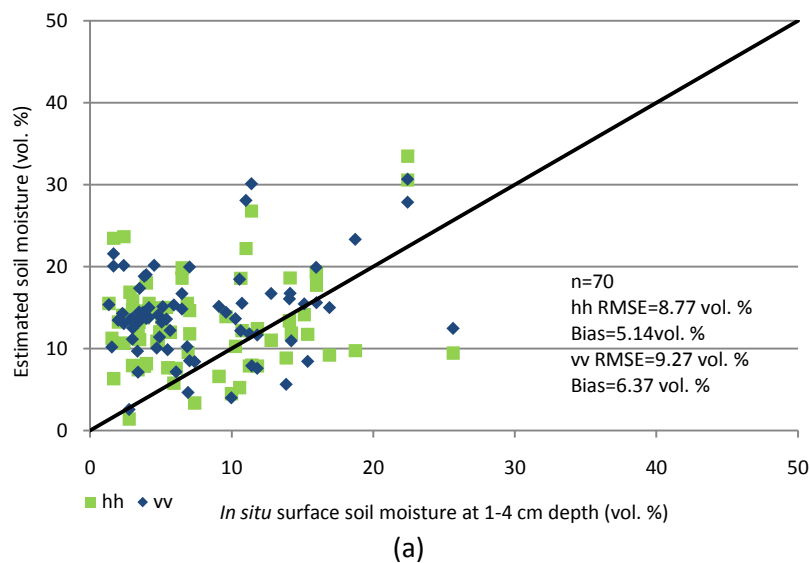
Figure 5.11 Comparison between *in situ* surface soil moisture measurements (at 1–4 cm and 5–8 cm depths) and estimated values from  $\sigma_{hv}^0$ , local incidence angle  $\theta$  and effective rms height  $k_s$ .

### 5.4.2. Dubois model

Even after corresponding backscattering coefficient corrections of 7dB and 2.4dB for HH and VV polarisations respectively, negative dielectric constants are shown in calculations from both  $\sigma_{HH}^0$  and  $\sigma_{VV}^0$  using the Dubois model, and therefore no meaningful overall surface soil moisture estimations are derived from the Dubois model.

### 5.4.3. The semi-empirical model for ERS imagery

The semi-empirical model is applied to ASAR images from 2007–2009 using the original coefficients as in the model description section. Figure 5.12 compares the *in situ* soil moisture measurements at both 1–4 cm and 5–8 cm depths and estimated values from the semi-empirical model for ERS imagery using the original coefficients. The comparison between model estimations and *in situ* soil moisture measurements at 5–8 cm depth appears to agree better than the comparison with *in situ* soil moisture measurements at 1–4 cm depth. For a total of 70 samples, compared with the *in situ* soil moisture at 5 cm depth, model estimations yield RMSE and bias as of 8.77 vol. % and 5.14 vol. % for HH polarisation and 9.27 vol. % and 6.37 vol. % accordingly for VV polarisation. The same 70 samples are used for *in situ* soil moisture measurements at 5–8 cm depth, where model estimations yield RMSE and bias of 6.77 vol. % and 0.72 vol. % for HH polarisation and 6.50 vol. % and 0.51 vol. % accordingly for VV polarisation.



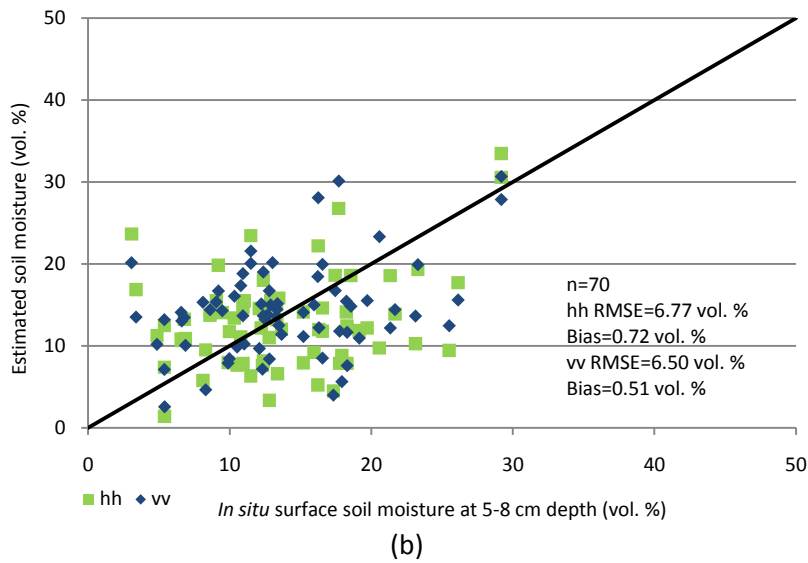


**Figure 5.12 Comparisons between in situ soil moisture measurements (at 1–4 cm (a) and 5–8 cm (b) depths) and estimated values using the semi-empirical model for ERS imagery.**

Figure 5.13 plots a better result by averaging model estimations from HH and VV polarisations. For a total of 70 samples, an RMSE of 6.21 and a bias of 0.11 vol. % are achieved.

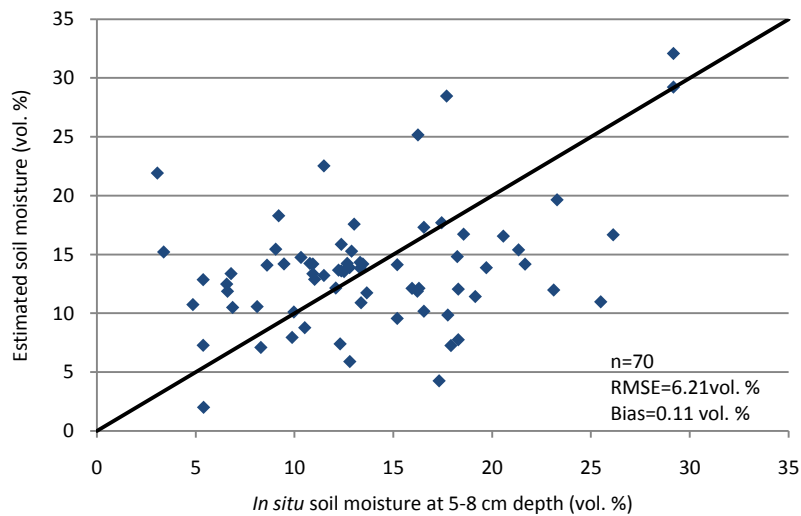


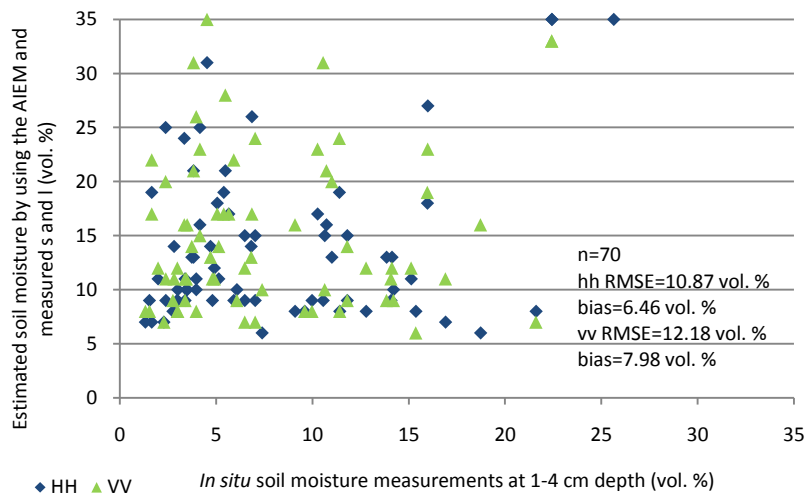
**Figure 5.13 Comparison between in situ soil moisture at 10 cm depth and estimated values by averaging estimations from the semi-empirical model for ERS imagery.**

#### 5.4.4. AIEM

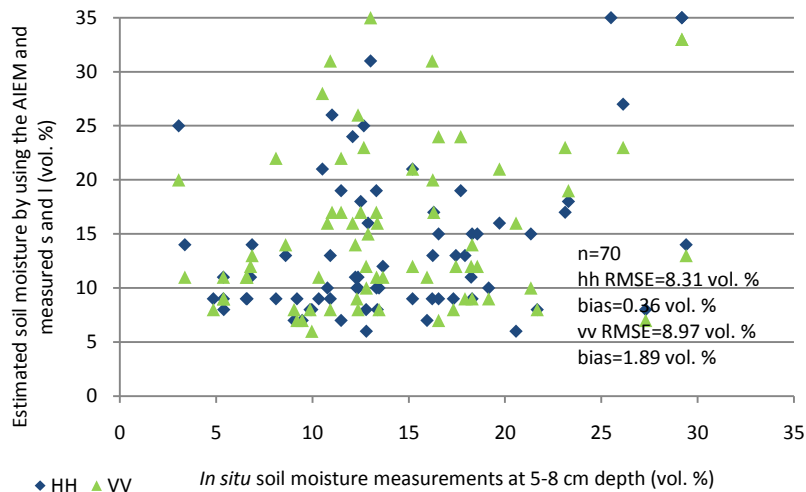
##### 5.4.4.1. Look-Up-Table approach

The first adopted approach for the AIEM is the conventional Look-Up-Table (LUT) approach, noting that a correction of 2.5dB is taken for backscattering coefficients from

HH and VV polarisations according to Figure 5.5. Again, this approach shows poor results in estimated soil moisture by comparing *in situ* measurements from both HH and VV polarisations from a total of 70 samples. Figure 5.14(a) compares model estimations with *in situ* soil moisture at 1–4 cm depth and shows significant RMSE and bias of 10.87 vol. % and 6.46 vol. % for HH polarisation and 12.18 vol. % and 7.98 vol. % for VV polarisation accordingly. Figure 5.14(b) compares model estimations with *in situ* soil moisture at 5–8 cm depth and shows only smaller RMSE and bias of 8.31 vol. % and 0.36 vol. % for HH polarisation and 8.97 vol. % and 1.89 vol. % for VV polarisation accordingly.



(a)



(b)

Figure 5.14 Comparisons between *in situ* soil moisture measurements (at 1–4 cm (a) and 5–8 cm (b) depths) and estimated values by using the AIEM with *in situ* measurements of *s* and *l*.

As in the previous section, an average of the estimations from HH and VV polarisations gives a better result as shown in Figure 5.15, where an RMSE of 8.15 vol. % and a bias of 1.67 vol. % are achieved for a number of 70 samples.

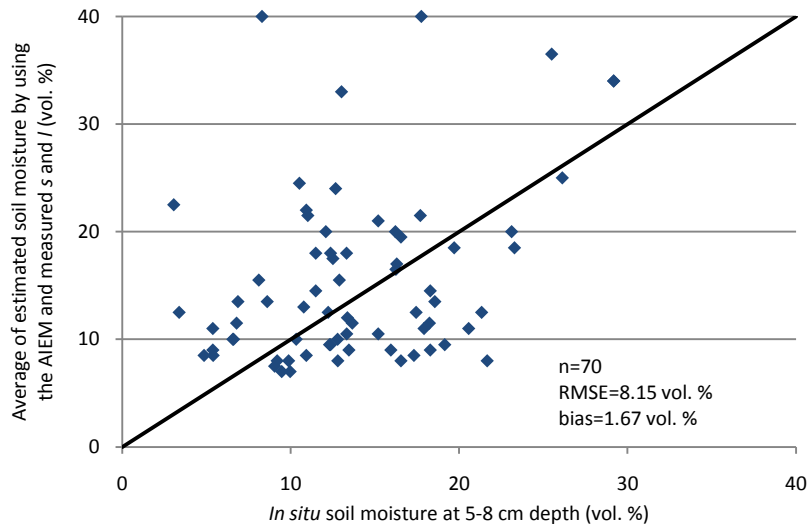


Figure 5.15 Comparison between in situ soil moisture at 5–8 cm depth and the average estimation by using the AIEM with in situ  $s$  and  $l$ .

#### 5.4.4.2. Baghdadi approach

Figure 5.16 illustrates the relationship between empirical correlation length  $l_{opt}$  (multiplied by the wave number  $k$ ) and measured rms height  $s$  (multiplied by the wave number  $k$ ) for different incidence angle ranges and both co-polarisations. Incidence angle ranges are set the same for both polarisations.

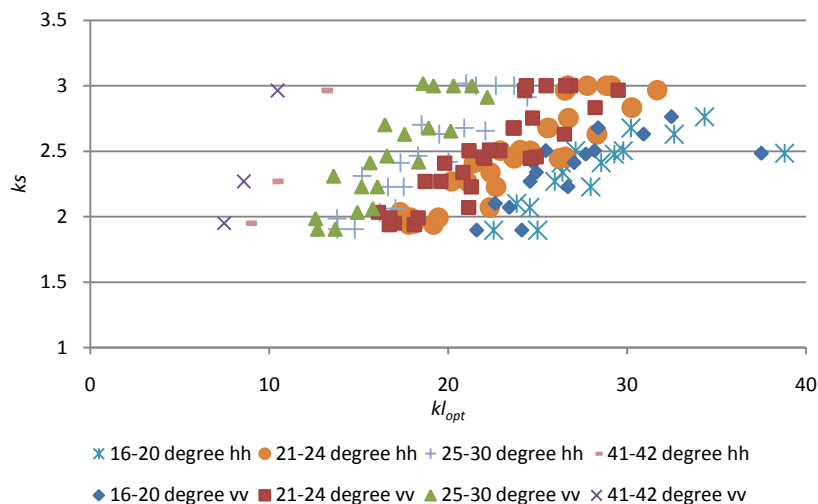
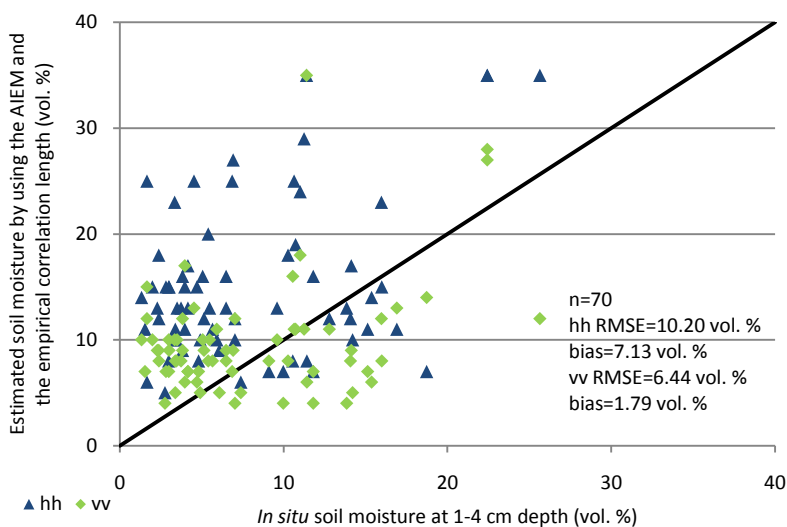


Figure 5.16 Empirical correlation length and rms height for different incidence angle ranges and polarisations .

Figure 5.17 shows the comparisons between *in situ* soil moisture measurements (at 1–4 cm (a) and 5–8 cm (b) depth) and estimated soil moisture using the AIEM and the empirical correlation length. For a total of 70 samples with *in situ* soil moisture measurements at 1–4 cm depth, model estimations show a better result from VV polarisation than HH polarisation. To be specific, the RMSE and bias for HH polarisation are 10.20 vol. % and 7.13 vol. % and for VV polarisation are 6.44 vol. % and 1.79 vol. % respectively. For the same number of samples with *in situ* soil moisture measurements at 5–8 cm depth, both polarisations yield a similar order of agreement in that the RMSE and bias are 7.30 vol. % and 1.27 vol. % for HH polarisation and are 7.33 vol. % and 4.07 vol. % respectively for VV polarisation.



(a)



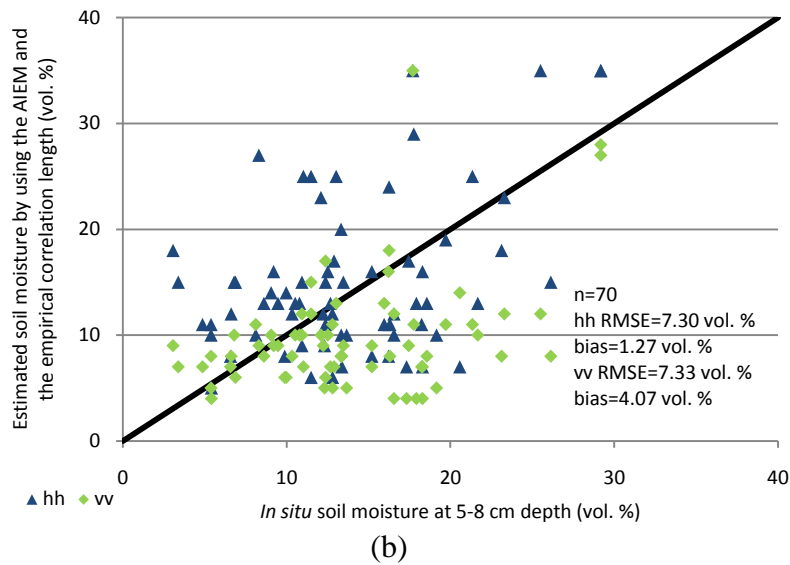


Figure 5.17 Comparisons between in situ soil moisture measurements (at 1–4 cm (a) and 5–8 cm (b) depths) and estimated values by using the AIEM with empirical correlation length  $l_{opt}$ .

By averaging model estimations from HH and VV polarisations, the RMSE and bias are reduced significantly to 6.19 vol. % and 1.40 vol. % respectively, from the AIEM coupling with measured  $s$  and the empirical correlation length  $l_{opt}$  as shown in Figure 5.18.

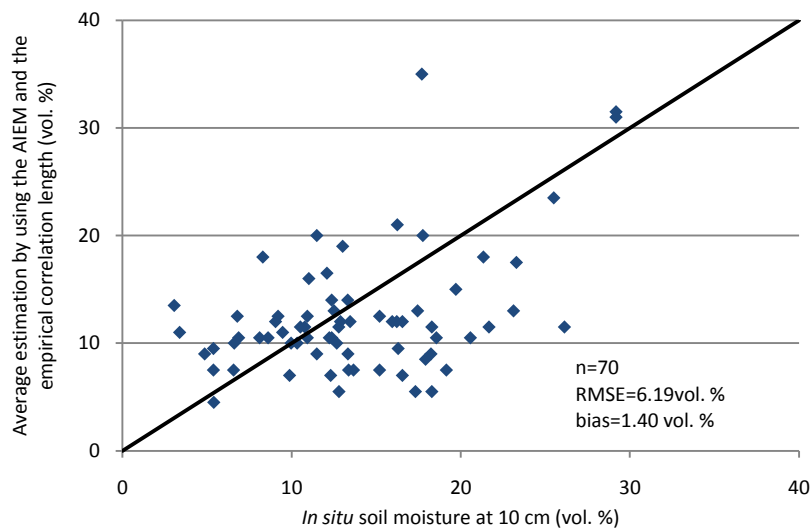


Figure 5.18 Comparison between in situ soil moisture at 5–8 cm depth and the average estimation using the AIEM with empirical correlation length  $l_{opt}$ .

#### 5.4.4.3. Rahman approach

Although the Rahman approach has been described in detail previously, please refer to Rahman et al. (2008) for a detailed flow chart of the approach. While incidence angles

in this study vary with those in the published dataset, coefficients corresponding to this study are derived individually. The rms height  $s$  is set between 0.5 cm and 4 cm, which fulfils the *in situ* situation. To be specific, the correlation length series with 0.5 cm step and the rms height series with 0.1 cm step are used for regression. Therefore the model is valid in the following conditions:  $0.5 \text{ cm} < s < 4 \text{ cm}$ ,  $1 \text{ cm} < l < 40 \text{ cm}$ ,  $\text{vol. \%} < m_v < 30 \text{ vol. \%}$  and  $10^\circ < \theta < 40^\circ$ . These settings fulfil general natural agricultural conditions (Davidson et al. 2000). Before all AIEM regressions, images are to be selected for the different steps as described before. Table 5.3 lists the SAR image selection for step 1 in Section 5.1.2.3. Note that for both parts of the field F32, the maximum differences in local incidence angle are unfortunately less than  $10^\circ$  in the available database, while for all other fields, the differences reach over  $20^\circ$ , which satisfies the published condition in Rahman et al. (2008). In addition, the surface soil moisture conditions are similar for each pair selected. While as previous sections found *in situ* soil moisture at 5–8 cm depth agrees better than the value at 1–4 cm depth with the empirical linear relationship with backscattering coefficients, the *in situ* measurement at 5–8 cm is set to have priority in consideration. Therefore in some cases, *in situ* measurements at 1–4 cm depth may have large bias, e.g. for F21.

Following the selected images, regressions based on specific local incidence angles and polarisations are taken by using the AIEM, noting that close approximations are given for incidence angles to reduce computational efforts, i.e. F11 and F21 will share the same coefficient set, while the two parts of F32 will share another coefficient set. The expression is given as:

$$Z = a\Delta\sigma^0 + b$$

**5.76**

The corresponding coefficients and their  $R^2$  are listed in Table 5.4.

**Table 5.3 Selected SAR images with large local incidence angle differences but similar surface geophysical conditions for model regression step 1.**

	Date	Field	Sensor	Loc Inc	$\sigma_{hh}$	$\sigma_{vv}$	$m_v$ 1–4 cm	$m_v$ 5–8 cm
Low inc	2007.08.03	F11	ASAR	14.84	-6.51	-7.11	21.61	27.30
	2007.06.29	F21	ASAR	14.04	-5.67	-4.73	17.80	24.00
	2008.05.28	F31	ASAR	18.44	-7.55	-8.16	6.49	9.20
	2009.05.13	F32low	ASAR	19.18	-8.37	-8.40	1.33	9.05
	2009.05.13	F32high	ASAR	17.82	-8.76	-8.71	2.29	9.47
High inc	2008.06.06	F11	ASAR	41.96	-8.58	-7.85	25.64	25.50
	2008.06.06	F21	ASAR	41.27	-9.03	-8.04	11.25	17.76
	2008.06.06	F31	ASAR	40.96	-8.61	-10.04	6.92	8.30
	2009.05.16	F32low	ASAR	27.63	-8.09	-9.23	3.35	12.09
	2009.05.16	F32high	ASAR	26.23	-8.33	-8.46	5.06	12.51

**Table 5.4 Coefficients for Rahman approach step 1.**

Field	F11 and F21		F31		F32low and F32high	
Polarisation	HH	VV	HH	VV	HH	VV
a	0.11	0.08	0.08	0.10	0.23	0.23
b	0.86	0.91	0.86	0.91	0.87	0.89
R <sup>2</sup>	0.85	0.87	0.88	0.89	0.80	0.82

After substituting the known  $\Delta\sigma^0$ , the Z-index is given for each field and polarisation as in Table 5.5.

**Table 5.5 Z-index for each field and polarisation.**

	F11	F21	F31	F32low	F32high
HH	0.64	0.50	0.78	0.94	0.97
VV	0.85	0.65	0.72	0.70	0.95

Table 5.6 lists selected SAR images for step 2 as in the model description section. Although local incidence angle varies from field to field, all images meet the conditions that top surface soil moisture is below 4 vol. %. It should be noted however that it is difficult to guarantee the top 10 cm surface of each test field remains completely dry, e.g. soil moisture on F11 and F21 at 10 cm depth is over 10 vol. % although their top surfaces at 5 cm are already dried up. For each local incidence angle range (in this case all local incidence angles can be approximated to 23 °), Equation 5.70 is calibrated to:

$$\sigma_{dry, hh}^0 = -21.74 + 26.63ks - 0.90kl - 16.81(ks)^2 + 0.02(kl)^2 + 0.83kskl + 2.32(ks)^3 + 0.02(ks)^2kl - 0.02ks(kl)^2$$

**5.77**

$$\sigma_{dry, vv}^0 = -21.26 + 24.12ks - 0.84kl - 15.98(ks)^2 + 0.01(kl)^2 + 0.96kskl + 2.26(ks)^3 - 0.01(ks)^2kl - 0.02ks(kl)^2$$

**5.78**

and their  $R^2$  are 0.96 and 0.95 respectively.

**Table 5.6 Selected SAR images in extremely dry surface soil conditions for model regression.**

Date	Field	Sensor	Loc Inc	$\sigma_{hh}$	$\sigma_{vv}$	$m_v$ 1–4 cm	$m_v$ 5–8 cm
2009.05.22	F11	Radarsat-2	20.67	-8.57	-8.58	3.83	15.20
2009.05.22	F21	Radarsat-2	19.82	-8.51	-8.72	2.99	10.93
2008.06.17	F31	Radarsat-2	23.63	-10.06	-10.14	3.39	5.38
2009.06.12	F32low	Radarsat-2	21.98	-9.30	-8.74	2.39	6.61
2009.06.12	F32high	Radarsat-2	23.16	-8.52	-8.37	3.74	8.61

After using an iterating method, the best fitting  $ks$  and  $kl$  for each field and polarisation are given in Table 5.7.

**Table 5.7 Estimated  $ks$  and  $kl$  using the AIEM for each field and polarisation.**

	HH		VV	
	$ks$	$kl$	$ks$	$kl$
F11	1.08	1.92	1.02	1.24
F21	1.98	11.00	1.07	1.82
F31	0.83	0.81	1.04	1.55
F32low	1.05	1.20	1.05	1.62
F32high	1.05	1.15	1.01	1.08

Equation 5.74 is then calibrated according to local incidence angle, *i.e.* 14°, 19°, 23°, 29°, and 41° and polarisations as in Appendix A. Soil moisture for each sample can be estimated by substituting estimated  $ks$  and  $kl$  for the corresponding expression according to the local incidence angle range and polarisation. However, the study finds that a large number of samples from  $\sigma_{VV}^0$  yield overwhelmingly high soil moisture estimations, larger than 50 vol. %. Therefore, only the results from  $\sigma_{HH}^0$  are shown in Figure 5.19,

where a total of 56 samples of soil moisture estimations from  $\sigma_{HH}^0$  yield RMSE and bias of 7.68 vol. % and 2.82 vol. %. Due to insignificant difference of local incidence angle between images for F32, soil moisture of higher than 100 vol. % is calculated for the field, and therefore the results for F32 are omitted as outlier.

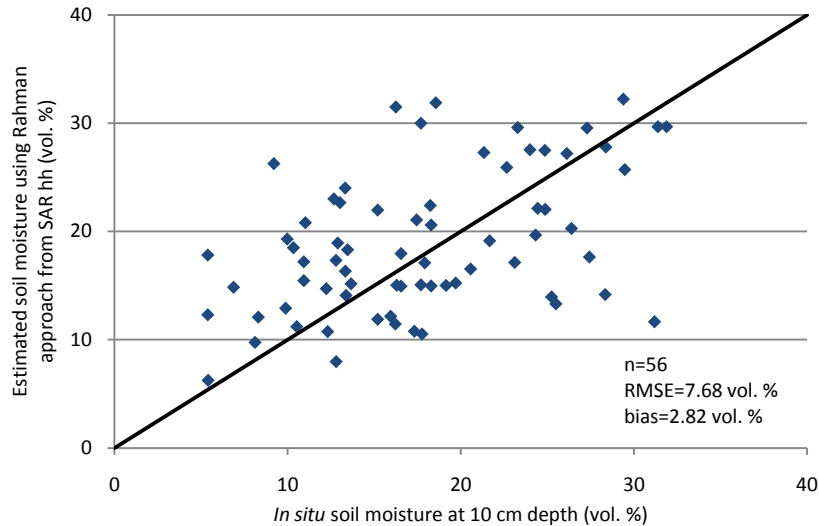


Figure 5.19 In situ soil moisture measurement at 5–8 cm depth and Rahman estimations from  $\sigma_{HH}$ .

## 5.5. Summary

This chapter describes in detail several semi-empirical models and theoretical models, as the foundation for the following experiments and applications. Before implementing these models in practice, field data and backscattering coefficients from SAR are verified through an empirical relationship between surface soil moisture and backscattering coefficients for HH and VV polarisations and for different ranges of incidence angle (Baghdadi et al. 2006b). Figure 5.2 proves good agreements between measured surface soil moisture and derived backscattering coefficients from SAR imagery. It is also found that measured soil moisture at 5–8 cm depth shows better results than soil moisture at 1–4 cm depth, especially in dry conditions, which may indicate a deeper penetration of microwave signal in the drier conditions.

After verification, the models are evaluated through comparisons between backscattering coefficient simulation and derived values from SAR imagery. The simulations are based on *in situ* soil moisture and roughness measurements/empirical correlation length.

Comparisons show overestimation of backscattering coefficients for both HH and VV polarisations in semi-empirical models universally. In particular, the Oh model in both its 2002 and 2004 versions show overestimations over 3dB for both co-polarisations, while a closer agreement is found for VV polarisation than for HH polarisation using the Dubois model. The Oh model shows large RMSE but close-to-zero bias for HV polarisation. The semi-empirical model for ERS imagery shows the best fitted result with overestimations of less than 2dB for both co-polarisations, while no *in situ* surface roughness information is needed. In terms of the theoretical model the AIEM two shapes of correlation function are tested for measured  $s$  and  $l$ . It is found that the AIEM coupled with the Gaussian ACF leads to significant RMSE for backscattering coefficients for both HH and VV polarisations. Similar to the Oh model, about 3dB overestimation of backscattering coefficients from both HH and VV polarisations are shown from the AIEM coupled with the exponential ACF. The best results are achieved by the AIEM coupled with the empirical correlation length (**Baghdadi et al. 2006a**), while bias is reduced to within 1dB for both co-polarisations.

After careful evaluation, all models/approaches are used for soil moisture conversion from SAR backscattering coefficients. “Backscattering corrections” are adopted for those models with significant overestimating performance during the evaluation process. Table 5.8 lists the best performance of each model/approach and their statistics in terms of RMSE and bias compared to *in situ* soil moisture measurements. The Dubois model is unable to provide meaningful soil moisture estimation for all samples due to its model condition limitation. An additional reason might be its limitation on fine scales (**Western et al. 2001**). Although the Oh model and the AIEM coupled with LUT approach are able to estimate surface soil moisture with RMSE around 8 vol. %, their requirements of different backscattering coefficient corrections limit the applicability of these models over other test areas as an operational approach. After averaging estimations from both co-polarisations, the RMSE is reduced significantly to 6.19 vol. %, equivalent to the best performance from the semi-empirical model for ERS imagery. The semi-empirical model for ERS imagery utilises a straightforward approach and provides good results with no limited *in situ* measurements, *i.e.* only soil texture information is needed during soil moisture conversion from the dielectric constant. However, roughness factors are removed out of the model concept by consideration of average

conditions of the test sites in the calibrated database (Loew et al. 2006a). Therefore, apart from soil moisture, there is no other perspective to assess this model's capability. The AIEM coupled with the empirical correlation length is able to estimate surface soil moisture with RMSE around 6 vol. % from dual-polarisation at field scale in this study without backscattering coefficient correction. The models require *in situ* rms height  $s$  for model initialisation.

Clearly, large uncertainties are introduced to backscattering models through roughness parameterisation especially of the correlation length. The inaccuracy could result in scale difference between the photogrammetric technique and SAR observations. First the sufficient scale of the photogrammetric technique still needs to be reassessed to better represent the field structure. Furthermore, when the measurements of the photogrammetric technique are upscaled to meet the SAR observation, additional errors may need to be taken into account. This in-field measurement induced inaccuracy can be overcome by the empirical correlation length. For a future operational approach, which needs roughness parameterisation, other remote sensing based roughness inversions are necessary, such as the polarimetric method (Hajnsek et al. 2003). Nevertheless, this study evaluates a number of widely used models and approaches. Results show that for a future operational approach with confident rms height available, the AIEM-Baghdadi approach is able to provide soil moisture estimation with RMSE in the order of 6 vol. %.

As an operational approach, the AIEM adapted Rahman approach has the advantage of no requirements of *in situ* measurements, and it can provide estimated rms height  $s$  and correlation length  $l$  for further model assessment. Note the model is calibrated on the following conditions:  $0.5 \text{ cm} < s < 4 \text{ cm}$ ,  $1 \text{ cm} < l < 40 \text{ cm}$ ,  $3 \text{ vol. \%} < m_v < 30 \text{ vol. \%}$  and  $10^\circ < \theta < 40^\circ$ , and therefore is only recommended be applied in these conditions. However, the model has the following limitations. First, the approach requires at least two images with large difference of local incidence angle, *i.e.* larger than  $20^\circ$ . A failure to satisfy this requirement will lead to a failure of soil moisture estimation, as for F32 in this study. Second, since the AIEM regression requires at least three SAR images, the arbitrary selection of images may introduce errors into the final estimation. Therefore, fewer arbitrary selections are preferred. Chapter 6 will focus on solving these limita-

tions through proposing a new model for soil moisture retrieval on fields of small size in a semi-arid environment.

**Table 5.8 Soil moisture conversion statistics.**

Model/approach	Polarisation	RMSE (vol. %)	Bias (vol. %)
Oh	VV	8.64	2.03
	HV	12.63	7.46
Semi-empirical model for ERS imagery	HH	6.72	0.72
	VV	6.50	0.51
	HH+VV	6.21	0.11
AIEM+LUT	HH	8.31	0.36
	VV	8.97	1.89
	HH+VV	8.15	1.67
AIEM+ $I_{opt}$	HH	7.30	1.27
	VV	7.33	4.07
	HH+VV	6.19	1.40
AIEM+Rahman	HH	7.68	2.82



There is never an end to learning. The dye  
extracted from the indigo is bluer than  
the plant; so is the ice colder than the  
water.

---Xun Zi

## **Chapter 6 Model Development, Evaluation and Sensitivity Analysis**

Chapter 5 focused on various models for soil moisture retrieval. The Rahman approach is considered to be a good operational approach to surface soil moisture retrieval. In addition, it is developed based on the theoretical backscattering model with solid concepts. As previously described, backscattering coefficients are related to the dielectric constant  $\epsilon$ , rms height  $s$ , correlation length  $l$ , ACF, local incidence angle  $\theta$  as well as SAR configurations, polarisation and signal frequency  $f$ . As the Rahman approach is able to estimate both soil moisture and roughness information without any auxiliary data, it is necessary to re-evaluate the model in detail as a whole backscatter system through backscattering coefficient simulation comparison with the derivation from SAR imagery. Chapter 5 also raises the issue of two limitations of the Rahman approach: its restriction on incidence angle requirements of SAR imagery and arbitrary selection of SAR imagery induced errors. Therefore, the current version of the Rahman approach has to be improved to overcome the two limitations.

This chapter proposes a new version of the Rahman approach for surface soil moisture retrieval from SAR. It starts with the rationale and a description of the proposed model in Section 6.1, followed by model assessment through comparison between model estimation of soil moisture and *in situ* measurement in section 6.2. In section 6.3, the Rahman approach is fully evaluated through backscattering coefficient simulation. After that, the model sensitivity analysis is conducted for a better understanding of the theoretical model, the AIEM and the proposed model's performance in section 6.4. The chapter is summarised in section 6.5.

## 6.1. Rationale and Description of the Updated Rahman Approach

### 6.1.1. The model rationale-- Limitations of Rahman approach

As previously mentioned, for an operational approach, the Rahman method has the advantage of having no requirement for auxiliary data, *i.e.* no *in situ* measurements are necessary for either calibration or parameterisation. The whole approach is built on theoretical models – the IEM (Rahman et al. 2008) and the AIEM as described in Chapter 5 is adopted for this study, and thus with strong physical meaning. However, limitations as found in previous chapter are:

- 1) The Rahman approach requires at least two images with large incidence angle difference but from similar geophysical conditions to eliminate the soil moisture effect on backscattering coefficients and hence to derive the *Z-index* for surface roughness estimation. Although the current SAR system can generally provide a large range of incidence angles over the same observation area, the minimum 20° of incidence angle difference can still be problematic, *e.g.* for F32 in this study as described in Chapter 5, where limited images are available with the maximum incidence angle difference of around 10°. In this case, no reasonable estimations can be made for surface roughness or soil moisture for the specific field or area.
- 2) The Rahman approach consists of three steps as described in Chapter 5, with a total of at least three images for coefficient regression. For step 1, two images are needed with considerable difference of incidence angle and close surface geophysical conditions; for step 2, one image in extremely dry conditions is needed to further eliminate the soil moisture effect on backscattering coefficients. In both cases, arbitrary selection of SAR images is unavoidable. Furthermore if the two images required for step 1 are not acquired at the same time of day and on close dates with similar meteorological conditions, it is not guaranteed that the selected images have similar surface geophysical condition without *in situ* measurement, which should be avoided in an operational approach. The *in situ* measurement of soil moisture is used for selecting images for coefficient regressions.

The above two limitations of the AIEM based Rahman approach mean that it has to be further developed and improved. A detailed model description is given in Section 6.1.2.

### **6.1.2. Description of the Baghdadi-Rahman model**

The empirical correlation length has been already described and evaluated in Chapter 5, where its capability of simulating backscattering coefficients correctly, with bias of no larger than 1dB, was demonstrated. Therefore, a new version of the Rahman approach based on the AIEM is proposed by coupling the empirical correlation length with the Rahman approach, namely the Baghdadi-Rahman model. The empirical correlation length will be used as a substitution of step 1 of the Rahman approach and represent the relationship between correlation length  $l$  and rms height  $s$ . Hence, in this case, only image(s) in extremely dry conditions are selected instead of three images with different imaging geometry. And the model restriction on incidence angle difference is avoided. Basically, the Baghdadi-Rahman model inverts surface soil moisture in a similar way to the original Rahman approach with the exception of implementing the empirical correlation length to express the correlation between rms height  $s$  and correlation length  $l$  instead of using the  $Z$ -index. Again, the model is calibrated on the following conditions:  $0.5 \text{ cm} < s < 4 \text{ cm}$ ,  $1 \text{ cm} < l < 40 \text{ cm}$ ,  $3 \text{ vol. \%} < m_v < 30 \text{ vol. \%}$  and  $10^\circ < \theta < 40^\circ$ .

### **6.1.3. Pre-assumption of the Baghdadi-Rahman model**

The validity of the proposed Baghdadi-Rahman model is based on one major pre-assumption, that the surface roughness variability during campaign periods has limited impacts on soil moisture inversion, which is satisfied through *in situ* roughness measurements described in Chapter 3.

## **6.2. Baghdadi-Rahman Model Assessment**

### **6.2.1. The first assessment**

Step 1 in the Rahman approach is substituted by the expressions of the empirical correlation length (**Baghdadi et al. 2006a**). Therefore the correlation lengths for HH and VV polarisations are expressed by Equations 5.67 and 5.68 respectively, instead of by  $s^2/Z$ -index in step 2. The Baghdadi-Rahman model starts with coefficient regression for

Equation 5.70. The same five images are selected for fields in the extremely dry conditions as in Chapter 5. Since the empirical correlation length adopts the Gaussian ACF, the Gaussian ACF is chosen for the AIEM regression instead of the exponential ACF in Chapter 5. Furthermore, the backscattering coefficient becomes more sensitive to incidence angles with Gaussian ACF than exponential ACF. Thus these five images are separated into two groups in terms of local incidence angle (i.e. 19° and 23°). Regression results are given in Equations 6.1–6.4:

$$\begin{aligned} \sigma_{dry, hh}^0(19^\circ) = & -14.83 + 27.17ks - 1.90kl - 23.12(ks)^2 - 0.13(kl)^2 + 3.39kskl \\ & + 4.68(ks)^3 - 0.81(ks)^2kl + 0.04ks(kl)^2 \end{aligned}$$

**6.1**

$$\begin{aligned} \sigma_{dry, vv}^0(19^\circ) = & -15.40 + 26.73ks - 1.66kl - 23.08(ks)^2 - 0.13(kl)^2 + 3.32kskl \\ & + 4.69(ks)^3 - 0.79(ks)^2kl + 0.03ks(kl)^2 \end{aligned}$$

**6.2**

$$\begin{aligned} \sigma_{dry, hh}^0(23^\circ) = & -14.17 + 30.48ks - 3.31kl - 25.81(ks)^2 - 0.13(kl)^2 + 4.32kskl \\ & + 5.14(ks)^3 - 0.93(ks)^2kl + 0.03ks(kl)^2 \end{aligned}$$

**6.3**

$$\begin{aligned} \sigma_{dry, vv}^0(23^\circ) = & -15.26 + 30.61ks - 2.88kl - 26.08(ks)^2 - 0.13(kl)^2 + 4.11kskl \\ & + 5.21(ks)^3 - 0.89(ks)^2kl + 0.02ks(kl)^2 \end{aligned}$$

**6.4**

where  $R^2$  are 0.983, 0.978, 0.989 and 0.983 respectively.

After using an iterating method, the best fitting  $ks$  and  $kl$  are derived for each test field and polarisation as listed in Table 6.1.

Table 6.1 Estimated  $k_s$  and  $k_l$  using the Baghdadi-Rahman model for each field and polarisation.

	HH		VV	
	$k_s$	$k_l$	$k_s$	$k_l$
F11	1.75	18.80	1.28	13.56
F21	1.63	18.61	1.66	18.27
F31	1.85	16.52	1.23	10.84
F32low	1.76	17.39	1.72	16.27
F32high	1.83	16.81	1.77	15.44

After substituting estimated  $k_s$  and  $k_l$  as well as SAR backscattering from both co-polarisations into Equations in Appendix A, surface soil moisture  $m_v$  is inverted and plotted in Figure 6.1. For a total of 70 samples, the result from HH polarisation gives RMSE and bias of 6.27 vol. % and 1.03 vol. % compared with *in situ* measurement at 5–8 cm depth. For the same number of samples, the result of VV polarisation performs slightly worse with RMSE and bias of 8.71 vol. % and 2.04 vol. % respectively.

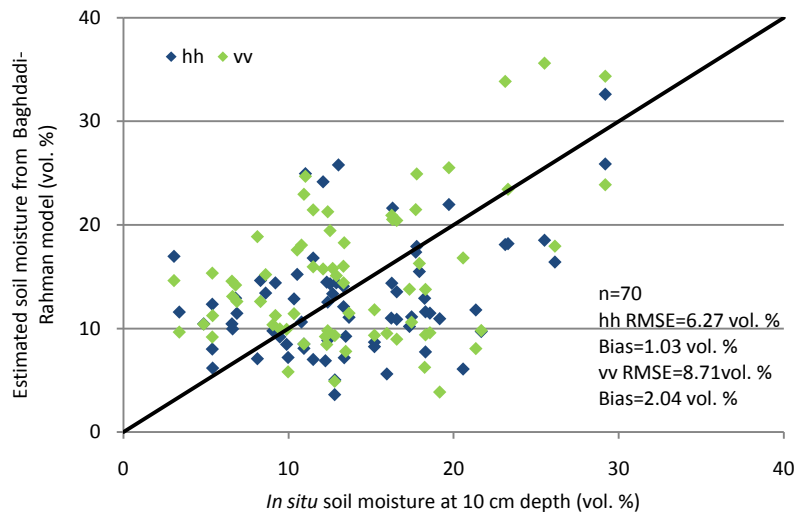
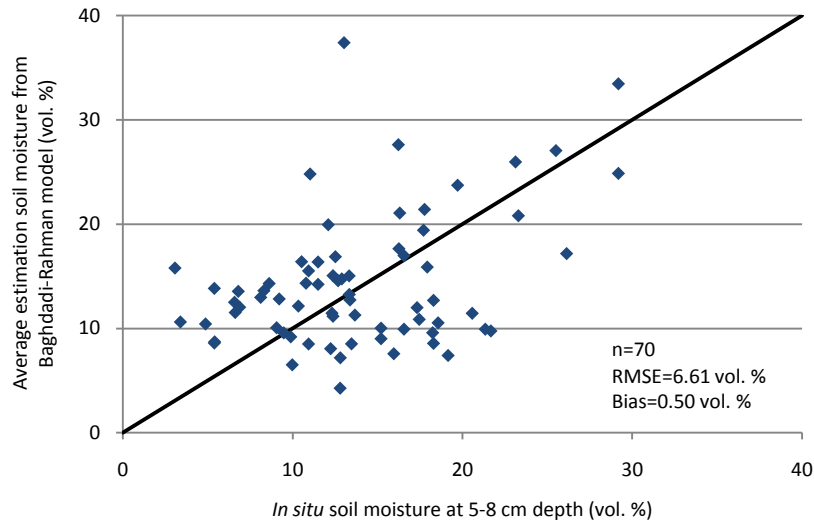


Figure 6.1 Estimated soil moisture from both co-polarisations using Baghdadi-Rahman model and *in situ* soil moisture at 5–8 cm depth.

As in Chapter 5, estimations from HH and VV polarisations are averaged and Figure 6.2 shows the comparison between *in situ* soil moisture at 5–8 cm depth and the averaged estimation from the Baghdadi-Rahman model. For a total of 70 samples, RMSE and bias are achieved as 6.61 vol. % and 0.50 vol. % respectively.



**Figure 6.2** Averaged estimation from Baghdadi-Rahman model and in situ soil moisture at 5–8 cm depth.

**6.2.2. In-field variability correction in extremely dry conditions**

For the study site in Sardinia, it is easy to get access to images for several days during the summer, with extremely dry surface conditions. Therefore, two images on close acquisition dates and close local incidence angles are selected for each test field for step 2 of the Baghdadi-Rahman model, instead of only one image for each field. The average of both backscattering coefficients and local incidence angles is taken to represent the condition. The selection of imagery is listed in Table 6.2.

**Table 6.2** Selected SAR images for extremely dry surface soil conditions for model regression.

Date	Field	Sensor	Loc Inc (°)	$\sigma_{HH}$	$\sigma_{VV}$
2009.05.19	F11	Radarsat-2	22.16	-8.37	-8.56
2009.05.23	F11	ASAR	24.68	-9.87	-7.38
	F11_mean		23.42	-9.12	-7.97
2009.06.01	F21	ASAR	22.94	-8.15	-8.26
2009.06.12	F21	Radarsat-2	22.43	-8.68	-8.40
	F21_mean		22.68	-8.41	-8.33
2008.06.17	F31	Radarsat-2	23.63	-10.06	-10.14
2008.06.16	F31	ASAR	22.93	-8.81	-8.65
	F31_mean		23.28	-9.44	-9.40
2009.06.12	F32low	Radarsat-2	21.98	-9.30	-8.74
2009.06.01	F32low	ASAR	23.49	-9.11	-7.74
	F32low_mean		22.74	-9.20	-8.24
2009.06.12	F32high	Radarsat-2	23.16	-8.52	-8.37
2009.06.01	F32high	ASAR	22.1	-9.25	-8.50
	F32high_mean		22.63	-8.88	-8.44

By using the same technique,  $ks$  and  $kl$  are estimated with the best fitting results for different fields and polarisations, as listed in Table 6.3.

**Table 6.3 Estimated  $ks$  and  $kl$  using the improved Baghdadi-Rahman model for each field and polarisation.**

	HH		VV		In situ average		RMSE			
	$ks$	$kl$	$ks$	$kl$	$ks$	$kl$	$ks,HH$	$ks,VV$	$kl,HH$	$kl,VV$
F11	1.84	16.65	1.77	15.25	2.78	19.94	0.62	0.68	4.91	6.02
F21	1.81	17.08	1.75	15.80	2.47	23.36				
F31	1.84	16.74	1.77	15.35	2.50	25.10				
F32low	1.81	17.05	1.75	15.75	2.10	17.62				
F32high	1.80	17.10	1.75	15.83	2.10	17.62				

After substituting estimated  $ks$  and  $kl$ , and regressed coefficients according to local incidence angle ranges and polarisations, surface soil moisture is inverted from backscattering coefficients as previously described. The comparison between *in situ* soil moisture at 5–8 cm depth and estimated values from the improved Baghdadi-Rahman model is plotted in Figure 6.3. For a total of 70 samples, similar to previous comparisons, HH polarisation yields better results than VV polarisation. The RMSE and bias are 6.32 vol. % and 0.93 vol. % for HH polarisation respectively and 7.04 vol. % and 0.98 vol. % for VV polarisation respectively. Compared to average *in situ* measurements, HH polarisation performs better than VV polarisation, while average errors of 26% and 28% are found for rms height from HH and VV respectively and 24% and 29% for correlation length correspondingly. Note that the Gaussian ACF is used for comparison in accordance with the ACF type used for the empirical correlation length.

Estimations from both co-polarisations are averaged and compared with *in situ* soil moisture at 5–8 cm depth. The result is plotted in Figure 6.4, where the RMSE is reduced to 5.60 vol. % for 70 samples over three years and the bias is limited to 0.04 vol. %. The Nash-Sutcliffe model efficiency coefficient  $E$  is achieved as 0.01. In addition, Figure 6.5 plots the estimated soil moisture errors and corresponding local incidence angle over the field, the errors being independent of local incidence angle.

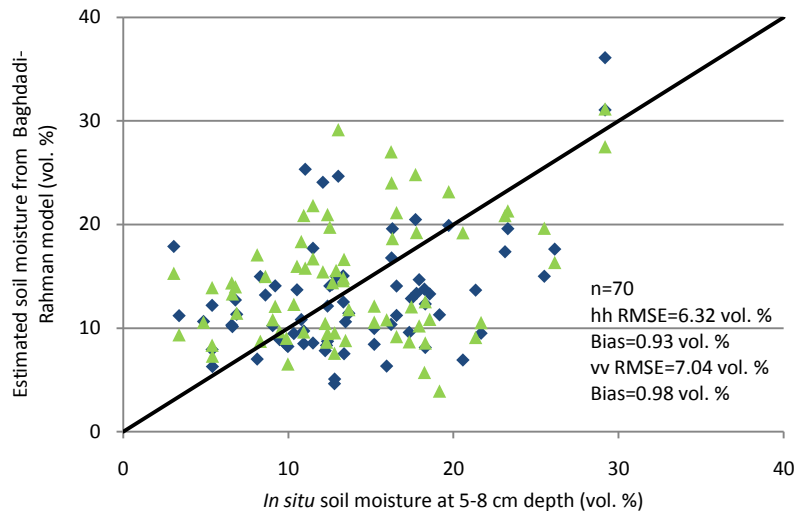


Figure 6.3 Estimated soil moisture from both co-polarisations using the improved Baghdad-Rahman model and in situ soil moisture at 5–8 cm depth.

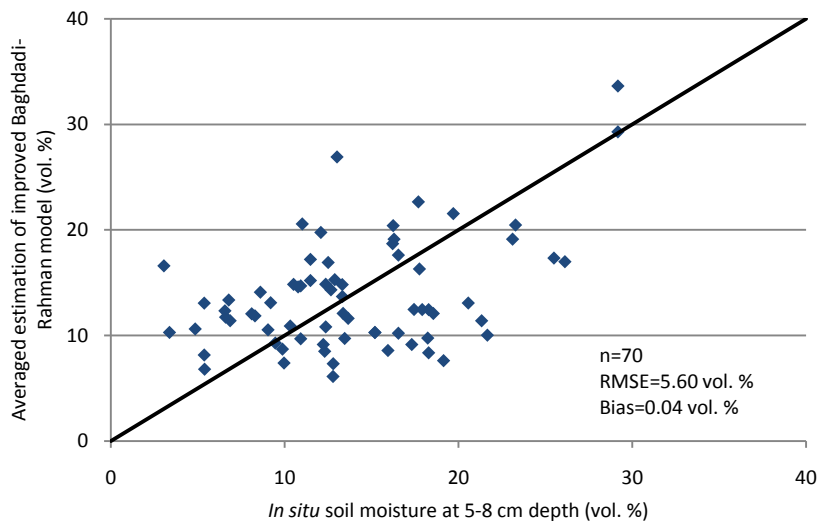


Figure 6.4 Averaged estimation from the improved Baghdad-Rahman model and in situ soil moisture at 5–8 cm depth.



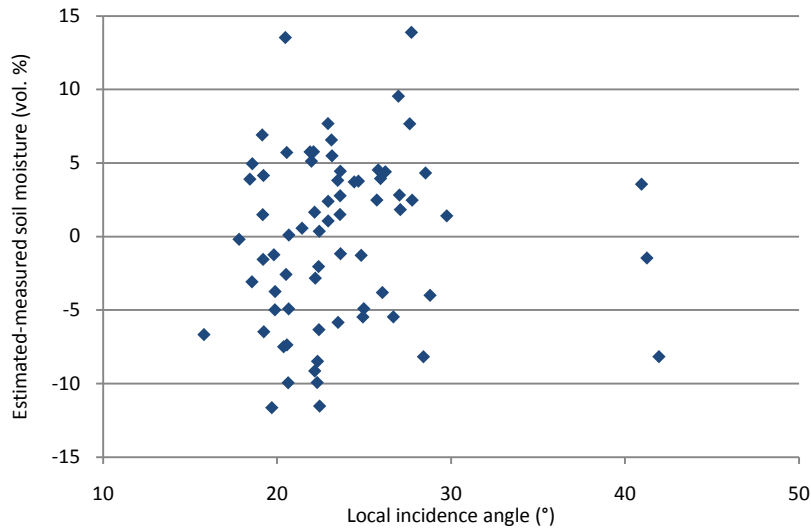


Figure 6.5 Estimated soil moisture errors and local incidence angle.

### 6.2.3. Application in crop fields

Applying the same approach to the crop fields, soil moisture estimations are compared with *in situ* measurements at 5–8 cm depth in Figure 6.6. A clear difference can be noticed for soil moisture conditions below and above 20 vol. % in terms of RMSE.

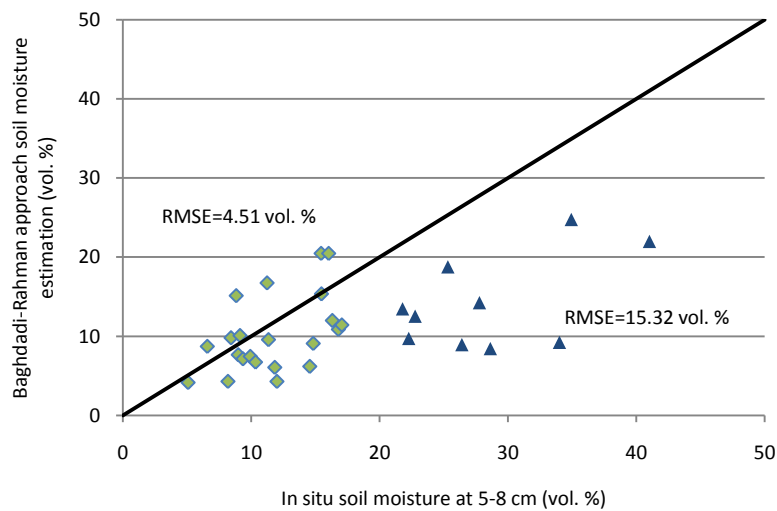


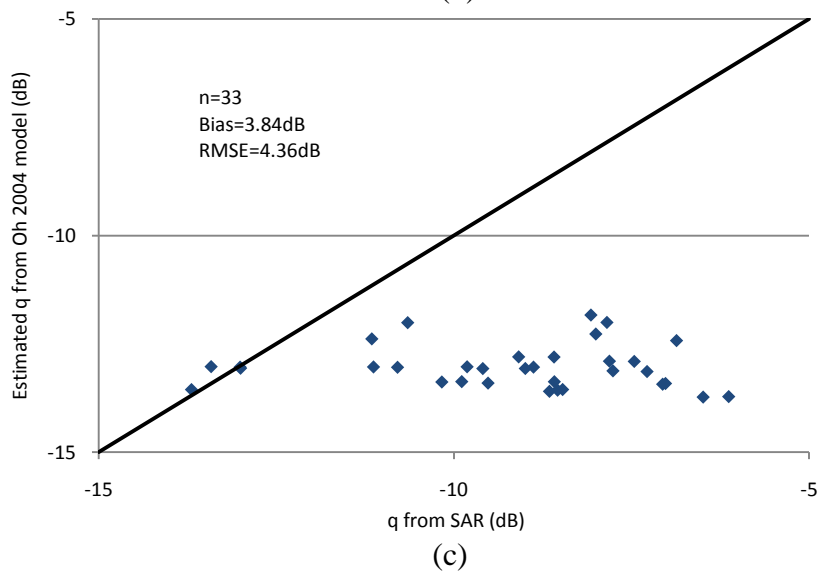
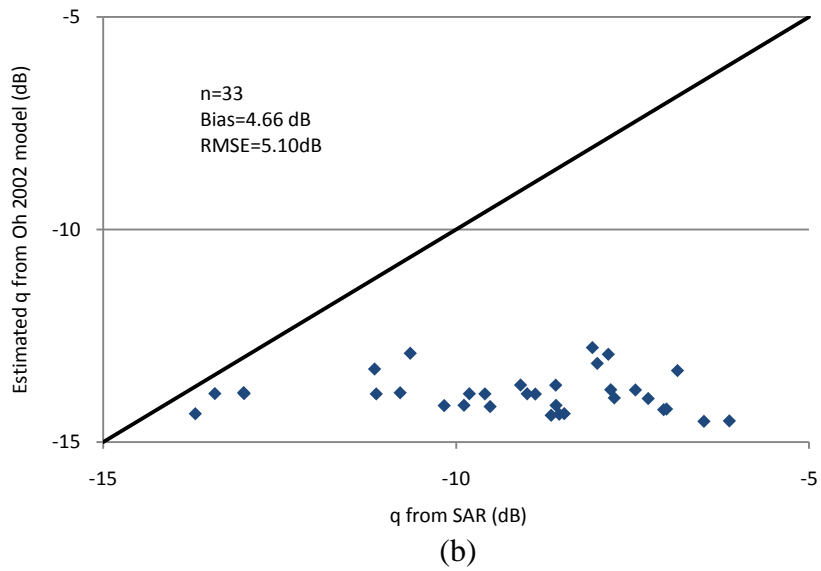
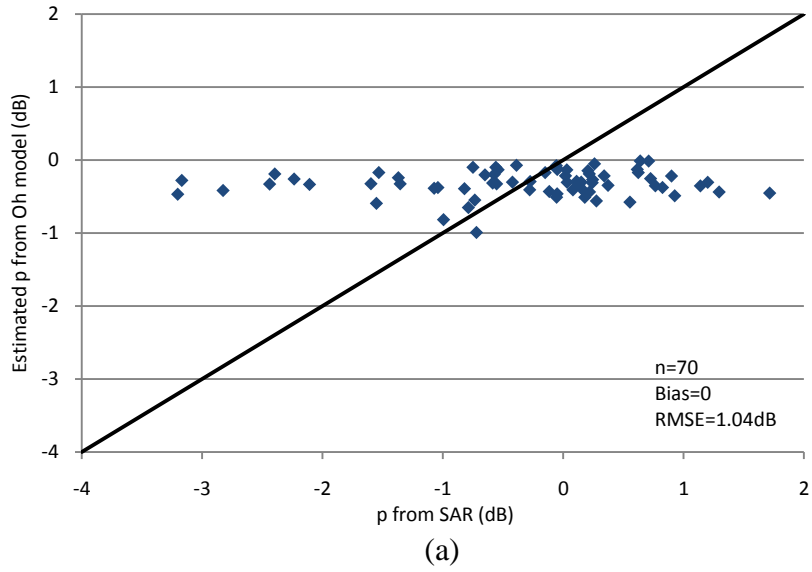
Figure 6.6 Soil moisture estimation from the Baghdadi-Rahman model and *in situ* soil moisture at 5–8 cm depth in crop fields, with separated RMSE for soil moisture lower than 20 vol. % and higher than 20 vol. %.

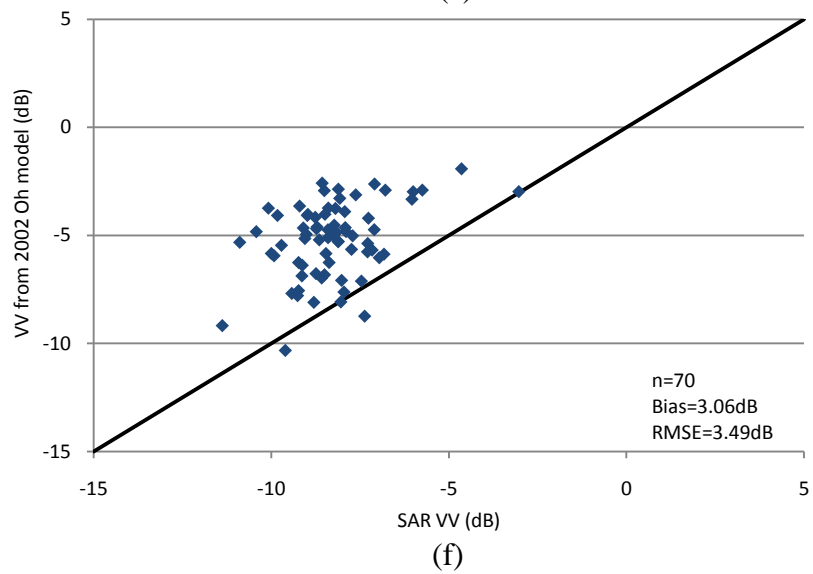
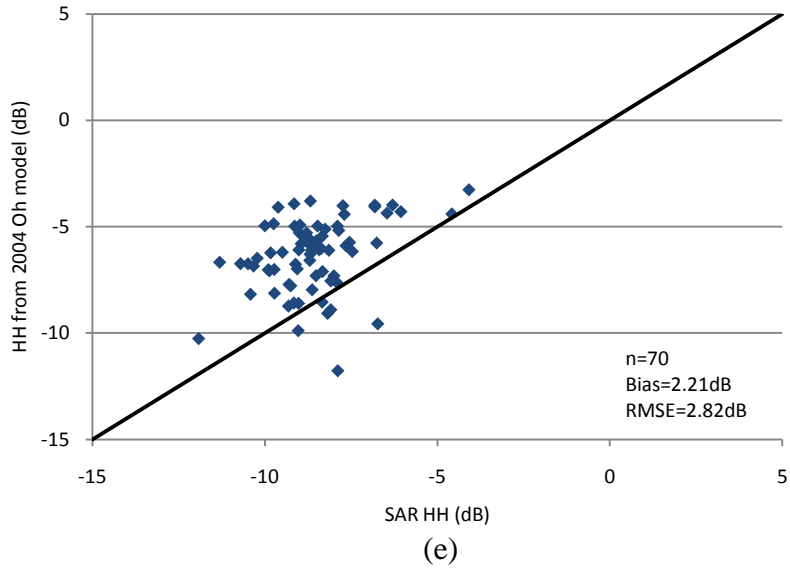
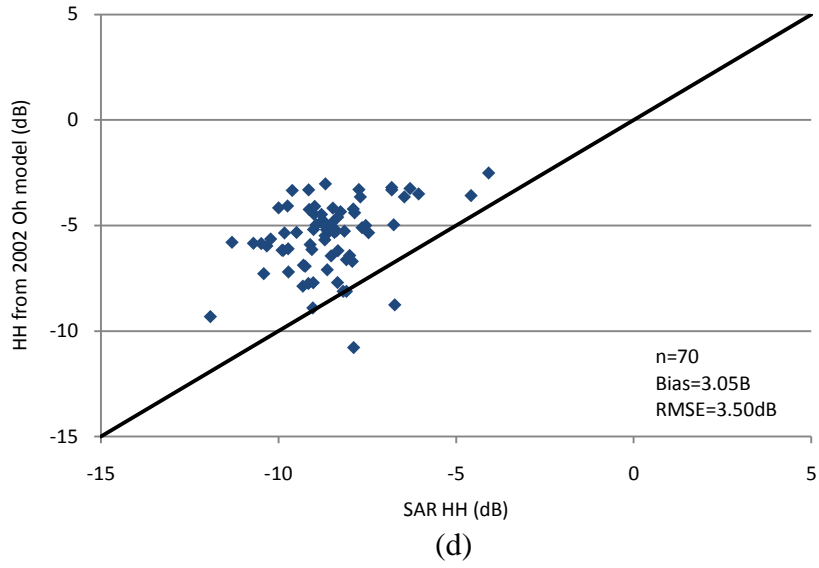
### 6.3. Evaluation of Baghdadi-Rahman Model

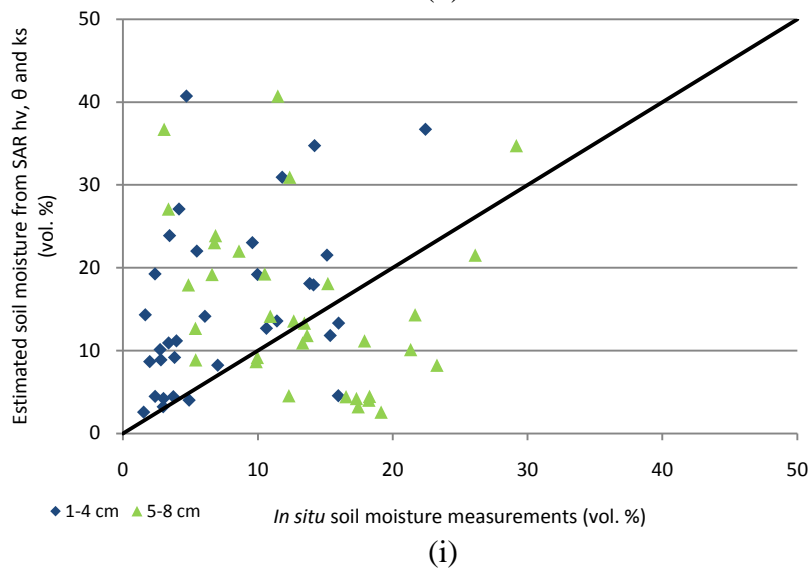
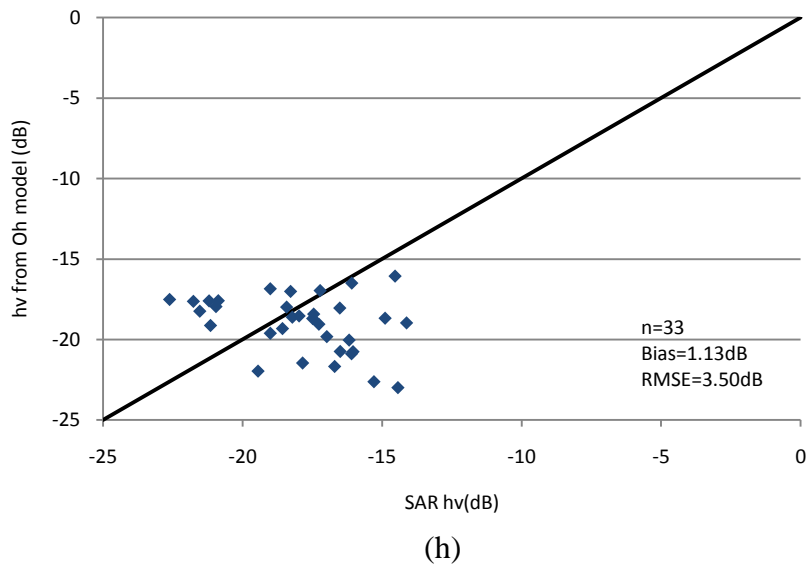
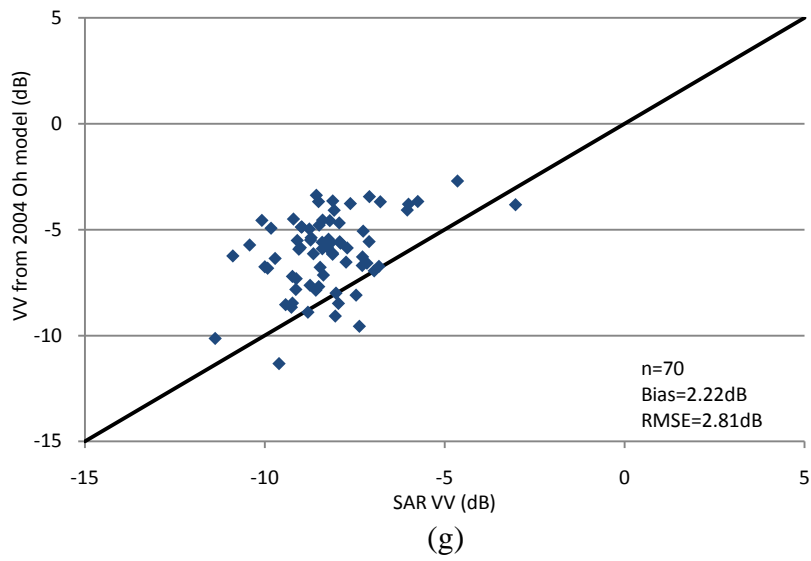
Surface soil moisture as well as rms height  $s$  and correlation length  $l$  can be estimated from the Baghdadi-Rahman model, which is based on the theoretical model, the AIEM. The aim of this study is to achieve an operational approach to invert surface soil moisture from SAR remote sensing over small bare fields in a semi-arid environment, and therefore roughness information is a parameter that must be considered in a conceptual way. The following part of the section will evaluate the proposed Baghdadi-Rahman model in terms of its by-product effective rms height  $ks$  and correlation length  $kl$ . The estimations of roughness parameters from Table 6.3 will be used as substituted input parameters to *in situ* measurements into the backscattering models used in Chapter 5 and the estimations from HH and VV polarisations are treated separately.

#### 6.3.1. Oh model

Figure 6.7 plots the performance of the Oh model (2002 and 2004 versions) after applying estimated rms height  $s$  and correlation length  $l$  from HH polarisation by using the proposed Baghdadi-Rahman model. Figure 6.7(a)–(j) shows the comparisons for the co-polarised ratio  $p$ , the cross-polarised ratio  $q$  using the 2002 version, the cross-polarised ratio  $q$  using the 2004 version,  $\sigma_{HH}^0$  using the 2002 version,  $\sigma_{HH}^0$  using the 2004 version,  $\sigma_{VV}^0$  using the 2002 version,  $\sigma_{VV}^0$  using the 2004 version,  $\sigma_{HV}^0$ ,  $m_v$  derived from  $\sigma_{HV}^0$  and  $m_v$  derived from  $\sigma_{VV}^0$ . Statistical comparisons between these results and the results using the *in situ* roughness measurements in terms of RMSE and bias are listed in Table 6.4 in section 6.3.1.3.







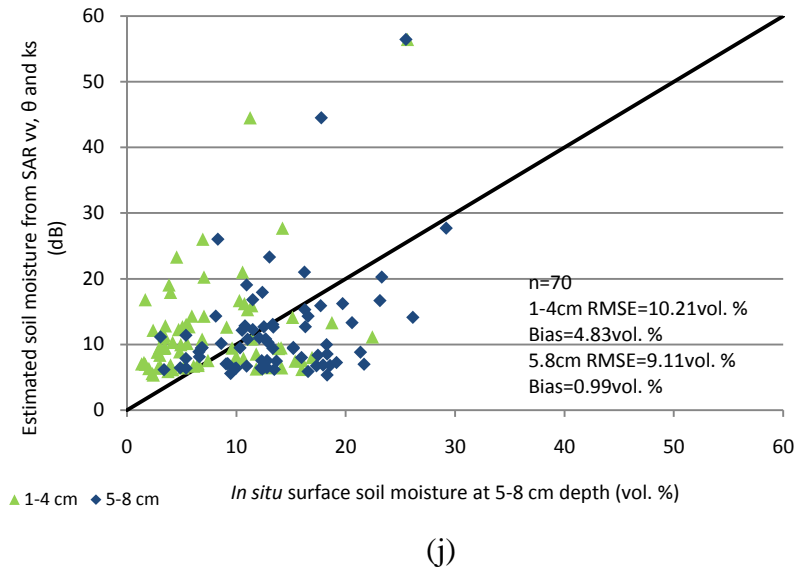
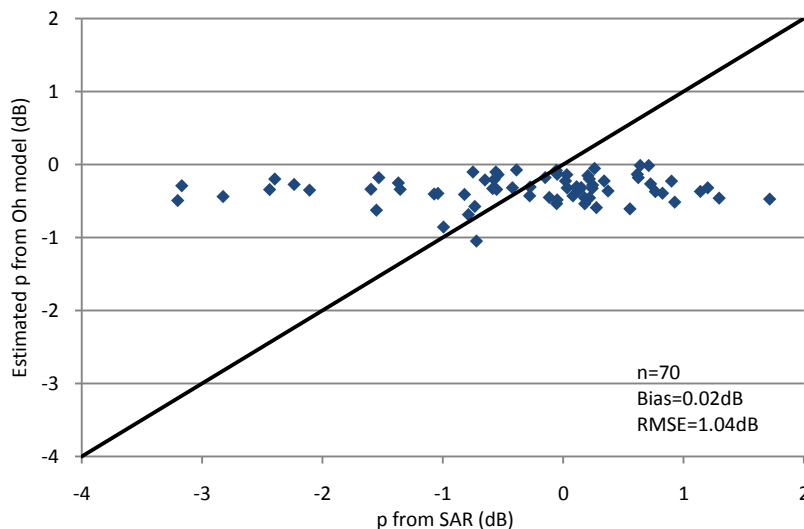
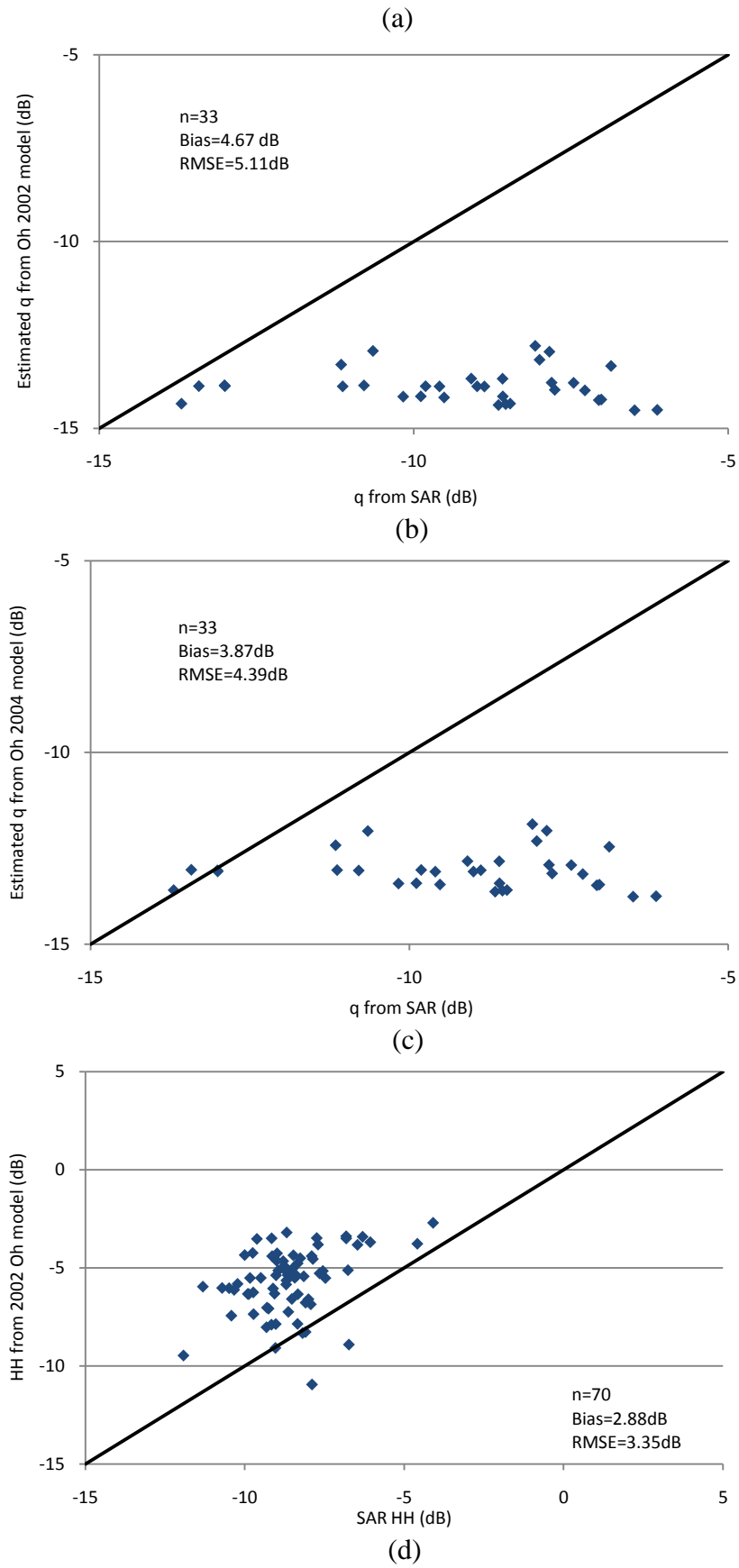
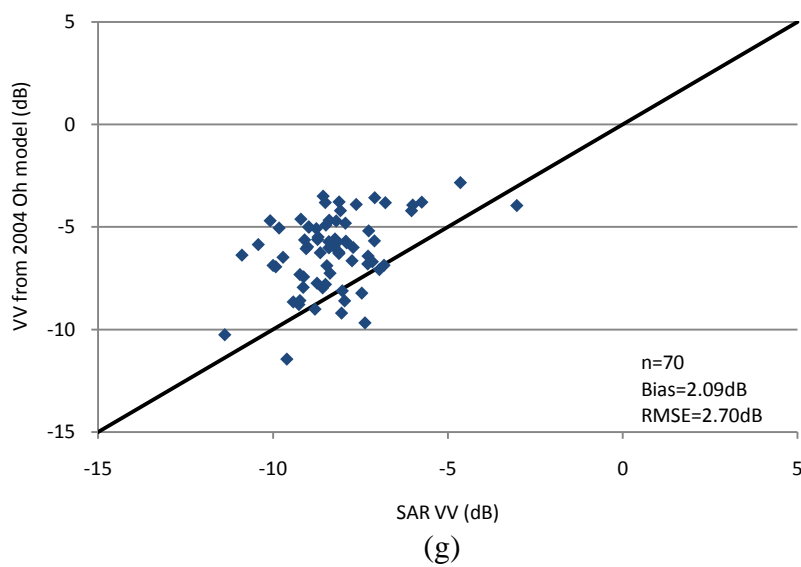
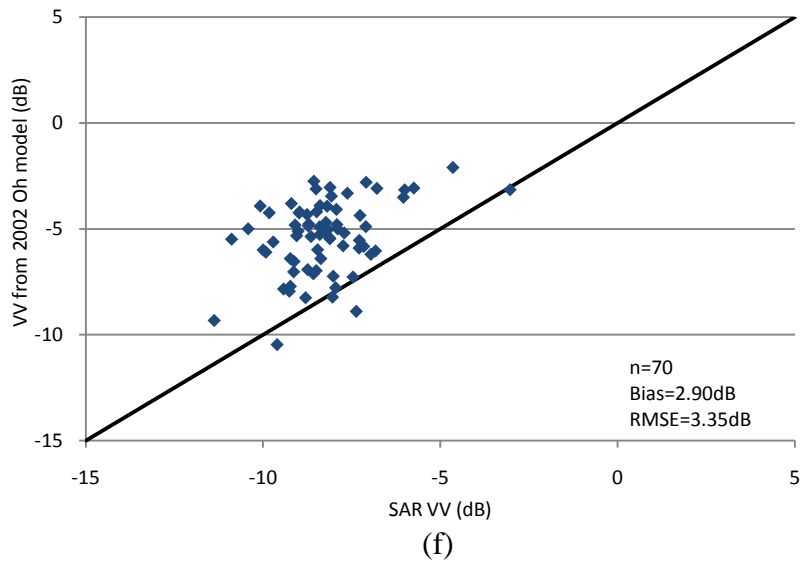
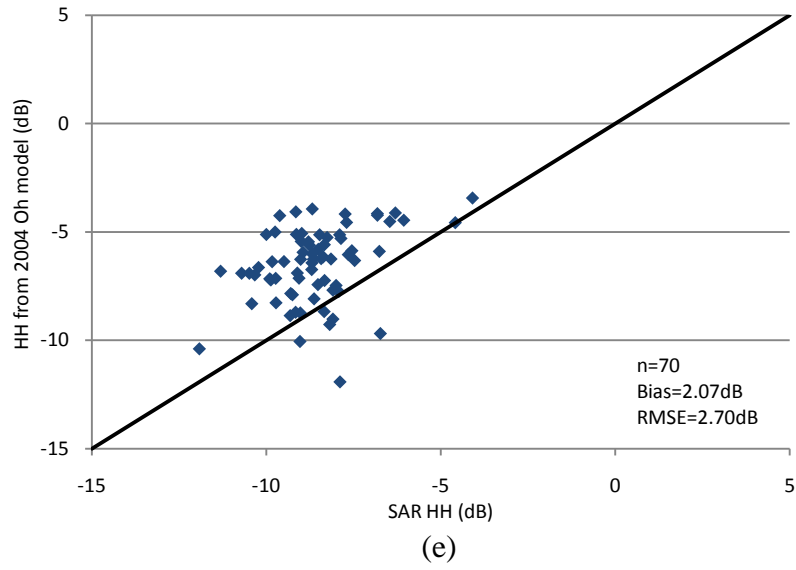


Figure 6.7 Oh model performance using estimated ks and kl from  $\sigma_{HH}^0$  using the Baghdadi-Rahman approach.

Figure 6.8 plots the performance of the Oh model (2002 and 2004 versions) after applying estimated rms height  $s$  and correlation length  $l$  from VV polarisation using the proposed Baghdadi-Rahman model. Figure 6.8(a)–(j) show the comparisons for the co-polarised ratio  $p$ , the cross-polarised ratio  $q$  using the 2002 version, the cross-polarised ratio  $q$  using the 2004 version,  $\sigma_{hh}^0$  using the 2002 version,  $\sigma_{hh}^0$  using the 2004 version,  $\sigma_{vv}^0$  using the 2002 version,  $\sigma_{vv}^0$  using the 2004 version,  $\sigma_{hv}^0$ ,  $m_v$  derived from  $\sigma_{hv}^0$  and  $m_v$  derived from  $\sigma_{vv}^0$ . Statistical comparisons between these results and the results using the *in situ* roughness measurements in terms of RMSE and bias are listed in Section 6.3.1.3.









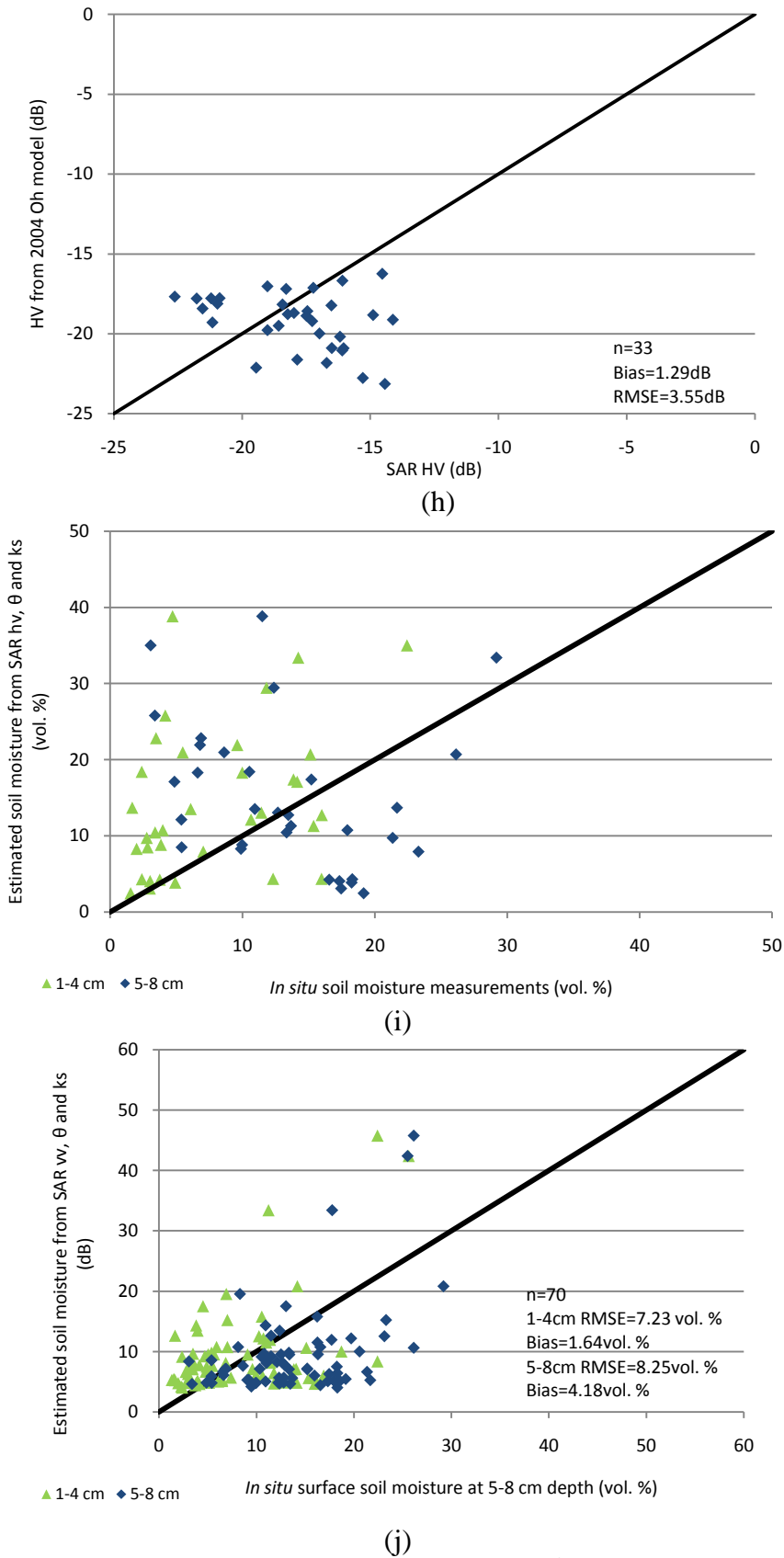


Figure 6.8 Oh model performance using estimated  $k_s$  and  $k_l$  from  $\sigma_{vw}^0$  using the Baghdadi-Rahman approach.

Table 6.4 compares Oh model products from co-polarised ratio  $p$ , the cross-polarised ratio  $q$  from both versions of the Oh model,  $\sigma_{HH}^0$  and  $\sigma_{VV}^0$  from both versions of the Oh model and  $\sigma_{HV}^0$  in dB and surface soil moisture estimations from  $\sigma_{HV}^0$  and  $\sigma_{VV}^0$  respectively in vol. %. Significant improvement in Oh model performance can be found in backscattering coefficient estimations and soil moisture estimation from  $\sigma_{HV}^0$ , with RMSE and bias reduced by ~1dB from the Oh model using *in situ* roughness measurement compared to using Baghdadi-Rahman model estimated roughness information. However, large RMSE and bias still exist in estimations of the cross-polarised ratio  $p$  and the co-polarised ratio  $q$ .

**Table 6.4 Comparison between Oh model performance using *in situ* roughness measurements and roughness estimations from Baghdadi-Rahman model in terms of RMSE and bias for the model products.**

Roughness source	<i>In situ</i> measurement		Baghdadi-Rahman model+ $\sigma_{HH}^0$		Baghdadi-Rahman model+ $\sigma_{VV}^0$	
	RMSE	Bias	RMSE	Bias	RMSE	Bias
p	1.03	0	1.04	0	1.04	0.02
q(2002)	4.86	4.39	5.10	4.66	5.11	4.67
q(2004)	4.15	3.58	4.36	3.84	4.39	3.87
$\sigma_{HH}^0(2002)$	4.44	4.05	3.50	3.05	3.35	2.88
$\sigma_{HH}^0(2004)$	3.68	3.18	2.82	2.21	2.70	2.07
$\sigma_{VV}^0(2002)$	4.31	3.93	3.06	3.49	3.35	2.90
$\sigma_{VV}^0(2004)$	3.57	3.06	2.81	2.22	2.70	2.09
$\sigma_{HV}^0$	3.08	0.06	3.50	1.13	3.35	1.29
$m_v$ from $\sigma_{HV}^0$	14.12	1.69	13.35	2.01	12.84	1.32
$m_v$ from $\sigma_{HV}^0$	8.64	2.03	9.11	0.99	8.25	4.18

### 6.3.2. AIEM

Backscattering coefficients are simulated based on the following parameters: both the real part and the imaginary part of the dielectric constant is calculated empirically from *in situ* soil moisture measurements at 5–8 cm depth (Hallikainen et al. 1985) and estimated  $ks$  and  $kl$  from the Baghdadi-Rahman model (Table 6.3). Noting that as 10 samples are used in the model assessment for deriving  $ks$  and  $kl$  (Table 6.2), the corresponding data are excluded in the following evaluation. Therefore the total number of samples is reduced from 70 to 60. Figure 6.9(a) and (b) compare the backscattering coefficients derived from SAR imagery and simulated by the AIEM, where roughness estimations from HH and VV polarisations are employed separately. For a number of 60 samples,

roughness estimations from HH and VV polarisations yield very close results. In both cases, the RMSE and bias are marginally smaller for simulated VV polarisation than for simulated HH polarisation. The best result is achieved by using estimated roughness from VV polarisation using the Baghdadi-Rahman model for simulating VV polarisation backscattering coefficients for SAR imagery with RMSE and bias of 2.39dB and 0.85dB respectively.

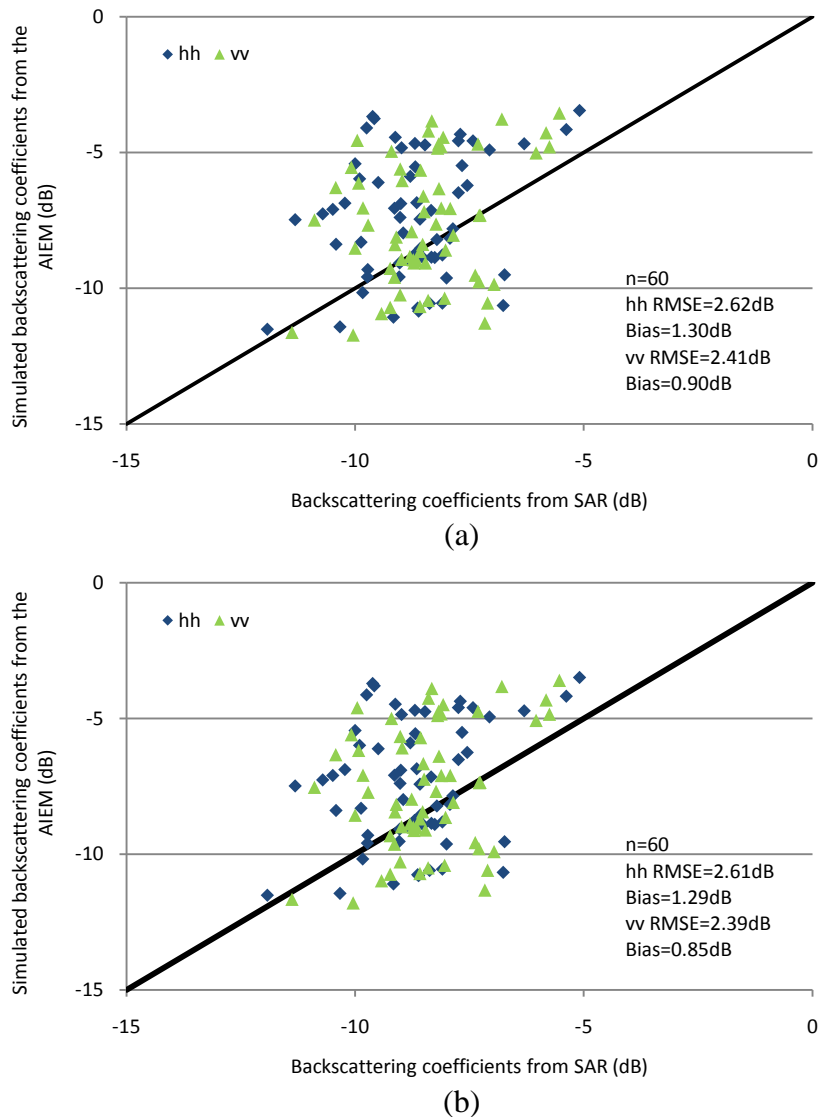


**Figure 6.9** Baghdadi-Rahman model evaluation through backscattering coefficient comparison between values derived from SAR imagery and simulated by the AIEM using in situ soil moisture values at 5–8 cm depth and estimated roughness ((a) from HH polarisation and (b) from VV polarisation) using the Baghdadi-Rahman model.

Table 6.5 compares all backscattering coefficient simulations using the AIEM in this study in terms of the RMSE, the bias, the Leave-One-Out-Cross-Validation (LOOCV) RMSE and the Nash-Sutcliffe model efficiency coefficient  $E$ . The averaged RMSE after the LOOCV are equal to the normal RMSE. It also shows that when using the roughness information from estimations of the Baghdadi-Rahman model, the RMSE and the bias are reduced by 0.6dB and over 1dB respectively compared to the AIEM simulation using *in situ ks* and *kl*, irrespective of the polarisation. However, the most accurate backscattering coefficient simulation is still achieved by using measured *ks* and the empirical correlation length  $l_{opt}$  as listed in the last column.

**Table 6.5 Comparison between all backscattering coefficient simulations using the AIEM.**

AIEM adopted roughness source	Estimations from Baghdadi-Rahman model+ $\sigma_{HH}^0$	Estimations from Baghdadi-Rahman model+ $\sigma_{VV}^0$	<i>In situ ks and kl</i>	Measured <i>ks</i> and $l_{opt}$	
$\sigma_{HH}^0$	RMSE	2.62	2.61	3.29	1.63
	Bias	1.30	1.29	2.71	0.25
	LOOCV	2.62	2.61	3.28	1.63
	Nash-Sutcliffe	-3.33	-3.29	-6.59	-0.86
$\sigma_{VV}^0$	RMSE	2.41	2.39	3.00	1.82
	Bias	0.90	0.85	2.38	0.95
	LOOCV	2.41	2.39	3.00	1.82
	Nash-Sutcliffe	-3.10	-3.03	-5.98	-1.59

## 6.4. Sensitivity Analysis

The models in section 6.3 are all based on the theoretical model. To determine the backscattering coefficient simulation, errors can be contributed to the AIEM by errors of the following parameters for C-band signal: rms height  $s$ , correlation length  $l$  and surface soil moisture  $m_v$ , for different incidence angles and polarisations. Therefore, a sensitivity analysis is necessary to help understand the AIEM performance through quantifying the sensitivity of the simulated backscattering coefficient to the surface geophysical parameters, according to different incidence angles and polarisations.

### 6.4.1. Parameterisation of the AIEM simulation

The average amount of proportion of sand (50%) and clay (27%) of the four bare fields is used for transforming the dielectric constant from soil moisture and they are assumed

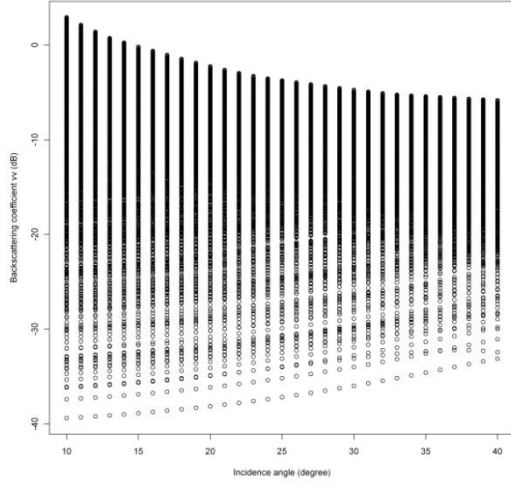
to represent the general soil texture (loam) over the region in the following AIEM simulations. For the roughness parameters, the rms height  $s$  is set ranging from 0.5 cm to 4 cm with 0.5 cm as a step and the correlation length  $l$  is set ranging from 1 cm to 40 cm with 1 cm as a step. The surface soil moisture  $m_v$  is set ranging from 3 vol. % to 30 vol. % with 3 vol. % as a step. Each valid value of these three parameters is used to create full possibility combinations of surface geophysical situations. Backscattering coefficients for co-polarisations for the range of incidence angle of  $10^\circ$  to  $45^\circ$  are simulated.

#### **6.4.2. Description of the AIEM simulation**

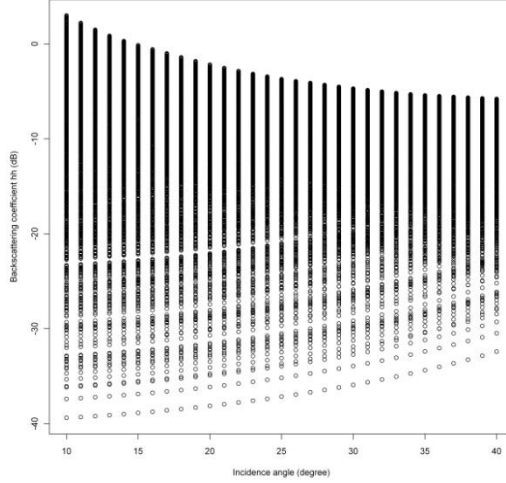
The relationships between radar backscattering coefficients and surface geophysical parameters as well as incidence angle (in the proposed ranges) are plotted in Figure 6.10. In general, both co-polarisations have similar performance compared to those parameters. The sensitivity of the backscattering coefficients on these different factors is summarised as follows:

- 1) For the range  $10^\circ \leq \theta \leq 40^\circ$ , backscattering coefficients become less sensitive when incidence angle increases. Peak values of backscattering coefficients are reduced with increase of incidence angle. When  $\theta = 40^\circ$ , backscattering coefficients are the least sensitive to other factors;
- 2) For correlation length shorter than ca. 10 cm, backscattering coefficients become less sensitive when the correlation length increases, where backscattering coefficients increase with  $l$ , while the sensitivity increases slightly with the correlation length when  $l \geq 10$  cm. Similarly, backscattering coefficients are the least sensitive to other factors when  $l \geq 10$  cm;
- 3) For surface soil moisture, the backscattering coefficients are most sensitive in dry regions, while they become much less sensitive when  $m_v \geq$  ca. 20 vol. %. For the whole range of surface soil moisture, backscattering coefficients have equivalent sensitivity to other factors. It is also clear that backscattering coefficients increase with surface soil moisture in the whole range of 3 vol. % to 30 vol. %;
- 4) Backscattering coefficients are very sensitive to rms height  $s$  in the whole range. Backscattering coefficients are the least sensitive to other factors when  $s = 1$  cm. Backscattering coefficients increase with  $s$  when  $s < 1$  cm and decrease with  $s$

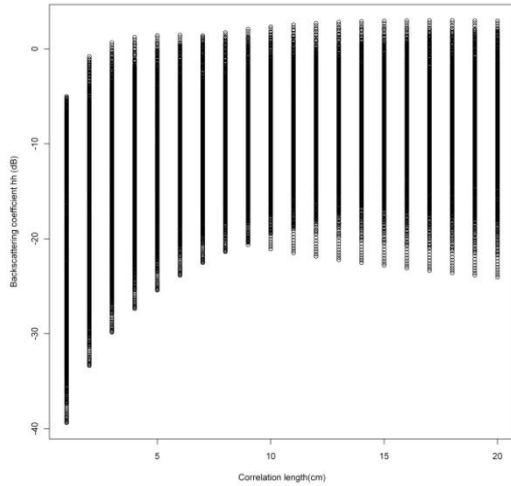
when  $s > 1$  cm. Backscattering coefficients become slightly more sensitive to other factors with  $s$  increases.



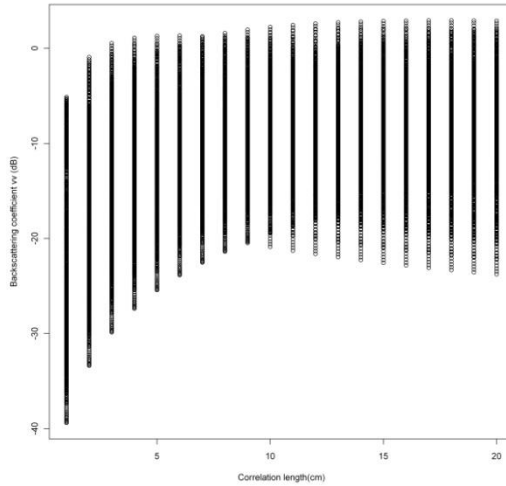
(a)



(b)



(c)



(d)

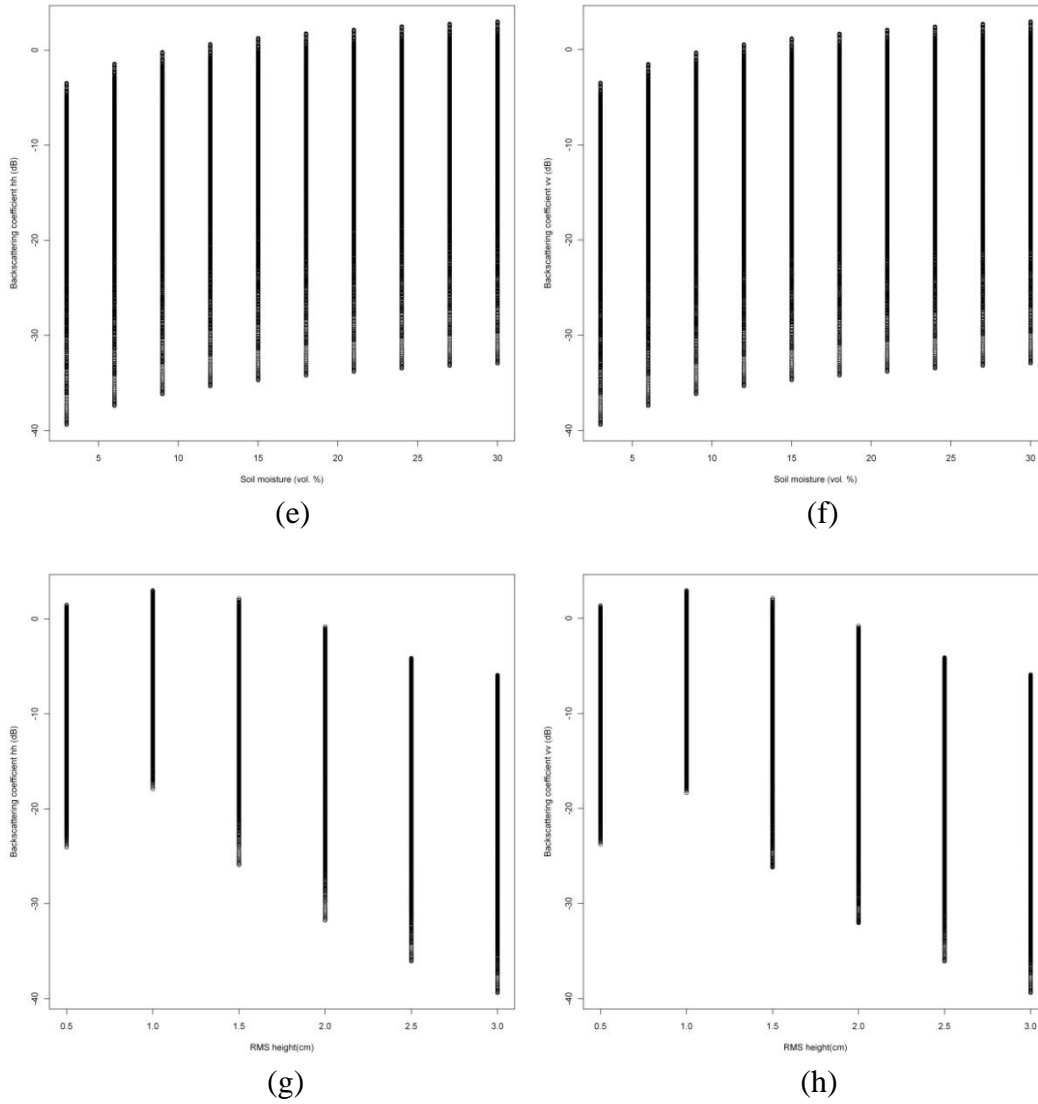


**Figure 6.10 Relationships between (a) incidence angle  $\vartheta$  and  $\sigma_{HH}^0$ ; (b) incidence angle  $\vartheta$  and  $\sigma_{VV}^0$ ; (c) correlation length  $l$  and  $\sigma_{HH}^0$ ; (d) correlation length  $l$  and  $\sigma_{VV}^0$ ; (e) surface soil moisture  $m_v$  and  $\sigma_{HH}^0$ ; (f) surface soil moisture  $m_v$  and  $\sigma_{VV}^0$ ; (g) rms height  $s$  and  $\sigma_{HH}^0$  and (h) rms height  $s$  and  $\sigma_{VV}^0$  plotted from the AIEM simulation.**

### 6.4.3. Impact factor

In addition to the qualitative analysis of backscattering coefficient sensitivity to surface geophysical parameters and incidence angle, it would also be helpful to conduct a quantitative sensitivity analysis. An index  $\zeta$  to quantify the impact of incidence angle  $\theta$  on backscattering coefficient  $\sigma_{pq}^0$  is introduced as:

$$\xi_{(\theta,pq)} = \Delta\theta/\Delta\sigma_{pq}^0$$

**6.5**

where  $pq$  denotes the transferred and received polarisations respectively, i.e. HH or VV. For the other factor,  $\alpha$ , its impact on backscattering  $\sigma_{pq}^0$  can be expressed by substituting  $\theta$  by  $\alpha$  in the numerator of Equation 6.5. By the definition, the mean and two percentiles – 95.4<sup>th</sup> and 68.2<sup>th</sup> percentiles of the index  $\xi$  of incidence angle  $\theta$ , rms height  $s$ , correlation length  $l$  and soil moisture  $m_v$  to  $\sigma_{HH}^0$  and  $\sigma_{VV}^0$  are listed in Table 6.6:

- 1) Soil moisture has a similar impact of just above 6 vol. %/dB on backscattering coefficients from both co-polarisations on average with about 9 vol. %/dB and 12 vol. %/dB as 68.2<sup>th</sup> and 95.4<sup>th</sup> percentiles;
- 2) The average impact factor  $\xi$  of incidence angle  $\theta$  is slightly larger on HH polarisation than on VV polarisation. However, the 95.4<sup>th</sup> percentile is extremely large as between 28 and 30 degree/dB for HH and VV polarisations while the 68.2<sup>th</sup> percentiles are about 5.5 degree/dB for both co-polarisations;
- 3) For rms height  $s$ , the mean of impact factor  $\xi$  is low from both co-polarisations. Both 95.4<sup>th</sup> and 68.2<sup>th</sup> percentiles are close for both HH and VV polarisations as about 1.08 cm/dB and 0.09 cm/dB respectively;
- 4) The mean values of the impact factor of correlation length are similar but larger percentile values are seen, about 11.78 cm/dB and 1.75 cm/dB for 95.4<sup>th</sup> and 68.2<sup>th</sup> percentiles respectively.

**Table 6.6 Statistics of the impact factor  $\xi$  of incidence angle  $\theta$ , rms height  $s$ , correlation length  $l$  and soil moisture  $m_v$  on backscattering coefficients of HH and VV polarisations.**

Impact factor $\xi$	Polarisation	Mean	95.4 <sup>th</sup> percentile	68.2 <sup>th</sup> percentile
Incidence angle (degree/dB)	HH	4.53	28.01	5.42
	VV	3.49	30.03	5.56
rms height (cm/dB)	HH	0.06	1.12	0.09
	VV	-0.47	1.05	0.09
Correlation length (cm/dB)	HH	-0.59	11.94	1.73
	VV	0.21	11.71	1.76
Soil moisture (vol. %/dB)	HH	6.49	12.39	8.97
	VV	6.31	12.15	8.51



## 6.5. Summary

The Baghdadi-Rahman model, which couples the empirical correlation length to the Rahman approach and the AIEM, is proposed in this chapter. Several advantages are achieved in the new model, which 1) follows the original Rahman approach, eliminates the problematic input surface roughness parameters as in conventional semi-empirical models, while requiring no auxiliary data from *in situ* measurements; 2) successfully reduces the SAR image requirements from three images in different surface geophysical conditions to one/two image(s) in extremely dry conditions only; 3) hence successfully overcomes the limitation on incidence angle differences between available SAR images; and 4) reduces the computational requirement for model coefficient regression. To achieve better model estimations, two treatments are used by 1) averaging backscattering coefficient values from two instead of one image in extremely dry conditions and 2) averaging model productions from HH and VV polarisations. The model is evaluated against *in situ* soil moisture measurements with the best performance of soil moisture estimation at an accuracy of 5.60 vol. % and a bias of only 0.04 vol. %. By applying this to crop fields, the model proves its capability in the relatively late phenological stages, when soil moisture conditions are also drier, for wheat, bean and canola fields with a high accuracy of 4.51 vol. %.

To evaluate the Baghdadi-Rahman model, its by-product rms height  $s$  and correlation length  $l$  are used as input instead of *in situ* roughness measurements as in the Oh model and the AIEM model. By comparing estimations of backscattering coefficients and surface soil moisture from co-polarisations from the Oh model, results are improved in terms of the RMSE, reduced by about 1dB for backscattering coefficients and 1 vol. % for soil moisture estimations. Further evaluation is conducted by implementing the estimated  $s$  and  $l$  for the AIEM parameterisation. The results of four sets of roughness parameters are inter-compared – estimated  $s$  and  $l$  from  $\sigma_{HH}^0$  and  $\sigma_{VV}^0$  using the Baghdadi-Rahman model, *in situ* roughness measurement and measured  $s$  coupling the empirical correlation length. Four statistical parameters are adopted for assessment, including the RMSE, bias, LOOCV and Nash-Sutcliffe. Among the results, using modelled roughness parameters, the AIEM yields significantly better results than using *in situ*  $ks$  and  $kl$ . However, the results using the empirical correlation length are still the best. This

can be explained by the average error of about 25% for rms height introduced into the Baghdadi-Rahman model compared to the *in situ* measurement.

Sensitivity analysis is conducted through the backscattering simulations by the AIEM in different surface scenarios over the ranges  $10^\circ \leq \theta \leq 40^\circ$ ,  $0.5 \leq s \leq 4$  cm,  $1 \leq l \leq 40$  cm and  $3 \text{ vol. \%} \leq m_v \leq 30 \text{ vol. \%}$ . It is found the backscattering coefficient sensitivity reduces with incidence angle. In general, the backscattering coefficient is more sensitive in drier conditions than in wetter conditions. Two sections are found in the whole range, while the sensitivity drops more quickly when  $m_v \leq \text{ca. } 20 \text{ vol. \%}$  than  $m_v > \text{ca. } 20 \text{ vol. \%}$ . The result also suggests that two thresholds of rms height  $s$  and correlation length  $l$  need to be taken into account for backscattering coefficient sensitivity, which are  $s = \text{ca. } 1 \text{ cm}$  ( $ks = \text{ca. } 1.11$  for C-band) and  $l = \text{ca. } 10 \text{ cm}$  ( $kl = \text{ca. } 11.1$ ). Backscattering coefficients are least sensitive near the thresholds. Further effort is conducted by introducing an impact index  $\zeta$  to quantify the sensitivity. The mean, 95.4<sup>th</sup> percentile and 68.2<sup>th</sup> percentile of the impact factor are given in Table 6.6. According to the mean impact factors, an accuracy of about  $4^\circ$  for incidence angle, about 0.5 cm for rms height and correlation length, a confidence of backscattering coefficient within 1dB can be simulated by the AIEM, which leads to a soil moisture accuracy of about 6 vol. %. However, these conditions vary significantly due to the large variance found in the impact factor.

Life is finite,  
while knowledge is infinite.

---Zhuang Zi

## Chapter 7 Conclusion and Outlook

### 7.1. Conclusions

This study explores an operational approach for surface soil moisture retrieval on agricultural lands for small-scale hydrological modelling in a semi-arid environment. The *Azienda San Michele* is chosen as the study site, on the island of Sardinia, a typical Mediterranean semi-arid but intensive agricultural area, where in particular four bare fields and five crop fields are prepared for intensive *in situ* and SAR observation through the year 2008–2009.

*In situ* observation is still regarded as the fundamental approach for geographic studies. Historical climate data have proved that Sardinia suffers from dry and hot summers. Under various climate change scenarios, the increasingly strong requirement especially for agricultural purposes magnifies the water scarcity and imbalance in the region of Sardinia. In this context, meteorological observations show a large variance in precipitation over the study area in May during the two-year study period, which then leads to significant differences in air temperature and hence surface soil moisture. In addition, a wide range of surface soil moisture, from totally dry to nearly 30 vol. %, is covered during the field trips. Within this range, an average difference of 10 vol. % can be identified between two different fields, which are separated by only a few hundred metres. Occasional rainfall events will further contribute to the temporal and spatial surface soil moisture variability. Therefore, an accurate and, more importantly, high temporal and spatial resolution observation and monitoring for surface soil moisture is crucial for a small-scale hydrological model and thus to support a well-grounded irrigation strategy in this water scarce agricultural region.

For *in situ* roughness measurements, the ability of the close-range digital photogrammetry technique for rms height estimation was approved because of its low in-field

variability. In addition, rms height varies little during the summer when precipitation is limited. However, much larger spatial variances are found on each field for correlation length estimation either for exponential ACF – 11%–46% – or for Gaussian ACF – 7%–42%. The observation scale of the adopted photogrammetry system is insufficient for the study at field scale.

For a timely and cost-effective operational approach to monitoring and mapping surface soil moisture, various existing semi-empirical and theoretical models are adopted to assess their capability in surface soil moisture retrieval from SAR observation at field scale. The empirically based linear relationship between surface soil moisture and SAR backscattering coefficients is reassessed against both co-polarisations and different available ranges of incidence angle. For drier conditions, in agreement with the theoretical study on EM penetration (Ulaby et al. 1996), the soil moisture measured at 5–8 cm depth presents better correlation with backscattering coefficients especially for HH polarisation, compared to corresponding soil moisture values at shallow layer, 1–4 cm depth.

The Dubois model is limited in its validity especially on SAR geometry and thus is not applicable in this study or further for an operational approach. Similar to the performance of the Dubois model, an overestimation of about 2–4dB is observed from simulated backscattering coefficients compared to SAR retrievals by using two versions of the Oh model. The cross-polarisation agrees well in terms of bias. From the theoretical model – the AIEM – empirical correlation length developed by Baghdadi et al. (2006a) proved to be a good substitution when insufficient *in situ* correlation length is available for model parameterisation and hence can be used for an operational approach when rms height can be accurately retrieved through remote sensing techniques. In this case, a confidence of about 6 vol. % can be achieved by using the AIEM and empirical correlation length from dual co-polarisations. The AIEM sensitivity analysis, along with the poor results of both backscattering simulation and soil moisture estimation from models based on *in situ* based parameterisation, reinforced the importance of precise roughness parameterisation, especially for correlation length.

A hybrid Baghdadi-Rahman model is developed to overcome limitations of the existing Rahman model but maintain its capability as an operational approach. With one or more

SAR images under the extremely dry conditions prevailing, surface soil moisture can be inverted with confidence of between 5–6 vol. % at field scale, regardless of SAR geometry. Further evaluation has proved the model's capability in conditions when surface soil moisture is less than 20 vol. %, and thus this model is feasible for providing crucial and promising soil moisture information in the dry season for hydrological modelling parameterisation. Surface soil moisture is mapped for a sample region in Appendix B.

Overall, it is operationally valid to adopt the AIEM-based model to estimate surface soil moisture (at 5–8 cm depth level) with a confidence of 5–6 vol. % over agricultural fields at field scale on a weekly basis from co-polarisation C-band SAR in the semi-arid environment.

## **7.2. Outlook**

The work successfully provides an operational approach for surface soil moisture inversion at small field scale from C-band SAR imagery in the semi-arid environment. Based on this approach, several developments can be foreseen.

From the technical point of view, errors from inverted surface roughness cannot be ignored. First, further utilisation of full-polarised data for an accurate roughness inversion is necessary based on various decomposition methods (**Cloude and Pottier 1996; Hajnsek et al. 2003**) or the recently advanced effective roughness modelling approach (**Lievens et al. 2011**). This is essentially useful for areas where surface roughness changes significantly, due to either natural or human intervention, during satellite passes. Second, further investigation in the capability of the photogrammetric technique on characterising surface roughness at field scale is required as a better reference database for model product evaluation. Last but not least, the shape of the ACF is also one difficult but important parameter in roughness characterisation, especially for parameterising the theoretical models.

For a robust approach to soil moisture inversion on agricultural lands, extensive studies are required on more diverse crop fields and a combined method is recommended based

on *e.g.* (**Hajnsek et al. 2009; Gherboudj et al. 2011**). Overall, an additional database is needed for further verification of the Baghdadi-Rahman approach.

From the application point of view, studies have demonstrated that the limited depth of surface soil moisture can be assimilated into land surface models and result in soil moisture at a much deeper profile (*e.g.* (**Houser et al. 1998; Reichle et al. 2002; Walker et al. 2002**)), although a great challenge exists in down- and up-scaling applications (**Bittelli 2011**). Furthermore, information on the model's impacts on irrigation management through small-scale hydrological modelling coupled with soil moisture information at deeper profiles is required. The timely and accurate surface soil moisture monitor at field scale and over large areas from various SAR sensors from the proposed Baghdadi-Rahman model, along with well integrated hydrological model and economics and policy based assessment, *e.g.* (**Storm et al. 2011; Tsai et al. 2011**) for irrigation management, will contribute to the future for sustainable water resource management for agricultural usage in the water scarce semi-arid environment within the CLIMB framework.

---

## References

1. Abu-Zreig, M. M., A. Tamimi & A. A. Alazba (2011) Soil Erosion Control and Moisture Conservation of Arid Lands with Stone Cover. *Arid Land Research and Management*, 25, 294-307.
2. Alvarez-Mozos, J., J. Casali, M. Gonzalez-Audicana & N. E. C. Verhoest (2006) Assessment of the Operational Applicability of Radarsat-1 Data for Surface Soil Moisture Estimation. *Geoscience and Remote Sensing, IEEE Transactions on*, 44, 913-924.
3. Alvarez-Mozos, J., N. Verhoest, A. Larranaga, J. Casali & M. Gonzalez-Audicana (2009) Influence of Surface Roughness Spatial Variability and Temporal Dynamics on the Retrieval of Soil Moisture from Sar Observations. *Sensors*, 9, 463-489.
4. Arnell, N. W. (2004) Climate Change and Global Water Resources: Sres Emissions and Socio-Economic Scenarios. *Global Environmental Change-Human and Policy Dimensions*, 14, 31-52.
5. Baghdadi, N. 2011. Personal Communication.
6. Baghdadi, N., J. Abou Chaaya & M. Zribi (2011a) Semiempirical Calibration of the Integral Equation Model for Sar Data in C-Band and Cross Polarization Using Radar Images and Field Measurements. *Ieee Geoscience and Remote Sensing Letters*, 8, 14-18.
7. Baghdadi, N., M. Aubert, O. Cerdan, L. Franchisteguy, C. Viel, E. Martin, M. Zribi & J. F. Desprats (2007) Operational Mapping of Soil Moisture Using Synthetic Aperture Radar Data: Application to the Touch Basin (France). *Sensors*, 7, 2458-2483.
8. Baghdadi, N., N. Boyer, P. Todoroff, M. El Hajj & A. Begue (2009) Potential of Sar Sensors Terrasar-X, Asar/Envisat and Palsar/Alos for Monitoring Sugarcane Crops on Reunion Island. *Remote Sensing of Environment*, 113, 1724-1738.
9. Baghdadi, N., P. Camus, N. Beaugendre, O. M. Issa, M. Zribi, J. F. Desprats, J. L. Rajot, C. Abdallah & C. Sannier (2011b) Estimating Surface Soil Moisture from Terrasar-X Data over Two Small Catchments in the Sahelian Part of Western Niger. *Remote Sensing*, 3, 1266-1283.
10. Baghdadi, N., O. Cerdan, M. Zribi, V. Auzet, F. Darboux, M. El Hajj & R. B. Kheir (2008) Operational Performance of Current Synthetic Aperture Radar Sensors in Mapping Soil Surface Characteristics in Agricultural Environments: Application to Hydrological and Erosion Modelling. *Hydrological Processes*, 22, 9-20.
11. Baghdadi, N., R. Cresson, P. Todoroff & S. Moinet (2010) Multitemporal Observations of Sugarcane by Terrasar-X Images. *Sensors*, 10, 8899-8919.
12. Baghdadi, N., N. Holah & M. Zribi (2006a) Calibration of the Integral Equation Model for Sar Data in C-Band and Hh and Vv Polarizations. *International Journal of Remote Sensing*, 27, 805-816.
13. --- (2006b) Soil Moisture Estimation Using Multi-Incidence and Multi-Polarization Asar Data. *International Journal of Remote Sensing*, 27, 1907-1920.
14. Baghdadi, N., C. King, A. Bourguignon & A. Remond (2002) Potential of Ers and Radarsat Data for Surface Roughness Monitoring over Bare Agricultural Fields: Application to Catchments in Northern France. *International Journal of Remote Sensing*, 23, 3427-3442.
15. Baghdadi, N., P. Paillou, G. Grandjean, P. Dubois & M. Davidson (2000) Relationship between Profile Length and Roughness Variables for Natural Surfaces. *International Journal of Remote Sensing*, 21, 3375-3381.

16. Bailey, R. J., S. J. Groves & E. Spackman (1996) A Model for Estimating Soil Moisture Changes as an Aid to Irrigation Scheduling and Crop Water-Use Studies: Ii. Field Test of the Model. *Soil Use and Management*, 12, 129-133.
17. Bastiaanssen, W. G. M., D. J. Molden & I. W. Makin (2000) Remote Sensing for Irrigated Agriculture: Examples from Research and Possible Applications. *Agricultural Water Management*, 46, 137-155.
18. Baup, F., E. Mougin, P. de Rosnay, F. Timouk & I. Chenerie (2007) Surface Soil Moisture Estimation over the Amma Sahelian Site in Mali Using Envisat/Asar Data. *Remote Sensing of Environment*, 109, 473-481.
19. Bindlish, R. & A. P. Barros (2000) Multifrequency Soil Moisture Inversion from Sar Measurements with the Use of Iem. *Remote Sensing of Environment*, 71, 67-88.
20. Bittelli, M. (2011) Measuring Soil Water Content: A Review. *Horttechnology*, 21, 293-300.
21. Blaes, X. & P. Defourny (2008) Characterizing Bidimensional Roughness of Agricultural Soil Surfaces for Sar Modeling. *Geoscience and Remote Sensing, IEEE Transactions on*, 46, 4050-4061.
22. Blenkinsop, S. & H. J. Fowler (2007) Changes in European Drought Characteristics Projected by the Prudence Regional Climate Models. *International Journal of Climatology*, 27, 1595-1610.
23. Blonquist, J. M., S. B. Jones & D. A. Robinson (2005) Standardizing Characterization of Electromagnetic Water Content Sensors: Part 2. Evaluation of Seven Sensing Systems. *Vadose Zone Journal*, 4, 1059-1069.
24. Brogioni, M., S. Pettinato, G. Macelloni, S. Paloscia, P. Pampaloni, N. Pierdicca & F. Ticconi (2010) Sensitivity of Bistatic Scattering to Soil Moisture and Surface Roughness of Bare Soils. *International Journal of Remote Sensing*, 31, 4227-4255.
25. Callens, M., N. E. C. Verhoest & M. W. J. Davidson (2006) Parameterization of Tillage-Induced Single-Scale Soil Roughness from 4-M Profiles. *Geoscience and Remote Sensing, IEEE Transactions on*, 44, 878-888.
26. Chen, J. M., P. M. Rich, S. T. Gower, J. M. Norman & S. Plummer (1997) Leaf Area Index of Boreal Forests: Theory, Techniques, and Measurements. *Journal of Geophysical Research-Atmospheres*, 102, 29429-29443.
27. Chen, K. S., W. Tzong-Dar, T. Leung, L. Qin, S. Jiancheng & A. K. Fung (2003) Emission of Rough Surfaces Calculated by the Integral Equation Method with Comparison to Three-Dimensional Moment Method Simulations. *Geoscience and Remote Sensing, IEEE Transactions on*, 41, 90-101.
28. Chessa, P. A. & A. Delitala. 1997. *Il Clima Della Sardegna*. Sassari.
29. Chow, V. T., D. R. Maidment & L. W. Mays. 1988. *Applied Hydrology*. New York: McGraw-Hill.
30. Cloude, S. R. & E. Pottier (1996) A Review of Target Decomposition Theorems in Radar Polarimetry. *Ieee Transactions on Geoscience and Remote Sensing*, 34, 498-518.
31. Cognard, A. L., C. Loumagne, M. Normand, P. Olivier, C. Otle, D. Vidalmadjar, S. Louahala & A. Vidal (1995) Evaluation of the Ers-1 Synthetic Aperture Radar Capacity to Estimate Surface Soil-Moisture - 2-Year Results over the Naizin Watershed. *Water Resources Research*, 31, 975-982.
32. Crimmins, T. R. (1985) Geometric Filter for Speckle Reduction. *Applied Optics*, 24, 1438-1443.
33. --- (1986) Geometric Filter for Reducing Speckle. *Optical Engineering*, 25, 651-654.
34. Curran, P. J. (1988) The Semivariogram in Remote-Sensing - an Introduction. *Remote Sensing of Environment*, 24, 493-507.
35. Darboux, F. & C. Huang (2003) An Instantaneous-Profile Laser Scanner to Measure Soil Surface Microtopography. *Soil Science Society of America Journal*, 67, 92-99.



36. Davidson, M. W. J., T. Le Toan, F. Mattia, G. Satalino, T. Manninen & M. Borgeaud (2000) On the Characterization of Agricultural Soil Roughness for Radar Remote Sensing Studies. *IEEE Transactions on Geoscience and Remote Sensing*, 38, 630-640.
37. Deroin, J. P., A. Company & A. Simonin (1997) An Empirical Model for Interpreting the Relationship between Backscattering and Arid Land Surface Roughness as Seen with the Sar. *Geoscience and Remote Sensing, IEEE Transactions on*, 35, 86-92.
38. Diffenbaugh, N. S., J. S. Pal, F. Giorgi & X. J. Gao (2007) Heat Stress Intensification in the Mediterranean Climate Change Hotspot. *Geophysical Research Letters*, 34.
39. Dubois, P. C., J. Van Zyl & T. Engman (1995) Measuring Soil-Moisture with Imaging Radars. *IEEE Transactions on Geoscience and Remote Sensing*, 33, 915-926.
40. Duce, P., A. Arca, S. Canu, D. Spano & A. Motroni. 2004. Effect of Future Climatic Variability on Agriculture in a Mediterranean Region. CNR-Institute of Biometeorology, Sassari.
41. ESA (2007) Asar Product Handbook.
42. Ferrazzoli, P., S. Paloscia, P. Pampaloni, G. Schiavon, S. Sigismondi & D. Solimini (1997) The Potential of Multifrequency Polarimetric Sar in Assessing Agricultural and Arboreous Biomass. *Geoscience and Remote Sensing, IEEE Transactions on*, 35, 5-17.
43. Flocas, H. A., M. Hatzaki, K. Tolika, C. Anagnostopoulou, E. Kostopoulou, C. Giannakopoulos, E. Kolokytha & I. Tegoulas (2011) Ability of Rcm/Gcm Couples to Represent the Relationship of Large Scale Circulation to Climate Extremes over the Mediterranean Region. *Climate Research*, 46, 197-209.
44. Frost, V. S., J. A. Stiles, K. S. Shanmugam, J. C. Holtzman & S. A. Smith (1981) An Adaptive Filter for Smoothing Noisy Radar Images. *Proceedings of the Ieee*, 69, 133-135.
45. Fung, A. K. 1994. *Microwave Scattering and Emission Models and Their Applications*. Boston ; London: Artech House.
46. Fung, A. K., Z. Li & K. S. Chen (1992) Backscattering from a Randomly Rough Dielectric Surface. *Geoscience and Remote Sensing, IEEE Transactions on*, 30, 356-369.
47. Fung, A. K. & G. W. Pan (1987) A Scattering Model for Perfectly Conducting Random Surfaces I. Model Development. *International Journal of Remote Sensing*, 8, 1579 - 1593.
48. Gabriels, D. & M. d. Boodt. 1980. *Assessment of Erosion*. Chichester: Wiley.
49. Gherboudj, I., R. Magagi, A. A. Berg & B. Toth (2011) Soil Moisture Retrieval over Agricultural Fields from Multi-Polarized and Multi-Angular Radarsat-2 Sar Data. *Remote Sensing of Environment*, 115, 33-43.
50. Hajnsek, I., T. Jagdhuber, H. Schon & K. P. Papathanassiou (2009) Potential of Estimating Soil Moisture under Vegetation Cover by Means of PolSar. *Geoscience and Remote Sensing, IEEE Transactions on*, 47, 442-454.
51. Hajnsek, I., E. Pottier & S. R. Cloude (2003) Inversion of Surface Parameters from Polarimetric Sar. *IEEE Transactions on Geoscience and Remote Sensing*, 41, 727-744.
52. Hallikainen, M. T., F. T. Ulaby, M. C. Dobson, M. A. Elrayes & L. K. Wu (1985) Microwave Dielectric Behavior of Wet Soil .1. Empirical-Models and Experimental-Observations. *IEEE Transactions on Geoscience and Remote Sensing*, 23, 25-34.
53. Heng, B. C. P., J. H. Chandler & A. Armstrong (2010) Applying Close Range Digital Photogrammetry in Soil Erosion Studies. *Photogrammetric Record*, 25, 240-265.
54. Hillel, D. 1998. *Environmental Soil Physics*. San Diego, CA: Academic Press.
55. Houser, P. R., W. J. Shuttleworth, J. S. Famiglietti, H. V. Gupta, K. H. Syed & D. C. Goodrich (1998) Integration of Soil Moisture Remote Sensing and Hydrologic Modeling Using Data Assimilation. *Water Resources Research*, 34, 3405-3420.
56. Huang, S. W., L. Tsang, E. G. Njoku & K. S. Chan (2010) Backscattering Coefficients, Coherent Reflectivities, and Emissivities of Randomly Rough Soil Surfaces at L-Band for Smap Applications Based on Numerical Solutions of Maxwell Equations in Three-

- Dimensional Simulations. *Ieee Transactions on Geoscience and Remote Sensing*, 48, 2557-2568.
57. IPCC. 2007. Climate Change 2007: Synthesis Report.
  58. Jester, W. & A. Klik (2005) Soil Surface Roughness Measurement - Methods, Applicability, and Surface Representation. *Catena*, 64, 174-192.
  59. Jonard, F., L. Weihermuller, K. Z. Jadoon, M. Schwank, H. Vereecken & S. Lambot (2011) Mapping Field-Scale Soil Moisture with L-Band Radiometer and Ground-Penetrating Radar over Bare Soil. *Ieee Transactions on Geoscience and Remote Sensing*, 49, 2863-2875.
  60. Jury, W. A. & R. Horton. 2004. *Soil Physics*. Hoboken, NJ ; [Chichester]: John Wiley.
  61. Kelleners, T. J., G. B. Paige & S. T. Gray (2009) Measurement of the Dielectric Properties of Wyoming Soils Using Electromagnetic Sensors. *Soil Science Society of America Journal*, 73, 1626-1637.
  62. Lascelles, B., D. Favis-Mortlock, T. Parsons & J. Boardman (2002) Automated Digital Photogrammetry: A Valuable Tool for Small-Scale Geomorphological Research for the Non-Photogrammetrist? *Transactions in GIS*, 6, 5-15.
  63. Le Morvan, A., M. Zribi, N. Baghdadi & A. Chanzy (2008) Soil Moisture Profile Effect on Radar Signal Measurement. *Sensors*, 8, 256-270.
  64. Lee, J. S. (1980) Digital Image-Enhancement and Noise Filtering by Use of Local Statistics. *Ieee Transactions on Pattern Analysis and Machine Intelligence*, 2, 165-168.
  65. --- (1981) Refined Filtering of Image Noise Using Local Statistics. *Computer Graphics and Image Processing*, 15, 380-389.
  66. --- (1983) A Simple Speckle Smoothing Algorithm for Synthetic Aperture Radar Images. *Ieee Transactions on Systems Man and Cybernetics*, 13, 85-89.
  67. Lee, J. S., M. R. Grunes & S. A. Mango (1991) Speckle Reduction in Multipolarization, Multifrequency Sar Imagery. *Geoscience and Remote Sensing, IEEE Transactions on*, 29, 535-544.
  68. Lee, J. S., L. Jurkevich, P. Dewaele, P. Wambacq & A. Oosterlinck (1994) Speckle Filtering of Synthetic Aperture Radar Images: A Review. *Remote Sensing Reviews*, 8, 313 - 340.
  69. Li, X. Y., S. Contreras, A. Sole-Benet, Y. Canton, F. Domingo, R. Lazaro, H. Lin, B. Van Wesemael & J. Puigdefabregas (2011) Controls of Infiltration-Runoff Processes in Mediterranean Karst Rangelands in Se Spain. *Catena*, 86, 98-109.
  70. Liang, L., S. Peng, J. Sun, L. Chen & Y. Cao (2010) Estimation of Annual Potential Evapotranspiration at Regional Scale Based on the Effect of Moisture on Soil Respiration. *Ecological Modelling*, 221, 2668-2674.
  71. Lievens, H., N. E. C. Verhoest, E. De Keyser, H. Vernieuwe, P. Matgen, J. Alvarez-Mozos & B. De Baets (2011) Effective Roughness Modelling as a Tool for Soil Moisture Retrieval from C-and L-Band Sar. *Hydrology and Earth System Sciences*, 15, 151-162.
  72. Lievens, H., H. Vernieuwe, J. Alvarez-Mozos, B. De Baets & N. E. C. Verhoest (2009) Error in Radar-Derived Soil Moisture Due to Roughness Parameterization: An Analysis Based on Synthetical Surface Profiles. *Sensors*, 9, 1067-1093.
  73. Linder, W. 2003. *Digital Photogrammetry : Theory and Applications*. Berlin ; London: Springer.
  74. Loew, A., R. Ludwig & W. Mauser (2006a) Derivation of Surface Soil Moisture from Envisat Asar Wide Swath and Image Mode Data in Agricultural Areas. *Ieee Transactions on Geoscience and Remote Sensing*, 44, 889-899.
  75. Loew, A. & W. Mauser (2006b) A Semiempirical Surface Backscattering Model for Bare Soil Surfaces Based on a Generalized Power Law Spectrum Approach. *Ieee Transactions on Geoscience and Remote Sensing*, 44, 1022-1035.

76. Ludwig, R., R. Roson, C. Zografos & G. Kallis (2011) Towards an Inter-Disciplinary Research Agenda on Climate Change, Water and Security in Southern Europe and Neighboring Countries. *Environmental Science & Policy*, In Press, Corrected Proof.
77. Macelloni, G., G. Nesti, P. Pampaloni, S. Sigismondi, D. Tarchi & S. Lolli (2000) Experimental Validation of Surface Scattering and Emission Models. *Ieee Transactions on Geoscience and Remote Sensing*, 38, 459-469.
78. Madgwick, H. A. & Brumfiel, G. I. (1969) Use of Hemispherical Photographs to Assess Light Climate in Forest. *Journal of Ecology*, 57, 537-&.
79. Marzahn, P. & R. Ludwig (2009) On the Derivation of Soil Surface Roughness from Multi Parametric Polarsar Data and Its Potential for Hydrological Modeling. *Hydrology and Earth System Sciences*, 13, 381-394.
80. Mattia, F., M. W. J. Davidson, T. Le Toan, C. M. F. D'Haese, N. E. C. Verhoest, A. M. Gatti & M. Borgeaud (2003) A Comparison between Soil Roughness Statistics Used in Surface Scattering Models Derived from Mechanical and Laser Profilers. *Ieee Transactions on Geoscience and Remote Sensing*, 41, 1659-1671.
81. Mattia, F., G. Satalino, L. Dente & G. Pasquariello (2006) Using a Priori Information to Improve Soil Moisture Retrieval from Envisat Asar Ap Data in Semiarid Regions. *Ieee Transactions on Geoscience and Remote Sensing*, 44, 900-912.
82. Mattia, F., G. Satalino, V. R. N. Pauwels & A. Loew (2009) Soil Moisture Retrieval through a Merging of Multi-Temporal L-Band Sar Data and Hydrologic Modelling. *Hydrology and Earth System Sciences*, 13, 343-356.
83. MDA. 2011. Radarsat-2 Product Details.
84. Merel, A. P. & P. J. Farres (1998) The Monitoring of Soil Surface Development Using Analytical Photogrammetry. *Photogrammetric Record*, 16, 331-345.
85. Merzouki, A., A. Bannari, P. M. Teillet & D. J. King (2008) Geostatistical Characterization of Spatial Variability of Soil Moisture with the Help of Maps from Radarsat-1 C-Band Synthetic Aperture Radar Data. *Canadian Journal of Remote Sensing*, 34, 376-389.
86. Merzouki, A., H. McNairn & A. Pacheco (2010) Evaluation of the Dubois, Oh, and Iem Radar Backscatter Models over Agricultural Fields Using C-Band Radarsat-2 Sar Image Data. *Canadian Journal of Remote Sensing*, 36, S274-S286.
87. Miller, J. B. (1967) A Formula for Average Foliage Density. *Australian Journal of Botany*, 15, 141-&.
88. Miller, J. D. & G. J. Gaskin. Thetaprobe MI2x: Principles of Operation and Applications.
89. Milly, P. C. D., K. A. Dunne & A. V. Vecchia (2005) Global Pattern of Trends in Streamflow and Water Availability in a Changing Climate. *Nature*, 438, 347-350.
90. Moran, M. S., D. C. Hymer, J. G. Qi & E. E. Sano (2000) Soil Moisture Evaluation Using Multi-Temporal Synthetic Aperture Radar (Sar) in Semiarid Rangeland. *Agricultural and Forest Meteorology*, 105, 69-80.
91. Moran, M. S., C. D. Peters-Lidard, J. M. Watts & S. McElroy (2004) Estimating Soil Moisture at the Watershed Scale with Satellite-Based Radar and Land Surface Models. *Canadian Journal of Remote Sensing*, 30, 805-826.
92. Morena, L. C., K. V. James & J. Beck (2004) An Introduction to the Radarsat-2 Mission. *Canadian Journal of Remote Sensing*, 30, 221-234.
93. Nearing, G. S., M. S. Moran, K. R. Thorp, C. D. H. Collins & D. C. Slack (2010) Likelihood Parameter Estimation for Calibrating a Soil Moisture Model Using Radar Backscatter. *Remote Sensing of Environment*, 114, 2564-2574.
94. Norrant, C. & A. Douguedroit (2006) Monthly and Daily Precipitation Trends in the Mediterranean (1950-2000). *Theoretical and Applied Climatology*, 83, 89-106.
95. Novak, L. M. & M. C. Burl (1990) Optimal Speckle Reduction in Polarimetric Sar Imagery. *Ieee Transactions on Aerospace and Electronic Systems*, 26, 293-305.

96. Oh, Y. (2004) Quantitative Retrieval of Soil Moisture Content and Surface Roughness from Multipolarized Radar Observations of Bare Soil Surfaces. *Ieee Transactions on Geoscience and Remote Sensing*, 42, 596-601.
97. Oh, Y. & Y. C. Kay (1998) Condition for Precise Measurement of Soil Surface Roughness. *Ieee Transactions on Geoscience and Remote Sensing*, 36, 691-695.
98. Oh, Y., K. Sarabandi & F. T. Ulaby (1992) An Empirical-Model and an Inversion Technique for Radar Scattering from Bare Soil Surfaces. *Ieee Transactions on Geoscience and Remote Sensing*, 30, 370-381.
99. --- (1993) An Empirical-Model for Phase Difference Statistics of Rough Surfaces. *Igarss'93: Better Understanding of Earth Environment, Vols I-Iv*, 1003-1005.
100. ---. 1994. An Inversion Algorithm for Retrieving Soil Moisture and Surface Roughness from Polarimetric Radar Observation. In *Geoscience and Remote Sensing Symposium, 1994. IGARSS '94. Surface and Atmospheric Remote Sensing: Technologies, Data Analysis and Interpretation., International*, 1582-1584 vol.3.
101. --- (2002) Semi-Empirical Model of the Ensemble-Averaged Differential Mueller Matrix for Microwave Backscattering from Bare Soil Surfaces. *Ieee Transactions on Geoscience and Remote Sensing*, 40, 1348-1355.
102. Oliver, M. A. & R. Webster (1986) Semi-Variograms for Modeling the Spatial Pattern of Landform and Soil Properties. *Earth Surface Processes and Landforms*, 11, 491-504.
103. Pierdicca, N., P. Castracane & L. Pulvirenti (2008) Inversion of Electromagnetic Models for Bare Soil Parameter Estimation from Multifrequency Polarimetric Sar Data. *Sensors*, 8, 8181-8200.
104. Porcello, L. J., N. G. Massey, R. B. Innes & J. M. Marks (1976) Speckle Reduction in Synthetic-Aperture Radars. *Journal of the Optical Society of America*, 66, 1305-1311.
105. Rahman, M. M., M. S. Moran, D. P. Thoma, R. Bryant, C. D. H. Collins, T. Jackson, B. J. Orr & M. Tischler (2008) Mapping Surface Roughness and Soil Moisture Using Multi-Angle Radar Imagery without Ancillary Data. *Remote Sensing of Environment*, 112, 391-402.
106. Rahman, M. M., M. S. Moran, D. P. Thoma, R. Bryant, E. E. Sano, C. D. H. Collins, S. Skirvin, C. Kershner & B. J. Orr (2007) A Derivation of Roughness Correlation Length for Parameterizing Radar Backscatter Models. *International Journal of Remote Sensing*, 28, 3995-4012.
107. Rao, K. S., Y. S. Rao & H. K. A. Jassar (2008) Retrieval of Soil Moisture Using Sir-C Polarimetric Data. *Photonirvachak-Journal of the Indian Society of Remote Sensing*, 36, 109-122.
108. Reichle, R. H., J. P. Walker, R. D. Koster & P. R. Houser (2002) Extended Versus Ensemble Kalman Filtering for Land Data Assimilation. *Journal of Hydrometeorology*, 3, 728-740.
109. Richards, J. A. 2009. *Remote Sensing with Imaging Radar*. Heidelberg: Springer.
110. Rieke-Zapp, D. H. & M. A. Nearing (2005) Digital Close Range Photogrammetry for Measurement of Soil Erosion. *Photogrammetric Record*, 20, 69-87.
111. Robert, A. & K. S. Richards (1988) On the Modeling of Sand Bedforms Using the Semivariogram. *Earth Surface Processes and Landforms*, 13, 459-473.
112. Rombach, M. & W. Mauser (1997) Multi-Annual Analysis of Ers Surface Soil Moisture Measurements of Different Land Uses. *Third Ers Symposium on Space at the Service of Our Environment, Vol 1*, 414, 27-34.
113. Rosich, B. & P. Meadows. 2004. Absolute Calibration of Asar Level 1 Products. ESA/ESRIN.
114. RSI. 2000. Radarsat Data Product Specification. RADARSAT International.
115. Ryerson, R. A. & American Society for Photogrammetry and Remote Sensing. 1998. *Manual of Remote Sensing*. New York: J. Wiley.
116. Safa, F. & G. Flouzat (1989) Speckle Removal on Radar Imagery Based on Mathematical Morphology. *Signal Processing*, 16, 319-333.

117. Sano, E. E. 1997. Sensitivity Analysis of C- and Ku-Band Synthetic Aperture Radar Data to Soil Moisture Content in a Semiarid Region. In *Department of Soil, Water and Environmental Science* University of Arizona.
118. Santanello, J. A., C. D. Peters-Lidard, M. E. Garcia, D. M. Mocko, M. A. Tischler, M. S. Moran & D. P. Thoma (2007) Using Remotely-Sensed Estimates of Soil Moisture to Infer Soil Texture and Hydraulic Properties across a Semi-Arid Watershed. *Remote Sensing of Environment*, 110, 79-97.
119. Sarabandi, K. (1992) Derivation of Phase Statistics from the Mueller Matrix. *Radio Science*, 27, 553-560.
120. Sarabandi, K., Y. Oh & F. T. Ulaby (1992) Measurement and Calibration of Differential Mueller Matrix of Distributed Targets. *IEEE Transactions on Antennas and Propagation*, 40, 1524-1532.
121. Saradjian, M. R. & M. Hosseini (2011) Soil Moisture Estimation by Using Multipolarization Sar Image. *Advances in Space Research*, 48, 278-286.
122. Schelde, K., R. Ringgaard, M. Herbst, A. Thomsen, T. Friborg & H. Sogaard (2011) Comparing Evapotranspiration Rates Estimated from Atmospheric Flux and Tdr Soil Moisture Measurements. *Vadose Zone Journal*, 10, 78-83.
123. Schmid, J. 2008. Wasserhaushaltsmodellierung in Einem Mediterranen Landwirtschaftsraum (Campidano, Sardinien). In *Department of Geography*. Munich: University of Munich.
124. Shi, J. C., K. S. Chen & Ieee. 2005. Estimation of Bare Surface Soil Moisture with L-Band Multi-Polarization Radar Measurements. In *Igarss 2005: Ieee International Geoscience and Remote Sensing Symposium, Vols 1-8, Proceedings*, 2191-2194. New York: Ieee.
125. Skolnik, M. I. 2001. *Introduction to Radar Systems*. Boston: McGraw Hill.
126. Song, K. J., X. B. Zhou & Y. Fan (2009) Empirically Adopted Iem for Retrieval of Soil Moisture from Radar Backscattering Coefficients. *Ieee Transactions on Geoscience and Remote Sensing*, 47, 1662-1672.
127. Srivastava, H. S., P. Patel, M. L. Manchanda & S. Adiga (2003) Use of Multiincidence Angle Radarsat-1 Sar Data to Incorporate the Effect of Surface Roughness in Soil Moisture Estimation. *Geoscience and Remote Sensing, IEEE Transactions on*, 41, 1638-1640.
128. Storm, H., T. Heckelei & C. Heidecke (2011) Estimating Irrigation Water Demand in the Moroccan Draa Valley Using Contingent Valuation. *Journal of environmental management*, 92, 2803-9.
129. Susan Moran, M., D. C. Hymer, J. Qi & E. E. Sano (2000) Soil Moisture Evaluation Using Multi-Temporal Synthetic Aperture Radar (Sar) in Semiarid Rangeland. *Agricultural and Forest Meteorology*, 105, 69-80.
130. Svoray, T. & M. Shoshany (2004) Multi-Scale Analysis of Intrinsic Soil Factors from Sar-Based Mapping of Drying Rates. *Remote Sensing of Environment*, 92, 233-246.
131. Tassoudji, M. A., K. Sarabandi & F. T. Ulaby. 1989. Design Consideration and Implementation of the Lcx Polarimetric Scatterometer (Polarscat). Radiation Lab., University of Michigan.
132. Thoma, D. P., M. S. Moran, R. Bryant, M. Rahman, C. D. Holifield-Collins, S. Skirvin, E. E. Sano & K. Slocum (2006) Comparison of Four Models to Determine Surface Soil Moisture from C-Band Radar Imagery in a Sparsely Vegetated Semiarid Landscape. *Water Resources Research*, 42, -.
133. Thoma, D. P., M. S. Moran, R. Bryant, M. M. Rahman, C. D. H. Collins, T. O. Keefer, R. Noriega, I. Osman, S. M. Skirvin, M. A. Tischler, D. D. Bosch, P. J. Starks & C. D. Peters-Lidard (2008) Appropriate Scale of Soil Moisture Retrieval from High Resolution Radar Imagery for Bare and Minimally Vegetated Soils. *Remote Sensing of Environment*, 112, 403-414.

134. Topp, G. C., J. L. Davis & A. P. Annan (1980) Electromagnetic Determination of Soil-Water Content - Measurements in Coaxial Transmission-Lines. *Water Resources Research*, 16, 574-582.
135. Tsai, Y., S. Cohen & R. M. Vogel (2011) The Impacts of Water Conservation Strategies on Water Use: Four Case Studies. *Journal of the American Water Resources Association*, 47, 687-701.
136. Ulaby, F. T., P. C. Dubois & J. vanZyl (1996) Radar Mapping of Surface Soil Moisture. *Journal of Hydrology*, 184, 57-84.
137. Ulaby, F. T., R. K. Moore & A. K. Fung. 1986. *Microwave Remote Sensing: Active and Passive, Volume II: Radar Remote Sensing and Surface Scattering and Emission Theory*. Artech House.
138. Ulaby, F. T., K. Sarabandi & A. Nashashibi (1992) Statistical Properties of the Mueller Matrix of Distributed Targets. *Radar and Signal Processing, IEE Proceedings F*, 139, 136-146.
139. USDA. 2011.
140. van der Linden, P. & J. F. B. Mitchell. 2009. *Ensembles: Climate Change and Its Impacts: Summary of Research and Results from the Ensembles Project*. Met Office Hadley Centre.
141. Vedula, S. & D. N. Kumar (1996) An Integrated Model for Optimal Reservoir Operation for Irrigation of Multiple Crops. *Water Resources Research*, 32, 1101-1108.
142. Verhoest, N. E. C., H. Lievens, W. Wagner, J. Alvarez-Mozos, M. S. Moran & F. Mattia (2008) On the Soil Roughness Parameterization Problem in Soil Moisture Retrieval of Bare Surfaces from Synthetic Aperture Radar. *Sensors*, 8, 4213-4248.
143. Verhoest, N. E. C., P. A. Troch, C. Paniconi & F. P. De Troch (1998) Mapping Basin Scale Variable Source Areas from Multitemporal Remotely Sensed Observations of Soil Moisture Behavior. *Water Resources Research*, 34, 3235-3244.
144. Vivoni, E. R., J. C. Rodriguez & C. J. Watts (2010) On the Spatiotemporal Variability of Soil Moisture and Evapotranspiration in a Mountainous Basin within the North American Monsoon Region. *Water Resources Research*, 46.
145. Vogiatzakis, I. N., G. Pungetti & A. M. Mannion. 2008. *Mediterranean Island Landscapes : Natural and Cultural Approaches*. [Dordrecht?]: Springer.
146. Vorosmarty, C. J., P. Green, J. Salisbury & R. B. Lammers (2000) Global Water Resources: Vulnerability from Climate Change and Population Growth. *Science*, 289, 284-288.
147. Wagner, W., G. Bloschl, P. Pampaloni, J. C. Calvet, B. Bizzarri, J. P. Wigneron & Y. Kerr (2007) Operational Readiness of Microwave Remote Sensing of Soil Moisture for Hydrologic Applications. *Nordic Hydrology*, 38, 1-20.
148. Walker, J. P. & P. R. Houser (2004) Requirements of a Global near-Surface Soil Moisture Satellite Mission: Accuracy, Repeat Time, and Spatial Resolution. *Advances in Water Resources*, 27, 785-801.
149. Walker, J. P., G. R. Willgoose & J. D. Kalma (2002) Three-Dimensional Soil Moisture Profile Retrieval by Assimilation of near-Surface Measurements: Simplified Kalman Filter Covariance Forecasting and Field Application. *Water Resources Research*, 38.
150. Wegmuller, U., C. Matzler, R. Huppi & E. Schanda (1994) Active and Passive Microwave Signature Catalog on Bare Soil (2-12 Ghz). *Geoscience and Remote Sensing, IEEE Transactions on*, 32, 698-702.
151. Wei, L., B. Zhang & M. Wang (2007) Effects of Antecedent Soil Moisture on Runoff and Soil Erosion in Alley Cropping Systems. *Agricultural Water Management*, 94, 54-62.
152. Weiß, M., M. Flörke, L. Menzel & J. Alcamo (2007) Model-Based Scenarios of Mediterranean Droughts. *Advances in Geosciences*, 12, 145-151.

153. Western, A., T. Sadek, W. Li, R. Grayson, H. Turrall & P. Troch (2001) Is Sar Capable of Mapping Small-Scale Spatial Patterns of Soil Moisture? *Igarss 2001: Scanning the Present and Resolving the Future, Vols 1-7, Proceedings*, 40-42.
154. Western, A. W., R. B. Grayson & G. Bloschl (2002) Scaling of Soil Moisture: A Hydrologic Perspective. *Annual Review of Earth and Planetary Sciences*, 30, 149-180.
155. Whalley, W. R. (1993) Considerations on the Use of Time-Domain Reflectometry (Tdr) for Measuring Soil-Water Content. *Journal of Soil Science*, 44, 1-9.
156. Whitmore, T. C., N. D. Brown, M. D. Swaine, D. Kennedy, C. I. Goodwinbailey & W. K. Gong (1993) Use of Hemispherical Photographs in Forest Ecology - Measurement of Gap Size and Radiation Totals in a Bornean Tropical Rain-Forest. *Journal of Tropical Ecology*, 9, 131-151.
157. Woodhouse, I. H. 2006. *Introduction to Microwave Remote Sensing*. New York ; London: Taylor & Francis.
158. Wu, T. D. & K. S. Chen (2004) A Reappraisal of the Validity of the Iem Model for Backs Cattering from Rough Surfaces. *Ieee Transactions on Geoscience and Remote Sensing*, 42, 743-753.
159. Wu, T. D., K. S. Chen, J. C. Shi, H. W. Lee & A. K. Fung (2008) A Study of an Aiem Model for Bistatic Scattering from Randomly Rough Surfaces. *Ieee Transactions on Geoscience and Remote Sensing*, 46, 2584-2598.
160. Zobeck, T. M. & C. A. Onstad (1987) Tillage and Rainfall Effects on Random Roughness: A Review. *Soil and Tillage Research*, 9, 1-20.
161. Zribi, M., N. Baghdadi & C. Guerin (2006a) Analysis of Surface Roughness Heterogeneity and Scattering Behavior for Radar Measurements. *Ieee Transactions on Geoscience and Remote Sensing*, 44, 2438-2444.
162. Zribi, M., N. Baghdadi, N. Holah & O. Fafin (2005) New Methodology for Soil Surface Moisture Estimation and Its Application to Envisat-Asar Multi-Incidence Data Inversion. *Remote Sensing of Environment*, 96, 485-496.
163. Zribi, M., N. Baghdadi, N. Holah & Ieee. 2006b. Estimation of Soil Moisture from Multi-Incidence Asar-Envisat Radar Data. In *2006 Ieee International Geoscience and Remote Sensing Symposium, Vols 1-8*, 2350-2352. New York: Ieee.
164. Zribi, M., A. Chahbi, M. Shabou, Z. Lili-Chabaane, B. Duchemin, N. Baghdadi, R. Amri & A. Chehbouni (2011) Soil Surface Moisture Estimation over a Semi-Arid Region Using Envisat Asar Radar Data for Soil Evaporation Evaluation. *Hydrology and Earth System Sciences*, 15, 345-358.
165. Zribi, M., V. Ciarletti, O. Taconet, J. Paille & P. Boissard (2000) Characterisation of the Soil Structure and Microwave Backscattering Based on Numerical Three-Dimensional Surface Representation: Analysis with a Fractional Brownian Model. *Remote Sensing of Environment*, 72, 159-169.
166. Zribi, M. & M. Dechambre (2003) A New Empirical Model to Retrieve Soil Moisture and Roughness from C-Band Radar Data. *Remote Sensing of Environment*, 84, 42-52.
167. Zribi, M., S. Saux-Picart, C. Andre, L. Descroix, C. Otle & A. Kallel (2007) Soil Moisture Mapping Based on Asar/Envisat Radar Data over a Sahelian Region. *International Journal of Remote Sensing*, 29, 3547-3565.

## Appendix A Regression Results for Adapted Rahman Approach

The equation of Rahman approach Step 3 in Chapter 4 is reassessed for different local incidence angle ranges and polarisations and their  $R^2$  are given.

$$\begin{aligned}
 \ln[m_v(14^\circ, hh)] &= -2.464 + 3.298 \ln(-\sigma^0) - 1.094\{\ln(-\sigma^0)\}^2 + 1.364 \ln(l) \\
 &- 1.170\{\ln(kl)\}^2 + 0.382\{\ln(kl)\}^3 - 0.046\{\ln(kl)\}^4 + 2.794 \ln(ks) \\
 &+ 4.569\{\ln(ks)\}^2 + 0.434\{\ln(ks)\}^3 + 0.086\{\ln(ks)\}^4 \\
 &+ 0.745 \ln(ks) \ln(kl) + 0.297\{\ln(ks)\}^2 \ln(kl) \\
 &+ 0.059\{\ln(ks)\}^3 \ln(kl) - 1.238 \{\ln(kl)\}^2 \ln(ks) \\
 &+ 0.174\{\ln(kl)\}^3 \ln(ks) - 0.170 \{\ln(kl)\}^2 \{\ln(ks)\}^2 \\
 &+ 0.053 \ln(-\sigma^0) \ln(ks) - 1.193 \ln(-\sigma^0) \ln(kl) \\
 &+ 0.254 \ln(-\sigma^0) \{\ln(kl)\}^2 - 0.824 \ln(-\sigma^0) \{\ln(ks)\}^2
 \end{aligned}$$

where  $R^2$  is 0.968.

$$\begin{aligned}
 \ln[m_v(14^\circ, vv)] &= -3.271 + 3.845 \ln(-\sigma^0) - 1.213\{\ln(-\sigma^0)\}^2 + 1.910 \ln(l) \\
 &- 1.352\{\ln(kl)\}^2 + 0.388\{\ln(kl)\}^3 - 0.041\{\ln(kl)\}^4 + 2.178 \ln(ks) \\
 &+ 3.977\{\ln(ks)\}^2 + 0.303\{\ln(ks)\}^3 + 0.067\{\ln(ks)\}^4 \\
 &+ 1.240 \ln(ks) \ln(kl) + 0.496\{\ln(ks)\}^2 \ln(kl) \\
 &+ 0.097\{\ln(ks)\}^3 \ln(kl) - 1.412 \{\ln(kl)\}^2 \ln(ks) \\
 &+ 0.191\{\ln(kl)\}^3 \ln(ks) - 0.190 \{\ln(kl)\}^2 \{\ln(ks)\}^2 \\
 &+ 0.149 \ln(-\sigma^0) \ln(ks) - 1.226 \ln(-\sigma^0) \ln(kl) \\
 &+ 0.245 \ln(-\sigma^0) \{\ln(kl)\}^2 - 0.726 \ln(-\sigma^0) \{\ln(ks)\}^2
 \end{aligned}$$

where  $R^2$  is 0.971.

$$\begin{aligned}
 \ln[m_v(19^\circ, hh)] &= -2.915 + 4.967 \ln(-\sigma^0) - 1.541\{\ln(-\sigma^0)\}^2 - 0.880 \ln(l) \\
 &+ 0.607\{\ln(kl)\}^2 - 0.137\{\ln(kl)\}^3 + 0.006\{\ln(kl)\}^4 + 4.507 \ln(ks) \\
 &+ 4.987\{\ln(ks)\}^2 + 1.128\{\ln(ks)\}^3 + 0.158\{\ln(ks)\}^4 \\
 &- 2.330 \ln(ks) \ln(kl) - 0.909\{\ln(ks)\}^2 \ln(kl) \\
 &- 0.145\{\ln(ks)\}^3 \ln(kl) - 0.187 \{\ln(kl)\}^2 \ln(ks) \\
 &+ 0.074\{\ln(kl)\}^3 \ln(ks) - 0.016 \{\ln(kl)\}^2 \{\ln(ks)\}^2 \\
 &+ 0.073 \ln(-\sigma^0) \ln(ks) - 1.184 \ln(-\sigma^0) \ln(kl) \\
 &+ 0.278 \ln(-\sigma^0) \{\ln(kl)\}^2 - 0.653 \ln(-\sigma^0) \{\ln(ks)\}^2
 \end{aligned}$$

where  $R^2$  is 0.984.



$$\begin{aligned}
 \ln[m_v(19^\circ, vv)] &= -4.673 + 6.248 \ln(-\sigma^0) - 1.808\{\ln(-\sigma^0)\}^2 + 0.104 \ln(l) \\
 &+ 0.067\{\ln(kl)\}^2 - 0.008\{\ln(kl)\}^3 - 0.001\{\ln(kl)\}^4 + 3.579 \ln(ks) \\
 &+ 5.039\{\ln(ks)\}^2 + 0.926\{\ln(ks)\}^3 + 0.135\{\ln(ks)\}^4 \\
 &- 1.560 \ln(ks) \ln(kl) - 0.599\{\ln(ks)\}^2 \ln(kl) \\
 &- 0.077\{\ln(ks)\}^3 \ln(kl) - 0.506 \{\ln(kl)\}^2 \ln(ks) \\
 &+ 0.112\{\ln(kl)\}^3 \ln(ks) - 0.048 \{\ln(kl)\}^2 \{\ln(ks)\}^2 \\
 &+ 0.235 \ln(-\sigma^0) \ln(ks) - 1.208 \ln(-\sigma^0) \ln(kl) \\
 &+ 0.252 \ln(-\sigma^0) \{\ln(kl)\}^2 - 0.496 \ln(-\sigma^0) \{\ln(ks)\}^2
 \end{aligned}$$

where  $R^2$  is 0.987.

$$\begin{aligned}
 \ln[m_v(23^\circ, hh)] &= -3.254 + 5.546 \ln(-\sigma^0) - 1.687\{\ln(-\sigma^0)\}^2 - 1.459 \ln(l) \\
 &+ 1.238\{\ln(kl)\}^2 - 0.326\{\ln(kl)\}^3 + 0.024\{\ln(kl)\}^4 + 4.820 \ln(ks) \\
 &+ 6.472\{\ln(ks)\}^2 + 1.428\{\ln(ks)\}^3 + 0.192\{\ln(ks)\}^4 \\
 &- 3.633 \ln(ks) \ln(kl) - 1.465\{\ln(ks)\}^2 \ln(kl) \\
 &- 0.243\{\ln(ks)\}^3 \ln(kl) + 0.316 \{\ln(kl)\}^2 \ln(ks) \\
 &+ 0.024\{\ln(kl)\}^3 \ln(ks) + 0.062 \{\ln(kl)\}^2 \{\ln(ks)\}^2 \\
 &+ 0.102 \ln(-\sigma^0) \ln(ks) - 1.181 \ln(-\sigma^0) \ln(kl) \\
 &+ 0.284 \ln(-\sigma^0) \{\ln(kl)\}^2 - 0.578 \ln(-\sigma^0) \{\ln(ks)\}^2
 \end{aligned}$$

where  $R^2$  is 0.991.

$$\begin{aligned}
 \ln[m_v(23^\circ, vv)] &= -5.842 + 7.636 \ln(-\sigma^0) - 2.130\{\ln(-\sigma^0)\}^2 - 0.500 \ln(l) \\
 &+ 0.569\{\ln(kl)\}^2 - 0.122\{\ln(kl)\}^3 + 0.008\{\ln(kl)\}^4 + 3.783 \ln(ks) \\
 &+ 5.293\{\ln(ks)\}^2 + 1.198\{\ln(ks)\}^3 + 0.173\{\ln(ks)\}^4 \\
 &- 2.799 \ln(ks) \ln(kl) - 1.104\{\ln(ks)\}^2 \ln(kl) \\
 &- 0.156\{\ln(ks)\}^3 \ln(kl) - 0.056 \{\ln(kl)\}^2 \ln(ks) \\
 &+ 0.069\{\ln(kl)\}^3 \ln(ks) + 0.025 \{\ln(kl)\}^2 \{\ln(ks)\}^2 \\
 &+ 0.301 \ln(-\sigma^0) \ln(ks) - 1.140 \ln(-\sigma^0) \ln(kl) \\
 &+ 0.235 \ln(-\sigma^0) \{\ln(kl)\}^2 - 0.374 \ln(-\sigma^0) \{\ln(ks)\}^2
 \end{aligned}$$

where  $R^2$  is 0.993.

$$\begin{aligned}
 \ln[m_v(29^\circ, hh)] &= -3.288 + 5.423 \ln(-\sigma^0) - 1.671\{\ln(-\sigma^0)\}^2 - 1.230 \ln(l) \\
 &+ 1.525\{\ln(kl)\}^2 - 0.421\{\ln(kl)\}^3 + 0.033\{\ln(kl)\}^4 + 4.099 \ln(ks) \\
 &+ 6.508\{\ln(ks)\}^2 + 1.595\{\ln(ks)\}^3 + 0.210\{\ln(ks)\}^4 \\
 &- 4.403 \ln(ks) \ln(kl) - 1.857\{\ln(ks)\}^2 \ln(kl) \\
 &- 0.318\{\ln(ks)\}^3 \ln(kl) + 0.688 \{\ln(kl)\}^2 \ln(ks) \\
 &- 0.016\{\ln(kl)\}^3 \ln(ks) + 0.128 \{\ln(kl)\}^2 \{\ln(ks)\}^2 \\
 &+ 0.252 \ln(-\sigma^0) \ln(ks) - 1.199 \ln(-\sigma^0) \ln(kl) \\
 &+ 0.274 \ln(-\sigma^0) \{\ln(kl)\}^2 - 0.493 \ln(-\sigma^0) \{\ln(ks)\}^2
 \end{aligned}$$

where  $R^2$  is 0.995.

$$\begin{aligned}
 \ln[m_v(29^\circ, vv)] &= -7.525 + 9.271 \ln(-\sigma^0) - 2.497\{\ln(-\sigma^0)\}^2 - 0.903 \ln(l) \\
 &+ 0.967\{\ln(kl)\}^2 - 0.185\{\ln(kl)\}^3 + 0.012\{\ln(kl)\}^4 + 3.158 \ln(ks) \\
 &+ 5.075\{\ln(ks)\}^2 + 1.374\{\ln(ks)\}^3 + 0.210\{\ln(ks)\}^4 \\
 &- 3.661 \ln(ks) \ln(kl) - 1.473\{\ln(ks)\}^2 \ln(kl) \\
 &- 0.213\{\ln(ks)\}^3 \ln(kl) + 0.323 \{\ln(kl)\}^2 \ln(ks) \\
 &+ 0.027\{\ln(kl)\}^3 \ln(ks) + 0.089 \{\ln(kl)\}^2 \{\ln(ks)\}^2 \\
 &+ 0.440 \ln(-\sigma^0) \ln(ks) - 0.977 \ln(-\sigma^0) \ln(kl) \\
 &+ 0.177 \ln(-\sigma^0) \{\ln(kl)\}^2 - 0.231 \ln(-\sigma^0) \{\ln(ks)\}^2
 \end{aligned}$$

where  $R^2$  is 0.996.

$$\begin{aligned}
 \ln[m_v(41^\circ, hh)] &= -1.441 + 3.131 \ln(-\sigma^0) - 1.213\{\ln(-\sigma^0)\}^2 + 0.527 \ln(l) \\
 &+ 1.365\{\ln(kl)\}^2 - 0.386\{\ln(kl)\}^3 + 0.031\{\ln(kl)\}^4 + 0.650 \ln(ks) \\
 &+ 5.365\{\ln(ks)\}^2 + 1.385\{\ln(ks)\}^3 + 0.161\{\ln(ks)\}^4 \\
 &- 4.141 \ln(ks) \ln(kl) - 1.836\{\ln(ks)\}^2 \ln(kl) \\
 &- 0.326\{\ln(ks)\}^3 \ln(kl) + 0.813 \{\ln(kl)\}^2 \ln(ks) \\
 &- 0.038\{\ln(kl)\}^3 \ln(ks) + 0.160 \{\ln(kl)\}^2 \{\ln(ks)\}^2 \\
 &+ 0.891 \ln(-\sigma^0) \ln(ks) - 1.333 \ln(-\sigma^0) \ln(kl) \\
 &+ 0.222 \ln(-\sigma^0) \{\ln(kl)\}^2 - 0.313 \ln(-\sigma^0) \{\ln(ks)\}^2
 \end{aligned}$$

where  $R^2$  is 0.995.

$$\begin{aligned} \ln[m_v(41^\circ, vv)] &= -11.10 + 12.07 \ln(-\sigma^0) - 3.053\{\ln(-\sigma^0)\}^2 - 0.918 \ln(l) \\ &+ 1.266\{\ln(kl)\}^2 - 0.204\{\ln(kl)\}^3 + 0.013\{\ln(kl)\}^4 + 0.910 \ln(ks) \\ &+ 4.165\{\ln(ks)\}^2 + 1.239\{\ln(ks)\}^3 + 0.245\{\ln(ks)\}^4 \\ &- 3.689 \ln(ks) \ln(kl) - 1.498\{\ln(ks)\}^2 \ln(kl) \\ &- 0.221\{\ln(ks)\}^3 \ln(kl) + 0.542 \{\ln(kl)\}^2 \ln(ks) \\ &- 0.007\{\ln(kl)\}^3 \ln(ks) + 0.128 \{\ln(kl)\}^2 \{\ln(ks)\}^2 \\ &+ 0.660 \ln(-\sigma^0) \ln(ks) - 0.677 \ln(-\sigma^0) \ln(kl) \\ &+ 0.062 \ln(-\sigma^0) \{\ln(kl)\}^2 - 0.242 \ln(-\sigma^0) \{\ln(ks)\}^2 \end{aligned}$$

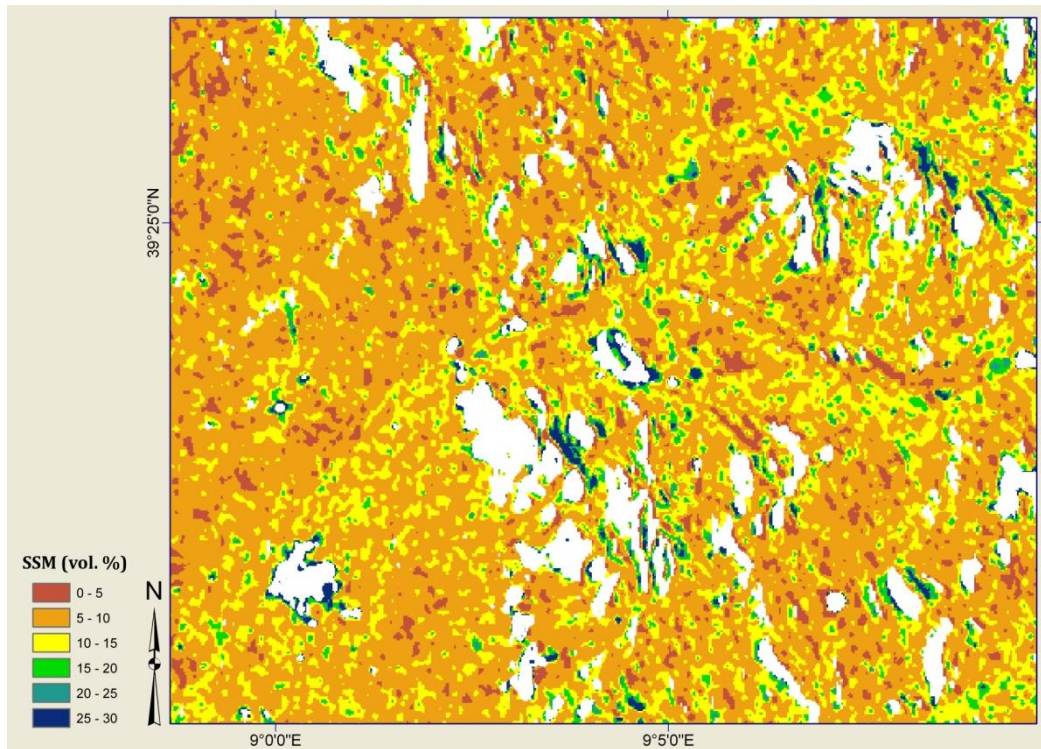
where  $R^2$  is 0.988.

## Appendix B Surface Soil Moisture Maps from the Baghdadi-Rahman Model

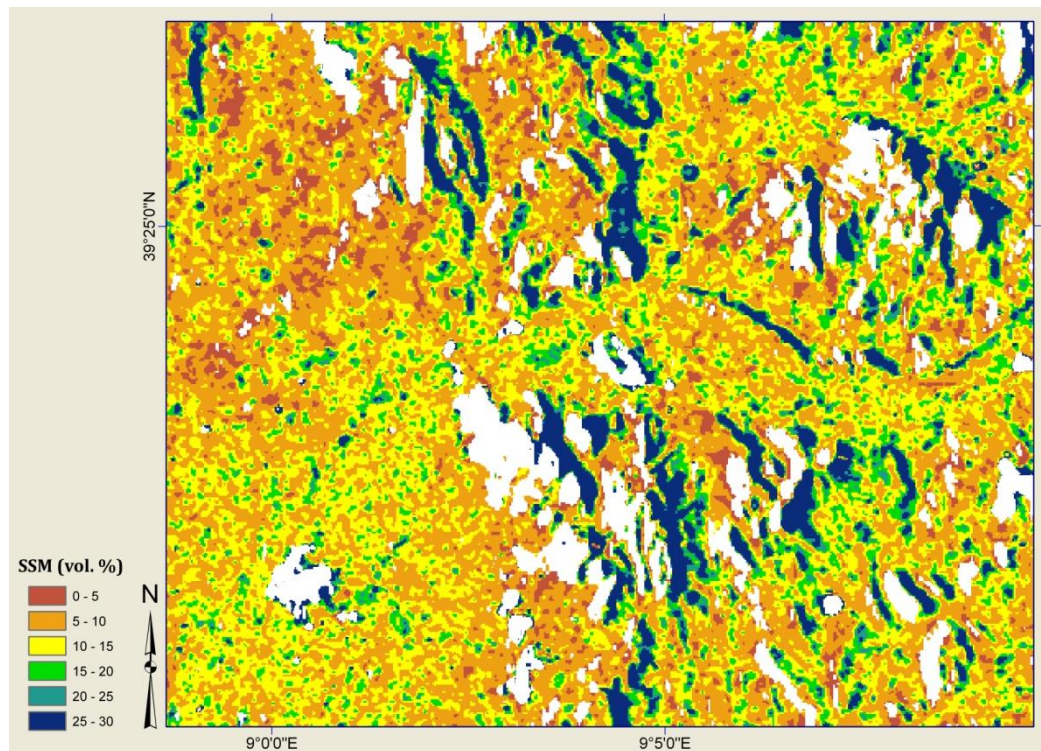
An area of about 200 km<sup>2</sup> is selected for mapping surface soil moisture by applying Baghdadi-Rahman model. The region covers the several towns and villages, such as *San Sperate, Monastir, Nuraminis, Ussana, Donori and Serdiana*, industry parks along the highway, wood lands in mountainous areas, with majority areas with flat cropland. Settlements, mountains areas and open water bodies are marked by a simple threshold of backscattering coefficients. Surface soil moisture maps are illustrated in a date order. Precipitation event on 29<sup>th</sup> May 2008, 6<sup>th</sup> Jun. 2008, 11<sup>th</sup> Jun. 2008, 12<sup>th</sup> Jun. 2008 and 14<sup>th</sup> May 2009 are well recorded from the surface soil moisture pattern as well as the general drying trend through the summer.



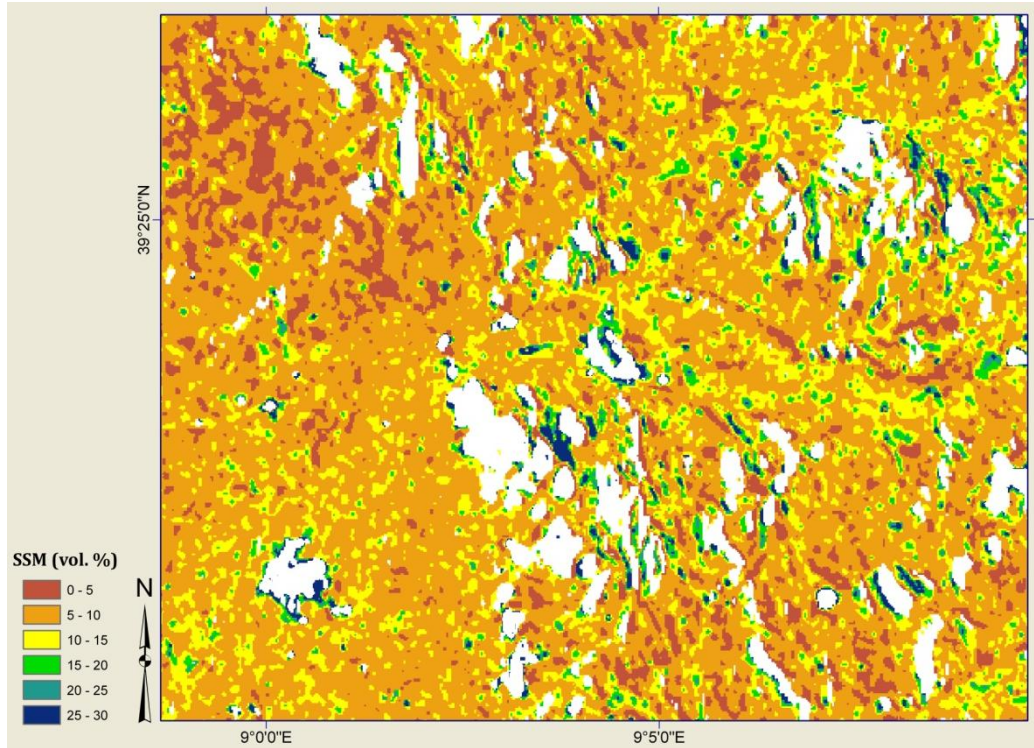
Overview of the mapping region from ETM+ image taken on 27<sup>th</sup> Oct. 2006.



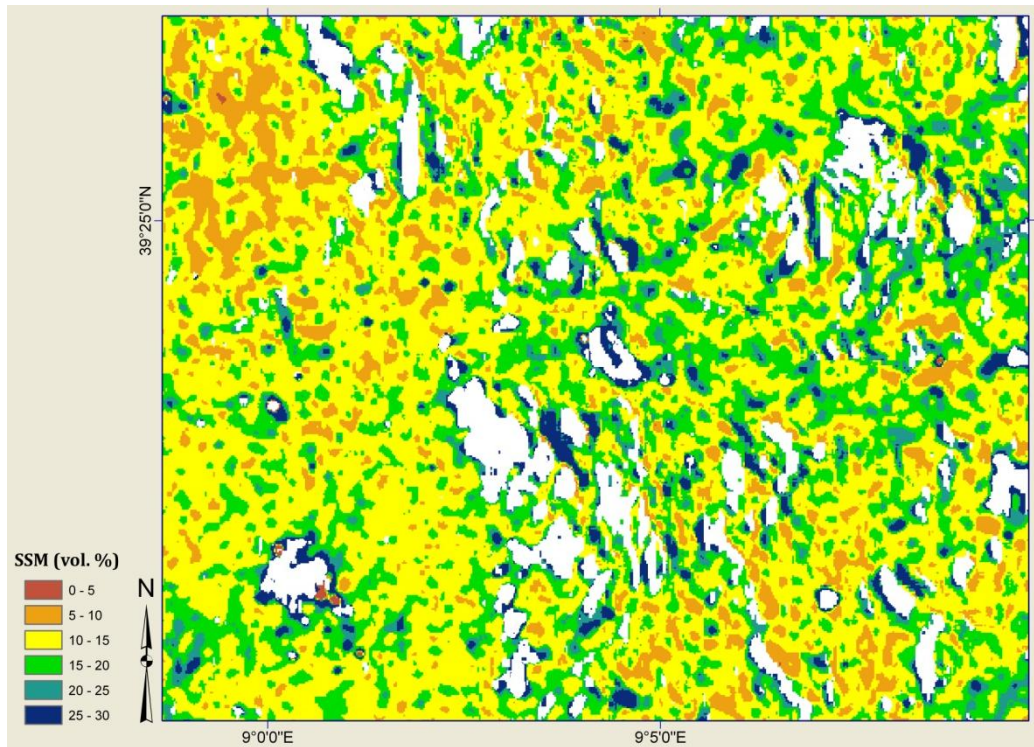
Surface soil moisture map for 22<sup>nd</sup> May 2008.



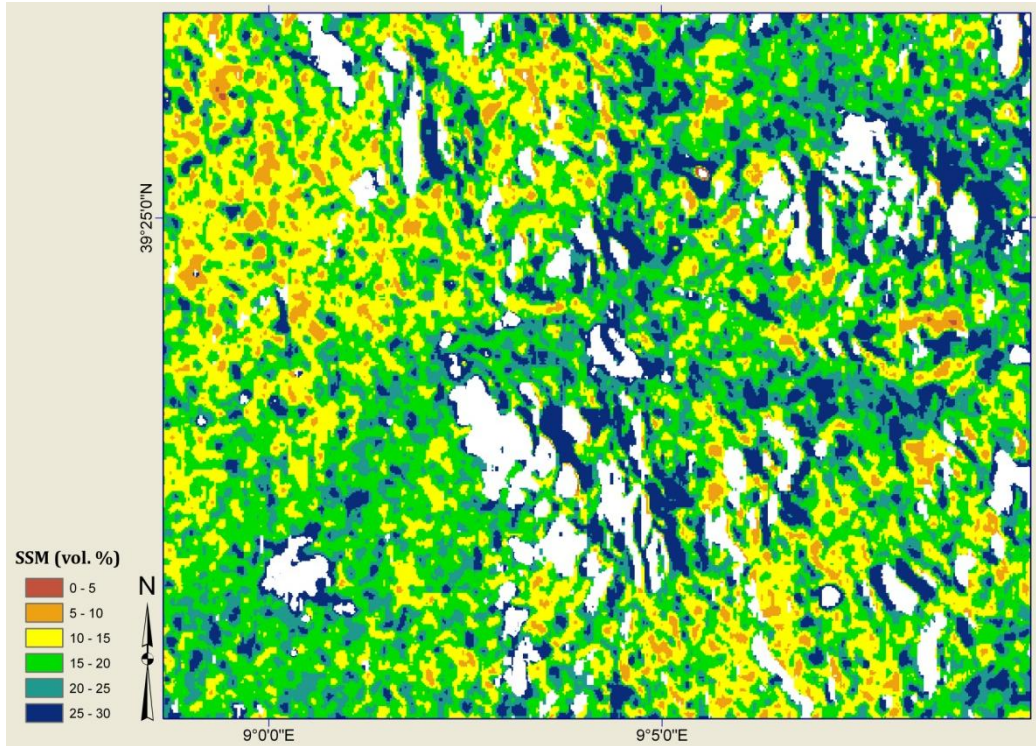
Surface soil moisture map for 27<sup>th</sup> May 2008.



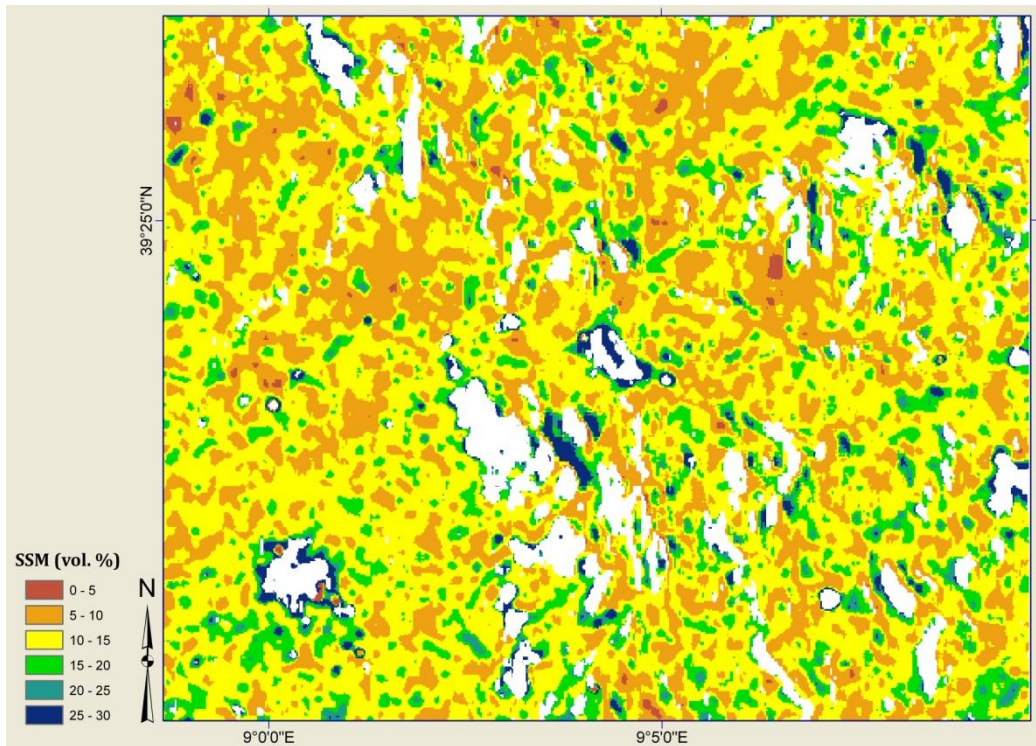
Surface soil moisture map for 28<sup>th</sup> May 2008.



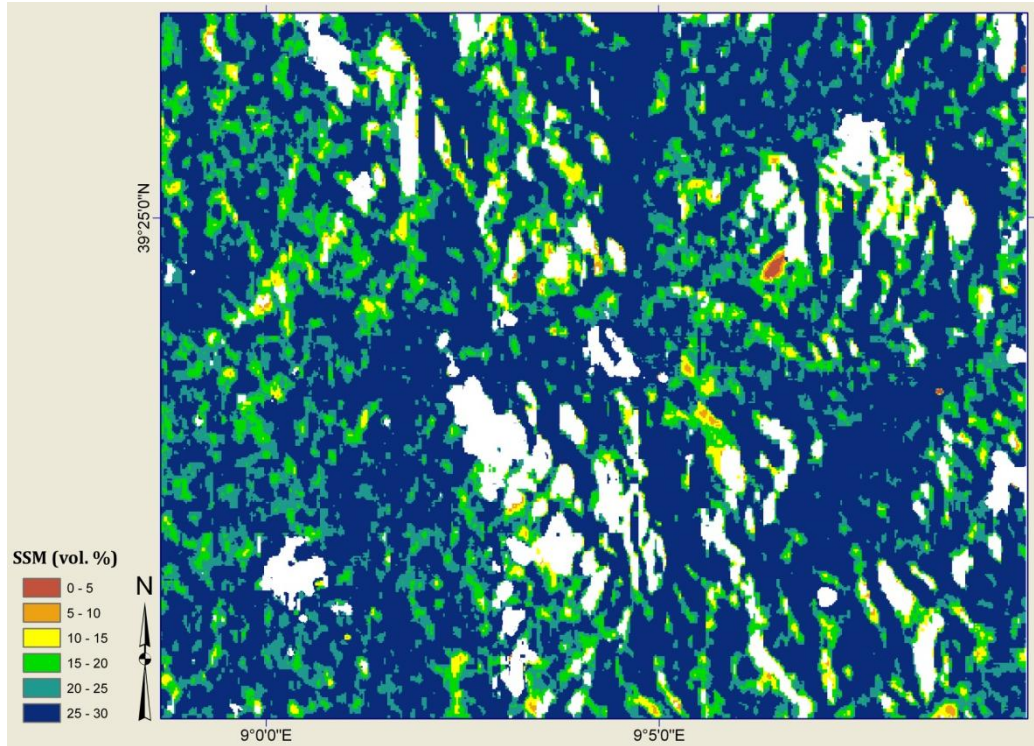
Surface soil moisture map for 31<sup>st</sup> May 2008.



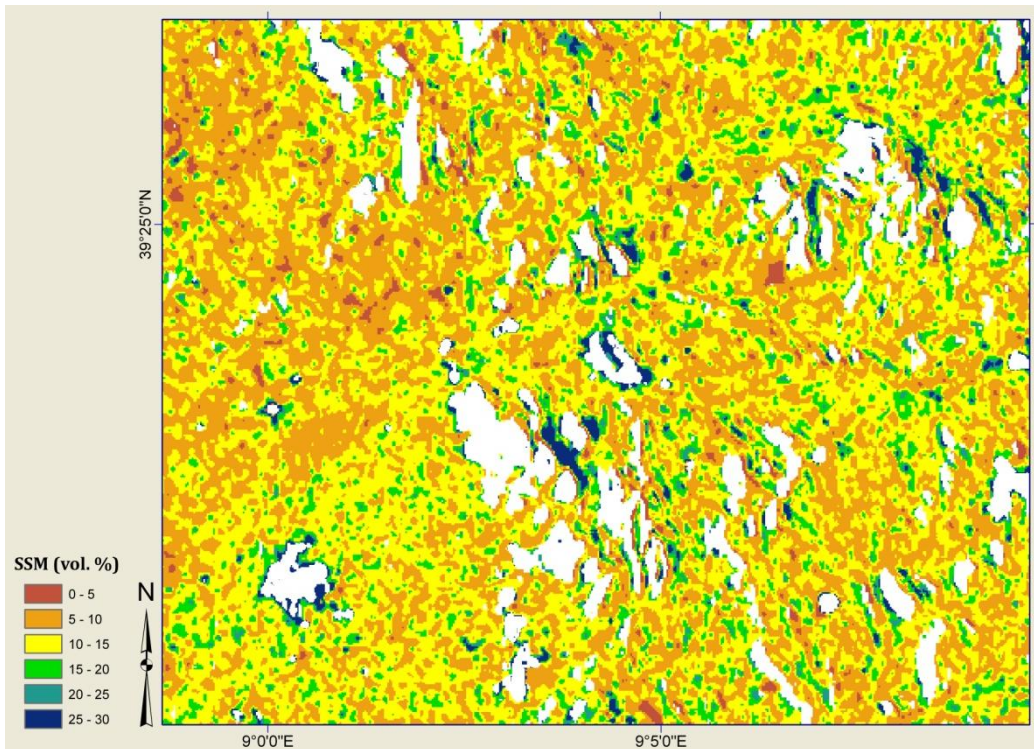
Surface soil moisture map for 16<sup>th</sup> Jun. 2008.



Surface soil moisture map for 13<sup>th</sup> May 2009.

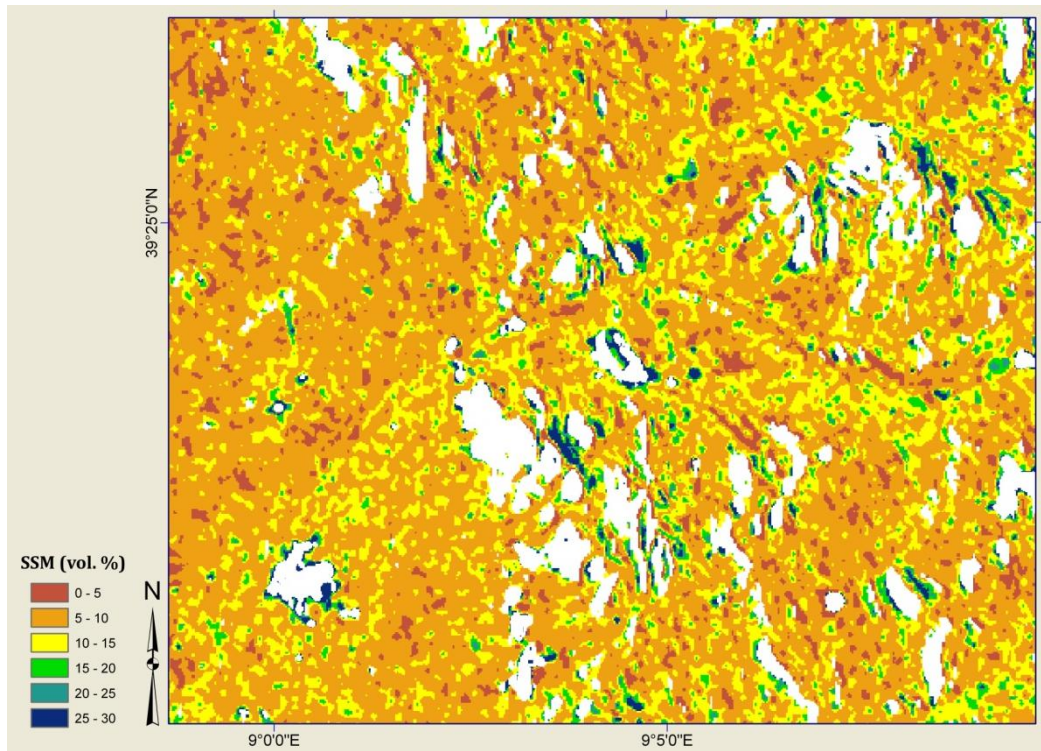


Surface soil moisture map for 16<sup>th</sup> May 2009.



Surface soil moisture map for 22<sup>nd</sup> May 2009.





Surface soil moisture map for 15<sup>th</sup> Jun. 2009.

---

## Curriculum Vitae

### Personal Information

Surname	Dong
First Name	Lu
Date of Birth	29th July 1983
Place of Birth	Wuhan, China
Nationality	Chinese
Marital Status	Single
Home Address	Hansastr.138, Munich, 81373 Germany
Work Address	Luisenstr.37, Department of Geography, LMU Munich, Munich, 80333 Germany
Telephone	+49 (0)89/2180-6665
Email Address	<a href="mailto:l.dong@iggf.geo.uni-muenchen.de">l.dong@iggf.geo.uni-muenchen.de</a>

### Education

2008 – 2011	DAAD Scholarship in „Studies and Research in Sustainability“
2005 – 2007	MSc. (by research) in GIS and Remote Sensing, Durham University, United Kingdom.  Master thesis: Evaluation of high quality topographic data for geomorphological and flood impact studies in upland area: North York Moors, UK
2001 – 2005	BEng. in GIS, Wuhan University, China
1998 – 2001	No. 6 Middle School, Wuhan, China
1995 – 1998	Yucai Middle School, Wuhan, China
1989 – 1995	Huiji Road Primary School, Wuhan, China